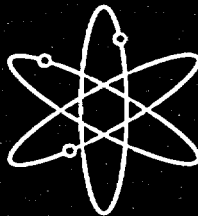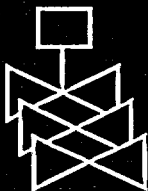# Steam Generator Tube Integrity Program

Semiannual Report
October 1998 – March 1999

Argonne National Laboratory

U.S. Nuclear Regulatory Commission
Office of Nuclear Regulatory Research
Washington, DC 20555-0001

Steam Generator Tube Integrity Program

Semiannual Report
October 1998 – March 1999

Steam Generator Tube Integrity Program:
Semiannual Report October 1998-March 1999

by

D. R. Diercks, S. Bakhtiari, K. E. Kasza, D. S. Kupperman,
S. Majumdar, J. Y. Park, and W. J. Shack

Abstract

This report summarizes work performed by Argonne National Laboratory on the Steam Generator Tube Integrity Program during the period October 1998 through March 1999. The program is divided into five tasks: (1) Assessment of Inspection Reliability, (2) Research on In-Service-Inspection (ISI) Technology, (3) Research on Degradation Modes and Integrity, (4) Integration of Results, Methodology, and Technical Assessments for Current and Emerging Regulatory Issues, and (5) Program Management. Under Task 1, progress is reported on the status of the steam generator tube mock-up, the effect of a thin oxide corrosion product on the eddy current signal from stress corrosion cracks, and the effectiveness of +Point eddy current techniques for profiling cracks and establishing maximum flaw depths. Under Task 2, efforts focused on the multiparameter analysis of eddy current nondestructive evaluation (NDE) results, and estimated depth profiles are provided for a set of 24 laser-notched specimens with single and multiple axial/circumferential notches. Under Task 3, pressurization and leak-rate test results are reported for tubes with electro-discharge machined (EDM) flaws as well as tubes with part-throughwall stress corrosion cracks. The design and construction of a new high-pressure test facility has also been initiated. Laboratory-induced cracking has been produced in hundreds of steam generator tubes that will subsequently be used for the evaluation of NDE equipment and techniques and for pressure and leak-rate testing. In addition, models for predicting the onset of crack growth and for calculating crack opening area and leak rate from a throughwall circumferential crack in a steam generator tube have been developed. Leak-rate models have been validated with tests on specimens with notched EDM slots, and simplified equations for calculating crack opening area have been verified with finite-element calculations. Finally, under Task 4, results of EC and ultrasonic examinations of two cracked test sections Electrosleeved by Framatome Technologies, Inc. are presented.

Contents

Figures

Tables

Executive Summary

Assessment of Inspection Reliability

Most levels of the mock-up have been completed. In addition to a full eddy current (EC) examination, outer diameter (OD) cracks are being examined with dye-penetrant before being incorporated into the mock-up tube bundle. Magnetite in the tube support plate (TSP) crevice is simulated by filling the crevice with magnetic tape or a ferromagnetic fluid. Magnetite-filled epoxy markers are placed on the ends of all test sections to provide a reference for angular location of flaws when collecting data with a rotating pancake coil (RPC) or array probe. Test sections are being inspected with mag-bias and non-mag-biased standard pancake, +Point, and high-frequency coils, as well as with bobbin coils. About 4000 scans of tubes with various combinations of flaws and artifacts have been accumulated and stored. For each scan, the probe passes through the degraded test section, a standard with 18 notches, and an ASME standard. A spreadsheet permits a quick reference to locate the optical disk and file number for any scan of a test section.

An indication that the cracks grown at ANL are representative of field cracks is derived from a comparison of McGuire steam generator bobbin coil voltages and phases with ANL stress corrosion crack (SCC) bobbin coil voltages and phases. A comparison of McGuire voltages and phases from axial ODSCC at the TSPs to voltages and phases from the ANL-grown axial ODSCC shows the values to be similar.

The effect of a corrosion product (thin oxide film) on the EC signal from an SCC is under evaluation. Alloy 600 tubes with axial ODSCC were exposed to PWR water chemistry conditions (300°C and oxygen at the ppb level) for about two months. The cracks were examined with both mag-bias bobbin and +Point coils before and after exposure. The voltages for the bobbin coil increased significantly with the creation of the thin oxide film, but the general shape of the Lissajous figures remained unchanged. In contrast, the results for the +Point coil are inconclusive at this time. The creation of corrosion products in the crack could lead to a reduction in the number of electrically conducting paths from contacting crack faces. In that case, the EC signal would be expected to increase, as observed, while the depth remains essentially the same.

A technique for profiling cracks has been tried. The phase angle from the Lissajous pattern generated by a +Point coil at 300 kHz was, at various deep points along the crack, compared to the phase angle for EDM notches with depths of 40, 60, 80, and 100% throughwall (% TW). Estimates of % TW were made at 1 mm intervals along the crack length, as long as reasonable signal-to-noise ratios were evident. For weaker signals and where phase analysis is not effective (depth <60-70%TW), a depth was established from the phase analysis at relatively deep points, and depth was then correlated with signal amplitude by using a linear extrapolation to 0% TW. As a result, the entire profile of the crack could be made.

Numerous test sections with 80% TW laser-cut slots and various geometrical configurations were examined with a +Point coil to help establish the reliability of +Point

phase analysis to estimate the maximum depth of cracks, especially segmented cracks. The results for 12 test sections are presented in this report. In all cases, the predicted depths of the 80% TW axially oriented laser-cut slots were less than the design depth, despite very high signal-to-noise ratios. The greatest deviation occurred when a ligament was present between the axial slots. Such ligaments provide a current path between slots, resulting in a phase shift of the Lissajous figure. For circumferentially oriented laser-cut slots, the estimate with the +Point coil is greater than the design depth This discrepancy may be due to the lack of contouring of the circumferentially oriented part of the +Point coil to the tube inner surface. The axially oriented part of the coil has a better fit to the inner surface of the tube.

Research on ISI Technology

Research efforts during this reporting period were associated primarily with multiparameter analysis of EC NDE results. Preliminary results are presented first on two separate multifrequency mixing procedures that could help improve bobbin coil (BC) detection of flaw indications in the presence of interfering artifacts at the same axial location along the tube axis. Both direct and indirect mixing techniques were evaluated. This investigation was initiated in part to assess alternate mixing methods that could help compensate for lack of similarity between simulated artifacts in tube standards and those in the field. To assess the validity of independent mix algorithms, BC readings on two tubes with laboratory-grown circumferential and axial stress-corrosion cracking (SCC) at the tube sheet (TS) roll transition region were examined. The outcome of this ongoing study suggests that BC detection could be improved through selective application of direct mixing methods.

A description of recent activities is provided on multiparameter data analysis of EC inspection results. Implementation of a rule-based computer-aided data analysis routine is initially discussed. The algorithm uses multiple-frequency EC readings from rotating probes to estimate the depth profiles of indications in a tube. Preliminary results are also presented on the application of this multifrequency phase-based algorithm to various sets of experimental data acquired with conventional rotating probes. Results of the analysis are presented for a set of 20 tubes that contained laboratory-produced cracks representative of those incorporated into the SG mock-up. Data analysis results are also presented for a single specimen with laboratory-produced cracking that exhibited reportable BC indication with no clear flaw signal from rotating probe inspections (pancake and +Point coils).

Finally, estimated depth profiles are provided for a set of 24 laser-cut specimens with single and multiple axial/circumferential notches (with and without ligaments) that simulate complex cracking geometries. The NDE and nominal flaw size on this set of 24 tubes, originally fabricated for pressure and leak-rate studies under Task 3 of this program, provide a useful means for assessing data analysis algorithms currently under investigation at ANL. Preliminary analyses of data on the laser-cut specimens used inspection data from bobbin and rotating probes. NDE data were initially analyzed with the Eddynet98™ analysis software. Subsequent multiparameter analyses of the laser-cut specimens was carried out with data from the 2.92-mm (0.115-in.)-diameter primary pancake coil of a three-coil rotating probe. Although all flaws were detected with all three techniques, the

sizing estimates vary significantly between bobbin and rotating pancake coil (RPC) probes and to a lesser extent between the two RPC methods. Initial analysis of BC data indicates an overall underestimation of depth for all available flaw types. Results from +Point coil inspections show improved sizing accuracy over the bobbin for the majority of indications and, in particular, for the ligamented flaws. The +Point™ results indicate some underestimation of axial flaw depths, particularly for the ligamented notches, and overestimation of depth for most circumferential flaws. The multiparameter sizing estimates, although closer to the single-frequency +Point estimates, show smaller overall scatter of the sizing results and better agreement with the nominal values for the notch depths.

Research on Degradation Modes and Integrity

The testing of flawed tubes continued in the Pressure and Leak-Rate Test Facility, with tests conducted on axial EDM OD notches of several different lengths and depths, including initial tests on multiple interacting flaws. For comparison with previous results from four laboratory-degraded tubes containing axial ODSCC produced using Na tetrathionate at room temperature (RT), tests have also been conducted on a tube containing an axial ODSCC flaw produced using doped steam. These tests addressed flaw leak stability at constant temperature and varying pressures up to 19.3 MPa (2800 psi). The various types of flaws were tested at both room and elevated temperature.

Results from the tests on tubes containing electro-discharge machined (EDM) notches indicate that the leak rates can be well predicted using a circular-hole orifice model after correcting for curvature effects. For all but the shortest (8.9-mm [0.35-in.]-long) part-throughwall flaw, the ligament rupture pressures were well predicted by structural analysis, and the subsequent flaw opening areas were also in agreement with predictions. Tests were also conducted on tubes containing two aligned axial throughwall notches, each 6.35 mm (0.25 in.) long and 0.19 mm (0.0075 in.) wide, separated by a 0.25-mm (0.01–in.)-long ligament. The ligament remained intact after pressurization to 17.2 MPa (2500 psi) at room temperature, despite a calculated failure pressure of >13.8 MPa (2000 psi), and the observed leak rate was essentially identical to that calculated for the two individual notches using the orifice model. A similar tube tested at 282°C (540°F) exhibited ligament tearing at 15.5 MPa (2250 psi), and the leak rate corresponded to that expected for a widened 0.5-in.-long notch.

Four Alloy 600 tubes with axial ODSCC of nominal length 12.7 mm (0.5 in.) were produced at ANL by exposure to sodium tetrathionate solution, and the results of pressurization tests on these tubes were presented in the previous annual report. A similar tube produced using a doped-steam process has now also been tested using the same procedure to compare its failure and leak-rate behavior with that observed for the ANL tubes. The tube cracked in doped steam also had a nominally 12.7-mm (0.5-in.)-long crack and was tested under both normal and MSLB conditions. Pressure plateaus were held for at least two hours, with shorter duration holds at intermediate pressures if flaw tearing, as indicated by a sudden increase in flow rate through the crack, was observed. The doped-steam cracked tube behaved qualitatively similar to one of the RT cracked tubes under leak testing, though it was slightly stronger, in agreement with pre-test characterization that indicated a slightly shallower maximum flaw depth. The doped-

steam tube, like the RT cracked tubes, exhibited a time-dependent increase of leak rate under constant temperature and pressure, apparently due to progressive ligament rupture. A theoretical basis for predicting such time-dependent ligament rupture is currently lacking.

A room-temperature, high-pressure (up to 52 MPa [0-7,500 psi]), low-flow-rate (45 L/min [12 gpm] max.) tube burst test facility has been designed and is being constructed. This facility will complement the Pressure and Leak-Rate Test Facility bt permitting the failure testing of tubes that cannot be failed at the 21 MPa (3000 psi) maximum pressure of the present system. The continuous pressurized water supply in the high-pressure facility will also permit long-term crack stability and jet-impingement testing, since it will not be limited by a finite water inventory. The new facility may also be used for testing service-degraded steam generator tubes that cannot be sufficiently decontaminated for testing in the Pressure and Leak-Rate Test Facility. A 3100 L (800 gal) water collection tank will allow containment and collection of any residual contamination during the testing of such tubes. It is anticipated that the high-pressure facility will be completed by September 1999.

Laboratory-induced cracking has been produced in hundreds of 22.2-mm (7/8-in.)-diameter Alloy 600 tubes under accelerated (chemically aggressive) conditions. These cracked tubes will be used for the evaluation of NDE equipment and techniques in the steam generator mock-up and for pressure and leak-rate testing. The SCCs produced in these tubes have six different basic configurations, namely circumferential cracks at the inner and outer (ID and OD) surfaces, axial cracks at the ID and OD, and skewed cracks at the ID and OD. Cracking has also been produced in roll-expanded and dented tubes. In some cases, multiple and segmented cracks have been produced. The cracks are detected by visual inspection, dye-penetrant techniques and also by nondestructive EC tests. Additional accelerated tube degradation facilities are being constructed.

Models for predicting the onset of crack growth and for calculating crack opening area and leak rate from a throughwall circumferential crack in an SG tube have been developed. It is shown that under normal operating and design-based accident conditions of PWRs, plasticity is confined to the plane of the crack. However, in failure tests conducted in the laboratory, plasticity spreads to sections away from the crack section. For typical SG tubes containing a circumferential throughwall crack at the top of the tube sheet, any crack of 180° or less does not reduce the failure pressure from the burst pressure of an unflawed tube. Also, tubes with throughwall cracks ≥240° will behave as though they were fully constrained against bending and will have significantly greater failure pressures than the same tubes under the free-bending condition. For typical PWR steam generator properties, the longest throughwall circumferential cracks at the top of tube sheet that are predicted to experience onset of crack initiation during normal operation and design-basis accident conditions are 340° and 310°, respectively. Crack opening areas during normal operation and design-basis accidents are small when compared with the tube cross-sectional area for an SG tube with ≤240°-throughwall crack at the top of the tube sheet. The driving force for crack instability, which is negligible as long as plasticity is confined to the crack plane, increases rapidly with plastic yielding away from the crack plane. However, failure by unstable tearing is more likely with short cracks (<180°) than with long cracks.

Failure pressures, leak rates, etc. depend on the mechanical properties (primarily the flow stress) of the tubing. The minimum ASME code requirements for yield and ultimate tensile strengths of Alloy 600 SG tube are 240 and 550 MPa (35 and 80 ksi), respectively, which correspond to a minimum flow stress of 400 MPa (58 ksi). Some of the older SGs may have tubes with properties close to the code minimum. The actual flow stress of SG tubes in most current plants can vary widely depending on the age and heat of material used. To compare results on one material with results on a different material, the effect of variations in the mechanical properties must be accounted for, i.e., the results must be normalized in terms of the flow stress. The analyses of the pressure and leak rate tests have been used to develop procedures for accounting for flow stress effects.

Models for leak rate at room temperature and high temperature have been validated with leak-rate tests on specimens with notched EDM slots. Simplified equations for calculating crack opening area have been verified with finite-element calculations. The models for crack opening area and leak rate have been used to develop calibration curves for converting leak-rate data from one material to a different material.

Detailed analyses of the tests on specimens with laboratory-grown SCC cracks show that if the pretest crack depth profile is reasonably uniform and deep (80-90%) as measured by eddy current +Point, a significant portion of the through-thickness crack tip ligament can rupture abruptly at a pressure that can be calculated by the ANL correlation. Post-test pictures of the OD surface did not reveal the presence of any surface ligaments in these specimens. Effective throughwall crack lengths estimated by the ligament rupture model using the EC +Point data are reasonably close to those estimated from the leak rate data and correspond closely to a segment of the crack that is >70% throughwall. In these specimens, the leak rate generally increased abruptly from 0 or ≤0.04 L/min (0.01 gpm) to >19 L/min (5 gpm) under increasing pressure loading, indicating sudden rupture of the ligament, and the leak rate did not increase under constant pressure hold subsequent to ligament rupture.

For specimens having highly nonuniform crack tip ligament thickness (as measured by EC +Point) with predicted ligament failure pressures that are greater than our system capability (i.e., 19.3 MPa [2800 psi]), the ligaments can fail locally during a constant-pressure hold at a lower pressure than the predicted failure pressure. The effective throughwall crack lengths for these specimens can subsequently increase due to time-dependent ligament rupture at both room temperature and 282°C. Based on very scant data, the time-dependent ligament rupture process appears to occur at a much slower rate (hours rather than minutes) in the higher-strength as-received tubes than in the lower-strength heat-treated ANL tubes. Also, the time-dependent rupture process occurs more rapidly at 282°C than at room temperature. A procedure for converting constant-pressure-hold data on the time-dependent leak rate from a heat-treated tube to an as-received tube must be developed in the future.

In all ANL specimens to date, the lengths of the throughwall segments of the cracks calculated from leak-rate data are close to the lengths of the most open part of the cracks, as evident visually from post-test pictures of the specimens. None of the pictures showed the presence of axial segments separated by ligaments. In one test, the post-test measured length of the throughwall segment of the crack (by a submerged bubble

technique) is reasonably close to that calculated from the measured leak rate. In contrast to the ANL specimens, the calculated throughwall crack length for the doped-steam specimens is much shorter than that observed visually. However, a post-test photograph of the OD surface of this specimen revealed at least three axial segments separated by ligaments, showing that the effective throughwall crack length can be seriously underestimated from the measured leak rate if the effects of the ligaments on the crack opening area are not taken into account

Development of Methodology and Technical Requirements for Current and Emerging Regulatory Issues

Several test sections with cracks grown at ANL have been Electrosleeved by FTI. Results of EC and ultrasonic examinations of two test sections are presented here. For the circumferential ODSCC and IDSCC, as well as EDM notches, the ultrasonic echoes have a very good signal-to-noise ratio. By using a frequency of ≈3-4 MHz, the distortion of the ultrasonic signal from the rough ID surface of the Electrosleeve is minimized. Propagation of waves nearly parallel to the tube axis allows echoes to be generated from cracks that do not intersect either the ID or OD, a situation in which the corner reflector (which can provide a strong echo for crack detection) is not present.

Acknowledgments

Acronyms and Abbreviations

ANL	Argonne National Laboratory
ASME	American Society of Mechanical Engineers
BC	bobbin coil
CIDSCC	circumferential inner-diameter stress corrosion crack/cracking
COA	crack opening area
CODSCC	circumferential outer-diameter stress corrosion crack/cracking
DE	destructive examination
EC	eddy current
EDM	electro-discharge machining/machined
EM	electromagnetic
EPRI	Electric Power Research Institute
FEA	finite element analysis
FEM	finite-element method
FS	free span
FTI	Framatome Technologies, Inc.
GPIB	general-purpose interface bus
GUI	graphical user interface
ID	inner diameter
IDSCC	inner-diameter stress corrosion crack/cracking
IGA	intergranular attack
IGSCC	intergranular stress corrosion crack/cracking
INEEL	Idaho National Engineering and Environmental Laboratory (formerly Idaho National Engineering Laboratory, or INEL)
ISG-TIP-2	International Steam Generator Tube Integrity Program—2
ISI	inservice inspection
LODSCC	longitudinal outer-diameter stress corrosion crack/cracking
LS	least squares
MP	multiparameter
MRPC	motorized rotating pancake coil
MSLB	main steam line break
NA	not available
NDD	no detectable degradation
NDE	nondestructive evaluation
NRC	U.S. Nuclear Regulatory Commission
OD	outer diameter
ODSCC	outer-diameter stress corrosion crack/cracking
ORNL	Oak Ridge National Laboratory
PNNL	Pacific Northwest National Laboratory
POD	probability of detection
PT	dye-penetrant technique
PWR	pressurized water reactor
PWSCC	primary-water stress corrosion crack/cracking
RPC	rotating pancake coil
RR	round-robin
RT	room temperature

SCC	stress corrosion crack/cracking
SG	steam generator
S/N	signal-to-noise ratio
SS	stainless steel
TGSCC	transgranular stress corrosion cracking
TS	tube sheet
TSP	tube support plate
TTS	top of tube sheet
TW	throughwall
UT	ultrasonic testing
UTEC	ultrasonic/eddy current

1 Introduction

The objective of this program is to provide the experimental data and predictive correlations and models needed to permit the U.S. Nuclear Regulatory Commission (NRC) to independently evaluate the integrity of steam generator (SG) tubes as plants age and degradation proceeds, new forms of degradation appear, and new defect-specific management schemes are implemented. The areas addressed by the program include assessment of procedures and equipment used for in-service inspection (ISI) of SG tubes, and recommendations for criteria and requirements to improve the reliability and accuracy of ISI; validation and improvement of correlations and models that are used to evaluate integrity and leakage of degraded SG tubes; and validation and improvement of correlations and models that predict the generation and progression of degradation in SG tubes as a function of aging, including the effects of the operational environment such as temperature, dry-out and concentration conditions, stresses, and primary- and secondary-side water chemistry.

The studies in this program focus primarily on Alloy 600 SG tubing in the mill-annealed condition, because this tubing material is (and will be) present in plants where SGs have not been replaced and because it is more susceptible to cracking than replacement materials such as thermally treated Alloy 600 or 690. Although most SGs that use mill-annealed Alloy 600 will probably require eventual replacement, the behavior of this material will be of concern for many more years. Thermally treated Alloy 600 and 690 will also be tested. Although these alloys are expected to be much less susceptible to degradation than mill-annealed Alloy 600, we must still be able to predict their behavior.

The bulk of the materials used in the program will be exposed to simulated operating conditions and more aggressive environments representing accelerated conditions during laboratory testing. Because of the necessity to use accelerated conditions and because service degradation, tubing conditions, and in-service operating and inspection conditions cannot always be faithfully represented in laboratory conditions and specimens, this program has obtained and will use service-degraded tubing for correlation with and validation of experimental data, integrity and degradation predictive models, and inspection capability. Comparisons are being made with the morphology and character of service-degraded flaws to help ensure that the flaws produced in the laboratory and used for studies on inspection reliability, pressurization, and leak-rate testing will be as realistic as possible. The reliability of flaw detection and accuracy of flaw sizing data will be assessed by typical ISI personnel, procedures, and equipment.

This program is divided into four technical tasks and one management task:

1. Assessment of Inspection Reliability,

2. Research on ISI Technology,

3. Research on Degradation Modes and Integrity,

4. Integration of Results, Methodology, and Technical Assessments for Current and Emerging Regulatory Issues,

5. Program Management.

This semiannual report describes program activities and results from October 1998 through March 1999.

2 Assessment of Inspection Reliability (D. S. Kupperman and S. Bakhtiari)

The objective of the inspection task is to evaluate and quantify the reliability of current and emerging inspection technology for current-day flaws, i.e., establish probability of detection (POD) and the capability to accurately size cracks. Both eddy current (EC) and ultrasonic testing (UT) techniques will be evaluated. The results of the NDE will be validated by inspection and destructive evaluation of service-degraded tubing.

A steam generator mock-up is being assembled for round-robin (RR) studies that will use use currently practiced techniques and commercial teams. The mock-up will also be used as a test bed for evaluating emerging technologies for the ISI of SG tubes. The RR test will attempt to include both EC and UT methods. Teams will report the flaw types, sizes, and locations, as well as other commonly used parameters such as voltage responses from the EC tests.

2.1 Steam Generator Tube Mock-Up Facility

Assembly of most of the nine mock-up levels has been completed, with levels B, E, F, G, H, and I filled. Levels F, G, H, and I and the 0.91-m (3-ft.)-long run-out section are connected (see Fig. 2.1). In addition to a full EC examination, all cracked test sections are examined with dye-penetrant before being incorporated into the mock-up tube bundle. Simulation of magnetite in the tube support plate (TSP) crevice is accomplished by filling the crevice with magnetic tape or a ferromagnetic fluid. Magnetite-filled epoxy markers are placed on the ends of all test sections. These markers provide a reference for the angular locations of flaws when collecting data with a rotating pancake coil (RPC) or array probe. Figure 2.2 shows an isometric plot (c-scan) indicating the EC response from a 400-μm (0.016-in.)-wide x 250-μm (0.010-in.)-thick x 25-mm (1-in.)-long, axially oriented magnetite filled epoxy marker located on the ID, at the end of a 22.2-mm (7/8-in.)-diameter Alloy 600 test section located in tube support plate simulation Level I. This test section also has an outer-diameter stress corrosion crack (ODSCC) at the TSP. These data were acquired at 400 kHz using a 2.0-mm (0.080-in.)-diameter high-frequency shielded pancake coil rotating at 300 rpm with an axial speed of 5 mm/s. The epoxy marker can also be seen clearly with a 2.9-mm (0.115-in.)-diameter pancake coil at 300 kHz.

A second type of circumferential reference marker has also been evaluated. Figure 2.3 shows the results using an epoxy-coated strip of 25-μm (0.001-in.)-thick magnetic tape. An isometric plot (c-scan) shows the EC response from a 100-μm (0.004-in.)-wide x 100-μm (0.001-in.)-thick x 20-mm (0.79-in.)-long, axially oriented epoxy-coated strip of magnetic tape located on the inner diameter (ID) at the end of a 22.2-mm (7/8-in.)-diameter Alloy 600 test section. These data were acquired at 300 kHz using a 2.9-mm (0.115-in.)-diameter standard pancake coil rotating at 300 rpm with an axial speed of

Back plate:
Carbon steel
(Drwng SGT17)

Carbon steel tubes,
914-mm (36-in.)-
long, 19.68-mm
(0.775-in.)-ID

Mechanical
slip fit
for Alloy 600
tubes

I

H

G

F

E

D

C

B

A

Polyethylene
plate

Alloy 600, 22.2-mm
(7/8-in.)-diameter
tube sections (3600)
are 305-mm(12-in.)
-long

Tube support plates:
Carbon steel
22.2-mm (3/4-in.)-
thick (Drwng SGT11)

Divider plates (9):
Polyethylene
22.2-mm (3/4-in.)-
thick (Drwng SGT13)

Spacer plate: Aluminum
6.3-mm (1/4-in.)-thick (Drwng SGT18)

Simulated tube
sheet 152-mm
(6-in.)-
carbon-steel-
collar, over
Alloy 600 tube]

Eddy current
probe

Tube bundle base plate: Carbon steel
12.7-mm(1/2-in.)-thick(Drwng SGT15)

Tube bundle support plate: Carbon steel
25.4-mm (1-in.)-thick

Fig. 2.1. Schematic representation of steam generator mock-up tube bundle.
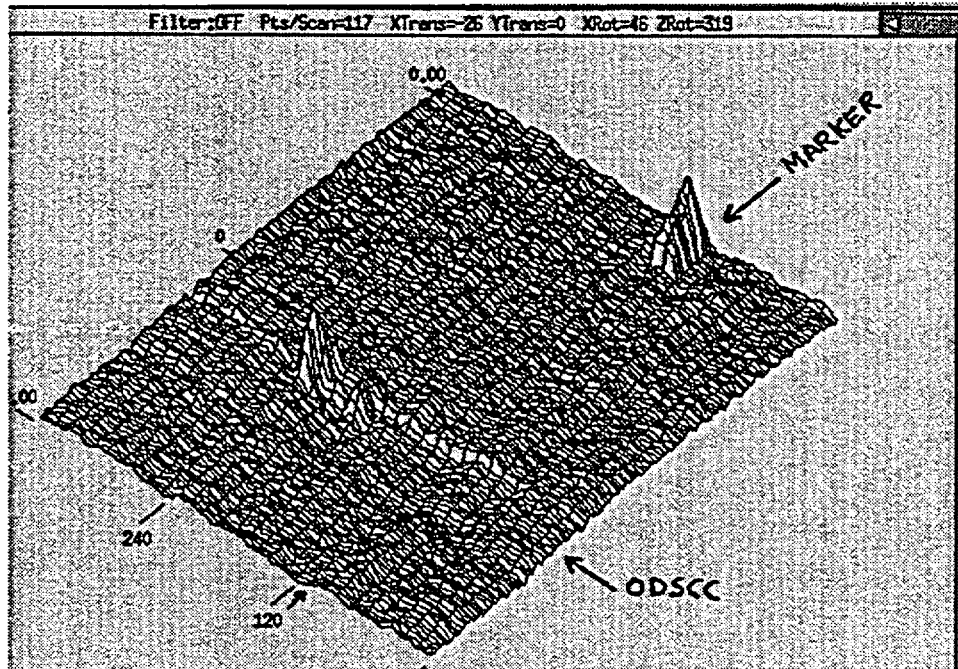
Fig. 2.2. *Isometric plot (c-scan) showing eddy current response from 400-μm (0.016-in.)-wide x 250-μm (0.010-in.)-thick x 25-mm (1-in.)-long, axially oriented magnetite-filled epoxy marker located on ID at end of 22.2-mm (7/8-in.)-diameter Alloy 600 tube. This type of marker is being used as a circumferential reference for location of flaws in mock-up test sections. Data were acquired at 400 kHz with a 2.0-mm (0.080-in.)-diameter high-frequency shielded pancake coil rotating at 300 rpm with axial speed of 5 mm/s. ODSCC in simulated tube support region can also be seen.*

5 mm/s. This type of marker could also provide a circumferential reference for location of flaws in mock-up test sections.

To ensure the uniformity of epoxy markers, a special tool was fabricated and tested for quick removal of excessive epoxy without scratching the tube wall. All test sections of assembled levels are cleaned and checked for obstruction and alignment with both a bobbin coil (BC) and a motorized RPC (MRPC) probe.

A magnetically biased three-coil probe that includes a +Point, 2.9-mm (0.115-in.)-diameter pancake and high-frequency shielded coil has been used on sensitized tubes with flaws. A comparison of magnetically biased and unbiased coils shows that the biasing eliminates the voltage shift and noise in the EC signal resulting from the tube sensitization.

All of the eddy current files accumulated for Task 1 are entered into a spreadsheet (Excel 4.0). About 4000 scans of tubes with various combinations of flaws and artifacts using both rotating and bobbin coil (BC) probes have been accumulated and stored. The spreadsheet now permits quick reference for locating the optical disk and file number for any scan of a test section. Each line in the spreadsheet has the tube identification number, type of probe used, flaw type, source of flaw, and nature of artifact if one was used in
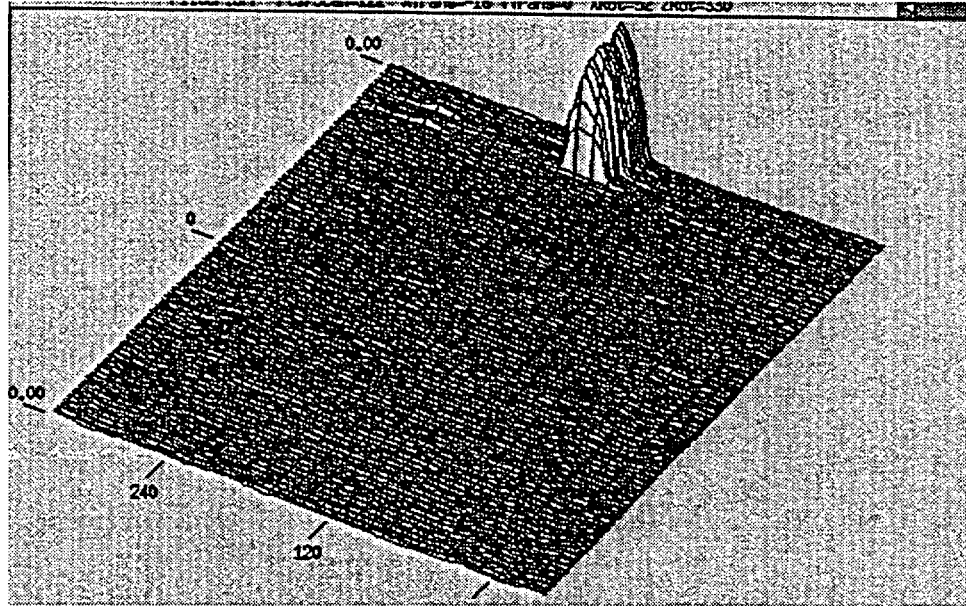
Fig. 2.3. Isometric plot (c-scan) showing eddy current response from 100-μm (0.004-in.)-wide by 100-μm (0.004-in.)-thick by 20-mm (0.79-in.)-long, axially oriented epoxy-coated piece of magnetic tape located on ID at the end of 22.2-mm (7/8-in.)-diameter Alloy 600 tube. Data were acquired at 300 kHz using a 2.9-mm (0.115-in.)-diameter standard pancake coil rotating at 300 rpm with axial speed of 5 mm/s. This type of marker could provide a circumferential reference for location of flaws in mock-up test sections.

collecting the data. The spreadsheet allows an easy search of the optical disk location and file number for any scan, given the tube identification number, acquisition date, artifact used, probe type, flaw type, or source of flaw. This spreadsheet is backed up on floppy disks and on an Argonne National Laboratory (ANL) computer backup system.

Significant effort has been expended in restoring to operation an EC system acquired from Oak Ridge National Laboratory (ORNL) that allows very precise spatial location of EC data during a tube scan. The device is capable of acquiring data every 25 μm (0.001 in.) in the axial direction. The system requires two interdependent computer programs, one running on a dedicated PC and the other on a Unix-based Hewlett Packard computer. The PC program controls the probe-positioning hardware. The effort to repair the hardware and to correct electrical problems has been completed. A program was written that uses a general-purpose interface bus (GPIB) card installed in a PC to send appropriate commands to the motion controller. Another program was written to compile the data acquisition program for the HP computer. Example programs were written to demonstrate that the motion controller system was working. In this system, the probe is fixed while the tube moves axially over and around the EC probe. Motors that control the axial and circumferential position of the tube can now be moved in a precise and prescribed manner. Further efforts will be required to allow the system to acquire EC data at very short intervals. This system could also be used with ultrasonic probes.

2.2 Round-Robin Protocol and Procedures

A comprehensive review of Task 1, including examination of EC signals from mock-up flaws, was made during the International Steam Generator Tube Integrity Program–2 (ISG-TIP-2) meeting held at ANL on October 19-23, 1998. Some of the suggestions made by the NDE Task Group, organized to provide input on the ANL SG NDE round-robin, are being followed. These suggestions are related to (a) the selection of probes for the round robin, (b) the use of artifacts, and (c) the documentation of procedures for the mock-up assembly to ensure that flaws are correctly located.

A magneto-optical disk with EC data from 24 degraded mock-up test sections was prepared for additional review. The data will be examined by industry analysts to confirm that the EC signals from the test sections adequately simulate signals from field flaws. The disk contains 67 separate files for the 24 flaws. The flaws were scanned with a BC probe and a three-coil probe that includes a standard 2.9 mm (0.115-in.)-diameter pancake coil, +Point coil, and the 2.0-mm (0.080-in.)-diameter high-frequency shielded coil. All test sections scanned are Alloy 600, 22.2 mm (7/8 in.) in diameter and 0.30 m (12-in.) long. For each scan, the probe passes through the degraded test section, a standard with 18 notches, and an ASME standard. To locate data files associated with a given test section, a table was prepared that shows (a) the type of flaw scanned; (b) location of the data file on the disk provided, and (c) whether the flaw is in a free span (FS), has a ring over it to simulate the tube support plate (TSP), or whether the tube has a steel collar over the lower half of the test section to simulate the tube sheet (TS). The table also indicates whether a simulated artifact (either a ring of sludge or a ring of magnetite) covers the area of the flaw. Other information indicates the test section identification number, location of the original data file at ANL and what probe was used to generate the EC data. This data could be used for the training of personnel involved in the round-robin (RR) and as part of the site specific exam.

Documents prepared by the NDE Task Group members provides technical direction for the EC examination, Site Specific Performance Demonstration, and Examination Technique Specifications Sheets. The documents have been reviewed by the Task Group and by ANL personnel, and several suggested changes have been incorporated into revised documents.

2.3 Eddy Current Signal from SCC with Corrosion Products

The effect of a corrosion product (thin oxide film) on the EC signal from an SCC is under evaluation. Alloy 600 tubes with axial ODSCC were exposed under PWR water chemistry conditions (300°C and 3-8 ppb oxygen) for about two months (see Section 4.1). The cracks have been examined with both mag-bias bobbin coils BCs) and a +Point coil before and after corrosion products were formed. The voltages for the BCs increased significantly with the creation of the thin oxide film. However, the general shape of the Lissajous figures remained unchanged. In contrast, the results for the +Point coil are inconclusive at this time. In two cases, no change in +Point voltage was observed, while in a third the voltage dropped significantly after the oxide film was formed. Figure 2.4 shows the change in the BC Lissajous figure, along with voltage and phase information for one of the tubes. Table 2.1 summarizes the BC results for two tubes. While voltages increased
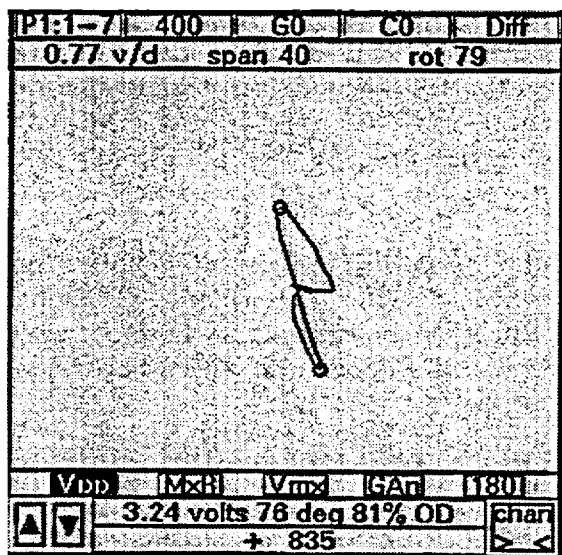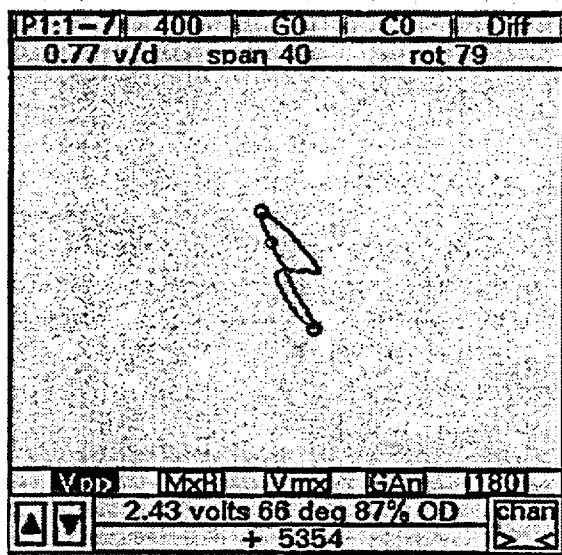
Fig. 2.4. *Mag-bias BC Lissajous figures before (top) and after (bottom) corrosion products (thin oxide film) were formed in a tube with axial ODSCC by exposing the tube to PWR conditions for about two months. Voltage increased from 2.43 to 3.24 volts, suggesting less contact at crack faces. Estimated depth changed from 87 to 81% TW.*

Table 2.1. Comparison of BC voltages and phase for two tubes before and after exposure to PWR water conditions, resulting in formation of corrosion products. Each tube has an axial ODSCC ≈15 mm (0.60 in.) long.

Tube #	BC Voltage	BC Phase Angle	BC % TW
SGL-197 (before)	2.43	66°	87
SGL-197 (after)	3.24	76°	81
SGL-149 (before)	3.27	87°	73
SGL-149 (after)	4.51	89°	72

significantly, the phase angle did not. The creation of corrosion products in the crack could lead to a reduction in the number of electrically conducting paths from contacting crack faces. In that case, the EC signal would be expected to increase, as observed, while the depth remains essentially the same. Further investigations are planned to better understand the effect of corrosion on EC signals from SCC.

2.4 Comparison of BC Voltages from Notches and ODSCC

The similarity of BC voltages for notches and cracks of comparable depth and length is illustrated in Table 2.2, which presents BC voltages for notches, four axial ODSCCs generated at ANL, and one ODSCC generated using doped steam.

The BC voltages for notches and cracks in the 80-90% throughwall (TW) range are all comparable, with voltage variations attributed to profile variations. As an example, the profile from the doped-steam-generated axial ODSCC is presented in Fig. 2.5. The phase angle from the Lissajous pattern generated by a +Point coil at 300 kHz was, at various deep points along the crack, compared to the phase angle of EDM notches of depths 40, 60, 80 and 100 % TW. The crack depth estimate was made every millimeter as long as reasonable signal-to-noise ratios (S/N) were evident. For smaller signals and where phase analysis is not effective (depth less than 70% TW in this case), a depth was established from the phase analysis at relatively deep points, and the depth was then correlated with signal amplitude using straight linear extrapolation to 0% TW. As a result, the entire EC profile of the crack could be made. Note that it is possible that small cracks emanating from the main crack are present. Those small cracks may not be detected by the +Point coil.

Variations in BC voltage for cracks, over the voltage range shown in Table 2.2, leads to relatively small changes in predicted failure pressure if the estimated failure pressure is from the alternate plugging criteria voltage-burst-pressure model for axial ODSCC at TSP. Figure 2.6 shows the variation in predicted failure pressure for the ANL SCC of Table 2.2.

Table 2.2. Mag-bias bobbin coil voltages for EDM notches and laboratory-grown SCC

Tube	Maximum Depth (% TW)	Flaw Length (in.)	Voltage
T1EATWx.5 (axial OD EDM notch)	100	0.5	74
T2EATWx.5 (axial OD EDM notch)	100	0.5	76
T15EATWx.5 (axial OD EDM notch)	100	0.5	78
T16EATWx.5 (axial OD EDM notch)	100	0.5	75
T10EA80x.5 (axial OD EDM notch)	80	0.5	4.4
T11EA80x.5 (axial OD EDM notch)	80	0.5	4.9
SGL-104 (ANL single axial ODSCC)	93	0.67 (EC)	9.2
SGL-219 (ANL single axial ODSCC)	90	0.67 (EC)	6.3
SGL-195 (ANL single axial ODSCC)	92	0.5	8.4
SGL-177 (ANL single axial ODSCC)	90	0.5	4.2
2-10 (doped-steam single axial ODSCC)	90	0.46 (W-PT) 0.87 (ANL-EC)	4.5

2.5 Comparison of Voltages from McGuire and ANL SCC

An indication that the cracks grown at ANL are representative of field cracks comes from a comparison of McGuire steam generator BC voltages and phases with ANL SCC BC voltages and phase. Figure 2.7 shows McGuire voltages and phases from axial ODSCCs at TSPs, together with voltages and phases from the ANL-grown axial ODSCCs. The plots of voltage vs. phase are comparable.
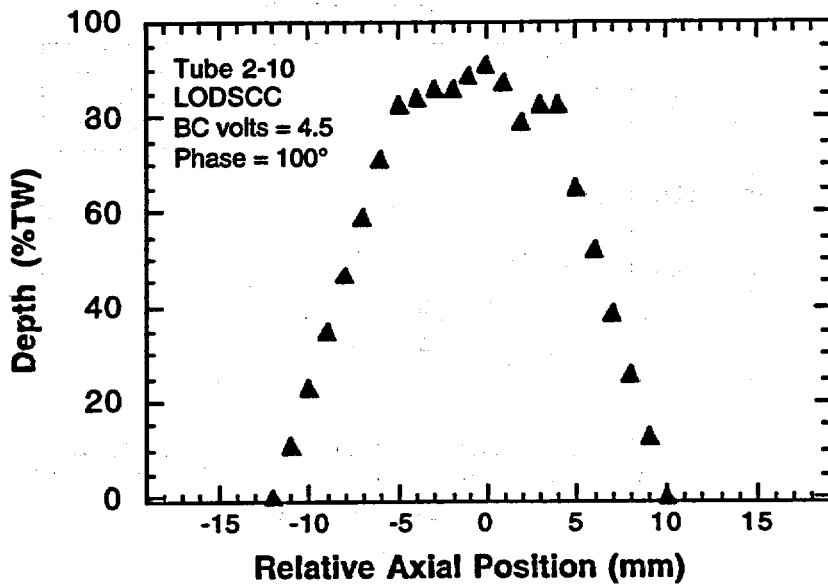
Fig. 2.5. Depth profile for Tube 2-10 containing single axial ODSCC grown under laboratory conditions using doped steam.
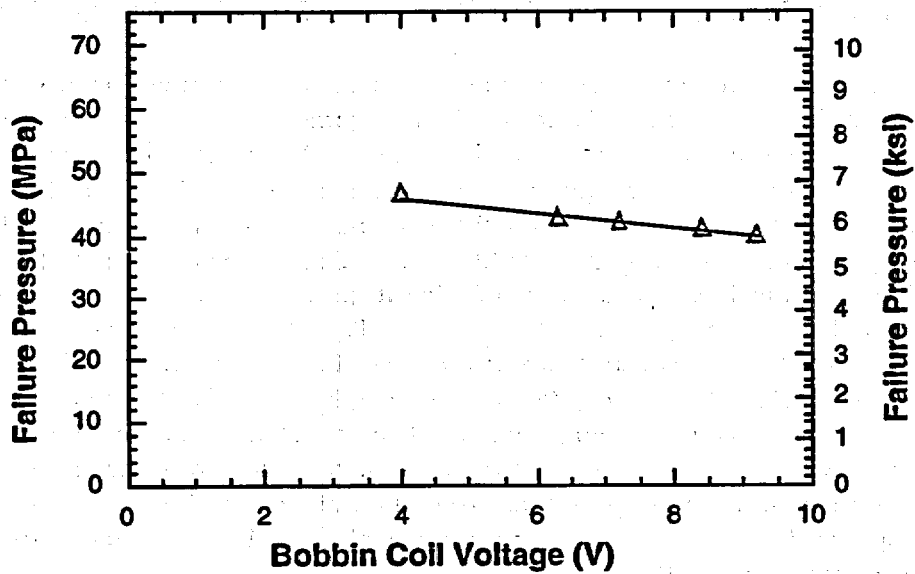
Fig. 2.6. Predicted failure pressure vs. BC voltage for five ANL-grown SCCs highlighted in Table 2. Estimated failure pressure is from alternate plugging criteria voltage-burst-pressure model for axial ODSCC at TSP.
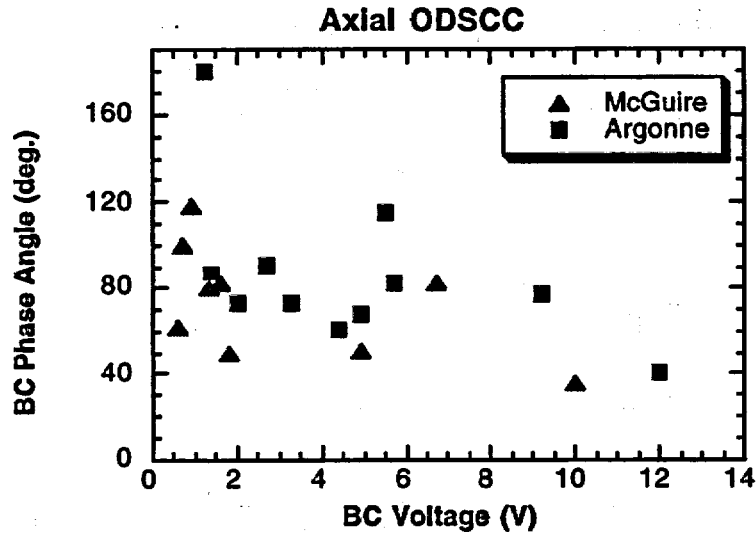
Axial ODSCC

Fig. 2.7. Comparison of McGuire steam generator D BC voltages and phase from axial ODSCCs at tube support plates to voltages and phase from ANL-produced axial ODSCC. Ranges of plots are comparable.

2.6 Depth Predictions of Laser-Cut Slots with Complex Geometries

Twenty-four specimens with laser-cut notches were obtained from Oxford Lasers, Ltd., as summarized in Table 2.3. These notched specimens were designed to help evaluate the relative strengthening effects of through-thickness ligaments and ligaments between axial segments on failure pressure and leak rate. The target depth of the laser-cut notches in these tubes was 40 to 80% TW, and these depths were measured by NDE at ANL from phase analysis using a +Point probe at 300 kHz. The purpose of these NDE measurements was to help establish the reliability of +Point phase analysis to estimate the maximum depth of cracks, especially segmented cracks. The results are presented in Table 2.3. In almost all cases, the measured depth of the 80% TW axially oriented laser-cut notches was less than the design depth despite very high S/N ratios for the very clean signals. The greatest deviation occurs when a ligament is present between the axial slots. Such ligaments provide a current path between slots, resulting in a phase shift of the Lissajous figure. One explanation proposed for the undersizing of the simple single slots is that bridging across the slot faces results in a phase shift of the Lissajous figure and a less-than-expected estimate of depth.

For one of the geometries where the measured depths were close to target depths, six 12.7-mm (0.5-in.)-long slots were cut parallel to each other with slot separations of 250 μm (0.010 in.) in one case and 500 μm (0.020 in.) in the other (Type 6 "6-claw" notch geometry). The six slots cannot be resolved by the EC probe. However, for this example, the depth predicted by EC phase analysis for the six slots will be the depth of the slot with the deepest predicted depth. With six slots, the possibility of finding one with minimum bridging is apparently fairly high, and consequently the predicted depth for this geometry

Table 2.3. Summary of preliminary NDE examination of tubes with laser-cut notches

Notch Geometry	Tube I.D.	Specimen Type	No. of Notches	Notch Length (mm)	Ligament Width (mm)	Notch Depth (% TW)	
						Target Value	+Point NDE
Single	5528-1-1	1	1	6.35	NA	80	75
	5528-1-2	1	1	6.35	NA	80	70
	5528-1-3	1	1	8.89	NA	80	72
	5528-1-4	1	1	8.89	NA	80	72
	5528-2-1	1	1	12.7	NA	80	70
	5528-2-2	1	1	12.7	NA	80	60
Ligament	5516-4-3	2	2	12.7	0.25	80	59
	5516-4-2	2	2	12.7	0.13	80	65
Dotted Line	5528-3-1	3	6	12.7	0.13	80	70
	5528-3-2	3	6	12.7	0.25	80	70
	5528-3-3	3	6	12.7	0.25	40	60
Side Step	5528-3-4	4	6	12.7	0.13	80	80
	5469-2-1	4	6	12.7	0.25	80	70
	5469-2-2	4	6	12.7	0.25	40	60
2x3 Side	5469-2-3	5	6	12.7	0.25	80	70
	5469-2-4	5	6	12.7	0.50	80	65
6 Claw	5469-3-1	6	6	12.7	0.25	80	75
	5531-3-1	6	6	12.7	0.50	80	75
Parallel	5469-3-3	7	2	360°	0.13	80	97
	5469-3-4	7	2	360°	0.25	80	93
p-Side Step	5469-4-1	8	6	360°	0.25	80	-
	5469-4-2	8	6	360°	0.13	80	-
T	5469-4-3	9	2	180° x 0.5	N/A	80	65 (?)
L	5469-4-4	10	2	180° x 0.5	N/A	80	65

Table 2.3. (Cont'd.)

Notch width
as narrow as
possible

Notch Length

80% Throughwall notch

Type 1 specimen

Notch Length

Notch width
as narrow as
possible

Ligament Width

80% Throughwall notch

Type 2 specimen

Ligament Width

Notch Length
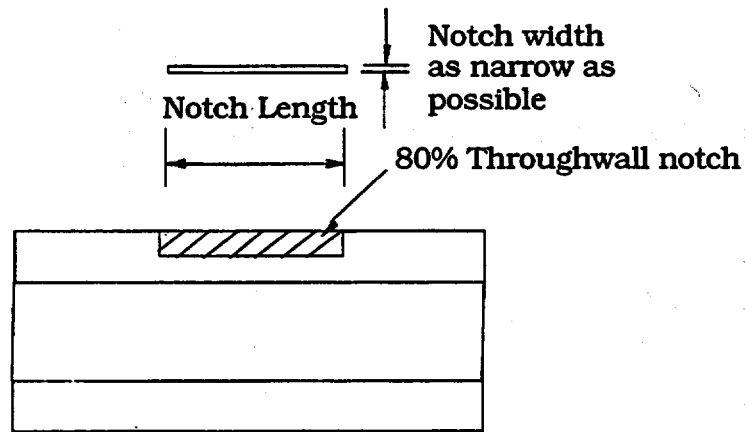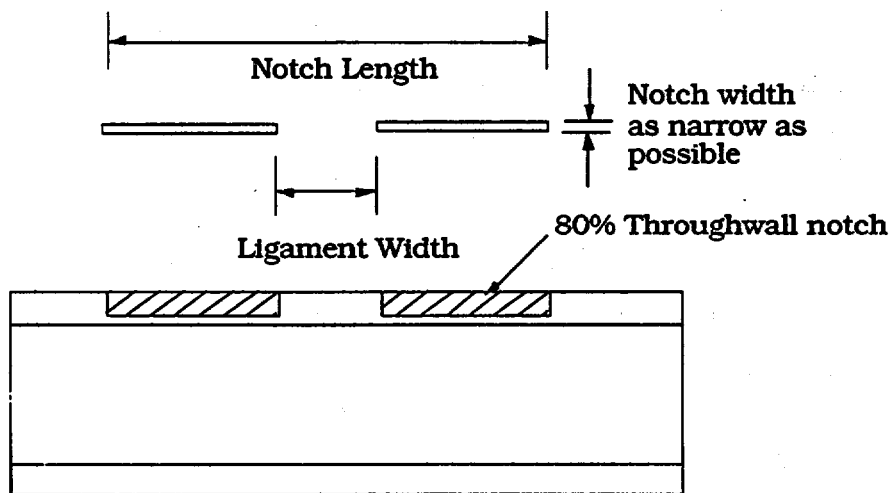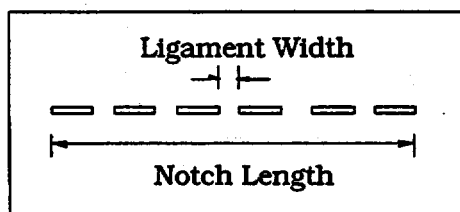
Type 3 specimen
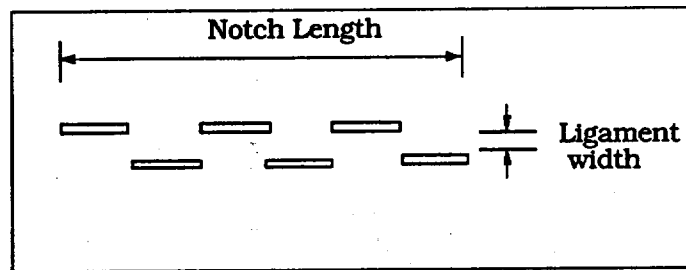
Table 2.3. (Cont'd.)

Type 4 specimen
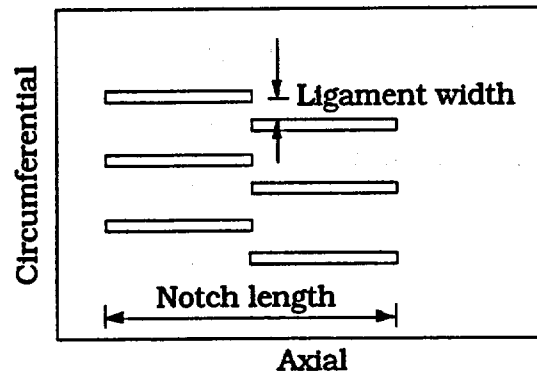
Type 5 specimen
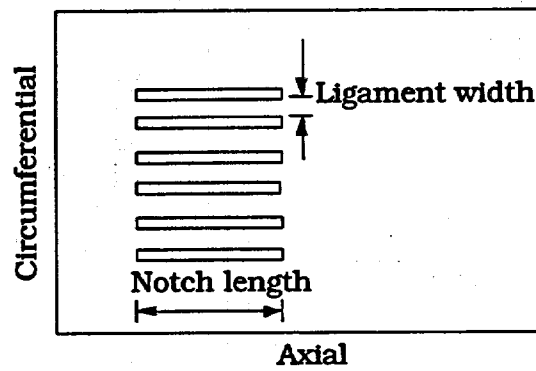
Type 6 specimen

Table 2.3. (Cont'd.)
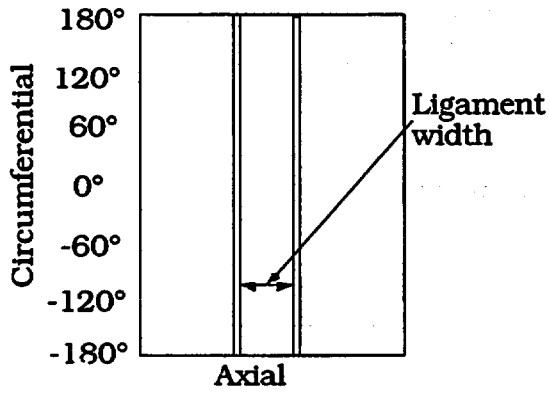
Type 7 specimen
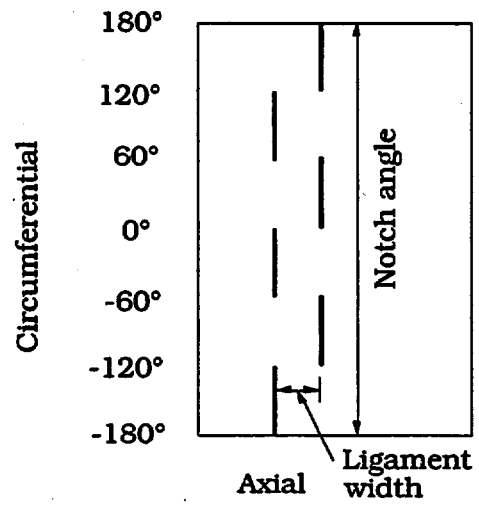
Type 8 specimen
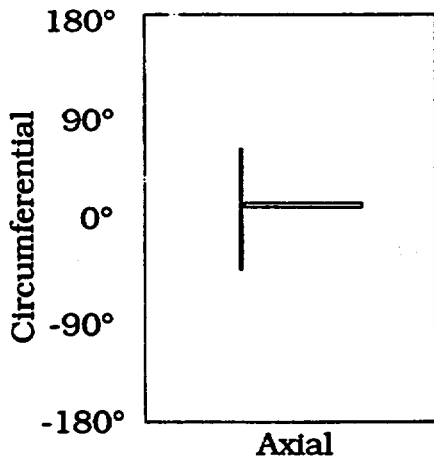
Type 9 specimen
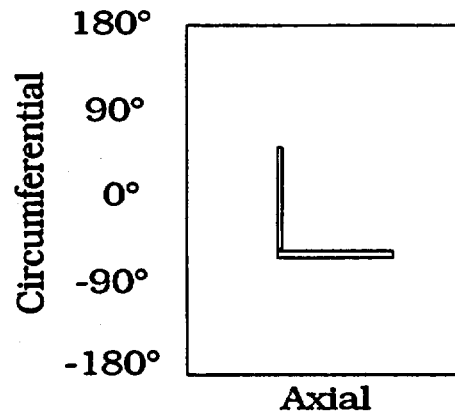
Type 10 specimen

is close to the target depth. For circumferentially oriented (Type 7 "parallel" notch geometry) laser-cut slots, the estimate with the +Point coil is greater than the design depth (Table 2.3). This discrepancy may be the result of lack of contouring of the circumferentially oriented part of the +Point coil to the tube inner surface. The axially oriented part of the coil has a better fit to the inner surface of the tube.

2.7 Technical Meetings

Members of the ANL staff met with the Nuclear Services Division of Westinghouse in Madison, PA on December 2, 1998 to discuss a number of areas related to steam generator tube integrity. In the area of NDE, the Westinghouse staff described the development and qualification of the Ghent rotating EC probe, the combined ultrasonic/eddy current (UTEC) tubing inspection system, and the Cecco-5 array probe. Steam generator tube crack morphologies and laser-welded sleeves were also discussed. The advantages and limitations of the Cecco-5 array were reviewed, and it was noted that its primary advantage is its high speed for screening tube regions. With regard to probe qualification for the Cecco-5, the EPRI-documented probability of detection (POD) for ODSCC at all locations is 88% at 90% confidence for depths greater than 60%. Applications of the Cecco-5 at four plants were discussed. Results using Cecco-5 and +Point probes were compared with destructive examination of pulled tubes. Information on the Ghent G3-4 transmit receive probe was also provided. Appendix H qualification is progressing for the G3-4. The objective is to have qualification for detection of axial and circumferential ODSCC and PWSCC, detection of intergranular attack (IGA), and sizing of ODSCC and PWSCC. A presentation was also made on the UTEC inspection system. The probe for the UTEC system includes four ultrasonic crystals and a conventional RPC. With this system, resolution of ligaments is possible, and the system can also be used to resolve discrepancies between EC techniques.

D. S. Kupperman attended a meeting in Rockville, MD on December 15, 1998 to discuss the status of the Farley Unit 1 steam generator. NDE issues were (a) a missed indication in the free span, (b) inadequate inspection at the end of sleeves, and (c) free span indications outside but within 25 mm (1 in.) of the edge of the TSP. Large increases in EC signal voltages were seen between outages. Improvements in free-span EC signal analysis are being made (with increased emphasis on reporting small flaw-like signals for inspection with a +Point probe), and a program to inspect the sleeve-end with a +Point probe has been initiated.

3 Research on ISI Technology (S. Bakhtiari and D. S. Kupperman)

The objective of this task is to evaluate advanced NDE and signal analysis techniques for the reliable ISI of original and repaired SG tubes. Improved correlations between EC probe response and flaw morphology, leak rate, and failure pressure will be developed and validated. In addition, the reliability of the voltage parameter and other EC parameters and techniques will be evaluated with respect to their ranges of applicability.

The present research on improved ISI of SG tubes focuses on four primary areas: (1) implementation of analytical methods for prediction of EC response as a function of probe design, flaw characteristics, and material properties; (2) development of effective signal analysis procedures; (3) development of flaw imaging and display methods for simple and accurate flaw characterization; and (4) evaluation of improved probe designs that use directional arrays so that defects of arbitrary orientation can be examined simultaneously. The reliability and effectiveness of improved inspection techniques and the robustness of potential correlations will ultimately be substantiated through laboratory testing of the SG tube bundle mock-up and of SG tubes that contain various flaw morphologies. Final validation will also utilize in–service-degraded SG tubes.

A description of Task 2 activities during the present reporting period is presented here. Research efforts that are associated primarily with multiparameter analysis of EC NDE results are discussed. Representative test cases are presented in Sec. 3.1 on a study that was initiated to evaluate potential advantages of alternate multifrequency mixing techniques involving more than two frequencies over standard two-frequency mixes. These alternate techniques could help improve BC detection of flaw indications in presence of interfering signals. Multiparameter data analysis is discussed in Sec. 3.2. Initial analysis of the results is provided on a set of 20 laboratory-grown specimens with various forms of cracking degradation. Flaw morphologies in these tubes are representative of those incorporated into ANL's tube bundle mock-up. Eddy current rotating probe readings on this set were analyzed by using an automated multifrequency data analysis algorithm that is currently under evaluation. Subsequently, analysis results are presented for a single laboratory-produced mockup specimen that exhibited a reportable BC signal without a clear rotating probe indication. Finally, data analysis results are presented on a set of laser-cut specimens with single and multiple axial/circumferential notches (with and without ligaments) that simulate complex cracking geometries. The NDE and nominal flaw size for this set of 24 tubes, originally constructed for high-pressure studies under Task 3 of this program, provide a useful means for assessing data analysis algorithms currently under investigation at ANL.

3.1 Multifrequency Mix for Improving Bobbin Coil Detection

Preliminary results are presented on two separate multifrequency mixing procedures that could possibly improve BC detection of flaw indications in the presence of interfering artifacts at the same axial location along the tube axis. This investigation was initiated in part to evaluate alternate mixing methods that might help compensate for lack of similarity between simulated artifacts in tube standards and those in the field. All data conversion and calibrations in this study were carried out automatically by using a MATLAB-based graphical user interface (GUI) tool that was implemented at ANL and described previously.[1]

3.1.1 Direct and Indirect Mix Processes

Recovery of defect-induced signals in the presence of strong background interference is an important and often challenging NDE problem when analyzing NDE results for ISI of SG tubing. Data analysis is further complicated when degradations are accompanied by tube ID variations such as design-related tube diameter changes or the presence of significant denting. These difficulties are associated with such factors as low S/N ratio and small phase separation between ID and deep OD indications. Multifrequency mixing is routinely applied to improve detection of flaw signals that are obscured by tubing artifacts. However, the mix channel information should be analyzed discerningly, particularly when more than two frequencies are used in the process. Conventional two-frequency least-squares (LS)-based mix algorithms that are optimized primarily to suppress a single OD artifact generally provide consistent outcomes. On the other hand, processed channel information from mixing algorithms that incorporate more than two frequencies could be unreliable for the interpretation of signals outside the segment where the mix coefficients were calculated. This in part is due to uneven perturbation of the signal amplitude and phase information that is introduced by higher-order (nonlinear) mix models.

Two separate approaches, direct (independent) and indirect (dependent) mixing algorithms, to suppress multiple unwanted indications from a composite signal were considered in this study. In an indirect mix, regression coefficients are determined by using a data segment from a simulated artifact such as a TSP ring on a reference standard tube, which is expected to closely resemble those present in the actual SGs. The aim of the regression model is to best reproduce the primary/base frequency signal by combining signal components from auxiliary frequency channel(s). This is the conventional approach that is used for the analysis of EC ISI results. Alternatively, independent mix procedures have the potential to suppress unwanted signals by using multiple-frequency readings on the same tube. This approach, primarily suggested for suppression of dominant signal features, is of particular interest when tube standards with simulated artifacts that resemble field-induced signals are not readily available. Representative test case results are presented next on recent studies associated with direct and indirect mixing techniques.

To initially evaluate direct mixing approach, a simulated composite BC signal was constructed by using normalized EC readings from an ASME tube standard. Individual signal components consisted of a simulated TSP ring and 10 and 20% ID circumferential grooves. The main objective was to develop a mixing procedure that would allow recovery of the shallow OD indication from the composite signal with minimal perturbation of the signal outside this region. A standard linear LS regression algorithm was initially utilized in this study. Various two- and three-frequency regression fits were implemented. Preliminary results indicated that two-frequency mixes are generally more consistent, so the approach was to sequentially apply two-frequency mixes for suppression of two unwanted indications at the same axial location. To improve the mix outcome, several modifications were made to our previously developed[1] standard mix algorithm. These consisted of energy scaling of each trace, resampling in frequency domain, and phase-angle referencing. Frequency resampling was done to increase the number of available independent variables. Phase-angle tracking was done to help reduce phase ambiguity from multiple application of linear regression coefficients. Based on the small number of cases tested so far, the amplitude renormalization consistently exhibited improved quality of mix outputs. This is believed to be a result of the weighting introduced by the energy-scaling process. It is worth noting that this transformation does not significantly

perturb the original phase information of original channels (i.e., the Lissajous patterns remain nearly unchanged).

Figure 3.1 shows the horizontal and vertical differential signal components of the calibrated original (top) and renormalized (bottom) traces at $f = 400$ kHz. Simulated indications from left to right consist of a 100% TW drilled hole, TSP ring, 10% OD and 20% ID circumferential grooves, and the composite signal that is made up of the last three indications. The drilled-hole signal was added to each trace to serve as the phase reference indication. Figure 3.2 shows intermediate results of the mix using a high- and low-frequency signal to suppress the TSP indication from each trace. Figure 3.3 displays the recovered differential and absolute channel signals for the shallow OD indication subsequent to combining the two intermediate mix outputs. In both cases, the 10% OD groove was recovered from the original composite trace. It should be noted that the three-frequency mix outputs shown in Fig. 3.3 do not have the identical phase angle information as the original traces. Nevertheless, the results show significant improvement over standard three-frequency LS mixing procedures that were examined as part of this study.

To assess the validity of independent mix algorithms, BC readings on two tubes with laboratory-grown circumferential and axial SCC at tube sheet (TS) roll transition region were utilized for analyses. Available metallography results indicate depths of 30% ID for the circumferential and 100% TW cracking for the axial flaw. The specimens used here were part of a 20-tube set of representative ANL mock-up tube specimens furnished by Pacific Northwest National Laboratory (PNNL). With reference to Fig. 3.4, the indications from left to right consist of 100% TW hole and two roll transitions with ID circumferential and OD axial SCC flaws, respectively. Once again, a throughwall indication from the ASME standard was attached to the beginning of each trace to serve as the phase reference. Figure 3.4 displays both the calibrated original and the renormalized traces at $f = 400$ kHz. As in the case of direct mix, regression coefficients were initially calculated for suppression of roll transition signals. The two intermediate mix outputs were once again produced by using the signal components from a high- and a low-frequency channel to suppress the strong signal from the tube diameter change. However, unlike the indirect mix, data from the first roll transition were used to suppress the artifacts. Subsequently, a final mix process was applied to recover the residual signal that is expected to predominantly contain information about the flaw.

Figure 3.5 displays the results of the independent mix for the differential and absolute channels, respectively. In both traces, the residuals at the roll transition regions (approximately located around data points 350 and 750) exhibit the presence of SCC flaws. A notable feature of the processed signal is the phase separation between the two indications and their relationship to the throughwall reference signal. This phase information cannot be recovered consistently with conventional multifrequency mixing techniques. Further evaluation of multifrequency mixing algorithms is currently being pursued under this program, and a more detailed discussion of the findings will be presented in future reports.
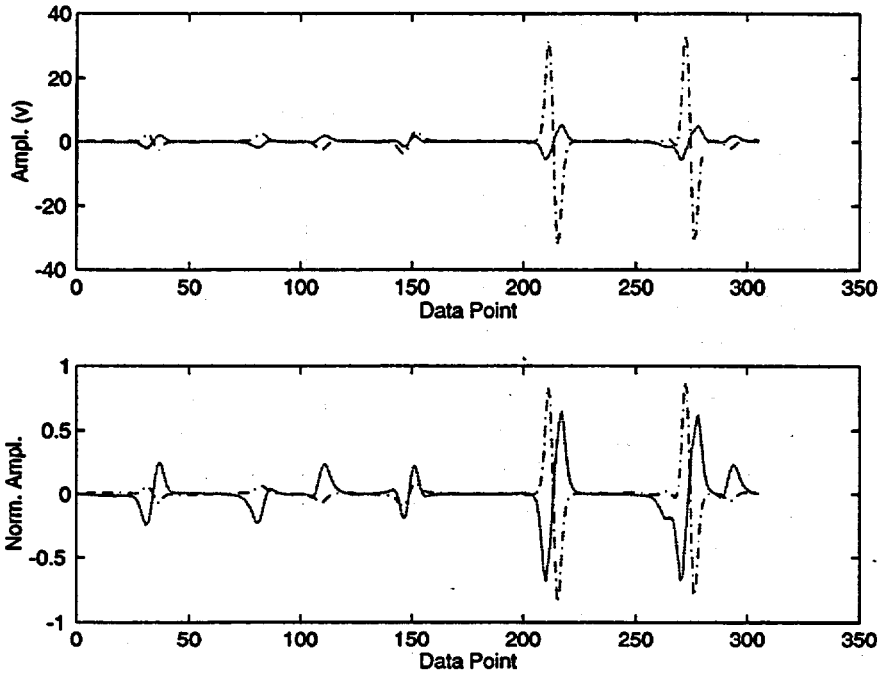
Fig. 3.1. *Differential BC horizontal and vertical signal components of calibrated original (top) and renormalized (bottom) traces at f = 400 kHz. Simulated indications from left to right consist of throughwall drilled hole, TSP ring, 10% OD and 20% ID circumferential grooves, and composite (of last three indications) signal.*
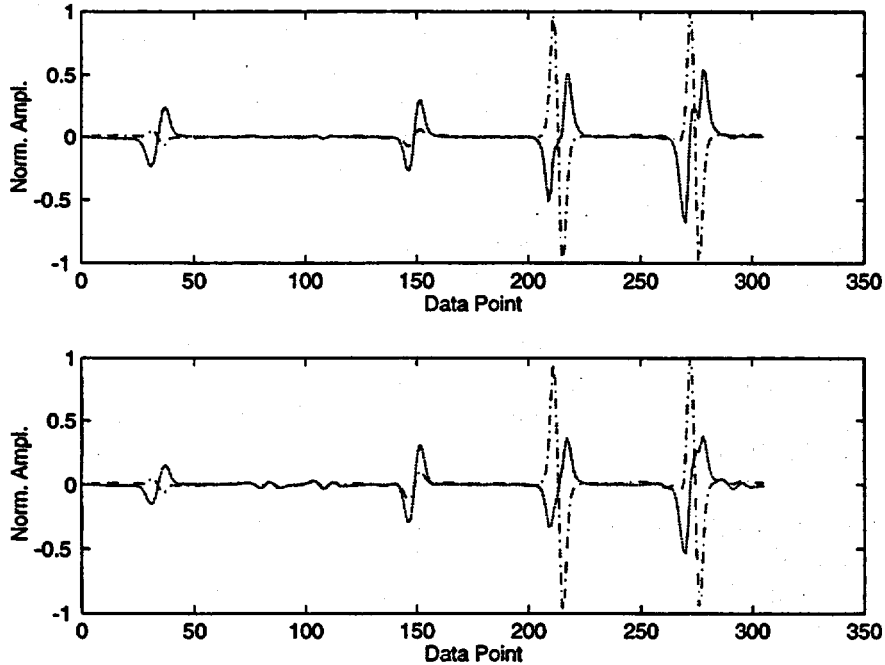
Fig. 3.2. *Intermediate mix outputs using high- and low-frequency signals to suppress TSP indication from bottom trace shown in Fig. 3.1.*
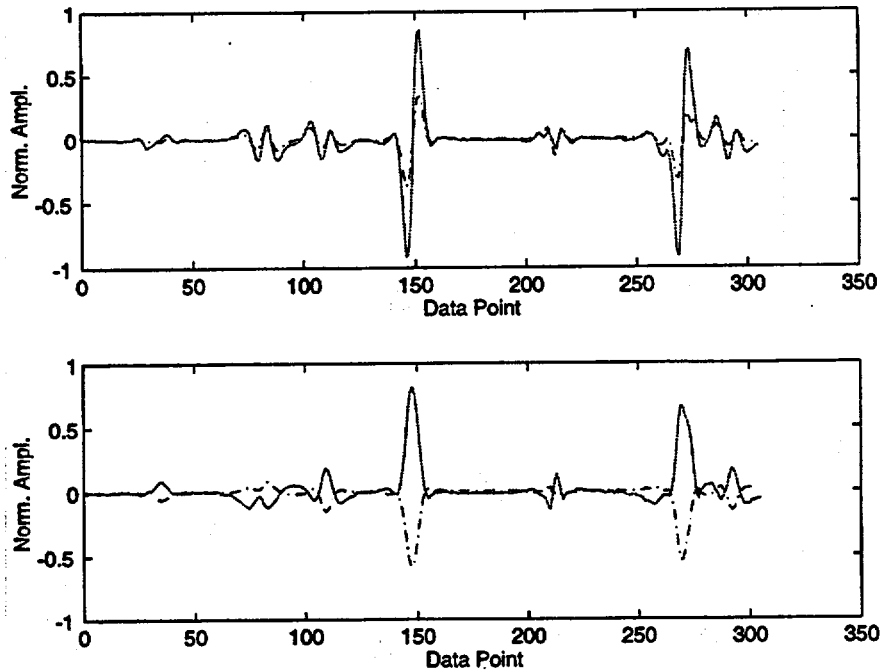
Fig. 3.3. *Residual differential (top) and absolute (bottom) mix channel signals for shallow OD indication subsequent to combining intermediate mix outputs.*
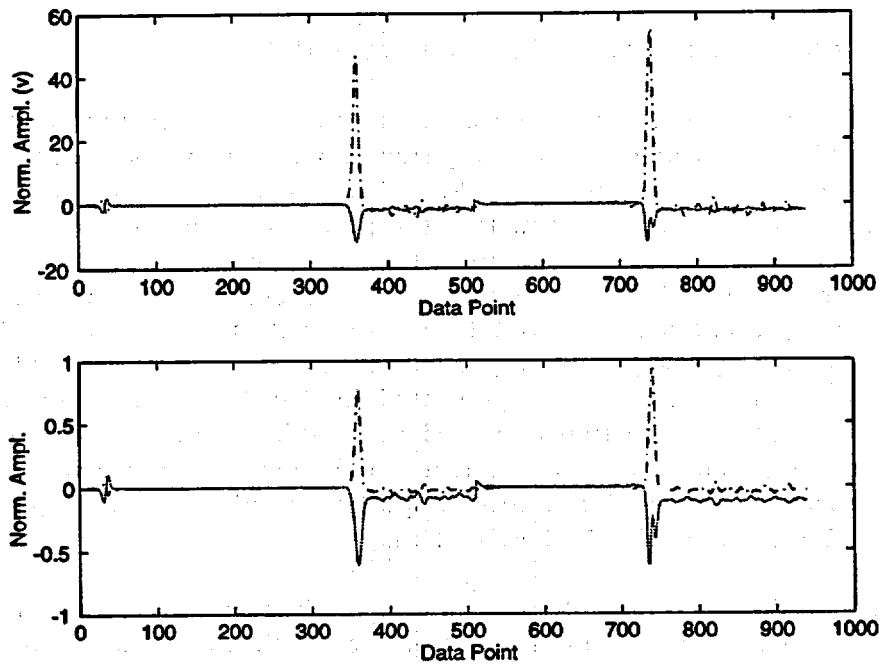
Fig. 3.4. *Differential BC horizontal and vertical signal components of calibrated original (top) and renormalized (bottom) traces at f = 400 kHz. Indications from left to right consist of throughwall reference hole and two roll transition zones with 30% ID circumferential and throughwall OD axial SCC, respectively.*
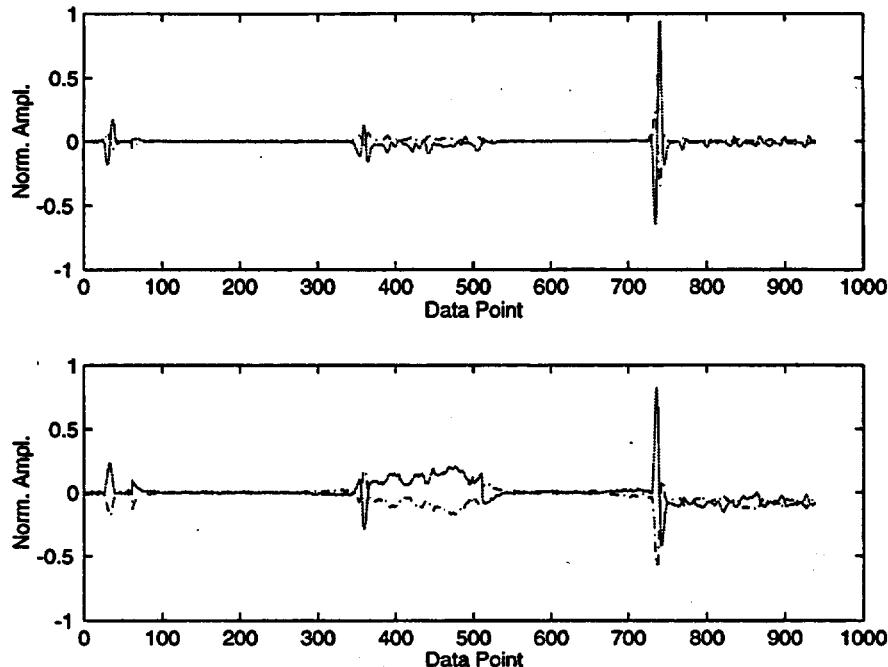
Fig. 3.5.   *Independent mix output signal for differential (top) and absolute (bottom) channels of data shown in Fig. 3.4.*

3.2   Multiparameter Analysis of Rotating Probe Data

This section provides a description of recent activities associated with multiparameter data analysis of EC inspection results. Implementation of a rule-based computer-aided data analysis routine is discussed in Sec. 3.2.1. The algorithm uses multiple-frequency EC readings from rotating probes to estimate depth profile of indications in a tube. Preliminary results are presented on the application of this multifrequency phase-based algorithm to various sets of experimental data acquired with conventional rotating probes. Initial results of the analysis are presented in Sec. 3.2.2 on a set of 20 tubes that contained laboratory-produced cracking morphologies that represent those that are incorporated into the ANL's SG mockup. Data analysis results are presented in Sec. 3.2.3 for a single specimen with laboratory-produced cracking that exhibited reportable BC indications with no clear flaw signal from rotating-probe inspections (pancake and +Point™ coils). Finally, estimated depth profiles are provided for a set of 24 laser-cut specimens with single, multiple, and ligamented notches of axial and acircumferential orientation.

Extensive studies are currently underway to analyze the NDE results from different coil configurations. Preliminary results in general suggest that EC readings from multiple coils could provide complementary information for more accurate sizing of difficult forms of degradations. Throughout this work, the rule-based algorithms that are described in this report will be refined as necessary to incorporate data analysis experiences acquired on new forms of degradation. More detailed description of ongoing studies on multiparameter data analysis of EC NDE results will be provided in our future reports.

3.2.1 Computer-Aided Data Analysis

A series of algorithms have been implemented in MATLAB programming script and are currently being refined to provide in real-time a profile of flaw depths in an SG tube from NDE results. The codes are integrated into a user interface tool to automatically process EC inspection results at multiple frequencies that are acquired with conventional bobbin and rotating probes. Figure 3.6 shows the main window of the graphical user interface (GUI) tool, *ETProf*, which incorporates various independent algorithms for processing of NDE results. Pull-down menus, push buttons, and editable text areas on the display can be activated to perform various stages of data analysis process.

Because estimates of flaw depth from phase angle information of multifrequency inspection data depend heavily on initial calibrations, it is expected that computer-aided data calibration routines would play an essential role in uniform and accurate normalization of raw EC data. Manual calibration of multifrequency rotating probe data is an especially time-consuming process and requires a great deal of effort. A series of GUI tools has been implemented to provide uniform and efficient calibration of raw EC inspection results. These codes, described in Ref. 1, were utilized in this study to carry out the initial calibration of raw EC readings.

The automated data analysis algorithm referred to in this work can be divided into three basic blocks. These blocks consist of various scripts that successively perform the calculation of S/N ratio for all channels, implement pre- and post-processing filters, and ultimately combine multiple frequency phase information from processed channels to provide an estimate of the depth profile for the entire length of the tube under examination. Initially, the S/N ratio is calculated from a user-defined approximate location along the trace baseline and minimum detectable amplitude from a calibration standard tube. Subsequently, this information is used to implement a set of filters that aid in suppressing signal background variations and in turn improve the S/N ratio. Filter characteristics are determined by taking into account both the coil configuration and the sampling frequency of the inspection data. Finally, the phase information at multiple frequencies is combined to calculate the depth profile for the entire tube in reference to known indications on a calibration standard tube. To reduce the ambiguity between OD (displayed as positive depth profile) and ID origin of an indication, the algorithm displays the depth information such that ID (and 100% TW) indications exhibit depth profiles with both positive and negative values along the depth axis. For ID indications, negative values provide the degradation extent. Currently, estimates of depth profile for each tube is made by direct comparison with known indications on a calibration standard tube. The algorithm is currently being refined to provide these values in a direct manner. This is done by fitting a polynomial to known flaw depths on the reference standard. Calculated coefficients of the regression fit would then be applied to the processed data channels to provide a continuous profile.

To verify the consistency of the outcomes, two calibration-standard tubes with different sets of machined flaw geometries were initially used for the analysis. With the EC response dependent on flaw geometry (i.e., length, depth, and width), the standards were selected to provide different flaw geometries with a similar range of depth variation. Figure 3.7 shows the original and processed channel traces for the two tube standards used in this study. The first tube contained five circumferential OD notches of nominal length and width
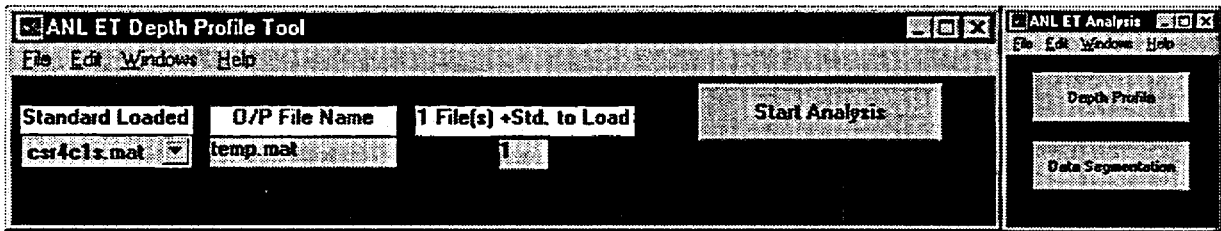
Fig. 3.6. A series of MATLAB-based Graphical User Interface (GUI) tools are currently under implementation to allow automated analysis of EC inspection results acquired with standard commercial instruments.

of 8 mm (0.315 in.) and 0.3 mm (0.012 in.), respectively, with depths ranging from 20% OD to throughwall. The second tube selected is an ASME standard with drilled holes of similar depth. This standard also contains a TSP simulation ring as well as 20 and 10% OD circumferential grooves. Figure 3.7(a) shows the calibrated amplitude traces at two frequencies. Examination of these data clearly indicates the presence of a nonlinear amplitude relationship that is dependent on both flaw geometry and operating frequency. Fig. 3.7(b) displays the estimated depth profiles for these tubes by combining the information from two and three channels, respectively. In all cases, the traces show similar depths for the entire range of OD indications. As mentioned earlier, the throughwall and ID indications have depth profiles that also extend in the negative direction. Although the results of analysis for the standards indicate similar results for two- and three-frequency depth profiles, studies so far have shown that for realistic flaws, more consistent estimates are generally achieved when three frequencies are used.

3.2.2 Analysis of 20-Tube Lab-Produced Specimens

The automated data analysis algorithm described in the previous section was utilized to estimate flaw sizes in a set of laboratory-grown specimens. Preliminary results on estimation of flaw depth profiles in this set of 20 tubes are presented next. Flaws in this set of 22.2-mm (0.875-in.)-diameter Alloy 600 tubing consisted mostly of longitudinal and circumferential ID/ODSCC, with a few samples containing shallow intergranular attack (IGA). The data set, which also contains metallography results, is currently being utilized to evaluate multiparameter sizing algorithms under evaluation in this program.

The preliminary outcome of the assessments presented here all pertain to the EC readings made with the primary 2.92 mm (0.115 in.) pancake coil of a three-coil rotating probe and at frequencies of 400, 300, and 200 kHz. The NDE results also contain information from several other probes that are also being evaluated as part of this study. Eddy current inspections were carried out by Zetec, with the frequency selection being limited to the range that is commonly used for ISI of 22.2-mm (0.875-in.)-diameter tubing. Attempts will be made throughout this study to evaluate potential improvement of the sizing capability by incorporating the inspection results from a wider range of frequencies.
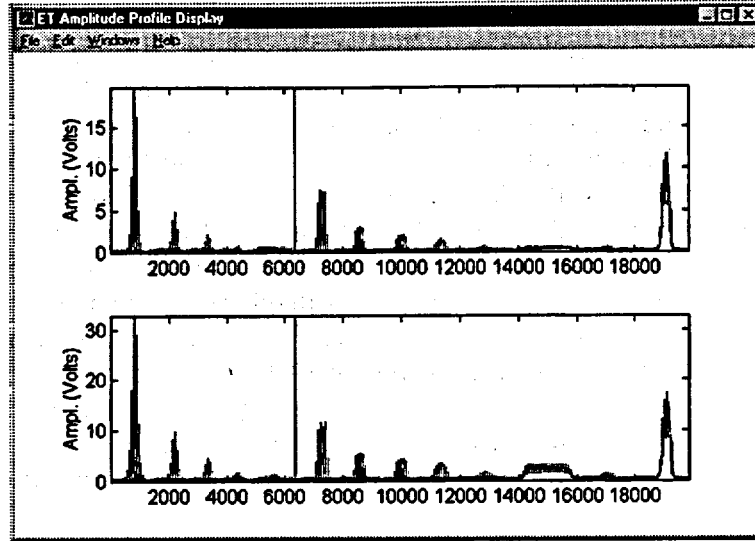
(a)
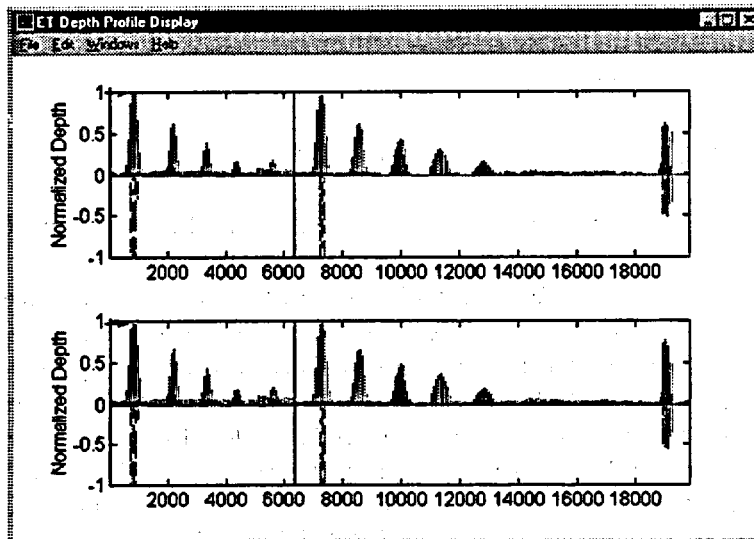
(b)

Fig. 3.7. Outputs of data analysis tool for estimation of defect depth profile for circumferential notch standard (left) containing five OD machined flaws ranging from 20-100% throughwall and an ASME standard (right) containing OD flat-bottom holes of same range, followed by TSP ring, 10% OD, and 20% ID grooves. Traces show (a) calibrated 400 kHz (top) and 200 kHz (bottom) amplitude (volts) and normalized depth profiles based on combining (b) two (top), and three (bottom) frequency channels. OD indications have positive trace and ID indications have both positive and negative traces. Eddy current readings are from 2.92 mm (0.115 in.) pancake of three-coil rotating probe.

27

Table 3.1 lists all the available information on the 20-tube subset of mock-up specimens, as well as the NDE depth estimates. For this initial investigation, NDE depth estimates are given at 20% intervals that cover the entire range of 0-100% of tube wall thickness. Figures 3.8-3.27 show preliminary results on the analysis of all specimens in the data set. For all samples, both the calibrated amplitude trace at 400 kHz and the estimated three-frequency normalized depth profile are displayed. Each trace from left to right consists of the OD circumferential notch standard followed by the degraded test specimen, with a vertical line separating the two tubes. To reduce the size of the data, only the section of the tube that contains the NDE suggested flaw indication(s) is displayed. Because the EC reading at each measurement location is, in effect, an integration of the current distribution over the entire field of view of the coil, it is not expected that point-type defects (e.g., specimen #2-11 shown in Fig. 3.12), if detected, will produce EC responses proportional to the actual flaw depth. Also, because the NDE results are dependent on the S/N ratio, estimation of depth (particularly for shallow OD indications) should take into consideration the level of noise present in each trace.

The data from different coil configurations are currently being analyzed using the 20-tube data set. Preliminary results generally suggest that EC readings from multiple coils could be utilized to provide complementary information for more accurate sizing of SG tubing degradations. Results of these ongoing studies will be provided in future progress reports. Efforts will continually be made to further refine the computer-aided data analysis codes currently being evaluated at ANL.

3.2.3   Reanalysis of Lab-Produced specimen SG-L432

NDE results from laboratory-produced specimen SG-L432, 22.2-mm (0.875-in.)-diameter Alloy 600 tubing, was also reanalyzed by using the multifrequency depth profile algorithm described earlier. This tube was reanalyzed because of the atypical nature of the original EC NDE results. Inspection results exhibited a BC indication with a relatively large flaw amplitude response, but without a discernible signal from midrange pancake and +Point coils. Figure 3.28(a) displays calibrated differential readings at 400 kHz primary and 100 kHz auxiliary frequencies that were acquired with an 18.3-mm (0.72-in.)-diameter magnetically biased bobbin probe. In the figure, the trace from an in-line ASME standard is shown on the left, and the response of the test specimen on the right. The lissajous patterns of the defected segment at the two frequencies are shown in Fig. 3.28(b). The bobbin results clearly suggest the presence of a shallow OD indication. The peak-to-peak signal amplitude and relative phase-angle for the flaw at 400 kHz were estimated to be 3.4 volts and 160°, respectively. This rather large bobbin signal amplitude and phase are indicative of a shallow volumetric degradation. Figure 3.29 shows calibrated readings from 0.115-in. pancake and midrange +Point™ coils at the same two frequencies. For both coils, any signals are buried within the noise level. The noise level in this tube is relatively high for both bobbin and pancake coils and is presumably associated with permeability variations introduced by sensitization of the specimen.

The raw EC readings from specimen SG-L432 were analyzed off-line by using the multifrequency algorithm that was described earlier. Information from three frequencies is used to estimate the flaw depth. Figure 3.30 displays the processed data showing the

Table 3.1. *Tabulated destructive examination and estimated EC NDE results by depth profile algorithm for 20-tube set of laboratory-grown specimens. Degradations were fabricated on 22.2-mm (0.875-in.)-diameter Alloy 600 tubes. NDE results are given in 20% depth intervals from 0 to 100% TW.*

Tube ID #	Flaw Type[a]	Roll Expansion	Max Depth (% TW) (Destructive Exam)	Depth Range (% TW) (NDE Estimate)
1-03	CIDSCC	X	44	40-60
1-11	LIDSCC	X	100	>80
1-19	LIDSCC	X	100	>80
2-06	LODSCC		100	>80
2-11	LODSCC		95[b]	60-80
2-19	LODSCC		46	20-40
2-20	LODSCC		16	<20
2-21	LODSCC		30	20-40
3-05	CIDSCC	X	69	60-80
3-14	LIDSCC	X	NA[c]	20-40
4-01	CODSCC	X	83	60-80
4-04	CODSCC	X	64	20-40
4-06	CODSCC	X	100	>80
4-10	CODSCC	X	100	>80
5-02	IGA		4	NDD[d]
5-03	IGA		5	<20
5-04	IGA		24	20-40
5-09	IGA		43	20-40
5-25	IGA		66	20-40
B-10-07	LODSCC		28	20-40

[a] LIDSCC: longitudinal IDSCC; CIDCSS: circumferential IDSCC; LODSCC: longitudinal ODSCC; CODCSS: circumferential ODSCC.

[b] A single point is identified as having 95% degradation extent with flaws on both sides <20% throughwall. All other crack networks (105 marked locations) are <38% TW.

[c] Destructive results not available (NA). Target depth is 30%-60% TW.

[d] No detectable degradation (NDD).
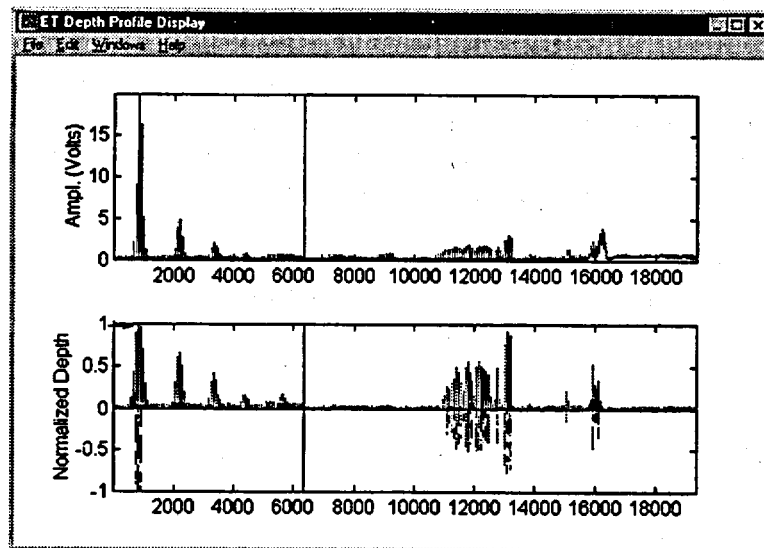
Fig. 3.8. *Output of data analysis tool for roll-expanded specimen #1-03 that was destructively identified as having 43% (max. depth) CIDSCC degradation. Traces show calibrated amplitude in volts (top), and normalized multifrequency depth profile (bottom) of notch standard (left) followed by sample tube, suggesting ≈40-60% range of degradation depth around scan locations 1.3 x 10⁴ and 1.6 x 10⁴. Eddy current readings are from 2.92 mm (0.115 in.) pancake of three-coil rotating probe.*
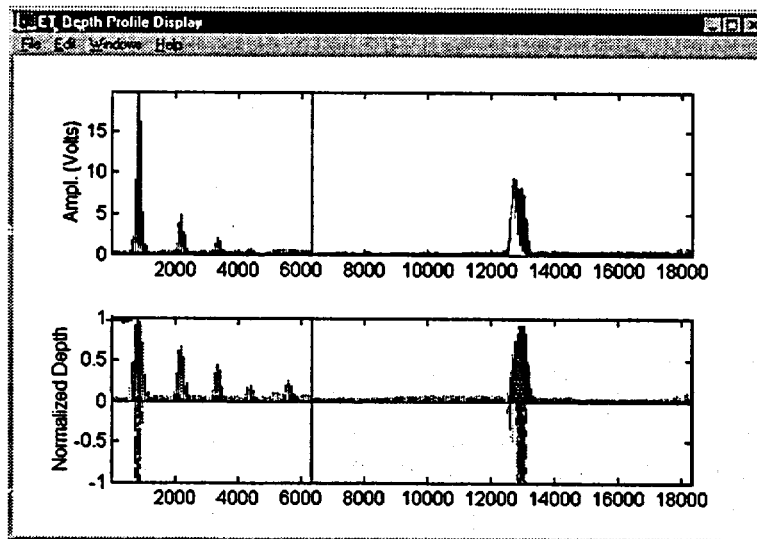
Fig. 3.9. *Output of data analysis tool for roll-expanded specimen #1-11 that was destructively identified as having 100% (max. depth) LIDSCC degradation. Traces show calibrated amplitude in volts (top), and normalized multifrequency depth profile (bottom) of notch standard (left) followed by sample tube, suggesting >80% degradation depth around scan location 1.3 x 10⁴. Eddy current readings are from 2.92 mm (0.115 in.) pancake of three-coil rotating probe.*
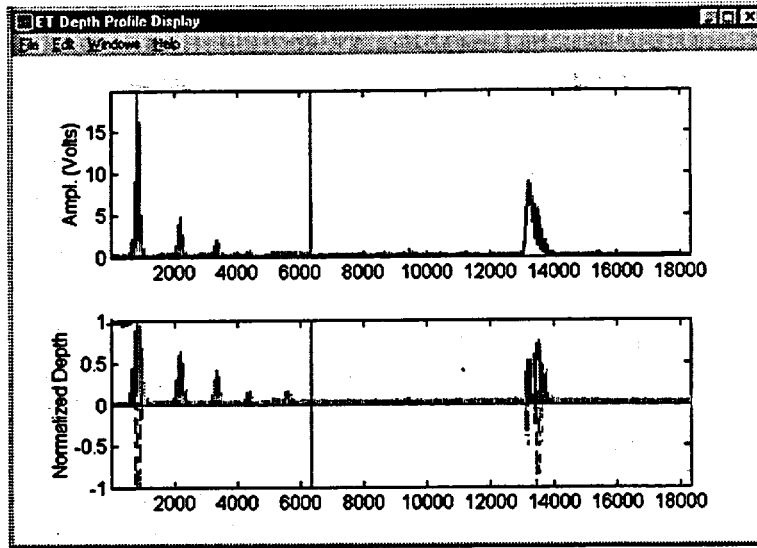
Fig. 3.10. Output of data analysis tool for roll-expanded specimen #1-19 that was destructively identified as having 100% (max. depth) LIDSCC degradation. Traces show calibrated amplitude in volts (top), and normalized multifrequency depth profile (bottom) of notch standard (left) followed by sample tube, suggesting >80% degradation depth around scan location 1.4×10^4. Eddy current readings are from 2.92 mm (0.115 in.) pancake of three-coil rotating probe.
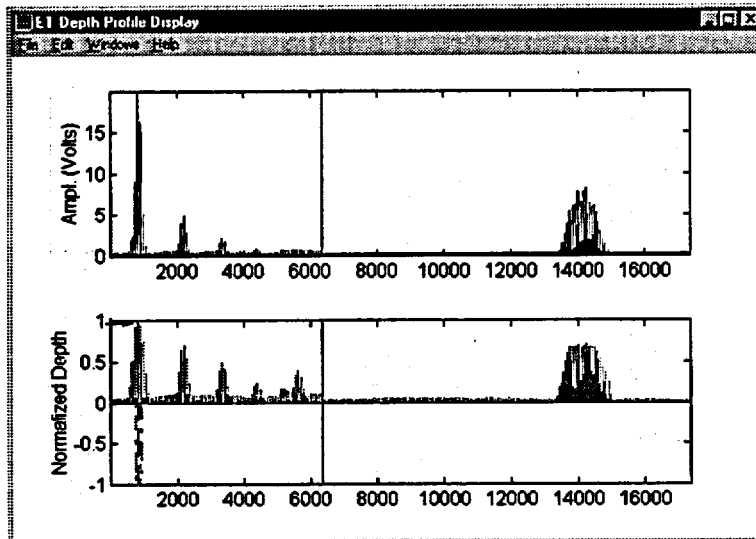
Fig. 3.11. Output of data analysis tool for roll-expanded specimen #2-06 that was destructively identified as having 100% (max. depth) LODSCC degradation. Traces show calibrated amplitude in volts (top), and normalized multifrequency depth profile (bottom) of notch standard (left) followed by sample tube, suggesting >80% degradation depth around scan location 1.4×10^4. Eddy current readings are from 2.92 mm (0.115 in.) pancake of three-coil rotating probe.
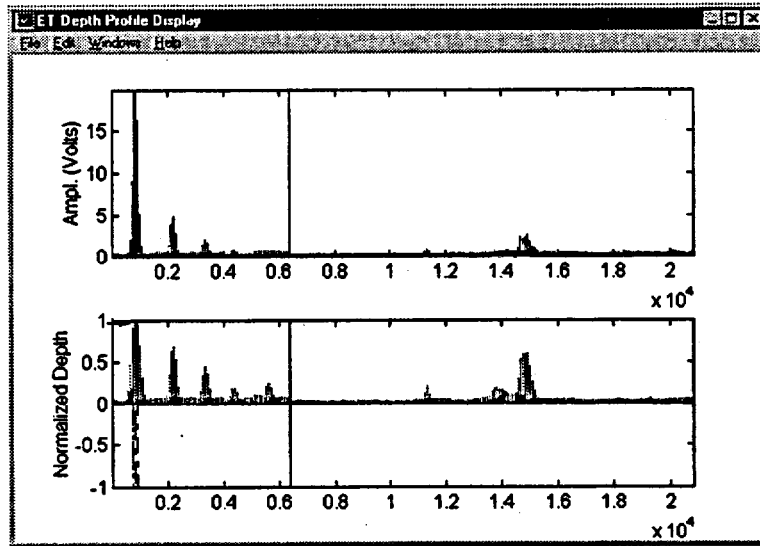
Fig. 3.12. Output of data analysis tool for specimen #2-11 that was destructively identified as having 95% (max. depth at a single point with all other indications marked <38%) LODSCC degradation. Traces show calibrated amplitude in volts (top), and normalized multifrequency depth profile.(bottom) of notch standard (left) followed by sample tube, suggesting 60-80% range of degradation depth around scan location 1.5 x 10⁴. Eddy current readings are from 2.92 mm (0.115 in.) pancake of three-coil rotating probe.
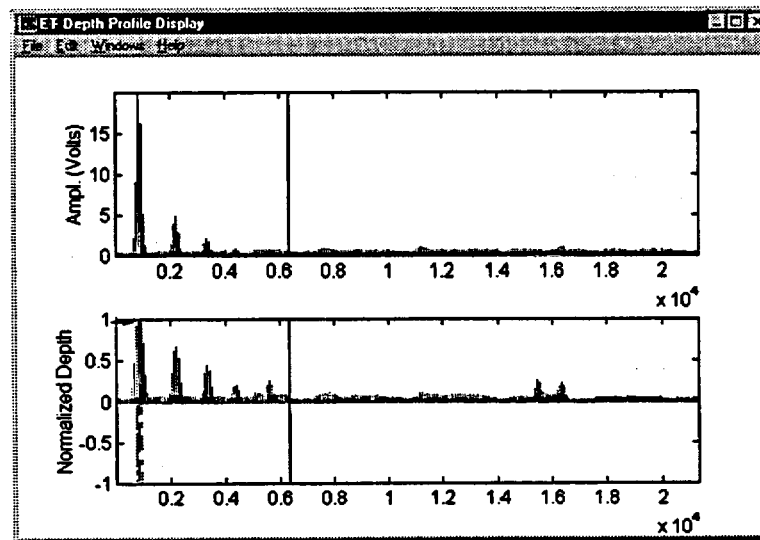
Fig. 3.13. Output of data analysis tool for specimen #2-19 that was destructively identified as having 46% (max. depth) LODSCC degradation. Traces show calibrated amplitude in volts (top), and normalized multifrequency depth profile (bottom) of notch standard (left) followed by sample tube, suggesting 20-40% range of degradation depth around scan location 1.6 x 10⁴. Eddy current readings are from 2.92 mm (0.115 in.) pancake of three-coil rotating probe.
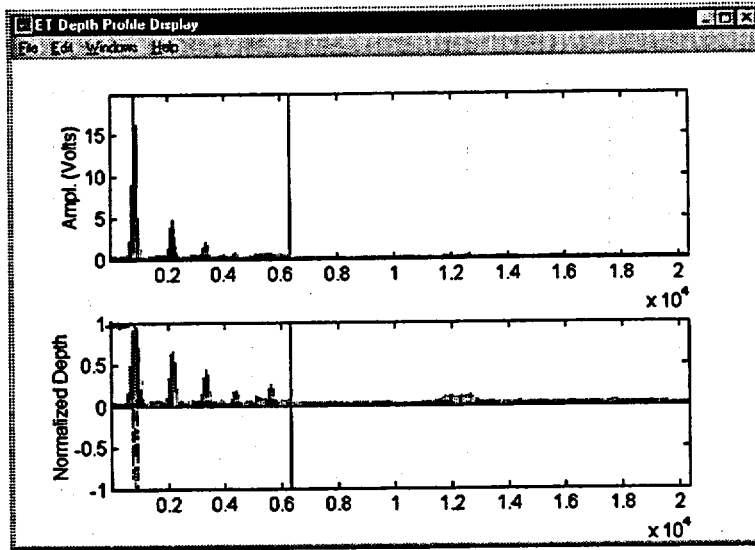
Fig. 3.14. *Output of data analysis tool for specimen #2-20 that was destructively identified as having 16% (max. depth) LODSCC degradation. Traces show calibrated amplitude in volts (top), and normalized multifrequency depth profile (bottom) of notch standard (left) followed by sample tube, suggesting <20% range of degradation depth around scan location 1.2×10^4. Eddy current readings are from 2.92 mm (0.115 in.) pancake of three-coil rotating probe.*
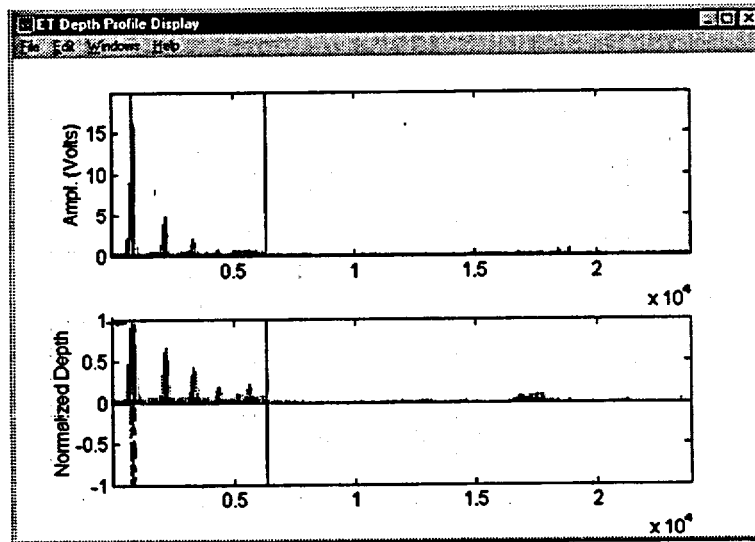
Fig. 3.15. *Output of data analysis tool for specimen #2-21 that was destructively identified as having 30% (max. depth) LODSCC degradation. Traces show calibrated amplitude in volts (top), and normalized multifrequency depth profile (bottom) of notch standard (left) followed by the sample tube, suggesting <20% range of degradation depth around scan location 1.7×10^4. Eddy current readings are from 2.92 mm (0.115 in.) pancake of three-coil rotating probe.*
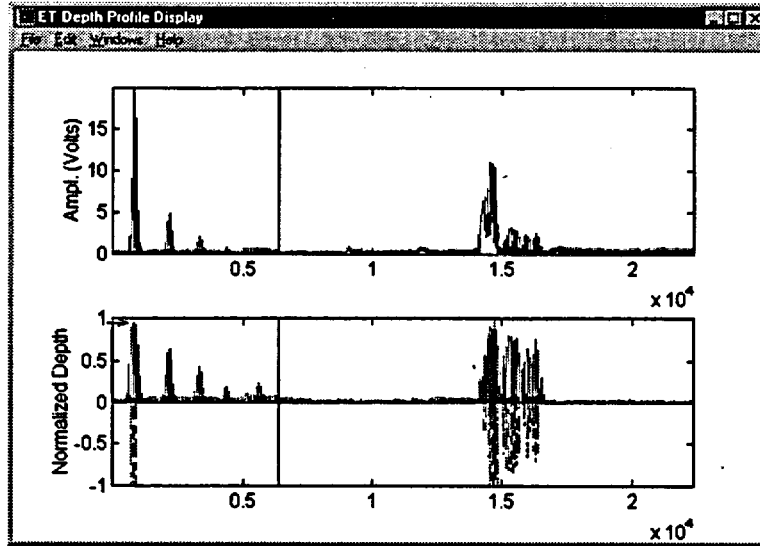
Fig. 3.16. *Output of data analysis tool for roll-expanded specimen #3-05 that was destructively identified as having ≈70% (max. depth) CIDSCC degradation. Traces show calibrated amplitude in volts (top), and normalized multifrequency depth profile (bottom) of notch standard (left) followed by sample tube, suggesting >80% range of degradation depth around scan location 1.5 x 10⁴. Eddy current readings are from 2.92 mm (0.115 in.) pancake of three-coil rotating probe.*

Fig. 3.17. *Output of data analysis tool for roll-expanded specimen #3-14 LIDSCC degradation (no DE results available; target value 30%-60%). Traces show calibrated amplitude in volts (top), and normalized multifrequency depth profile (bottom) of notch standard (left) followed by sample tube, suggesting 40%-60% range of degradation depth around scan location 1.4 x 10⁴. Eddy current readings are from 2.92 mm (0.115 in.) pancake of three-coil rotating probe.*
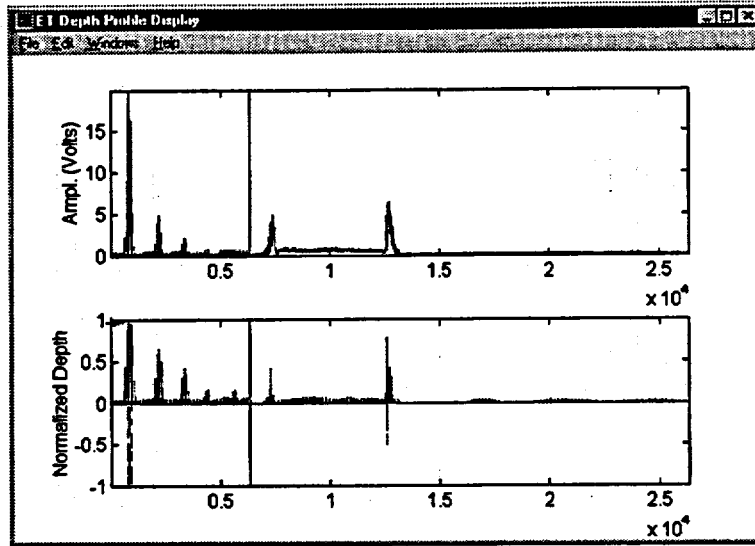
Fig. 3.18. *Output of data analysis tool for roll-expanded specimen #4-01 that was destructively identified as having 83% (max. depth) CODSCC degradation. Traces show calibrated amplitude in volts (top), and normalized multifrequency depth profile (bottom) of notch standard (left) followed by sample tube, suggesting 60%-80% range of degradation depth around scan locations 0.7×10^4 and 1.25×10^4. Eddy current readings are from 2.92 mm (0.115 in.) pancake of three-coil rotating probe.*
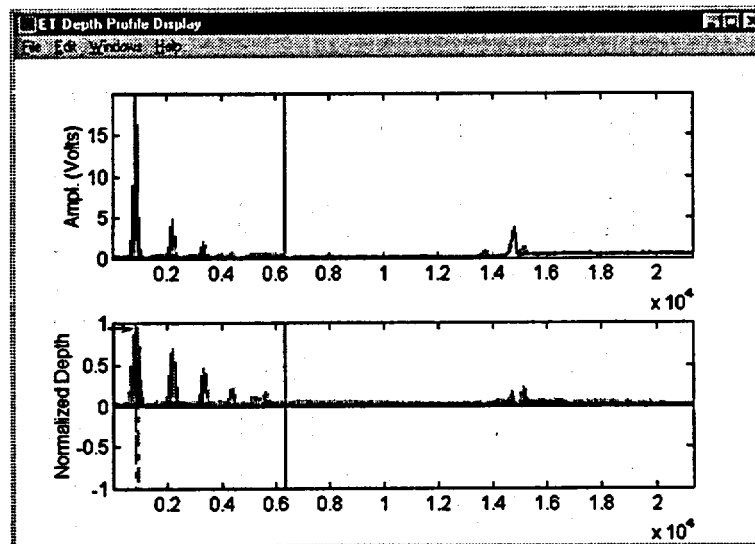
Fig. 3.19. *Output of data analysis tool for roll-expanded specimen #4-04 that was destructively identified as having 64% (max. depth) CODSCC degradation. Traces show calibrated amplitude in volts (top), and normalized multifrequency depth profile (bottom) of notch standard (left) followed by sample tube, suggesting >40% range of degradation depth around scan location 1.5×10^4. Eddy current readings are from 2.92 mm (0.115 in.) pancake of three-coil rotating probe.*
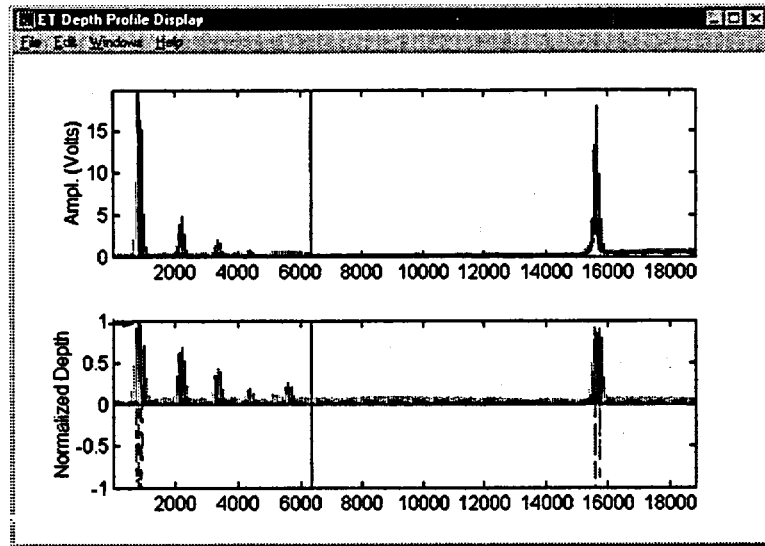
Fig. 3.20. Output of data analysis tool for roll-expanded specimen #4-06 that was destructively identified as having 100% (max. depth) CODSCC degradation. Traces show calibrated amplitude in volts (top), and normalized multifrequency depth profile (bottom) of notch standard (left) followed by sample tube, suggesting >80% range of degradation depth around scan location 1.6 x 10⁴. Eddy current readings are from 2.92 mm (0.115 in.) pancake of three-coil rotating probe.
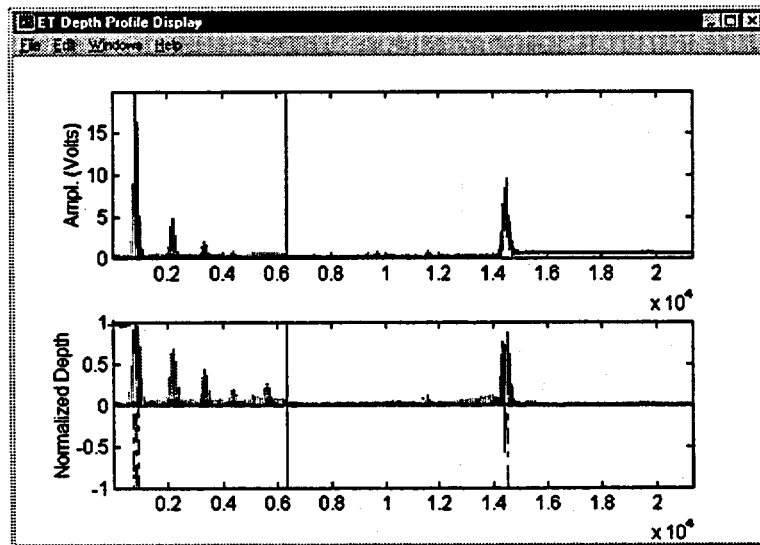
Fig. 3.21. Output of data analysis tool for roll-expanded specimen #4-10 that was destructively identified as having 100% (max. depth) CODSCC degradation. Traces show calibrated amplitude in volts (top), and normalized multifrequency depth profile (bottom) of notch standard (left) followed by sample tube, suggesting >80% range of degradation depth around scan location 1.4 x 10⁴. Eddy current readings are from 2.92 mm (0.115 in.) pancake of three-coil rotating probe.
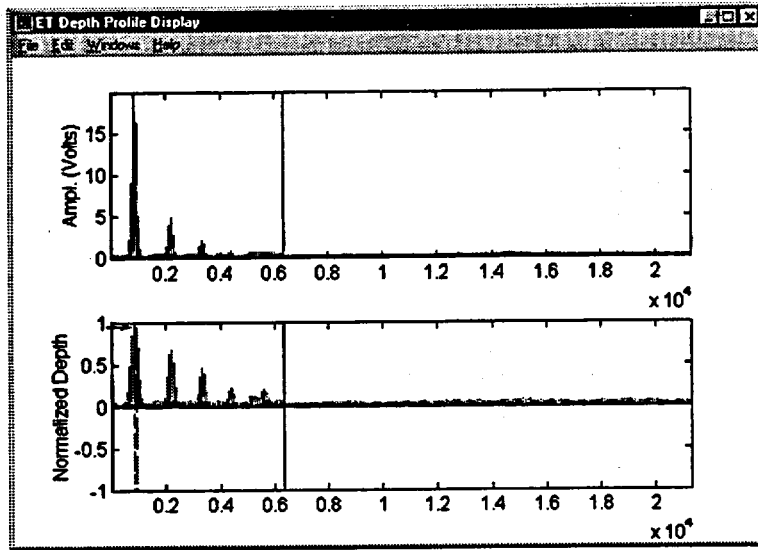
Fig. 3.22. *Output of data analysis tool for roll-expanded specimen #5-02 that was destructively identified as having 4% (max. depth) IGA degradation. Traces show calibrated amplitude in volts (top), and normalized multifrequency depth profile (bottom) of notch standard (left) followed by sample tube, suggesting no detectable degradation. Eddy current readings are from 2.92 mm (0.115 in.) pancake of three-coil rotating probe.*
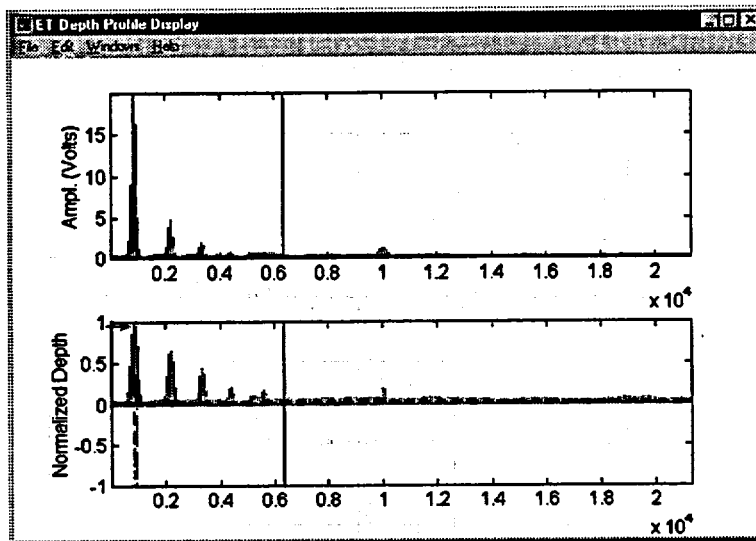
Fig. 3.23. *Output of data analysis tool for roll-expanded specimen #5-03 that was destructively identified as having 5% (max. depth) IGA degradation. Traces show calibrated amplitude in volts (top), and normalized multifrequency depth profile (bottom) of notch standard (left) followed by sample tube, suggesting <20% range of degradation depth around scan location 1 x 10^4. Eddy current readings are from 2.92 mm (0.115 in.) pancake of three-coil rotating probe.*
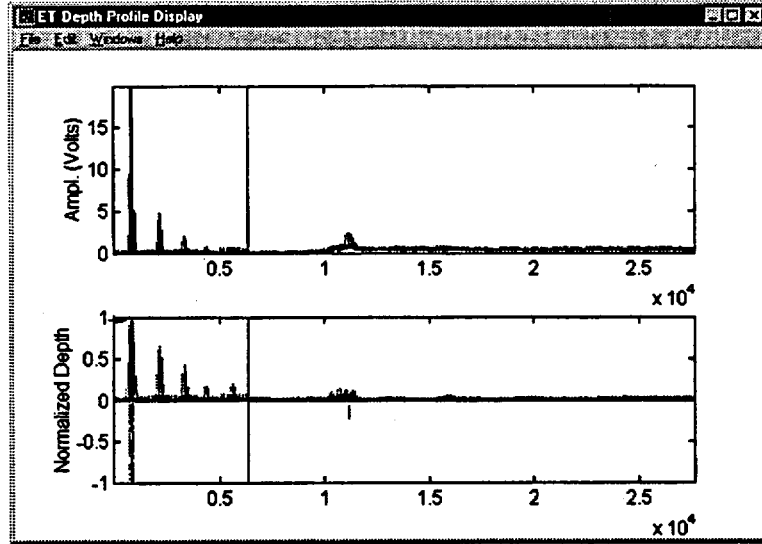
Fig. 3.24. *Output of data analysis tool for roll-expanded specimen #5-04 that was destructively identified as having 24% (max. depth) IGA degradation. Traces show calibrated amplitude in volts (top), and normalized multifrequency depth profile (bottom) of notch standard (left) followed by sample tube, suggesting 20%-40% range of degradation depth around scan location 1.1×10^4. Eddy current readings are from 2.92 mm (0.115 in.) pancake of three-coil rotating probe.*
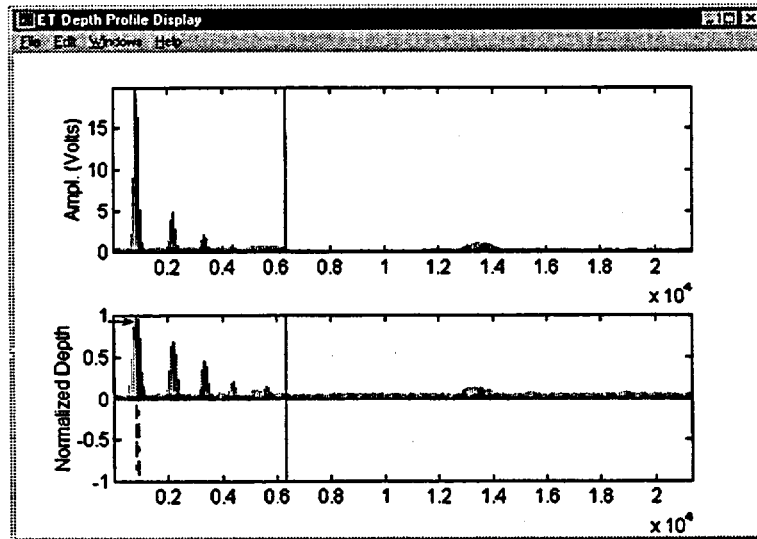
Fig. 3.25. *Output of data analysis tool for roll-expanded specimen #5-09 that was destructively identified as having 43% (max. depth) IGA degradation. Traces show calibrated amplitude in volts (top), and normalized multifrequency depth profile (bottom) of notch standard (left) followed by sample tube, suggesting 20%-40% range of degradation depth around scan location 1.3×10^4. Eddy current readings are from 2.92 mm (0.115 in.) pancake of three-coil rotating probe.*
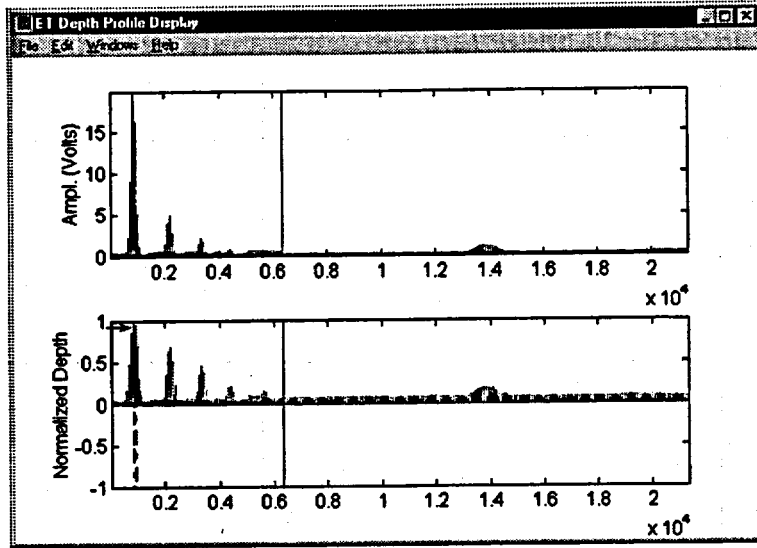
Fig. 3.26. *Output of data analysis tool for roll-expanded specimen #5-25 that was destructively identified as having 66% (max. depth) IGA degradation. Traces show calibrated amplitude in volts (top), and normalized multifrequency depth profile (bottom) of notch standard (left) followed by sample tube, suggesting 20%-40% range of degradation depth around scan location 1.4×10^4. Eddy current readings are from 2.92 mm (0.115 in.) pancake of three-coil rotating probe.*
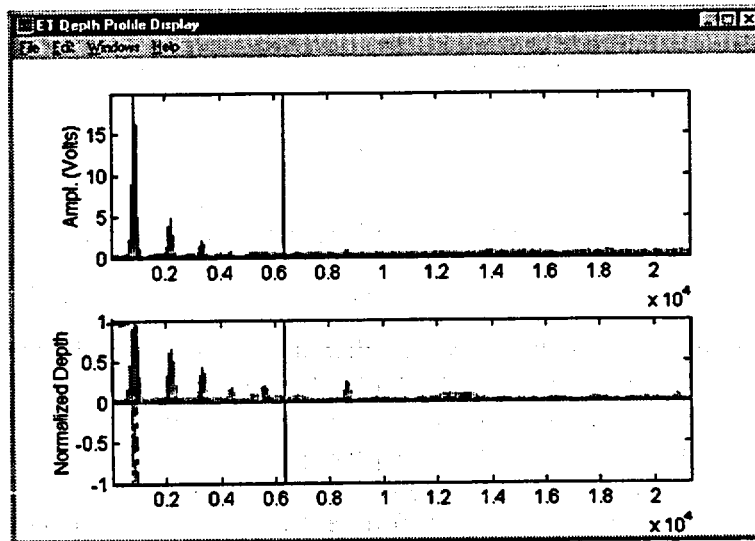
Fig. 3.27. *Output of data analysis tool for roll-expanded specimen #B10-07 that was destructively identified as having 28% (max. depth) LODSCC degradation. Traces show calibrated amplitude in volts (top), and normalized multifrequency depth profile (bottom) of notch standard (left) followed by sample tube, suggesting 20-40% range of degradation depth around scan locations 0.9×10^4 and 1.3×10^4. Eddy current readings are from 2.92 mm (0.115 in.) pancake of three-coil rotating probe.*
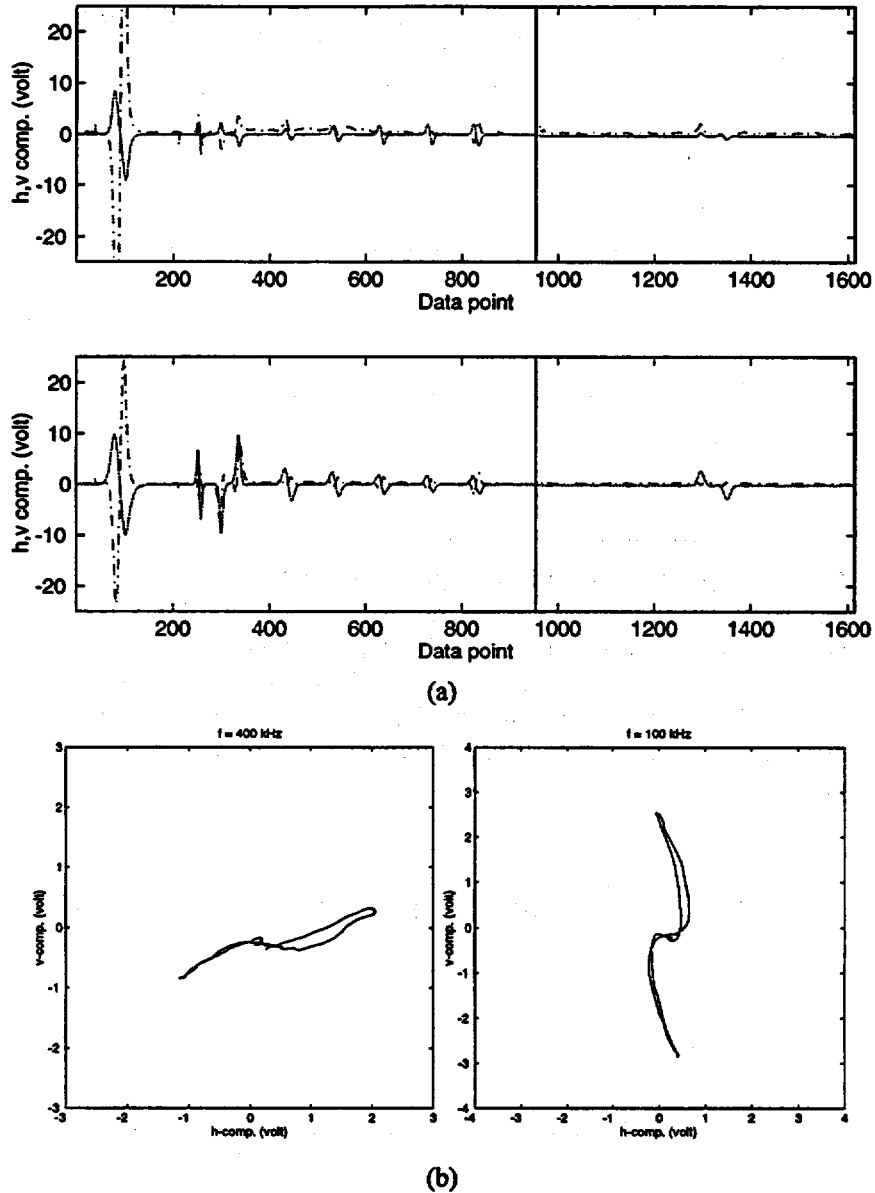
Fig. 3.28. (a) Stripchart and (b) Lissajous display of calibrated differential readings at 400 kHz (top) and 100 kHz (bottom) frequencies made with 18.3-mm (0.72-in.)-diameter magnetically biased bobbin probe on 22.2-mm (0.875-in.)-diameter Alloy 600 tube. Response from in-line ASME standard is shown on left; response of test specimen SG-L432 is on right. Calibrated signal amplitude and phase at 400 kHz was estimated to be 3.4 V and 160°, respectively, suggesting <20% OD degradation.
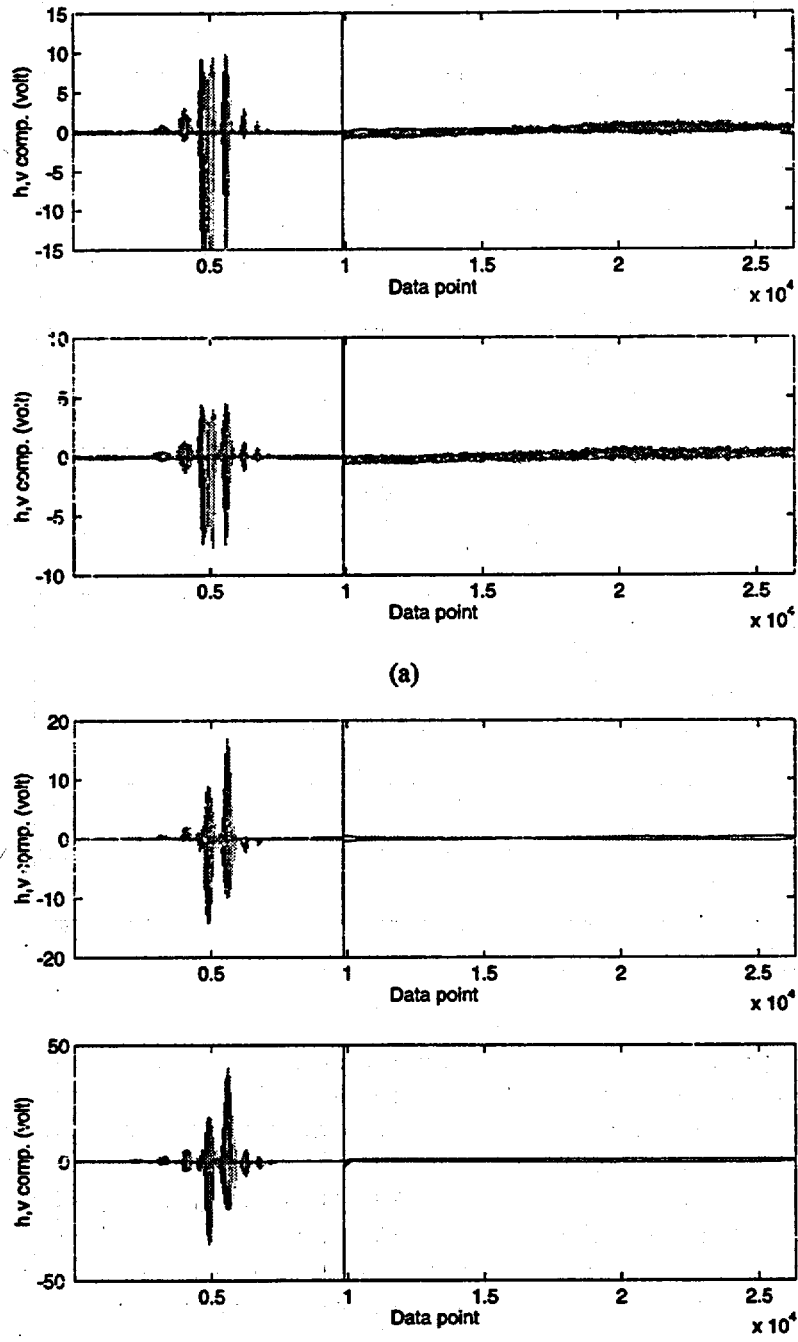
Fig. 3.29. Calibrated readings with (a) 2.92 mm (0.115-in.) pancake and (b) midrange +Point coils of three-coil rotating probe at 400 kHz (top) and 100 kHz (bottom) frequencies on 22.2-mm (0.875-in.)-diameter Alloy 600 tube. Response from 20-100% OD, 6.35-mm (0.25-in.)-long axial/circumferential EDM notches from in-line standard is shown on left; signal from test specimen SG-L432 is on right. No discernible indications are present in these traces, although a BC indication is present, as shown in Fig. 3.28.
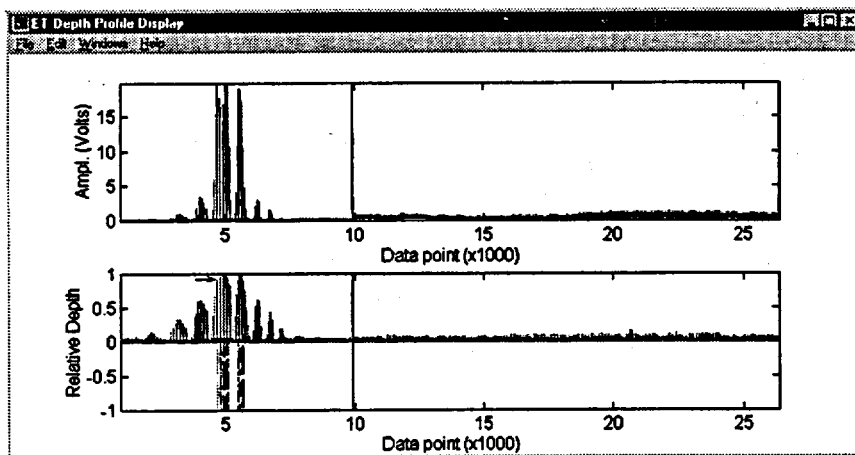
(a)
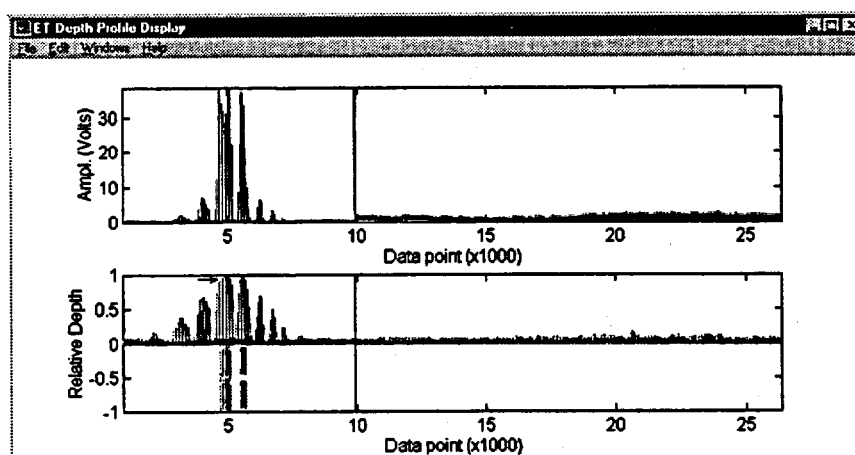
(b)

Fig. 3.30. *Outputs of multifrequency depth profile algorithm at (a) 400|300|200 kHz and (b) 300|200|100 kHz for specimen SG-L432. Selected data segments show calibrated amplitude in volts (top), and normalized multifrequency depth profile (bottom) for 20-100% OD, 6.35-mm (0.25-in.)-long axial/circumferential EDM notches from in-line standard followed by test specimen. Degradation extent around scan location 20 x 10³ suggests ≈20-40% OD flaw with maximum depth being slightly to right. Eddy current readings are from 2.92 mm (0.115-in.) pancake of three-coil rotating probe.*

calculated depth profiles at 400|300|200 and 300|200|100 kHz frequencies. Responses from an in-line EDM notch standard with 10 axial and circumferential OD indications are displayed on the left side of the trace; a comparison of the response from the indication with these responses provides an estimate of relative depth. In both cases, a shallow OD indication is visible just past data point No. 20,000, which is consistent with the location of the flaw based on the bobbin profile. The position of the flaw relative to the tube end was calculated by converting the number of measurement points to axial position along the tube using the locations of known markings on the standard. The phase-based flaw depth is estimated to be 20-40% OD TW (relative to the level of noise). Slight improvement is achieved with the lower

set of frequencies. This was expected because of the OD nature of the flaw. Although the bobbin response shows an axially long flaw profile, only the leading edge of the flaw is clearly discernible from the pancake coil results. This suggests a nonuniform depth profile of the degradation. Further testing of magnetically biased coils is planned to determine whether such probes can provide improved flaw depth estimates in sensitized tubing.

3.2.4 Analysis of Laser-Cut Specimens

Eddy current inspection results from a collection of 22.2-mm (0.875-in.)-diameter Alloy 600 tubes with laser-cut notches are currently being evaluated by conventional and alternate data analysis methods. Multiple-frequency EC inspection results were collected on all the available specimens with bobbin and rotating probes. Manufactured defect geometries range from single axial/circumferential notches to multiple ligamented notches. Nominal OD flaw depths for the majority of tubes were specified to be 80% TW, with two samples having 40% TW depths. However, the actual flaw depths have not yet been determined and may vary significantly along the flaw length. The geometries of all the available flaw types for laser-cut notch specimens were depicted previously in Table 2.3.

Raw EC readings for all specimens were converted, normalized, and reassembled in smaller segments for off-line analysis. Figures 3.31-3.35 display images of representative samples from the available data set at a frequency of 400 kHz. Each image is composed of reconstructed data segments from an EDM notch standard, followed by the tube containing the laser-cut flaw. In all cases, the EC profile conforms to the actual flaw geometry. However, the lack of spatial resolution in most cases limits the image to provide the necessary detail to view small ligaments (nominal widths of ≈0.13-0.50 mm [0.005-0.02 in.]) between segmented flaws. The resolution of the EC probe that is dependent on the coil dimensions and frequency of operation dictates the coil's field of view. The image resolution is also limited by the sampling rate and probe travel speed that is typically adjusted to provide a reasonable trade-off between resolution and data size.

Spatial resolution could be improved through application of signal enhancement and restoration schemes. Resolution enhancement techniques such as frequency and spatial domain deconvolution algorithms are currently being evaluated. A detailed description of the findings on the analysis of laser-cut specimens through utilization of multiparameter depth estimation and Fourier domain deconvolution will be provided in future reports. Comparative studies are being carried out to evaluate the accuracy of these techniques against conventional data analysis procedures. This collection of specimens that will be utilized for the pressure and leak-rate studies provide an ideal data set for assessing conventional EC NDE methods and will be used in our ongoing studies for implementation and verification of improved data analysis algorithms.

Conventional and multiparameter analysis of laser-cut specimens

Preliminary analysis of EC inspection results on the laser-cut specimens was performed using inspection data from bobbin and RPC probes. All data were analyzed with the Eddynet98™ analysis software. Bobbin results were calibrated with reference to an in-line ASME machined hole standard in accordance with the conventional bobbin calibration of
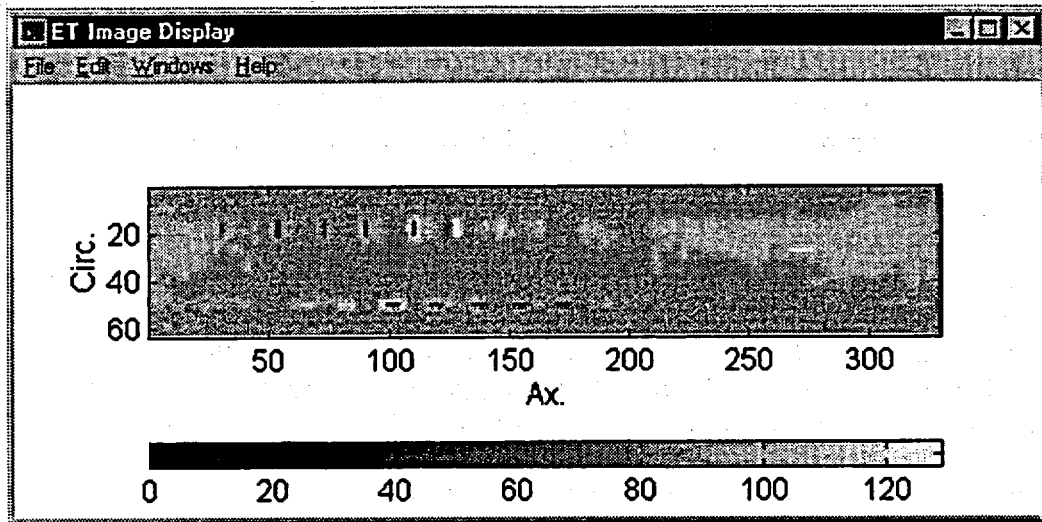
Fig. 3.31. Image display of RPC inspection results at 400 kHz showing data segments from in-line standard followed by Type-1 laser-cut specimen. Response from in-line standard with 6.35-mm (0.25-in.)-long axial/circumferential EDM notches of various depths is at left; response from laser-cut specimen containing 6.35-mm (0.25-in.)-long 80% OD (nominal depth) axial notch is at right.
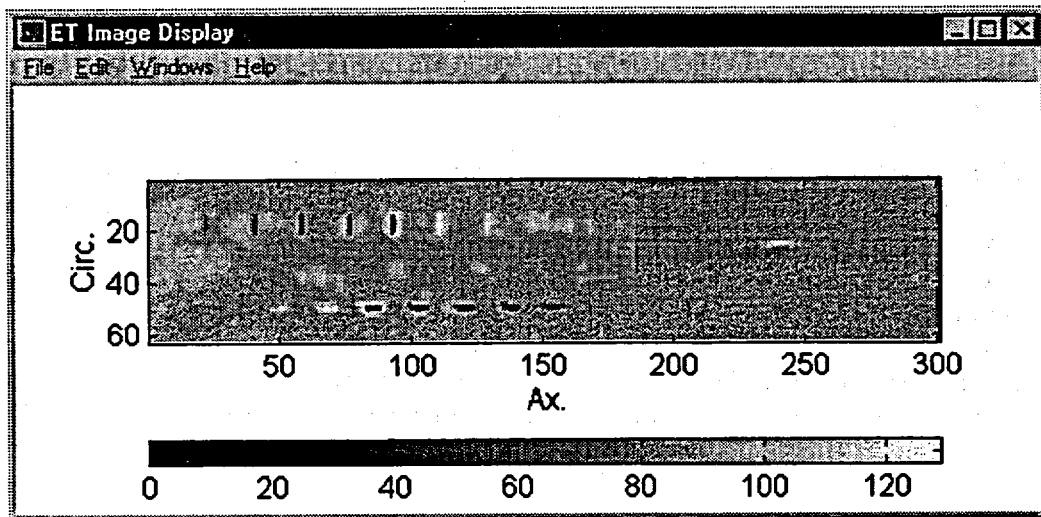
Fig. 3.32. Image display of RPC inspection results at 400 kHz showing data segments from in-line standard followed by Type-2 laser-cut specimen. Response from in-line standard with 6.35-mm (0.25-in.)-long axial/circumferential EDM notches of various depths is at left; response from laser-cut specimen containing two 12.7-mm (0.25-in.)-long 80% OD (nominal depth) axial notches with 0.25-mm (0.01-in) axial ligament is at right.
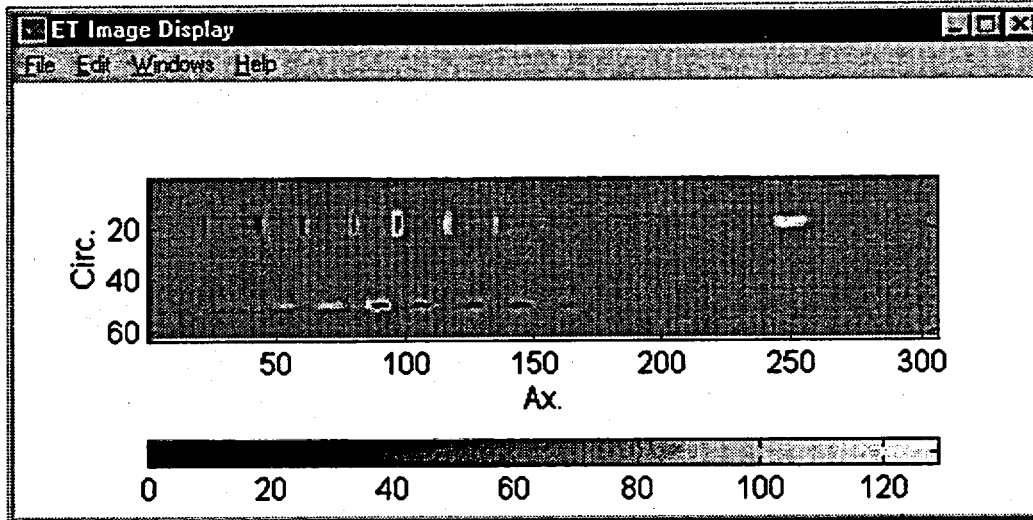
Fig. 3.33. *Image display of RPC inspection results at 400 kHz showing data segments from in-line standard followed by Type-5 laser-cut specimen. Response from in-line standard with 6.35-mm (0.25-in.)-long axial/circumferential EDM notches of various depths is at left; response from laser-cut specimen containing two sets of 12.7-mm (0.25-in.)-long, 80% OD TW circumferentially offset parallel flaws (three axial notches) with 0.51-mm (0.02-in)-wide ligaments is at right.*
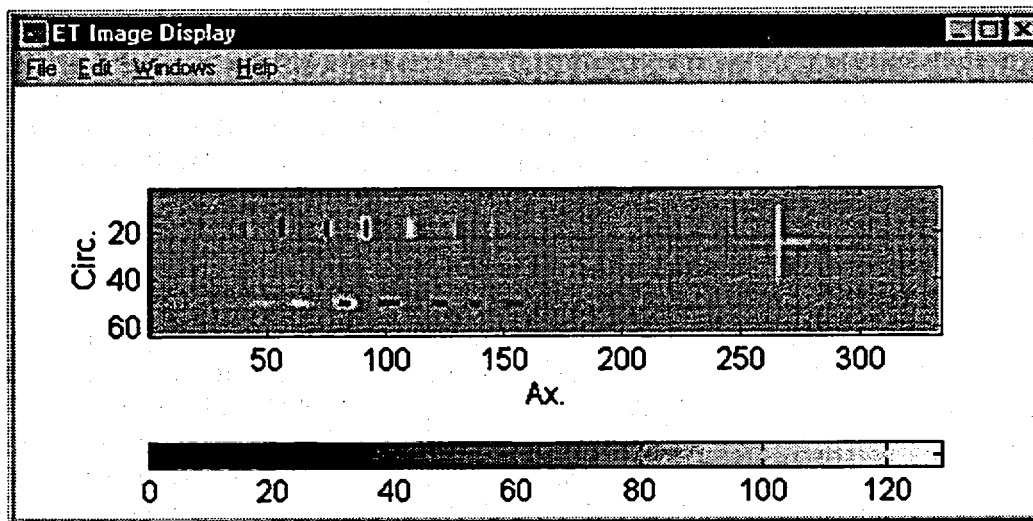
Fig. 3.34. *Image display of RPC inspection results at 400 kHz showing data segments from in-line standard followed by Type-9 laser-cut specimen. Response from in-line standard with 6.35-mm (0.25-in.)-long axial/circumferential EDM notches of various depths is at left; response from laser-cut specimen containing T-shaped flaw composed of 12.7-mm (0.5-in.)-long axial and 180° long circumferential notch of 80% OD (nominal depth) TW is at right.*
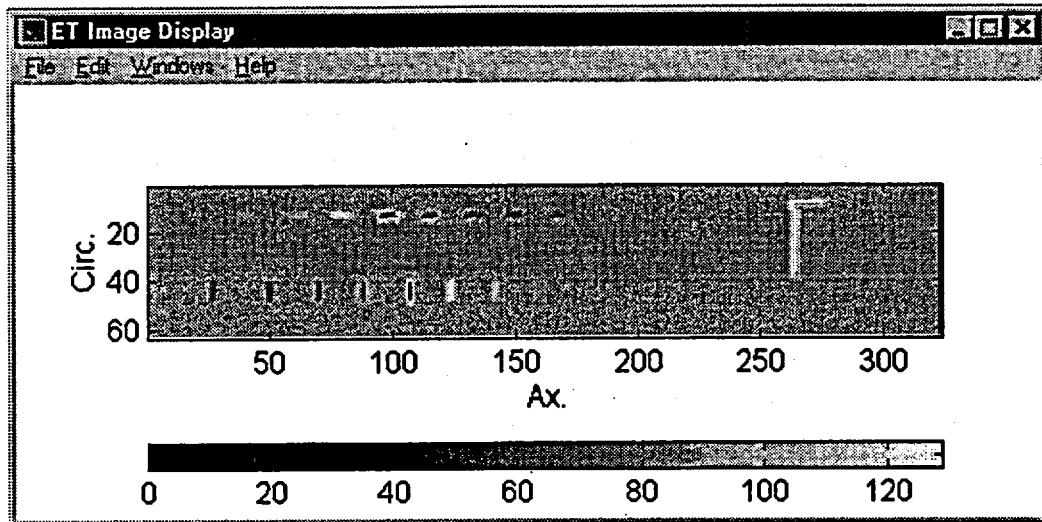
Fig. 3.35. Image display of RPC inspection results at 400 kHz showing data segments from in-line standard followed by Type-10 laser-cut specimen. Response from in-line standard with 6.35-mm (0.25-in.)-long axial/circumferential EDM notches of various depths is at left; response from laser-cut specimen containing L-shaped flaw composed of a 12.7-mm (0.5-in.)-long axial and 180° long circumferential notch of 80% OD (nominal depth) TW is at right.

voltage amplitude and phase. The primary frequency was taken as f = 400 kHz, and the signal amplitude for all other channels was normalized in reference to the primary channel. The +Point™ results were calibrated in reference to an 18-notch EDM standard containing 6.35–mm (0.25-in.)-long axial/circumferential flaws of various OD/ID depths, taking f = 300 kHz as the primary channel. A single OD calibration curve for the bobbin and two separate (OD/ID axial and circumferential) +Point phase-angle calibration curves were used to size the flaws.

Representative stripchart, Lissajous, and isometric plots of inspection results with magnetically biased (mag-biased) bobbin and mid-range +Point probe for two laser-cut specimens are shown in Figs. 3.36 and 3.37. Figures 3.38(a) and (b) are plots of nominal versus estimated NDE depths for bobbin and +Point probes, respectively. Although all flaws were detected with both types of probes, the sizing estimates vary significantly for the two probe types. Preliminary analysis of BC data indicates an overall underestimation of depth for all the available flaw types. Results from +Point coil inspections show improved sizing accuracy over that from the BC for the majority of the ligamented flaws. The +Point results indicate some underestimation of axial flaw depths, particularly for the ligamented notches and overestimation of depth for the circumferential flaws.

Some basic remarks should be made regarding the analysis of laser-cut specimens. The phase-angle-based depth estimates provided here for both probe types are not based on
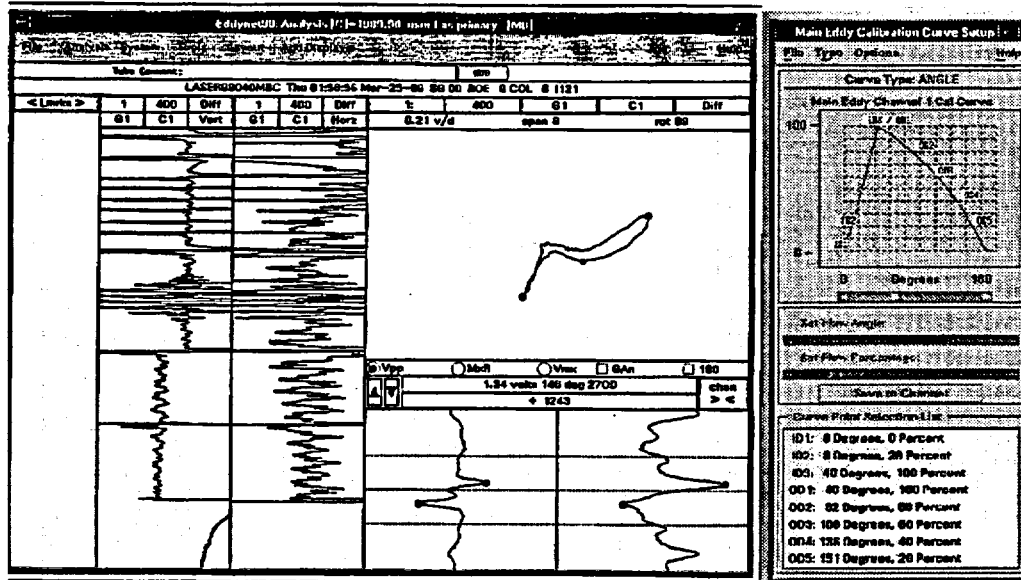
(a)
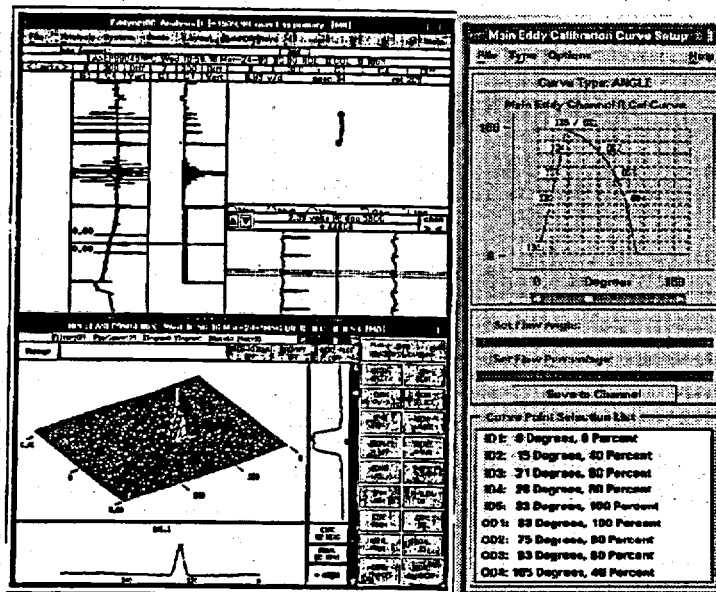
(b)

Fig. 3.36. *Representative stripchart, Lissajous, and isometric plots of inspection results with (a) mag-biased bobbin and (b) mid-range +Point probe for laser-cut type-1 specimen #5528-2-2 analyzed with Eddynet98 software. Also shown at right of each figure is phase-angle calibration curve used for estimating flaw depths. Bobbin results were calibrated in reference to an in-line ASME machined hole standard, taking f = 400 kHz as primary channel. +Point results were calibrated in reference to 18-notch EDM standard with 6.35-mm (0.25-in.)-long axial/circumferential flaws of various OD/ID depths, taking f = 300 kHz as primary channel.*
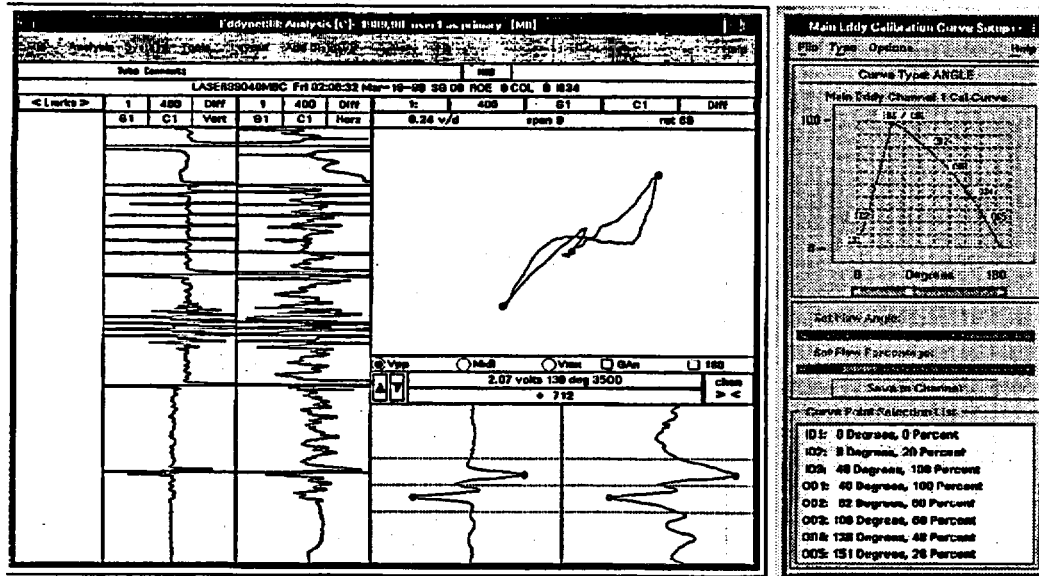
(a)
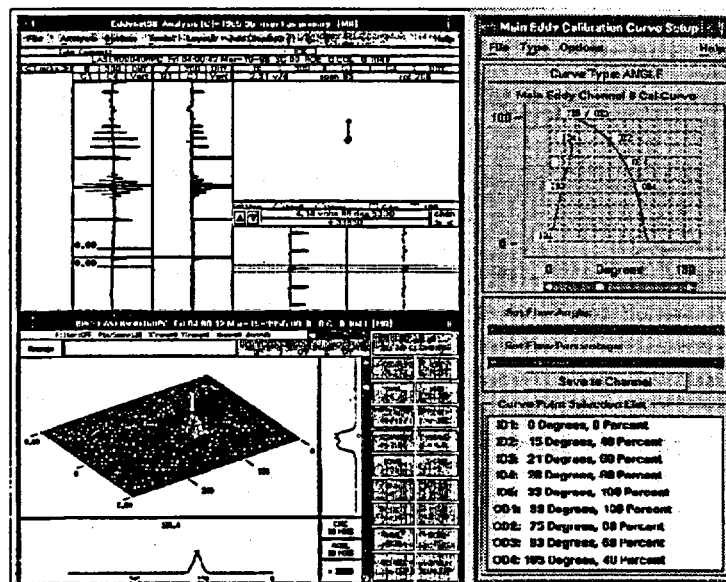
(b)

Fig. 3.37. *Representative stripchart, Lissajous, and isometric plots of inspection results with (a) mag-biased bobbin and (b) mid-range +Point probe for laser-cut type-2 specimen #5516-4-3 analyzed with Eddynet98 software. Also shown at right of each figure is phase-angle calibration curve used for estimating flaw depths. Bobbin results were calibrated in reference to in-line ASME machined hole standard, taking f = 400 kHz as primary channel. +Point results were calibrated in reference to 18-notch EDM standard with 6.35-mm (0.25-in.)-long axial/circumferential flaws of various OD/ID depths, taking f = 300 kHz as primary channel.*
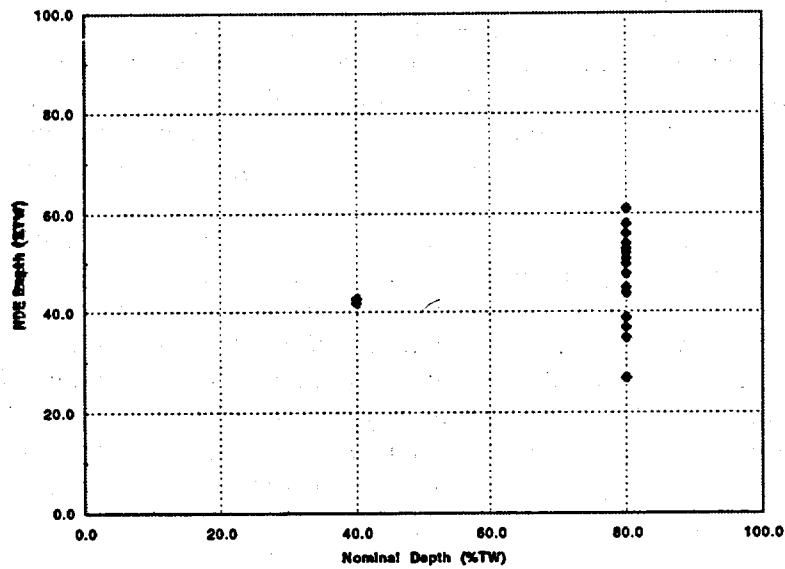
(a)
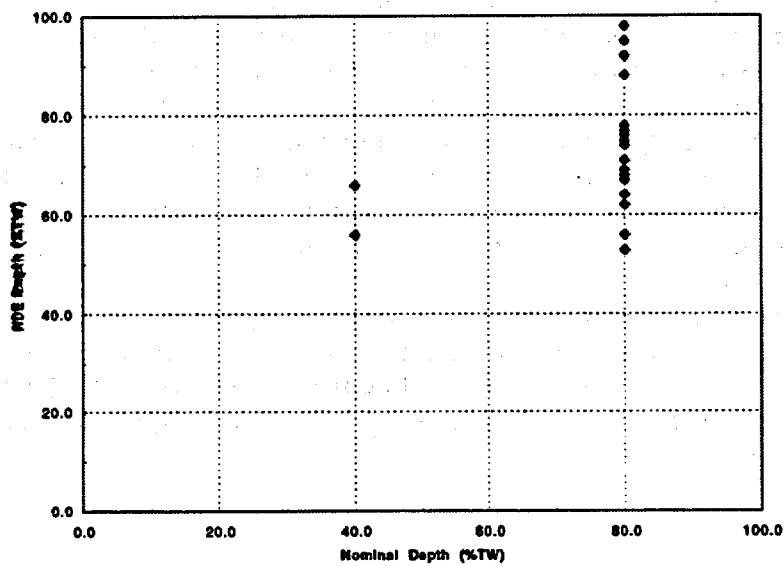
(b)

Fig. 3.38. Estimated vs. nominal flaw depth for (a) mag-biased bobbin (f = 400 kHz as primary channel) and (b) +Point rotating probe (f = 300 kHz as primary channel) for all available laser-cut slot specimens.

qualified sizing methods for all flaw types available in the data set. Also, the nominal flaw depths associated with laser-cut specimens may not represent the true depth. On the other hand, it is expected that the scatter of sizing results shown in Figs. 3.38(a) and (b) would increase for field-induced flaws. This is primarily due to factors such as complexity of flaw morphology, overall tightness of crack openings, difficulty of signal interpretation due to distortions introduced by internal/external discontinuities (e.g., design discontinuities, dimensional variations, deposits, and tube ID conditions), and analyst variability.

Subsequent multiparameter analysis on the laser-cut specimens used the data from 2.92 mm (0.115-in.) primary pancake coil of a three-coil rotating probe at 400, 300, and 200 kHz frequencies. Figures 3.39-3.44 display selected results of the analysis using the multiparameter approach. Each figure contains the voltage amplitude and relative depth of the selected sample. Figure 3.45 is a plot of nominal versus estimated NDE depths. Similar results are shown in Fig. 3.45 for the multiparameter technique. Table 3.2 lists the nominal dimensional information for all the available laser-cut samples, along with the analysis results with bobbin and +Point probes discussed in the previous section, as well as the multiparameter estimates.

Although all flaws were detected with all three techniques described in this section, the sizing estimates vary significantly between bobbin and RPC probes and, to a lesser extent, between the two RPC methods. Preliminary analysis of BC data indicates an overall underestimation of depth for all the available flaw types. Results from +Point coil inspections show improved sizing accuracy over that of the BC for the majority of indications and, in particular, for ligamented flaws. The +Point results indicate some underestimation of axial flaw depths, particularly for ligamented notches, and overestimation of depth for most circumferential flaws. The multiparameter sizing estimates, although closer to the single-frequency +Point estimates, show smaller overall scatter of the sizing results and better agreement with the nominal values for the notch depths.

Studies are currently underway to further analyze the laser-cut notch specimens by various alternative data analysis and signal processing schemes. A more detailed description of the results of this work will be provided in our upcoming reports. Comparative studies are being carried out to evaluate the accuracy of these techniques against conventional data analysis procedures.
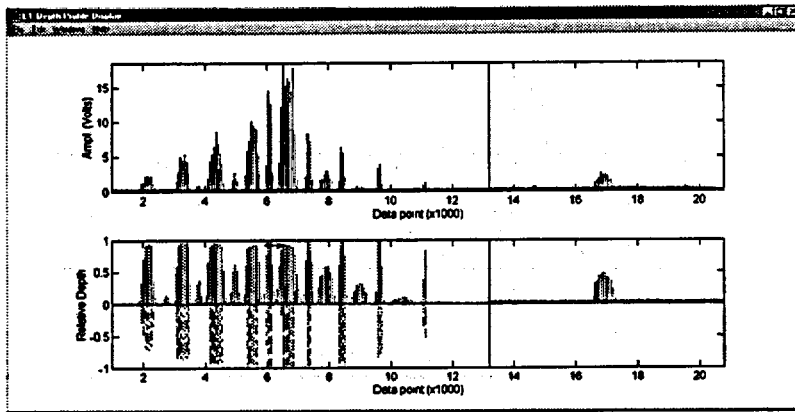
Fig. 3.39. *Representative display of mutiparameter analysis results showing calibrated voltage amplitude profile (top) and estimated relative depth. Profiles are composed of 18-notch standard (left) with axial/circumferential OD/ID EDM flaws followed by Type-1 specimen #5528-1-1 (right).*
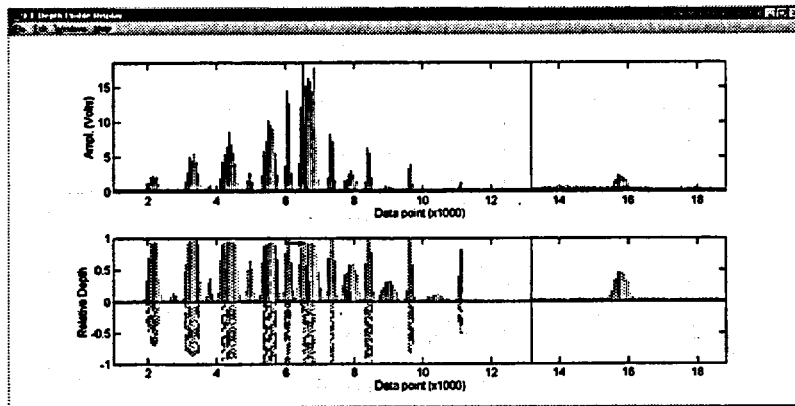
Fig. 3.40. *Representative display of multiparameter analysis results showing calibrated voltage amplitude profile (top) and estimated relative depth. Profiles are composed of 18-notch standard (left) with axial/circumferential OD/ID EDM flaws followed by Type-1 specimen #5528-1-2 (right).*
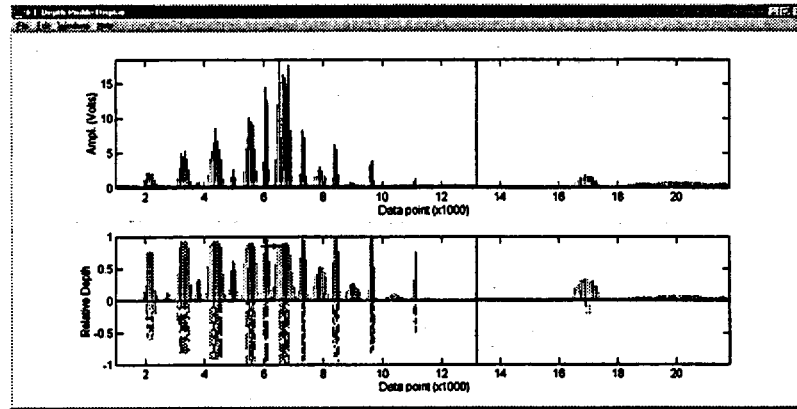
Fig. 3.41. *Representative display of multiparameter analysis results showing calibrated voltage amplitude profile (top) and estimated relative depth. Profiles are composed of 18-notch standard (left) with axial/circumferential OD/ID EDM flaws followed by Type-2 specimen #5516-4-3 (right).*
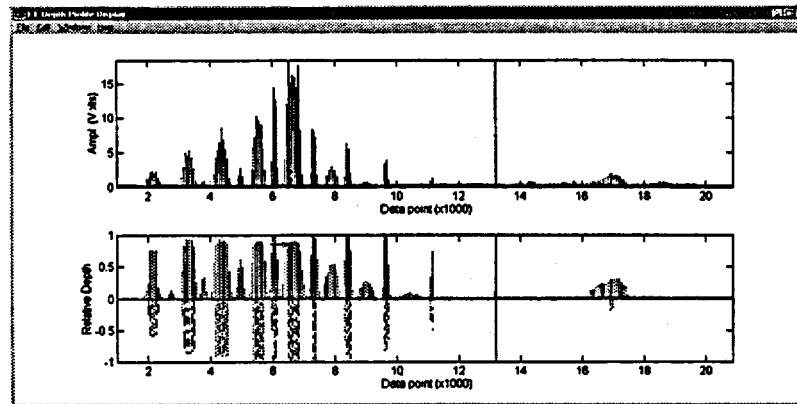
Fig. 3.42. *Representative display of multiparameter analysis results showing calibrated voltage amplitude profile (top) and estimated relative depth. Profiles are composed of 18-notch standard (left) with axial/circumferential OD/ID EDM flaws followed by Type-2 specimen #5516-4-2 (right).*
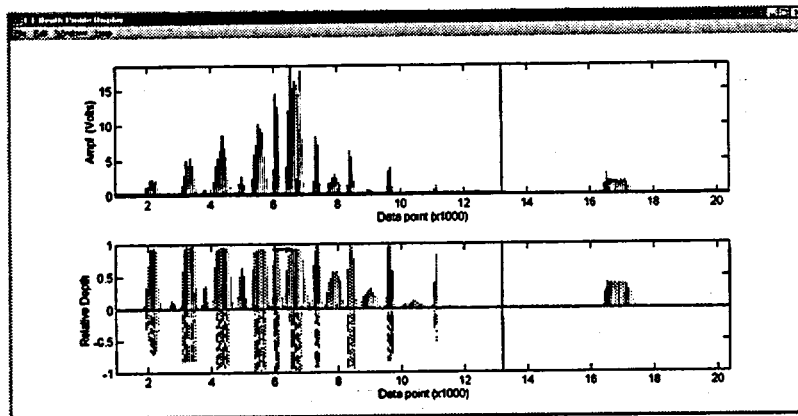
Fig. 3.43. *Representative display of multiparameter analysis results showing calibrated voltage amplitude profile (top) and estimated relative depth. Profiles are composed of 18-notch standard (left) with axial/circumferential OD/ID EDM flaws followed by Type-9 specimen #5469-4-3 (right).*
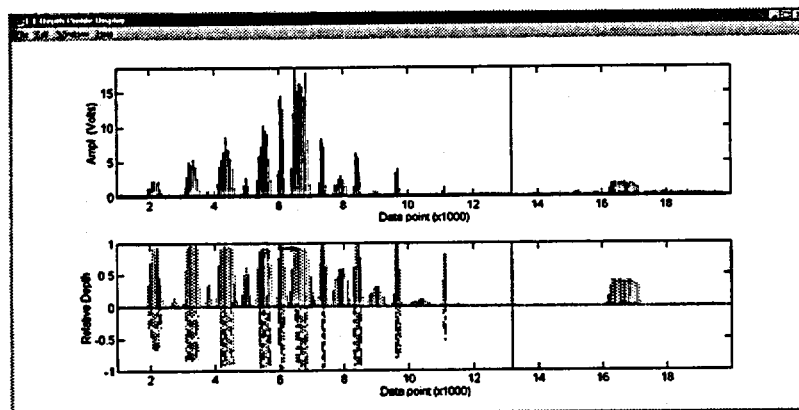
Fig. 3.44. *Representative display of multiparameter analysis results showing calibrated voltage amplitude profile (top) and estimated relative depth. Profiles are composed of 18-notch standard (left) with axial/circumferential OD/ID EDM flaws followed by Type-10 specimen #5469-4-4 (right).*
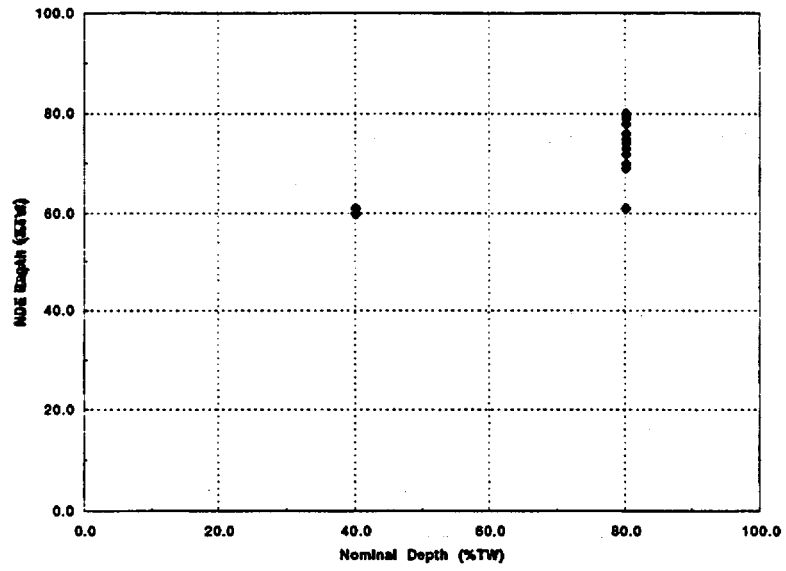
Fig. 3.45. *Multiparameter estimate vs. nominal flaw depth for all available laser-cut slot specimens.*

55

Table 3.2. *All available laser-cut samples and their nominal dimensions. Also listed are single-frequency NDE results from mag-biased bobbin and +Point probes, along with multiparameter (M.P.) estimate with 2.92 mm (0.115-in.) pancake probe.*

Tube I.D.	Specimen Type	No. of Notches	Notch Length (mm or °)	Notch Depth (% TW)	Ligament Width (mm)	Bobbin Coil Results Ampl. (v)	Bobbin Coil Results % TW	+Point Results Ampl. (v)	+Point Results % TW	Multiparameter % TW
5528-1-1	1	1	6.35	80	NA	2.71	58	6.13	75	75
5528-1-2	1	1	6.35	80	NA	2.83	51	5.47	68	74
5528-1-3	1	1	8.89	80	NA	2.77	56	5.92	75	76
5528-1-4	1	1	8.89	80	NA	2.50	58	5.99	75	73
5528-2-1	1	1	12.7	80	NA	1.79	44	3.97	67	69
5528-2-2	1	1	12.7	80	NA	1.34	27	2.39	56	61
5516-4-3	2	2	12.7	80	0.25	2.07	35	4.14	53	72
5516-4-2	2	2	12.7	80	0.13	1.54	50	4.40	62	70
5528-3-1	3	6	12.7	80	0.13	1.64	53	3.85	69	70
5528-3-2	3	6	12.7	80	0.25	1.64	45	3.95	74	73
5528-3-3	3	6	12.7	40	0.25	0.92	42	2.71	66	61
5528-3-4	4	6	12.7	80	0.13	1.47	61	4.83	75	76
5469-2-1	4	6	12.7	80	0.25	2.00	45	4.48	71	74
5469-2-2	4	6	12.7	40	0.25	1.22	43	3.08	56	60
5469-2-3	5	6	12.7	80	0.25	5.11	52	10.08	77	79
5469-2-4	5	6	12.7	80	0.50	4.37	45	7.03	64	78
5469-3-1	6	6	12.7	80	0.25	6.79	56	11.77	78	80
5531-3-1	6	6	12.7	80	0.50	9.15	58	13.37	76	79
5469-3-3	7	2	360°	80	0.13	4.43	44	3.25	95	75
5469-3-4	7	2	360°	80	0.25	4.12	37	2.77	92	74
5469-4-1	8	6	360°	80	0.25	1.56	39	2.54	88	70
5469-4-2	8	6	360°	80	0.13	1.46	54	2.52	98	70
5469-4-3	9	2	180° x 0.5	80	N/A	2.63	48	6.18	62	69
5469-4-4	10	2	180° x 0.5	80	N/A	2.01	53	4.44	68	72

4 Research on Degradation Modes and Integrity (D. R. Diercks, K. E. Kasza, S. Majumdar, and W. J. Shack)

4.1 Production of Laboratory-Degraded Tubes

Because degraded tubing from operating or retired SGs is difficult and expensive to obtain and the availability of such tubing is limited, it is necessary to produce prototypical degradation in tubes as a part of this program. These tubes are to be used to evaluate NDE equipment and techniques in the SG mock-up and for pressure and leak-rate testing. Techniques for Alloy 600 tubes have been developed to produce SCC degradation of various sizes, depths, and orientations that are prototypical of field-degraded SG tubes.

4.1.1 Production of Cracked Tubes

The production of laboratory-degraded tube specimens continued throughout the reporting period. Alloy 600 tubes of 22.2-mm (7/8-in.) diameter (Heat nos. NX8527 and NX7968) have been subjected to the cracking treatment. These tubes were cracked by exposing them to a 1 M aqueous solution of sodium tetrathionate ($Na_2O_6S_4 \cdot 2H_2O$) at room temperature and atmospheric pressure. Before exposure to the tetrathionate solution, the specimens were solution heat treated at 1100°C ($\approx$2000°F) for 10 min and aged at 600°C ($\approx$1100°F) for 48 h to produce a microstructure that is susceptible to cracking.[1] During this reporting period, $\approx$200 tube specimens were heat treated, including tubes from Heat NX8527 and Heat NX7968. Approximately 100 of these tubes have been processed for cracking in the tetrathionate solution, including tubes with axial ODSCC, tubes with ODSCC in the roll-expanded region, and dented tubes with axial IDSCC. Some of the heat-treated tubes have been installed as uncracked blanks in the NDE SG tube mock-up (see Section 1).

Several techniques have been explored in an effort to produce segmented SCC, including surface defects, shot-peening, localized environmental exposure, low load, and applied electrochemical potential. A localized electrochemical potential technique with low applied load and area masking appears to be most effective to date. Five tubes were prepared with surface defects that had associated reductions of wall thickness of 10% (tubes SGL311-SGL315). All five developed throughwall OD axial cracks, but there was no evidence that the surface defects helped produce segmented SCC. Twelve tubes were shot-peened before sensitization at the specific location where cracking was desired to introduce localized plastic deformation and increased susceptibility to cracking. However, the results indicated that the shot peening was not effective in producing segmented SCC.

Degraded tubes have nondestructively been examined by optical microscopy, dye-penetrant techniques, and EC NDE. The lengths and orientations of cracking varied widely in the tubes. Cracking depth also ranged from 5 to100% TW, as determined by EC NDE. Figure 4.1 shows an example of the dye-penetrant examination of axial ODSCC cracks in Specimen SGL288. Two axial cracks of lengths 6 and 3 mm are seen. Figure 4.2 shows EC NDE results for the two axial ODSCC cracks in Specimen SGL288. The maximum depth of these cracks was estimated to be $\approx$40% TW.
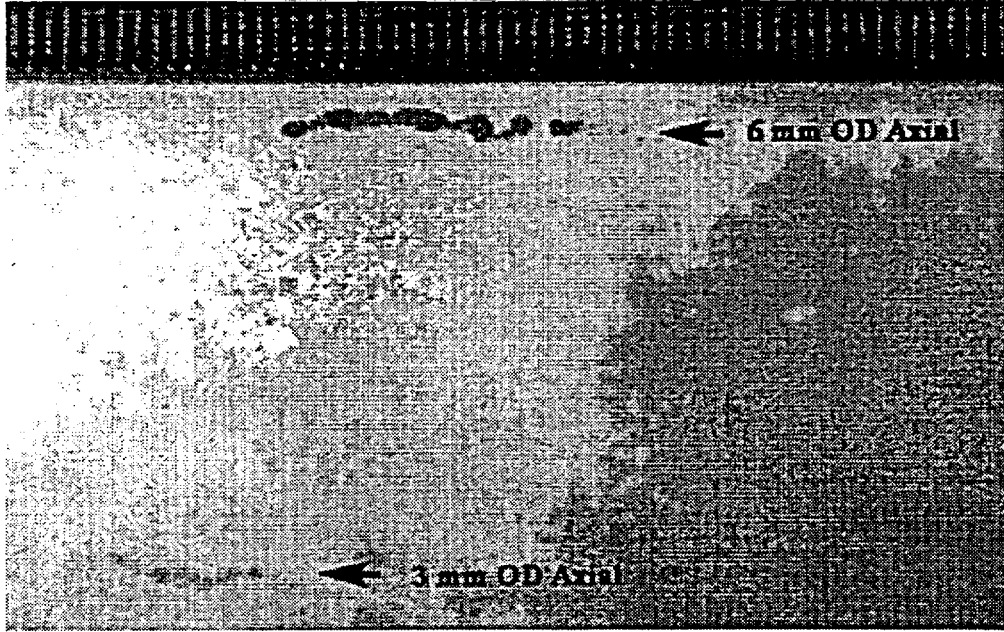
Fig. 4.1. Dye-penetrant examination of Specimen SGL288 showing two axial cracks.
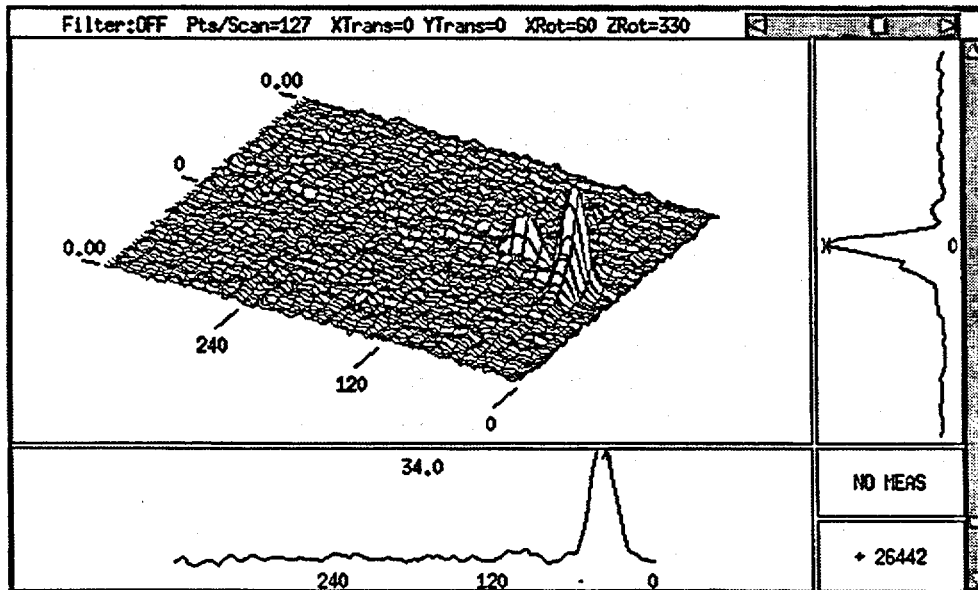
Fig. 4.2. Eddy current NDE test results from Specimen SGL288 showing axial ODSCC indication.

Figure 4.3 is an optical photomicrograph of the axial ODSCC at the surface at a magnification of 100x. Figure 4.4 is another example of the dye-penetrant examination of axial ODSCC in Specimen SGL415, showing that the crack is segmented. Figure 4.5 is an EC NDE result for a 40% TW axial ODSCC in specimen SGL-415. Two parallel axial SCCs are indicated. Figures 4.6 and 4.7 are dye-penetrant examination results and EC NDE results for a throughwall axial-circumferential ODSCC in Specimen SGL-418. Figure 4.8 shows the EC NDE result for axial ODSCC introduced into specimen SGL479. Three axial SCCs are indicated in the figure. Figure 4.9 is a dye-penetrant examination of segmented axial ODSCC in Specimen SGL495, and Figure 4.10 is the EC NDE. Two axial SCCs (5 and 12 mm long) are separated by a 12-mm segment. Figure 4.11 is another example of the dye-penetrant examination of OD axial cracks in specimen SGL365, showing a segmented 4-mm-long axial crack. Figures 4.12 and 4.13 show NDE results for multiple ODSCC introduced into the roll-expanded area of Specimens SGL357 and SGL366, respectively.

The crack depth is estimated to be ≈60% TW for SGL357 and ≈45% TW for SGL366.

A technique to introduce axial SCC in dented tubes was developed during the reporting period. Ten (Heat No. NX8527) and five (Heat No. NX7968) dented tubes were processed for axial IDSCC. Figure 4.14 is a macrophotograph of specimen SGL397 showing a 12.7-mm (0.5-in.)-long mechanical dent introduced on the OD surface. Figures 4.15 and 4.16 are EC NDE results for the specimen SGL397 before and after the introduction of axial IDSCC, respectively. The depth of the IDSCC is estimated to be ≈60% TW.

The solution and sensitization heat treatments cause grain growth and a reduction in hardness and flow stress. Tensile tests were performed for eight tube specimens (SGMC001 through 008) at room temperature to measure the reduction of flow stress for Alloy 600 tubes (Heat NX8527). The results show that ultimate tensile and yield strengths of the as-received mill-annealed tubes are 696 ± 14 MPa (101 ± 2 ksi) and 317 ± 14 MPa (46 ± 2 ksi), while the corresponding values for the heat-treated tubes are 600 ± 14 MPa (87 ± 2 ksi) and 179 ± 14 MPa (26 ± 2 ksi), respectively. Thus, the flow stress of the material is reduced by ≈20% due to the heat treatments. A correction for this effect on mechanical properties will be required when these tubes are used for subsequent pressure and leak-rate testing. The solution and sensitization heat treatments may also change the magnetic properties of the alloy and influence EC measurements. To examine this, two 22.2-mm (7/8-in.)-diameter Alloy 600 tubes (Heat NX8527) with EDM notches have been treated with the solution and sensitization heat treatments, and EC results are being compared before and after the heat treatments.

To examine influence of oxide film on EC response, 10 cracked tubes were oxidized in high-temperature water environments. Of these, five tubes (SGL114, 159, 170, 182, and 187) were oxidized in deionized high-purity water with 8 ppm dissolved oxygen at 290°C (554°F) and 8.8 MPa (1280 psi) for 1680 h. Five additional tubes (SGL127, 149, 169, 189, and 197) were oxidized in deionized high-purity water with 3 ppm dissolved oxygen at 290°C (554°F) for 120 h and then in a simulated primary water environment (1200 ppm B and 2 ppm Li) at 320°C (608°F) and 12.4 MPa (1800 psi) for 1400 h. Eddy current NDE was performed before and after the oxidation treatment. Results from the EC examinations of these specimens are described under Task 1 (Section 2.3).
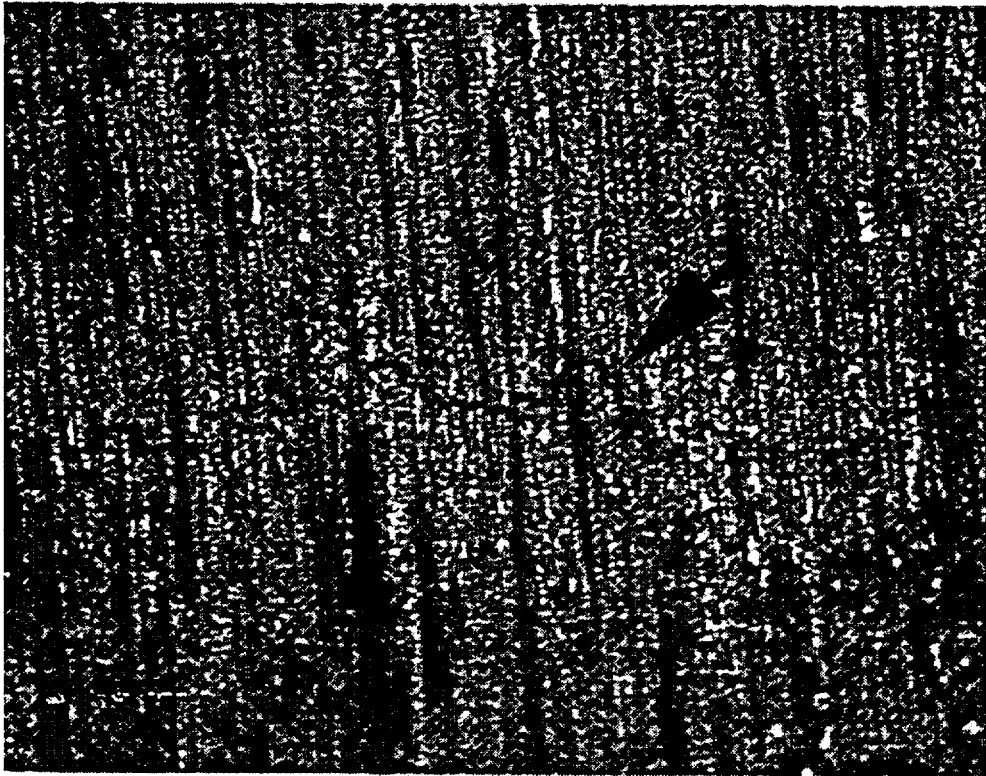
Fig. 4.3. Optical microscopy of axial ODSCC in Specimen SGL288 at 100X.
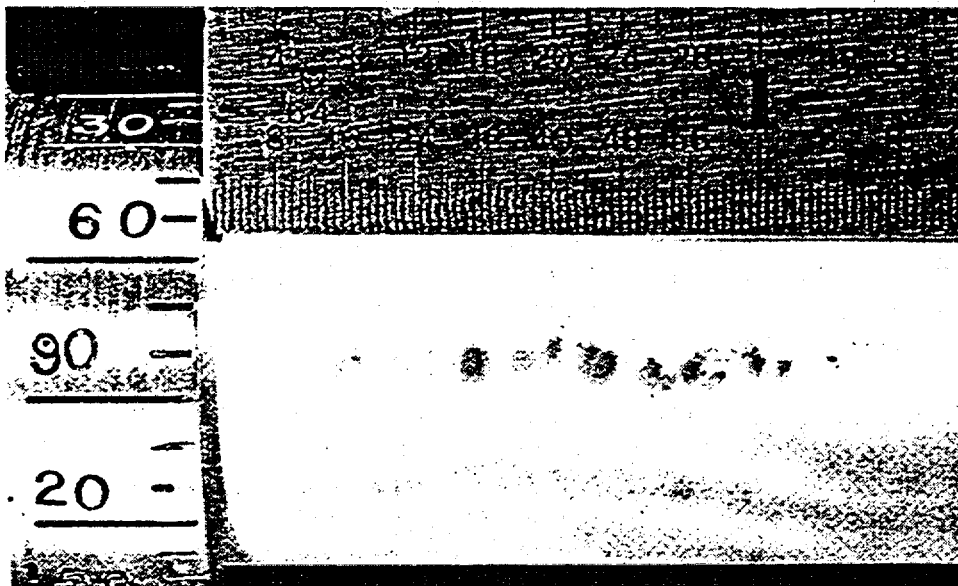
Fig. 4.4. Dye-penetrant examination of Tube SGL-415 showing segmented axial ODSCC.
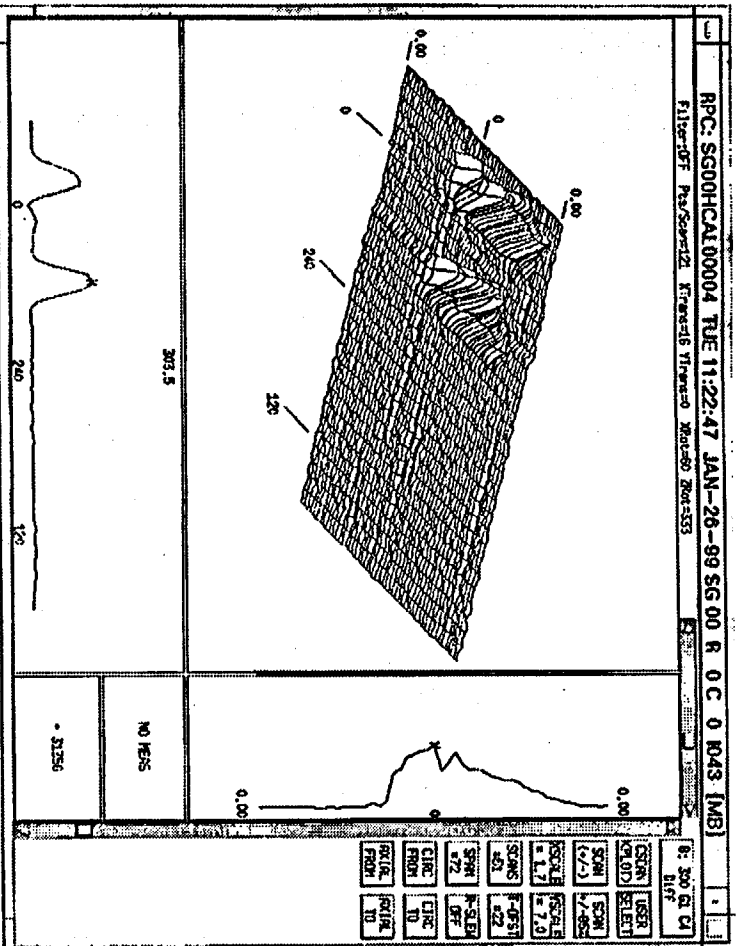
Fig. 4.5. *Eddy current NDE test results for Tube SGL-415 showing ≈40% TW axial ODSCC indication.*

Fig. 4.6. *Dye penetrant examination of tube SGL-418 showing circumferential-axial ODSCC.*
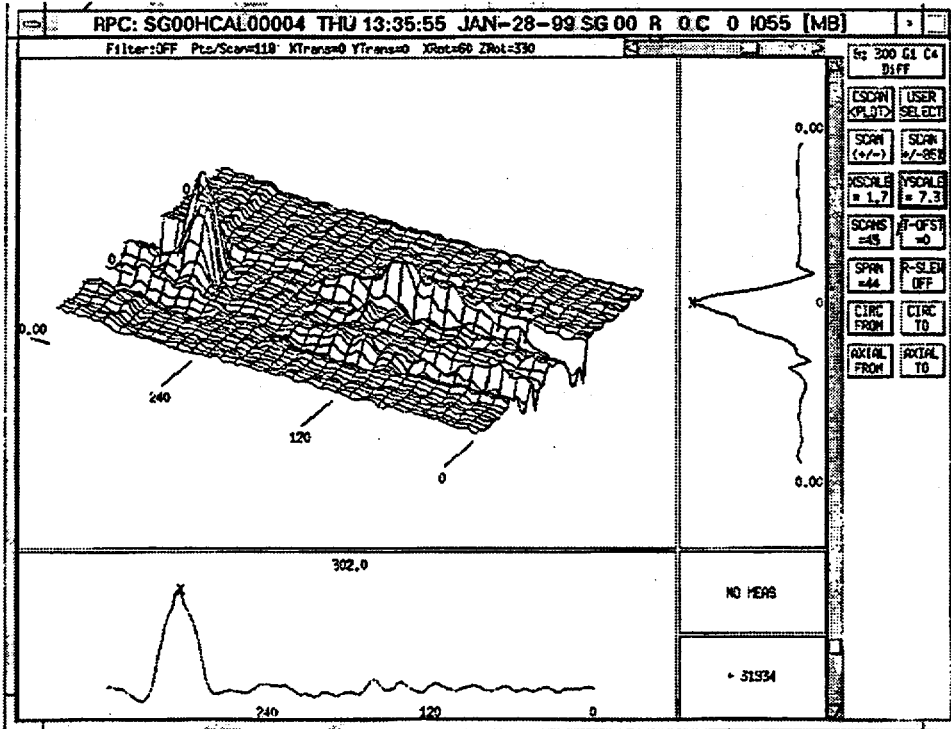
Fig. 4.7. Eddy current NDE test results for tube SGL-418 showing throughwall circumferential-axial ODSCC indication.
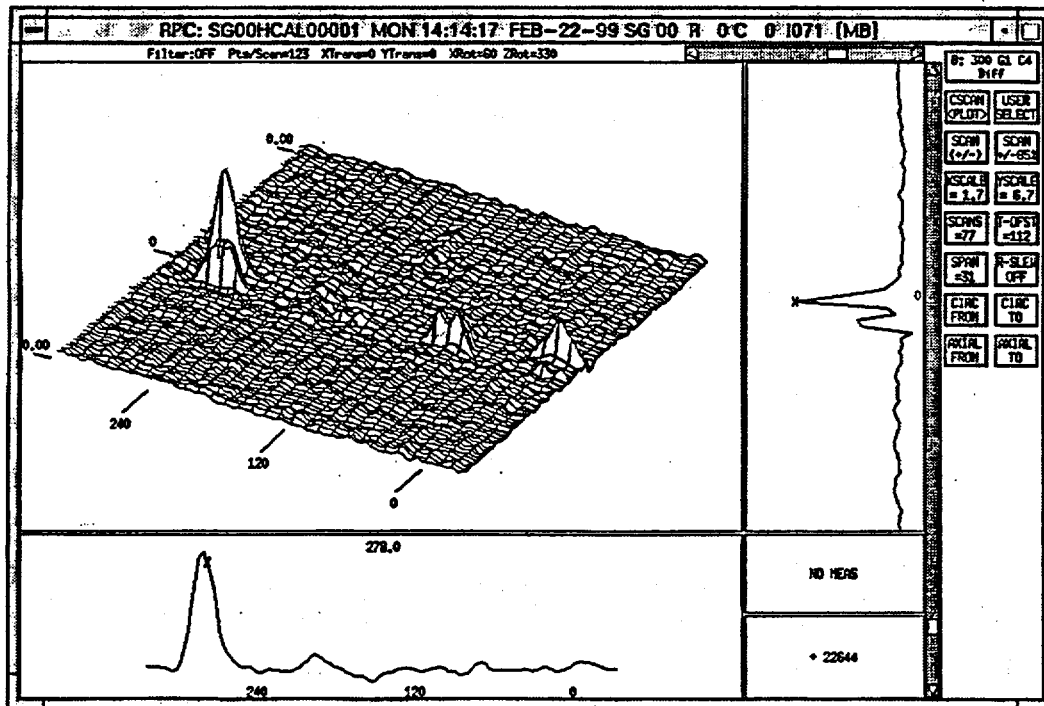
Fig. 4.8. Eddy current NDE test results for Alloy 600 tube SGL479 showing three OD axial crack indications.

Fig. 4.9. *Dye-penetrant examination results for Alloy 600 tube SGL495 showing segmented ODSCC indications.*
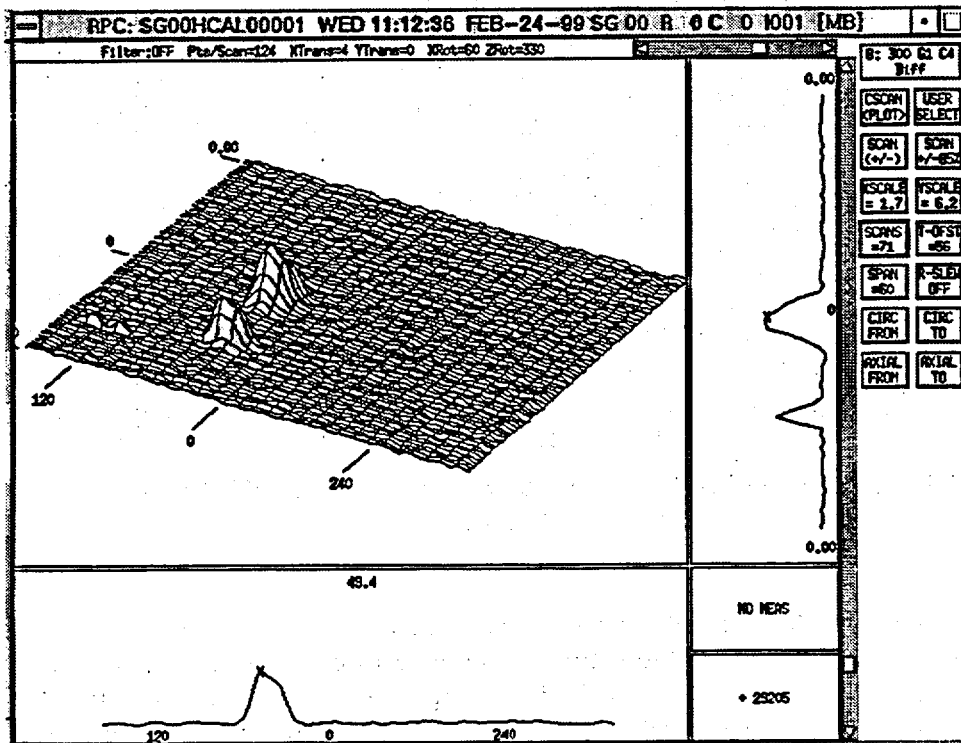
Fig. 4.10. *Eddy current NDE test results for Alloy 600 tube SGL495 showing segmentation of axial ODSCC.*
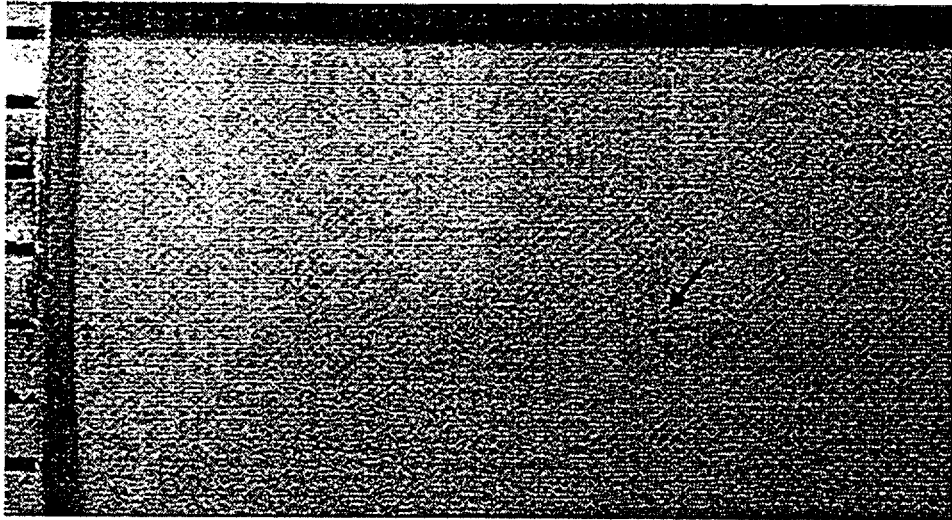
Fig. 4.11. Dye-penetrant examination of specimen SGL365 showing segmented axial ODSCC indication.
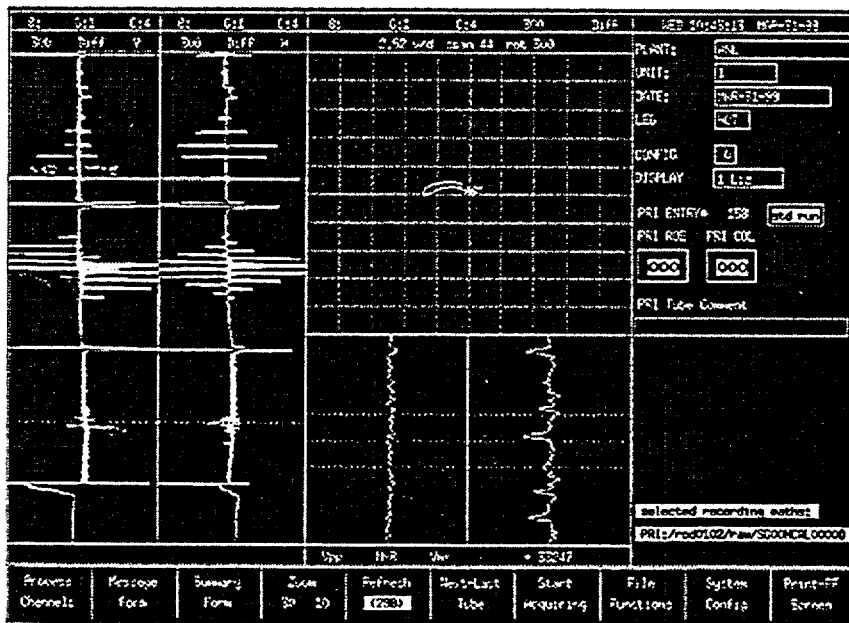
Fig. 4.12. Eddy current NDE test results from specimen SGL357 with axial ODSCC in roll-expanded area.

Three additional cracking facilities were constructed to increase production rate. Each will be able to handle four individual tube specimens to produce axial ODSCC. The existing cracking facilities were also refurbished to improve the stability of the applied loads. Efforts are continuing to produce additional degraded tubes with more complex geometries prototypical of field SCC, e.g., axial ODSCC with ligaments between small multiple cracks. Future efforts will focus on degrading tubes with denting or on producing cracking at the roll expansion.
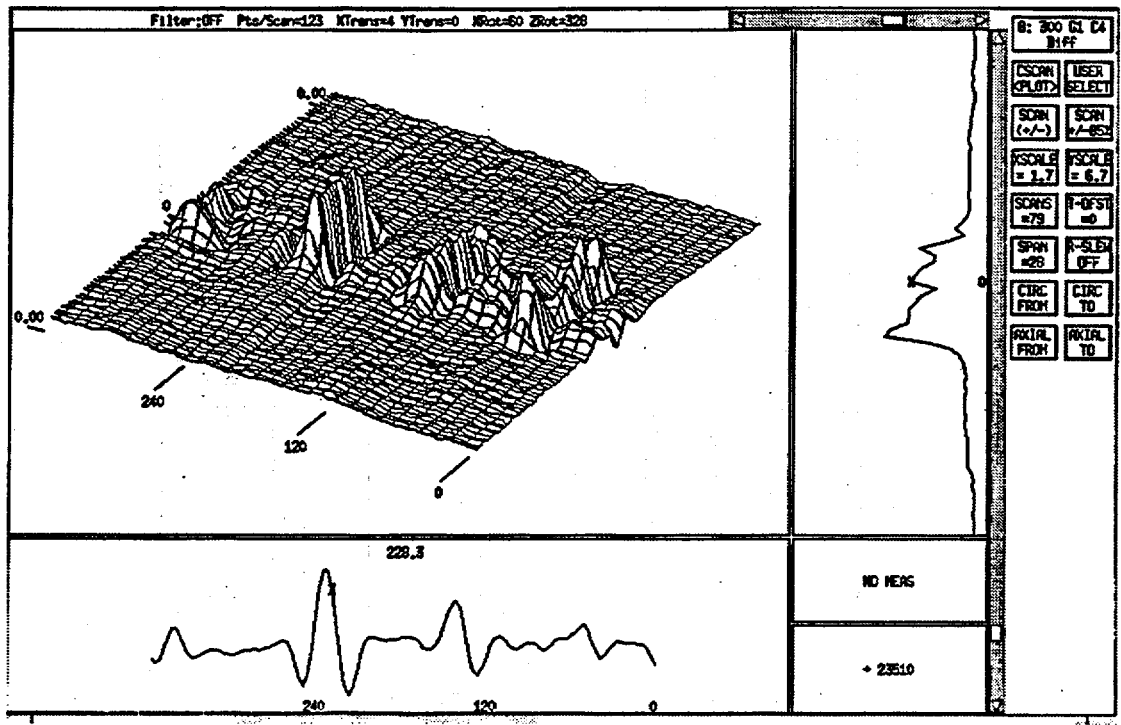
Fig. 4.13. *Eddy current NDE test results for Alloy 600 tube SGL366 showing ODSCC indications in roll-expanded area.*
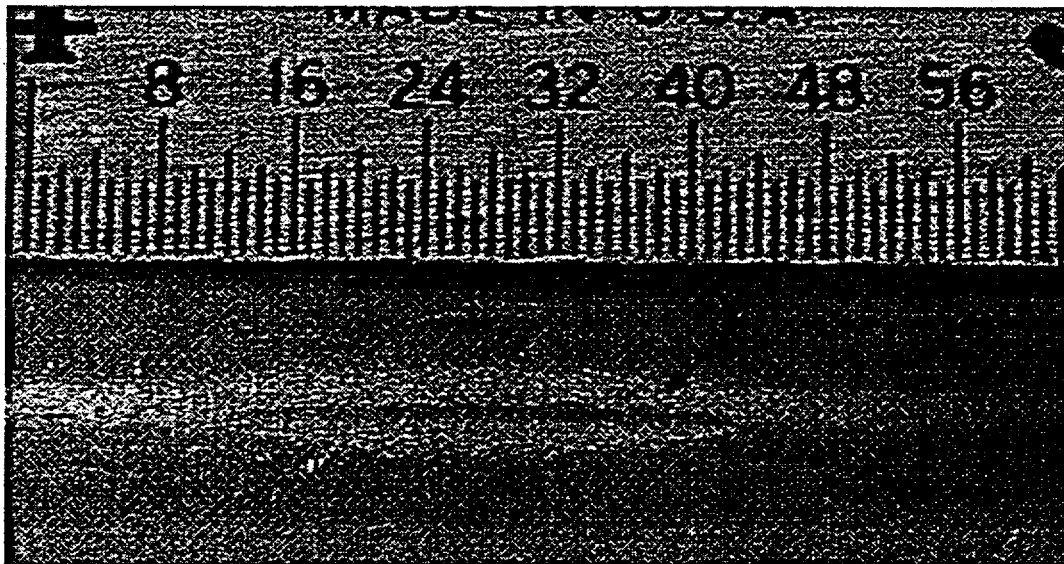
Fig. 4.14. *Macrophotograph of specimen SGL397 showing axial dent on OD surface.*
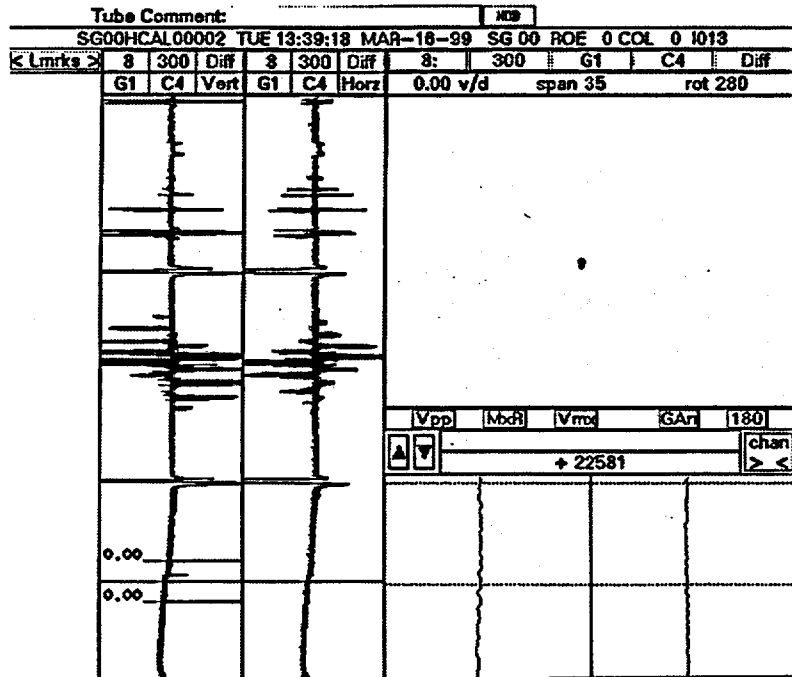
Fig. 4.15. Eddy current NDE test results from SGL397 before degradation.
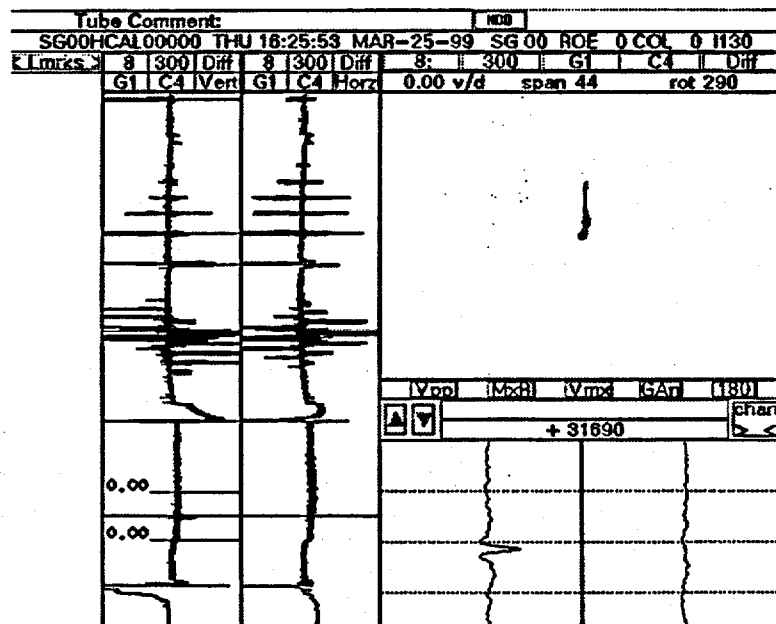
Fig. 4.16. Eddy current NDE test results from specimen SGL397 after degradation.

4.2 Model Boiler Tube Cracking Facility

A model boiler multitube corrosion cracking facility has been designed and partly assembled to closely simulate SG thermal-hydraulic and chemistry conditions for the secondary-side tube/TSP crevice geometry. In particular, heat transfer conditions across the tube wall from the primary side to the secondary side in this facility will be maintained to cause concentration of impurity species in secondary-side crevices and thereby promote SCC on the outside of the tube. This facility will permit the production of cracked tubes under nearly prototypical conditions. These cracked tubes can be used in pressure and leak-rate tests and NDE characterization at ANL. The facility can also be used to study SCC at a more mechanistic level. The detailed features of this facility were described in Ref. 1. As stated in that progress report, detailed hardware specifications have been completed for all facility components, and requests for component fabrication bids were issued. The fabricator has delivered the boiler to ANL. However, further work on the facility has been postponed until additional resources for its completion can be made available.

4.3 Pressure and Leak-Rate Test Facility

The testing of flawed tube has continued in the Pressure and Leak-Rate Test Facility. All tested specimens were made from 22.2-mm (7/8-in.)-diameter Alloy 600 SG tubing (Valinco heat NX8524). Additional tests beyond the preliminary tests described in the previous annual report[2] have been conducted on tubes containing axial OD EDM notches of several different lengths and depths. Tests were also conducted on tubes containing multiple interacting flaws. The flawed tubes were all 0.56 m (22 in.) long, with the flaw centered at 0.15 m (6 in.) from the end of the tube fitted with a welded plug. The unplugged end of the tube is held in place in the test module vessel by a Swagelock fitting mounted on a blind flange with a hole that allows the flow from the blowdown vessel to enter the flawed tube. Tests have also been conducted on a specimen containing an axial ODSCC crack produced using doped steam for comparison purposes. All SCC flaws were analyzed structurally, and the results are discussed in the analysis (Section 4.6). These tests were directed at addressing questions concerning flaw leak stability under constant temperature and pressure associated with normal operating and MSLB conditions. Tests were conducted at both room temperature and 282°C (549°F) to assess flaw behavior dependence on temperature. Plans are also in place to test additional EDM and laser-cut axial and circumferential flaws having multiple interacting notches separated by ligaments of various sizes.

4.3.1 Tube Leak and Rupture Testing

All flaws tested in the Pressure and Leak-Rate Test Facility are characterized before and after testing. In general, the EDM flaws tested are relatively easy to characterize with respect to flaw dimensions, but characterization of the SCC flaws is much more difficult. Because of the need to evaluate leak-rate and flaw-opening-pressure prediction capabilities and improve the models if necessary, accurate information on flaw pre- and post-test dimensions and leak area is essential. Procedures have been developed and implemented to obtain these data, using the following flaw characterization steps:

1. Eddy current NDE is used to obtain crack depth profiles and voltage information.

2. Finite-element code structural calculations are utilized to estimate crack opening pressures from NDE crack depth profiles.

3. The flaw regions are characterized using dye-penetrant techniques and digital photography with computerized image analysis.

4. The tubes are bubble-tested with low-pressure (276 kPa or 40 psi) air in a water bath to identify regions of throughwall penetration.

5. Post-test destructive examination of specimens with part-throughwall flaws will be carried out in some cases to validate NDE depth measurement and to assess tube structural wall tear characteristics.

For SCC flaws (as opposed to EDM notches), the use of dye-penetrant inspection and digital photography is an essential part of pre- and post-test flaw characterization to relate flaw characteristics to leak behavior. These procedures, along with image processing techniques, are used to obtain flaw information such as crack area, total linear length, location, and number of branch points. Computerized digital image analysis of flaw images yields a more systematic and less subjective characterization of flaw features than using an optical microscope or making measurements manually from photographs.

In addition to SCC flaw characterization by dye-penetrant, digital photography, and image analysis, a procedure has also been developed for characterizing the subregion(s) of the surface crack pattern for throughwall flaws. With the dye-penetrant still in the crack, the capped tube is mounted in a low-pressure (276 kPa, or 40 psi) pressurization apparatus and submerged in a water bath. The flaw region is observed with a low-magnification optical microscope underwater for gas bubble leaks along the crack, and the regions of leakage are recorded.

All the above procedures for crack and leak characterization are performed before and after testing to characterize crack changes after being subjected to high pressure and temperature. The tests conducted to date have yielded important information on influence of crack geometry, temperature, and pressure on flaw behavior, and they have helped to optimize the pre- and post-test flaw characterization procedures. Results from these tests are summarized in the following sections.

Testing of Specimens with EDM Axial Notches. A number of tests on tubes with axial EDM notches have been performed. These flaws are simplified representations of SCC flaws and, as such, permit a systematic parametric study of the influence of flaw size, shape, placement, multiple flaw interactions, and tube properties on leak rate and flaw opening characteristics. During this reporting period, single axial notches of length 25.4, 12.7, and 9.0 mm (1.0, 0.5, and 0.35 in.) were tested at room and elevated temperature. These tests expand the data base on larger flaws reported previously.[2]

Testing of multiple interacting axial flaws also began during this reporting period. Tests on tubes with circumferential and various patterns of multiple interacting flaws separated by ligaments are also planned. Tubes with field and laboratory SCC cracks frequently exhibit these complex flaw patterns, and EDM notches and laser-cut notches, which can be fabricated to be considerably tighter than EDM notches, will be used to

simulate these complex flaw patterns. The influence of these parameters and sensitization heat treatment on tube mechanical/structural properties and flaw behavior, as highlighted in the previous report,[2] has been studied further, and the results are presented in the data analysis section of this report.

Flow through rectangular notches of high-aspect-ratio (flaw length to width), which more closely approximate SCC flaws in SG tubes, has not been studied nearly as thoroughly as throughwall circular orifices. Furthermore, a very-high-aspect-ratio notch having the same flow area as a circular hole may exhibit a greatly different flow rate if the notch width is of the order as the tube material grain size. This difference is caused by the dramatically different flow behavior in the narrow flow passage resulting from surface roughness and tortuosity effects. The criteria for defining when a flaw is tight are not well understood or demonstrated because of lack of an adequate data base. Furthermore, the hole leak rate can be significantly affected by whether the flaws are sharp-edged (i.e., the flow turns abruptly 90° to enter the flaw) or the inlet edge of the flaw is more smoothly contoured. For example, a sharp-inlet-edge circular orifice has a discharge coefficient of 0.6, whereas an orifice of the same flow area with a smooth inlet can have a coefficient approaching unity. Hence, a simple measurement of flow area can be grossly inadequate.

Results from testing a nonsegmented throughwall EDM 25-mm (1-in.)-long axial notch of initial width 0.19 mm (0.0075-in.) at room temperature in two stages (tube T14EATWX1) are presented next. In the first stage, the internal pressure was increased in four steps (0.69, 6.9, 10.3, and 13.8 MPa [100, 1000, 1500, and 2000 psi]), at which point the test was stopped and the tube removed to measure flow area prior to higher-pressure testing in which unstable tearing was anticipated. This permitted a check on our ability to predict the flaw opening and the flow rate at this intermediate stage of pressurization. The photograph of the flaw shown in Fig. 4.17 was analyzed to obtain a flaw flow area of 52 mm^2 (0.081 in.^{2}), based on a two-dimensional projection of the flaw. The measured flaw length was 24.9 mm (0.98 in.), and the maximum flaw width was 2.8 mm (0.11 in.). Based on the measured opening area, a pressure differential of 13.8 MPa (2000 psi), an orifice coefficient of 0.6, and the fluid density at 75°F, the ANL orifice flow model predicted a flow rate of 312 L/min (82.5 gpm). This is in good agreement with the experimentally observed flow rate of 302 L/min (79.8 gpm).

For the second stage of testing, the tube (T14EATWX1) was reinstalled in the facility and pressurized to higher levels. The test was restarted by quickly raising the pressure to 13.8 MPa (2000 psi) and holding for a short period of time to reestablish a flow rate of 302 L/min (79.8 gpm), in agreement with that observed when the test was interrupted. The pressure was then raised in a series of 0.69 MPa (100 psi) increments, and the flaw leak increased significantly at each increment. At ≈15.9 MPa (2300 psi), the flow rate increased abruptly and the pressure dropped momentarily before stabilizing at 12.8 MPa (1859 psi), at which point a flow rate of 1,098 L/min (290.0) gpm was observed. Figure 4.18 shows the post-test flaw opening area, and the tearing that apparently occurred at 15.9 MPa (2300 psi) is seen at each end of the notch. Figure 4.19 shows a side view of the flaw bulge. An image analysis of Fig. 4.18 determined a two-dimensional flow area of 170 mm^2 (0.264 in.^{2}), an overall flaw two-dimensional length of 21.8 mm (0.86-in.), and a maximum flaw width of 11.7 mm (0.46 in.). Based on the measured opening area, a pressure differential of 12.8 MPa (1859 psi), an orifice coefficient of 0.6, and the fluid
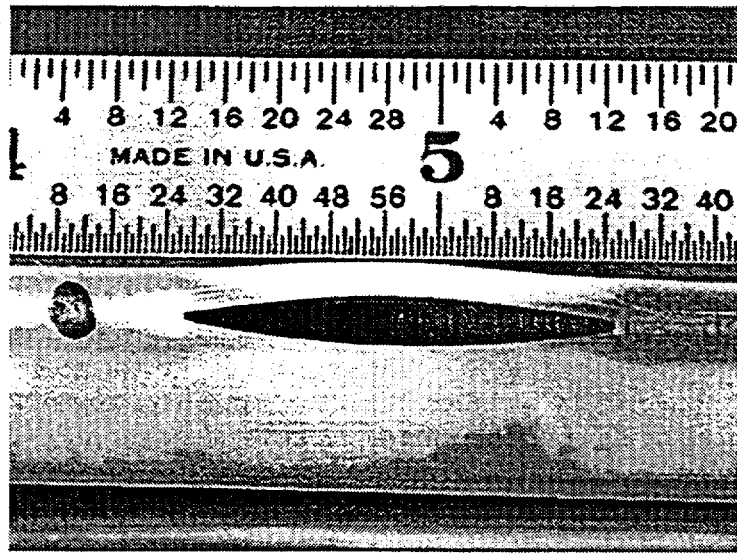
Fig. 4.17. Opening of 25.4-mm (1-in.)-long axial throughwall EDM notch (tube T14EATWX1) after test was interrupted at 13.8 MPa (2000 psi) to measure flaw area.
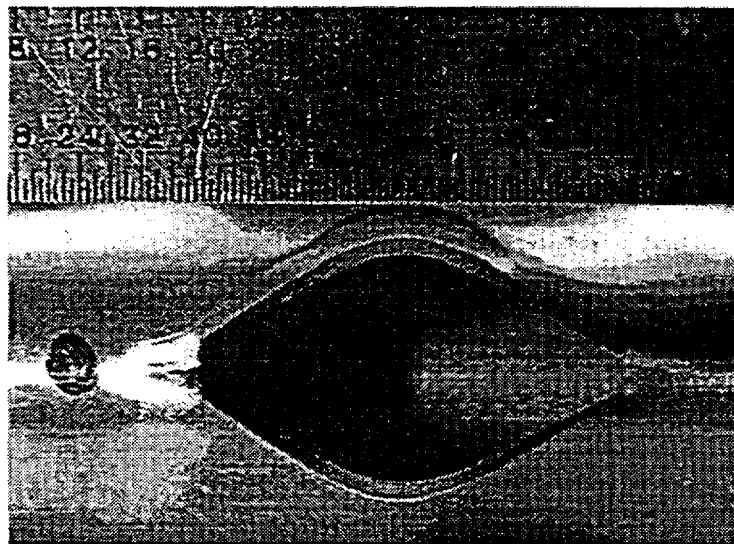
Fig. 4.18. Opening of 25.4-mm (1-in.)-long axial throughwall EDM notch in tube shown in Fig. 4.17 (tube T14EATWX1) after continuing test to 15.9 MPa (2300 psi).
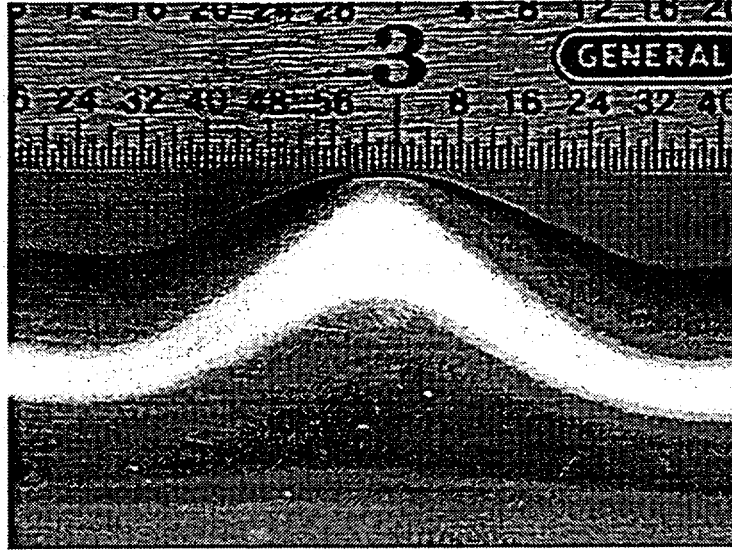
Fig. 4.19. Side view of tube specimen shown in Fig. 4.18, showing three-dimensional bulging at failure site.

density at 75°F, the ANL orifice flow model predicts a flow rate of 984 L/min (260 gpm), which is 114 L/min (30 gpm) lower than that observed. It is believed that this underprediction (in contrast to the accurate prediction for the first stage of the test) is primarily the result of the large amount of bulging associated with the flaw (Fig. 4.19). This bulging results in an actual flaw opening that is three-dimensional. Hence, the two-dimensional area measured from Fig. 4.18 is smaller than the actual area through which the flow occurs. The curved arc length of the flaw between the ends of the notch was measured as 24.3 mm (0.958 in.) in Fig. 4.19. This length, when divided by the two-dimensional length of 21.8 mm (0.86 in.) measured from Figure 4.18, yields a ratio of 1.114. Applying this correction factor to the flaw opening area gives a three-dimensional area of 190 mm^2 (0.294 in.^{2}), from which the orifice flow model predicts a flow rate of 1,096 L/min (289.5 gpm), in good agreement with experiment. The validity of this area correction for highly bulged flaws will be checked further on data from other large flaw tests.

Also tested during this period was tube T13EA90X.35 with a partial throughwall axial OD EDM flaw of length 8.9 mm (0.35 in.), width of 0.19 mm (0.0075-in.), and a uniform 90% throughwall depth. This flaw length is shorter than any previously tested. The tube was first tested at room temperature, with the pressure increasing in 0.69 MPa (100 psi) increments up to 19.3 MPa (2800 psi). No flaw opening or tube leakage occurred, and the test was terminated at this pressure when the facility overpressurization relief valve began to leak. (Full opening of this valve is avoided whenever possible because of potential difficulties in valve reseating.) Upon removal and inspection, the tube showed virtually no crack widening or bulging of the tube wall. The tube was reinstalled and tested at 282°C (540°F) at increasing pressure up to 19.3 MPa (2800 psi). Again the tube did not leak, and post-test inspection revealed no change in the flaw width or tube bulging. The observed >19.3 MPa (2800 psi) ligament failure pressure exceeds the prediction of both the ANL and Battelle models. The ANL model predicts a failure pressure of 18.6 MPa (2700 psi) at room temperature and 16.9 MPa (2450 psi) at 282°C (540°F), and the Battelle model

predictions are 12.4 and 11.0 MPa (1800 and 1600 psi), respectively. Failure pressures observed in previous tests on tubes with notches of 12.7 mm (0.5 in.) or longer were very close to the predicted values. The reason for the increased strength of the shorter notch is being evaluated.

In an initial effort to evaluate the behavior of multiple interacting notches, two tubes (one for room-temperature testing and the other for elevated-temperature testing) with two aligned axial EDM throughwall notches separated by a short axial ligament were prepared for testing. These tests evaluated the influence of small ligaments on the link-up behavior of aligned axial flaws and on the resulting leak and flaw-opening pressures. The two aligned axial throughwall notches were each 6.35-mm (0.25-in.) long and 0.19-mm (0.0075-in.) wide and were separated by a 0.25-mm (0.01-in.)-long full-wall-thickness ligament.

The first of these two tubes (T24EATWX.5 LIG) was tested at room temperature at pressures up to 17.2 MPa (2500 psi). Figure 4.20 shows a post-test photograph of the flaw; little structural distortion is evident, and the flaw exhibited only a 50-75 μm (0.002-0.003 in.) increase in width next to the ligament. The results for this test show that the flaw was much more robust than predicted. Calculations indicated that the ligament would tear at a pressure considerably lower than 13.8 MPa (2000 psi). However, post-test inspection after pressurization to 17.2 MPa (2500 psi) with no failure revealed no tearing of the ligament, although stretch marks were evident on the ligament outer surface. The observed leak rate through the flaw during the test was essentially identical to that calculated for the two individual notches. At pressures of 14.5 and 17.7 MPa (2100 and 2500 psi), the flaw flow rate was 14.8 and 18.5 L/min (3.9 and 4.9 gpm), respectively. The reason for the stronger-than-anticipated nature of the ligament is being evaluated by structural code analyses. However, as described earlier, single axial notches shorter than ≈12.7 mm (0.5 in.) appear to exhibit higher strengths (i.e., higher opening pressures and smaller flow areas) than predicted by the models that have been found to accurately predict the behavior of longer axial notches.

The second tube (T25EATWX.5 LIG) was tested next, at 282°C (540°F). In contrast to the room-temperature test of the same flaw geometry described above, tube T25EATWX.5 LIG experienced ligament tearing at a pressure of 15.5 MPa (2250 psi). This tearing coincided with an abrupt increase in flow rate during the test as the two notches merged. The resulting leak rate corresponded to that expected for a widened 12.7-mm (0.5-in.)-long notch. This ligament tearing appears to be the result of the somewhat reduced flow stress of Alloy 600 at 282°C (540°F). The post-test appearance of tube T25EATWX.5 LIG after testing at pressures up to 17.9 MPa (2600 psi) is shown in Fig. 4.21. Ligament tearing and appreciable flaw widening are apparent.

At pressures of 14.5 MPa (2100) (ligament intact) and 17.2 MPa (2500 psi) (ligament torn), the flow rates for tube T25EATWX.5 LIG were 17.0 and 32.2 L/min. (4.5 and 8.5 gpm), respectively. At the maximum test pressure of 17.9 MPa (2600 psi), the rate was 35.6 L/min. (9.4 gpm). This tube had a higher flow rate at all pressures, even before ligament tearing, than did tube T24EATWX.5 LIG at room temperature. The higher flow rates observed both before and after ligament tearing for the elevated-temperature test are caused by notch widening because of the somewhat reduced flow stress of the material.
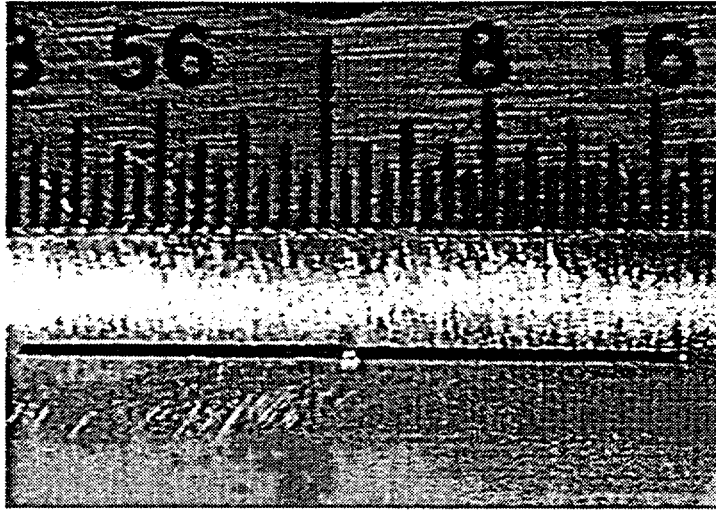
Fig. 4.20. Post-test photograph of tube T24EATWX.5 LIG tested at room temperature at pressures up to 17.2 MPa (2500 psi), showing little flaw distortion and intact ligament.
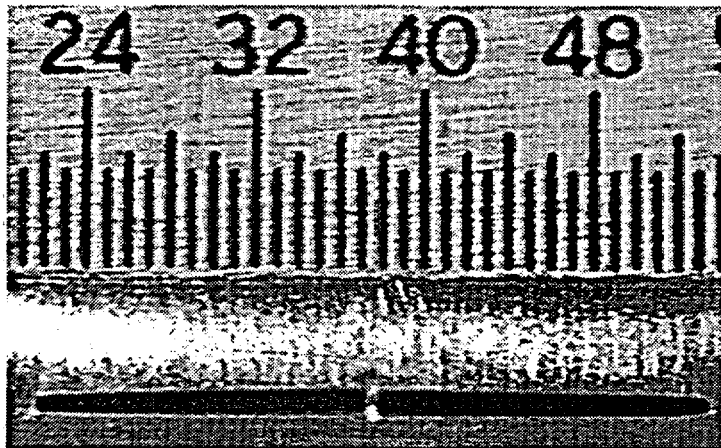
Fig. 4.21. Post-test photograph of tube T25EATWX.5 LIG tested at 282°C (540°F) at pressures up to 17.9 MPa (2600 psi), showing appreciable flaw notch widening and torn ligament.

After tearing, the notch behaved like a longer, and hence weaker, flaw. Additional tubes containing multiple interacting flaws are scheduled for testing.

Testing of specimens with laboratory-produced SCC flaws. Results from tests on four Alloy 600 tubes with laboratory-produced axial ODSCC of nominal length 12.7 mm (0.5-in.) were presented in the previous annual report.[2] The tubes were cracked at ANL in an aqueous sodium tetrathionate solution after a sensitization heat treatment. These tests in the ANL facility yielded some interesting results on flaw leak stability under constant temperature and pressure conditions and also provided some early insight into the adequacy of pre-test flaw characterization procedures being developed.

A 22.2-mm (7/8-in.)-diameter Alloy 600 tube with an axial ODSCC flaw produced using doped steam has now also been tested. This test was performed on tube T505CATW2-10 and is identified as Test W 2-10. The tube cracked using doped steam underwent the same four-step pre-test flaw characterization process as the ANL tubes and was tested with the same protocol as the four ANL tubes.

The tests on all five tubes were designed to gain information on flaw stability under constant temperature and pressure conditions associated with normal SG operation and MSLB, i.e., T = 282°C (540°F) and p = 8.3 and 17.2 MPa (1200 and 2500 psi), respectively. These pressure plateaus were held for at least 2 h (depending on leak rate and amount of water in the blowdown vessel), with extended duration holds at intermediate pressures if flaw tearing (as indicated by a sudden increase in flow) was observed. ANL tubes 177 and 195 were tested at room temperature and ANL tubes 104 and 219 were tested at 282°C (540°F). The tube cracked using doped steam was tested at both temperatures.

For comparison, the test results from the four ANL-produced SCC tubes (Tests SGL-177, SGL-195, SGL-104, and SGL-219), as well as for the tube cracked using doped steam tested at R.T. and 282°C (540°F), are summarized in Table 4.1. This table also includes information on the results of analyses of these tests discussed subsequently in Section 4.7.3.

The following observations on the above four tests are relevant:

1. All SCC flaws were very tight and had regions of throughwall penetration, as determined by bubble testing. However, none of the four flaws exhibited detectable water leakage at pressures below 8.3 MPa (1200 psi), nor was leakage detected during a 2-h (or greater) hold time at this pressure. Detectable leakage did not occur until much higher pressures were attained.

2. Post-test inspection of the flaws showed that three flaws opened up significantly in width along their entire length, even into the extremities of the Y branches on each end of the main flaw. The exception was Test SGL-177, for which the nominal EC voltage of 4 V was considerably lower than the values of 6-10 V observed for the other three tubes. Additionally, the latter three tubes had several obvious post-test secondary cracks emanating from the main crack, even though these cracks were barely perceptible in pre-test characterizations. Furthermore, the region around the flaws was raised noticeably upward, or puckered, suggesting the presence of a weakened region in the vicinity of the cracking. However, Test SGL-177 exhibited very little puckering. Tests previously conducted on 12.7-mm (0.5-in.)-long axial EDM notches over the same pressure range produced significantly less puckering, though this difference may be attributable to the fact that these tubes were not sensitized. Sensitized tubes with 12.7-mm (0.5-in.)-long notches will be tested to further evaluate this effect.

3. Specimens in three of the four tests (SGL-195, SGL-177, and SGL-219) exhibited crack tearing under constant temperature and pressure conditions, which caused the leak rate to increase under constant pressure.

Table 4.1. Summary of results from pressure and leak-rate tests on Alloy 600 steam generator tubes with laboratory-grown SCC cracks, along with estimated throughwall crack lengths and calculated ligament rupture pressures.

Test Number	Test Temp. [°C (°F)]	Initial OD Flaw Length [mm (in.)]	Initial Leakage Conditions		Constant-Pressure Hold Conditions			Final Test Conditions		Estimated Final Throughwall Crack Length [mm (in.)] by		Predicted Ligament Rupture Pressure [MPa (psi)]
			Press. [MPa (psi)]	Flow Rate [L/min/ (gpm)]	Press. [MPa (psi)]	Flow Rate (L/min/[gpm]) Initial	Final	Press. [MPa (psi)]	Flow Rate [L/min/ (gpm)]	Leak Rate Model	Ligament Rupture Model	
SGL-177	R.T.	12.2 (0.48)	16.9 (2450)	0 (0)	16.9 (2450)	0.04[a] (0.01)	0.26 (0.069)	19.3 (2800)	1.7 (0.44)	9.9 (0.39)	9.9 (0.39)	18.0 (2610)
SGL-195	R.T.	13.7 (0.54)	14.7 (2130)	0 (0)	14.7 (2130)	<0.04 (<0.01)	<0.04 (<0.01)	15.5 (2250)	32.6[b] (8.6)	11.9 (0.47)	12.2 (0.48)	16.5 (2390)
SGL-104	282 (540)	10.4 (0.41)	16.2 (2350)	21.2 (5.6)	16.2 (2350)	21.2 (5.6)	21.2 5.6	17.2 (2500)	23.5 (6.2)	5.3 (0.21)	8.9 (0.35)	30.3 (4350)
SGL-219	282 (540)	14.0 (0.55)	13.3 (1925)	3.7 (0.97)	15.9 2300	14.0 (3.7)	39.0 (10.3)	16.2 (2350)	39.0 (10.3)	10.9 (0.43)	10.4 (0.41)	20.0 (2900)
W 2-10[c]	R.T.	12.4 (0.49)	17.2 (2500)	0 (0)	17.2 (2500)	0.04[d] (0.01)	0.068[d] (0.018)	17.2 (2500)	0.068 (0.018)	-	-	-
W 2-10[c]	282 (540)	12.4 (0.49)	18.6 (2700)	? ?	18.6 (2700)	0.30 (0.08)	0.72 (0.19)	18.6 (2700)	0.72 (0.19)	4.8 (0.19)	10.9 (0.43)	20.2 (2930)

[a] Leakage started after 100 min hold time at 16.9 MPa (2450 psi).

[b] Flow rate increased abruptly to 29.9 L/min (7.9 gpm) when pressure of 15.1 MPa (2190 psi) was reached during ramping, and leak rate stabilized at 32.6 L/min (8.6 gpm) when pressure was stabilized at 15.5 MPa (2250 psi).

[c] Same specimen tested at R.T. and then at 282°C (540°F).

[d] Leakage started after 3-h hold at 17.2 MPa (2500 psi) and increased gradually during additional 15-h hold.

4. Specimen flaws in three of the four tests (SGL-195, SGL-104, and SGL-219) suddenly opened to their full extent at pressures less than that associated with MSLB, yielding flow rates of 23 to 38+ L/min (6 to 10+ gpm). These three tubes had the highest EC voltages (6-10 V). This behavior suggests that once a small ligament tears, there is a strong tendency for other ligaments to tear in a domino fashion (sometimes after a delay under constant pressure) until the crack is completely open over its full extent. Test SGL-177, which had the lowest voltage (4 V) had a leak rate of only 1.7 L/min (0.44 gpm) and did not exhibit this behavior.

The four ANL-produced tubes were selected as having the same nominal axial ODSCC crack length of 12.7 mm (0.5 in.), as determined by dye-penetrant examination, as well other similarities. The tube cracked using doped steam had an axial ODSCC flaw of similar length. Figure 4.22 shows the pre-test digital image of the flaw in the doped-steam tube accentuated by dye-penetrant. The flaw is axial and has an overall length of 12.4 mm (0.49 in.). Bubble-testing at 276 kPa (40 psi) revealed that the doped-steam flaw had two locations of throughwall penetration, coinciding with the two largest dye stains in Fig. 4.22. Each penetration exhibited very small intermittent bubble generation. The largest dye stain on the right exhibited a larger bubble size and higher generation frequency than that on the left.

Eddy current examinations indicated that all four ANL-produced SCC flaws had variable crack depths along their lengths (see analysis section), with maximum depths of 75 to 95%. The tube cracked using doped steam exhibited a similar crack depth profile. The throughwall regions identified by bubble testing in both the doped-steam and the four ANL flaws were not seen by EC techniques because of their tightness and very small axial extents. The EC BC voltage for the doped-steam tube was 4.5 V, which is very close to the 4.0 V exhibited by the ANL tube in Test SGL-177. The other three ANL tubes had higher EC voltages in the range 6-10 V. The crack depth profile for the doped-steam tube was used not only to qualitatively prescreen the flaw for similarity with the ANL flaws but also in calculations to estimate the initial flaw-opening pressure. Details on the structural analysis of this flaw and the others are presented in the analysis section. Calculations of flaw-opening pressures indicated that the doped-steam tube was most similar to the ANL tube in Test SGL-177, although somewhat stronger. Hence, the pre-test crack characterizations suggested that the doped-steam tube would exhibit leak characteristics most similar to the ANL tube. Because of the similarity to the ANL tube, which was tested at room temperature, the initial testing phase for the doped-steam tube was also conducted at room temperature, with follow-on testing at 282°C (540°F).

For room-temperature testing of the doped-steam tube, the pressure was increased from 0 in 1.4-2.1 MPa (200-300 psi) increments, with hold times of 15-30 min at each level until 8.3 MPa (1200 psi) was reached. The pressure was then held at this level for 2 h. Like the four ANL specimens, the doped-steam tube exhibited no observable water leakage during this portion of the test, even though all of these tubes exhibited localized throughwall penetration during bubble testing at very low pressure. The cracks thus appear to be very tight. Following the 2-h hold at 8.3 MPa (1200 psi), the pressure was increased in a series of steps to 17.2 MPa (2500 psi) over a time span of 45 min. Again, no leak was observed during this time. After a subsequent hold time of 3.25 h at this pressure, a leak rate of ≈0.04 L/min (0.01 gpm) was detected. The 17.2 MPa (2500 psi)
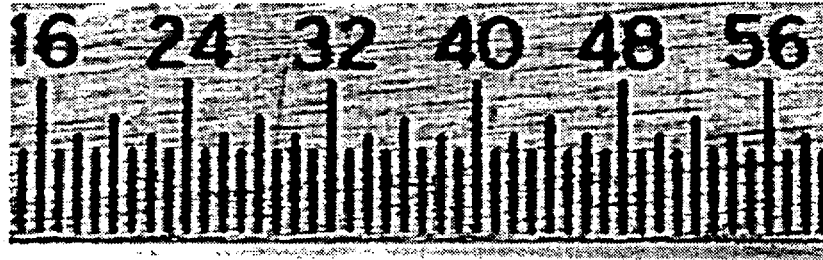
Fig. 4.22. Pretest dye-penetrant digital image of ODSCC cracked tube produced using doped steam (Test T505CATW2-10).

pressure was held overnight, and the tube continued to leak, with the leak rate increasing to ≈0.068 L/min (0.018 gpm) by the following morning. In comparison, the ANL Test SGL-177 leaked ≈0.26 L/min. (0.07 gpm) under an extended hold time at 17.2 MPa (2500 psi). The pressure was then raised to 18.6 MPa (2700 psi) and held at this level for 5.5 h, at which time a leak rate of 0.12 L/min (0.032 gpm) was measured. The room-temperature phase of the test was terminated at this point. In comparison, ANL test SGL-177 exhibited a leak rate of 1.7 L/min (0.44 gpm) at 19.3 MPa (2800 psi). Thus, the doped-steam tube, like this ANL test, developed a leak under constant pressure and exhibited an increasing leak rate over an extended hold period, although at somewhat lower rates.

The blowdown tank was refilled with water, and the tube was then tested at 282°C (540°F) and 18.6 MPa (2700 psi) to determine leak rate at high temperature and to see if the crack would open further. The flow rate was observed to increase from ≈0.30 L/min (0.08 gpm) to 0.72 L/min (0.19 gpm) during a 2-h hold time at this pressure. The test was then terminated and the tube was removed. A post-test photograph of the flaw is shown in Section 4.7 (Fig. 4.61). The flaw had opened slightly over its entire axial extent (see pre-test photograph in Fig. 4.22). Like ANL Test SGL-177, no flaw zone puckering was evident.

In conclusion, the doped-steam flawed tube in Test W 2-10 behaved in a qualitatively similar manner to the ANL tube in Test SGL-177 under leak testing. Pre-test flaw characterization indicated that the two flawed tubes were similar, although the doped-steam flaw was expected to be somewhat stronger because of its slightly shallower depth, in agreement with the data.

The above behavior suggests that ligament failure in an SCC flaw may occur progressively (sometimes with delays under constant loading conditions) until the crack is completely open over its full extent. In various flawed specimens with quite different ligament thicknesses, initial leakage occurred abruptly at pressures significantly lower than those predicted by the equivalent rectangular crack approach. The experimental evidence of time-dependent increase of leak rate possibly due to progressive ligament rupture at 282°C (540°F), as well as at room temperature, highlights the fact that no criterion for predicting time-dependent ligament rupture is currently available. More laboratory-cracked tubes with SCC flaws and, eventually, service-degraded tubes with SCC flaws will be tested to develop a better understanding of tube flaw behavior. The detailed structural analysis predictions and a proposed flaw behavior model for these flaws is presented in Section 4.7.

4.4 High-Pressure Tube Pressurization Facility

During this reporting period, design and construction of a room-temperature, high-pressure (0-52 MPa [0-7,500 psi]), low flow rate (0-45 L/min. [0-12 gpm]) tube burst test facility was initiated. This facility will complement the Pressure and Leak-Rate Test Facility by permitting the failure testing of tubes that cannot be failed at the 20.7 MPa (3000 psi) maximum pressure of the present system. This new facility utilizes a commercial 60-hp-high-pressure triplex pump that has already been acquired. Additional instrumentation, controls, water storage, and safety devices are being incorporated into the unit to provide the desired operational features.

The facility's continuous pressurized water supply of 45 L/min (12 gpm) will permit many flaw failure tests to be conducted without the use of an internal bladder and shim, even for small throughwall flaws. In addition, the continuous flow of pressurized water means that test durations are not limited by the 760-L (200-gal) capacity of a pressurized water reservoir, as is the case for the Pressure and Leak-Rate Test Facility. This will permit long-term crack stability and jet-impingement testing. Other features being incorporated into the facility design include the capability to measure extremely low leak rates (considerably less than the 0.04 L/min (0.01 gpm) lower limit for the Pressure and Leak-Rate Test Facility) by collecting and measuring the amount of water leaked in a specified time period. The open optical path to the crack location in this facility means that real-time ultra-high-speed video recording (2000-12,000 frames/s) of crack and jet dynamic behavior during testing is possible with existing video equipment. The specimen will be surrounded by a test module consisting of an 0.46-m (18-in.)-diameter by 1.02-m (40-in.)-long stainless steel pipe, and a coarse metal mesh pad lining its inner wall in the zone of jet impact will absorb the jet energy and reduce spray to facilitate flaw leak collection and video photography. The test module will also have a flaw-viewing port for the video camera and a second port for illuminating the flaw. An internal lateral tube support system in the form of a two-point variable position clamping mechanism (simulating tube support plates) is being designed. This support can be moved to different axial locations on the tube. Lateral support will be important in testing tubes with circumferential flaws, where flaw behavior is sensitive to support characteristics, and for testing axially flawed tubes, where jet thrust may cause bending of a tube supported only at one end.
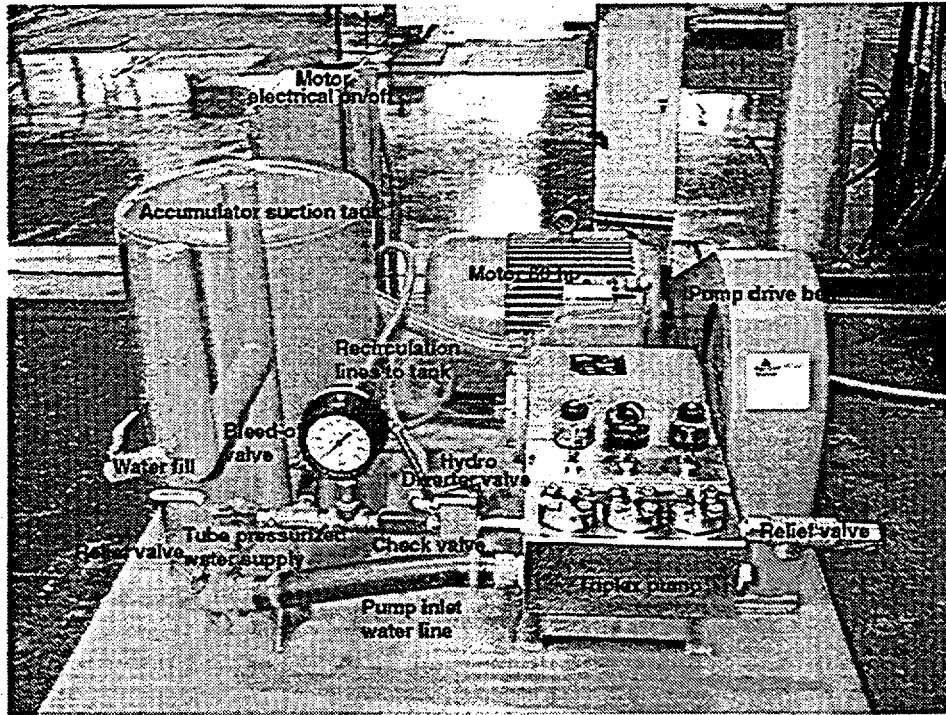
Figure 4.23. High-pressure pump and related components for high-pressure tube test facility.

Figure 4.23 shows the high-pressure pump and related components. The system has two over-pressurization protection safety relief valves; one is located on the triplex pump and the other on the 150-L (40-gal) water accumulator suction tank. Briefly, the tester operates as follows:

1. The tube to be tested (with or without an internal bladder and shims, depending on the flaw characteristics), is filled with water and fastened by a Swagelock fitting to the supply pipe feeding water from the triplex pump.

2. The accumulator suction tank (114-150 L [30-40 gal]) is filled with water. If some leakage is expected before failure, the water supply line to the accumulator tank can be opened to provide a continuous water supply for long-duration testing. Both tap water and deionized water are available.

3. The high-pressure bleed-off valve and the diverter control valve are both set wide open, allowing the initial flow generated by the pump to recirculate through the suction tank.

4. The constant-speed pump motor is then turned on, causing flow recirculation through the accumulator suction tank. The tube specimen will be pressurized at <276 kPa (40 psi) at this point. For long-duration tests, the water will be cooled to minimize heating of the water temperature by the pump.

5. The high-pressure bleed-off valve is then fully closed and the hydro control diverter valve is slowly moved to shunt the pump-generated flow into the test specimen,

causing its internal pressure to rise. The diverter control valve allows the pressure to be maintained at any value in the range from 0.7-52 MPa (100-7500 psi). The pressure is read on a gauge and is measured and recorded by a pressure transducer. A sustained flow of 45 L/min. (12 gpm) can be maintained at the maximum pressure. Releasing the diverter valve will result in the specimen being held at constant pressure for a nonleaking tube because of the check valve located in the test specimen supply line. The pressure in the tube can be increased by moving the diverter valve forward, which will open the check valve.

6. When the desired maximum test pressure has been reached or the tube has failed, the test is terminated by releasing the diverter valve, turning the pump off, and opening the high-pressure bleed-off valve.

Design and construction of the test facility is well underway. The area where this system will be located has been cleaned, and the pressurizer has been moved into position. Electrical power has been connected. A first-level safety review for this new facility has been completed, and permission has been granted for initial operation of the facility pressurizer to establish its performance characteristics. The triplex pump has three single-acting 25-mm (1-in.)-diameter plungers, and the associated pressure pulsations will be monitored at various flow rates. If they are found to be excessive, an antipulsation module will be installed on the supply line to the test specimen. Additionally, the diverter control valve will be evaluated for smoothness of pressure variation over the entire range from 0-52 MPa (0 to 7500 psi) for flow rates from 0-45 L/min (0-12 gpm).

Many of the 70-MPa (10,000 psi) pipe fittings and valving for connecting the pressurizer to a leaking tube simulator (consisting of a valve and an orifice nozzle) have been procured and installed. The 45 L/min (12 gpm) discharge from the orifice at 52 MPa (7500 psi) constitutes a very-high-energy jet that must be safely contained. For the initial checkout of the facility, the nozzle is mounted into the sidewall port of a closed 3000-L (800-gal) stainless steel tank that will dissipate the jet energy and facilitate collection of the water for routing to a drain. When fully closed, the valve located upstream of the orifice will allow simulation of the pressurization of a nonleaking tube over the full 0–52 MPa (0-7500 psi) pressure range. Partly opening the valve will provide simulated leak rates in the range 0-45 L/min (0-12 gpm). The 3000-L (800-gal) tank may also be used for testing some flawed service-degraded SG tubes that cannot be sufficiently decontaminated for testing in the Pressure and Leak-Rate Test Facility. The tank will allow containment and collection of any residual contamination that maybe liberated during testing of such tubes.

It is anticipated that facility construction and shakedown testing will be completed by September 1999.

4.5 Pre-Test Analysis of Crack Behavior

4.5.1 Model for Predicting Failure of Partially Supported Tube with a Circumferential Crack

Circumferential cracks in SG tubes are often detected at the top of the tube sheet in PWR nuclear generating plants. Analytical models[3] for the failure of tubes with circumferential cracks predict that the pressure required to cause onset of crack

extension may fall within the design-basis accident condition (17 MPa) if the tube section that contains the crack is free to bend and the crack is sufficiently long (>180°). It is also known that if the crack section is fully constrained against rotation, the failure pressures are significantly increased and cracks must be much longer (>300°) to be of concern. In an actual SG, the tubes are neither free to bend nor fully constrained. The degree of constraint on a circumferential crack at the top of the tube sheet depends on the span between the top of the tube sheet and the first TSP or baffle plate (15-125 cm). Recent tests on SG tubes have shown that failure pressures of tubes that are laterally supported can be significantly higher than those of tubes that are free to bend.[4]

An extensive series of tests on failure and leak rates in circumferentially flawed reactor coolant piping subjected to externally applied forces and moments has been conducted at Battelle under the USNRC-sponsored Degraded-Piping[5] and Short Cracks in Piping and Piping Welds Programs.[6] At the same time, finite-element analyses (FEAs) led to the development of the fracture-mechanics-based leak-rate estimation model SQUIRT.

A simplified stability analysis of circumferentially cracked reactor piping was presented by Tada et al.,[7] who analyzed the pipe as a beam whose cracked section was subjected to plastic limit moment. A similar approach was followed by Smith to analyze failure[8] and leakage[9] of a throughwall circumferential crack in piping. Smith[10] also emphasized the importance of the crack-system compliance on the onset and stability of crack extension and leakage through a crack. In all of these analyses, plasticity was confined to the crack section, while the rest of the pipe responded elastically. In this report, we use the same approach to analyze the problem of SG tube failure under internal pressure loading in the absence of externally applied forces and moments, and we consider the case where plastic deformation may spread to sections other than that of the crack.

4.5.1.1   Description of model

Consider a tube of mean radius R, wall thickness h, and length L, containing a throughwall circumferential flaw of angular length 2θ at any axial location. The tube can be subjected to various edge conditions. For example, the tube may be clamped at one end (simulating the tubesheet) and simply supported at the other end (simulating the first TSP). Figure 4.24 shows such a tube with the crack at the top of the tube sheet. Under internal pressure loading, finite element analysis shows that a tube in the configuration of Fig. 4.24 deforms as shown in Fig. 4.25 with a definite crack flank rotation and crack tip opening displacement. In the present report, limit load analysis will be used to estimate failure pressure of tubes made of ductile materials such as Alloy 600.

We assume that the tube is thin and is under internal pressure loading only (no constraint on axial deformation of the tube), and that the onset of crack extension occurs after the attainment of the limit state. The last assumption is valid provided that the Battelle Screening Criterion[11] is satisfied, i.e.,

$$\frac{E\delta_c}{R\bar{\sigma}}\left(1-\frac{\theta}{\pi}\right) \geq 1, \tag{4.1}$$
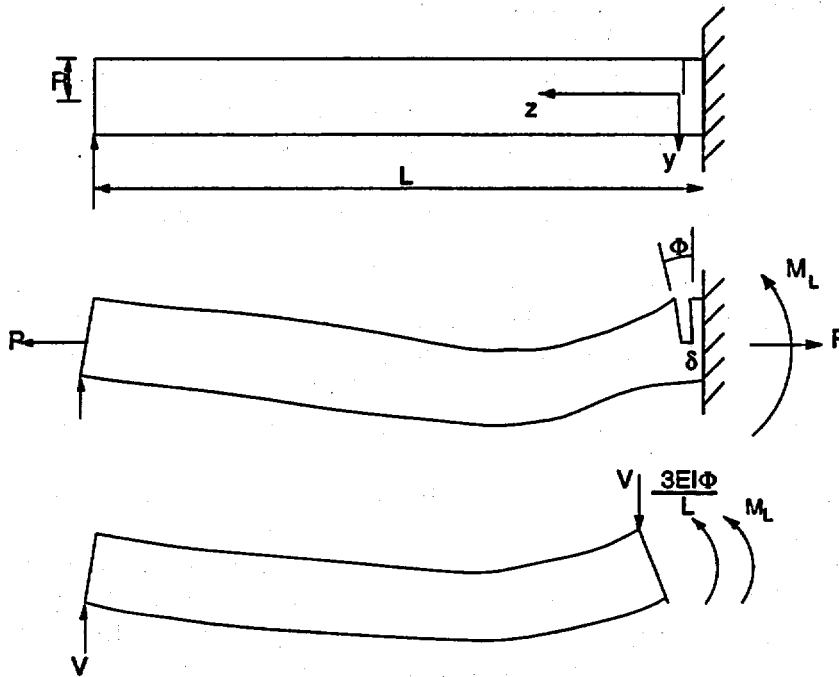
Fig. 4.24. *Geometry, loading, and idealized deformation of tube with single throughwall circumferential crack.*
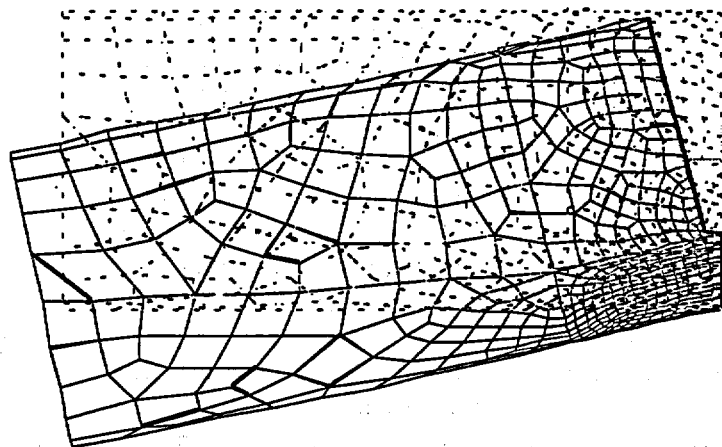
Fig. 4.25. *Calculated (by FEA) displaced (solid line) and original (dashed line) shape of laterally supported tube (L/R = 26) with single 240° throughwall circumferential crack at clamped edge.*

where E is the Young's modulus, δ_c is the critical crack tip opening displacement, and $\overline{\sigma}$ is the flow stress. Thus, for Alloy 600 SG tubing with E = 207,000 MPa (30,000 ksi), $\overline{\sigma}$ = 483 MPa (70 ksi), R = 10 mm (0.4 in.), and 2θ = 270°, we find that $\delta_c \geq 0.1$ mm (0.004 in.), which is generally satisfied by all ductile alloys.

The stress distribution through the section containing the crack at the limit-state is shown in Fig. 4.26. We further assume that plastic deformation is limited to only the section containing the crack, while the rest of the tube responds elastically.

The bending moment (about the tube centerline) and axial force equilibria of the stress distribution of the limit-state (Fig. 4.26) give the following:

$$M_L = 4\overline{\sigma}R^2h\left(\frac{1}{2}\sin\theta - \sin\beta\right) \tag{4.2}$$

and

$$\beta = \frac{\pi - \theta}{2} - \frac{P}{4\overline{\sigma}Rh} = \frac{\pi - \theta}{2} - \frac{\pi p R}{4\overline{\sigma}h}, \tag{4.3a}$$

or

$$\frac{p}{p_b} = \frac{pR}{\overline{\sigma}h} = 2\left(1 - \frac{\theta}{\pi}\right) - \frac{4\beta}{\pi}, \tag{4.3b}$$

where β defines the location of the plastic neutral axis, p is the internal pressure, and p_b is the burst pressure of an unflawed tube.

Plasticity confined to crack section. Denoting the calculated bending moment (positive counterclockwise in Fig. 4.24) in an undefected tube at the crack location (z = 0) by M (for internal pressure loading, M = 0) and by considering the equilibrium of the bending moment in the elastic part of the pipe just to the left of the crack section with the limit moment acting on the crack section (see Fig. 4.24),

$$M = -M_L + \frac{3EI\phi}{L} = 0, \tag{4.4}$$

where I is the bending moment of inertia ($\pi R^3 h$), and Φ is the rotation at the cracked section due to crack opening (Fig. 4.24). Equation 4.4 is applicable for the configuration shown in Fig. 4.24. It can be generalized for any set of edge conditions and crack locations by using an effective length L_e. The generalized version of Eq.4.4 is as follows:

$$M = -M_L + \frac{EI\phi}{L_e} = 0. \tag{4.4a}$$

The relationships between L and L_e for several crack locations and edge conditions are given in Table 4.2. The plastic rotation Φ_c about the neutral axis at the onset of crack extension is related to the critical crack tip opening displacement δ_c by
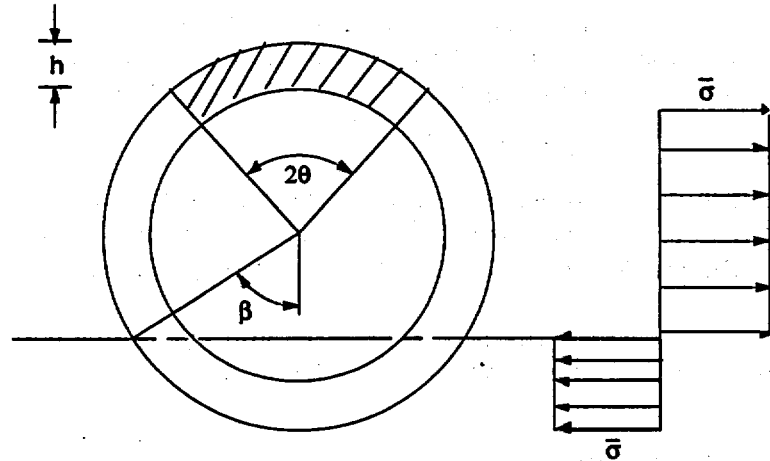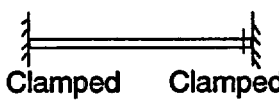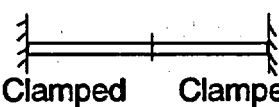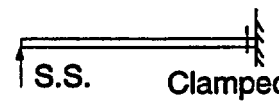
Fig. 4.26. Stress distribution through section at collapse of a tube with single throughwall circumferential crack.

Table 4.2. Effective lengths of tubes for several circumferential crack locations and edge conditions.

Edge conditions and crack location	Effective length
Clamped Clamped	$L_e = L/4$
Clamped Clamped	$L_e = L$
S.S. Clamped	$L_e = L/3$

$$\phi_c = \frac{\delta_c}{R(\cos\beta + \cos\theta)}. \tag{4.5}$$

Combining Eqs. 4.2, 4.4a, and 4.5 at the point of crack initiation

$$\left(\tfrac{1}{2}\sin\theta - \sin\beta\right)(\cos\beta + \cos\theta) - c = 0, \tag{4.6a}$$

where

$$c = \frac{\pi E \delta_c}{4 L_e \bar{\sigma}}. \tag{4.6b}$$

Equation 4.6a can be solved for the critical value $\beta = \beta_c$, which when substituted in Eq. 4.3b gives the crack initiation pressure p_c. Note that the equation for the free-bending case can be obtained by setting $L_e = \infty$, i.e., $c = 0$ in Eq. 4.6a.

The onset of crack extension can also be expressed in terms of the critical value of the plastic component of the deformation J integral J_P, which, for the bending case, is defined in terms of the plastic rotation ϕ as follows:

$$J_P = -\int_0^\phi \left(\frac{\partial M}{\partial A}\right)_\phi d\phi, \tag{4.7}$$

where $A = 2Rh\theta$. In the context of limit analysis $J = J_P$ and $M = M_L$, as given in Eq. 4.2. Differentiating Eq. 4.2 with respect to θ and noting from Eq. 4.2 that at constant rotation, i.e., at constant pressure,

$$\frac{\partial \beta}{\partial \theta} = -\frac{1}{2},$$

$$J = R\overline{\sigma}\int_0^\phi (\cos\beta + \cos\theta)d\phi = R\overline{\sigma}\phi(\cos\beta + \cos\theta). \tag{4.8}$$

Thus, the critical plastic rotation is given in terms of the critical J integral J_c as follows:

$$\phi_c = \frac{J_c}{R\overline{\sigma}(\cos\beta + \cos\theta)}. \tag{4.9a}$$

Comparing Eq. 4.5 and 4.9, we recover the familiar equation

$$J_c = \overline{\sigma}\delta_c. \tag{4.9b}$$

A plot of the fracture toughness $K_{JC} = \sqrt{EJ_C}$ versus the critical crack tip opening displacement is shown in Fig. 4.27. For ductile alloys, the critical crack tip displacement is somewhere in the range of 0.03-0.1 in.

Crack opening area (COA). If the critical crack opening displacement is not exceeded and there is no crack extension, the crack opening area can be expressed in terms of the rotation Φ and crack size by

$$A = 2R^2\phi\int_0^\theta (\cos\beta + \cos\alpha)d\alpha = 2R^2\phi(\theta\cos\beta + \sin\theta). \tag{4.10a}$$

Using Eqs. 4.4a and 4.2, Eq. 10a reduces to (for $\phi \le \phi_c$)

$$A = \frac{8L_e R\overline{\sigma}}{\pi E}(\theta\cos\beta + \sin\theta)\left(\frac{1}{2}\sin\theta - \sin\beta\right). \tag{4.10b}$$

At the point of crack initiation, $\phi = \phi_c$ and $\beta = \beta_c$, which when substituted in Eq. 4.10b, gives (using Eq. 4.5)
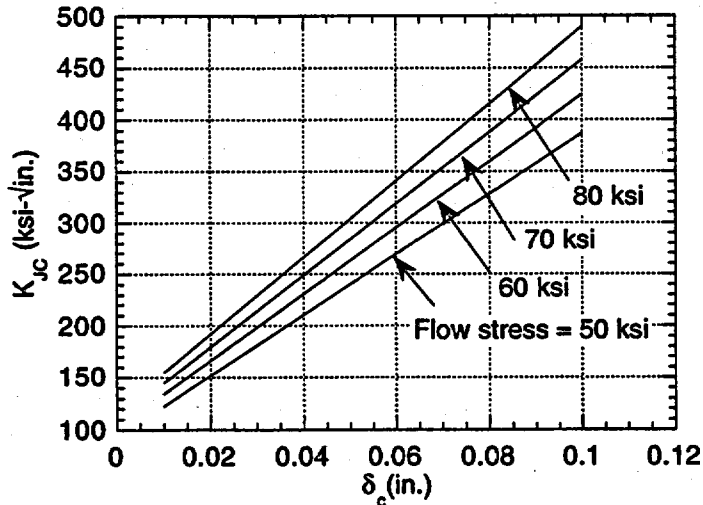
Fig. 4.27. Variation of fracture toughness with critical crack tip opening displacement.

$$A = A_c = 2R\delta_c \frac{(\theta \cos \beta_c + \sin \theta)}{(\cos \beta_c + \cos \theta)}. \tag{4.10c}$$

Instability. Unstable failure need not necessarily be associated with onset of crack extension. If the crack is to be unstable at onset of crack extension under constant loading, the following condition must be satisfied (using Eq. 4.4a) for

$$\frac{dM}{d\phi} = \left.\frac{dM_L}{d\phi}\right|_{\text{I}} + \frac{EI}{L_e} < 0, \tag{4.11}$$

with $\dfrac{dM_L}{d\phi}$ measured at the onset of crack extension. Equation 4.11 can be expressed in terms of the familiar tearing modulus by first differentiating Eq. 4.8 with respect to θ,

$$\frac{dJ}{d\theta} = \frac{\partial J}{\partial \theta} + \frac{\partial J}{\partial \phi}\frac{d\phi}{d\theta} = R\overline{\sigma}\left[-\phi\left(\sin \theta - \frac{1}{2}\sin \beta\right) + \frac{d\phi}{d\theta}(\cos \beta + \cos \theta)\right] \tag{4.12a}$$

and then solving

$$\frac{d\phi}{d\theta} = \frac{\dfrac{dJ}{d\theta} + J\dfrac{\sin \theta - \dfrac{1}{2}\sin \beta}{\cos \beta + \cos \theta}}{R\overline{\sigma}(\cos \beta + \cos \theta)}. \tag{4.12b}$$

Differentiating Eq. 4.2 with respect to ϕ, using Eq. 4.12b, and rearranging, we obtain the condition of instability as

$$\frac{2L_e}{\pi R}(\cos \beta + \cos \theta)^2 - \frac{EJ}{R\overline{\sigma}^2}\frac{\sin \theta - \dfrac{1}{2}\sin \beta}{\cos \beta + \cos \theta} > \frac{E}{\overline{\sigma}^2}\frac{dJ}{da}, \tag{4.13a}$$

where a is the crack length $(Rd\theta = da)$. We can identify the left-hand-side of Eq. 4.13a as the applied tearing modulus, T_{APP}, and the condition of instability can be written as

$$T_{APP} = \frac{2L_e}{\pi R}(\cos\beta + \cos\theta)^2 - \frac{EJ}{R\bar{\sigma}^2}\frac{\sin\theta - \frac{1}{2}\sin\beta}{\cos\beta + \cos\theta} > T_{MAT}. \tag{4.13b}$$

Note that Eq. 4.13b is the same as that given by Smith.[8] For ductile materials with high crack growth resistance, the J-term is usually negligible. In such cases, we can simplify Eq. 4.13b as

$$T_{APP} \approx \frac{2L_e}{\pi R}(\cos\beta + \cos\theta)^2 > T_{MAT}. \tag{4.13c}$$

For many ductile alloys, $T_{MAT} \approx 200$.

Results. A plot of the failure (onset of crack extension) pressure versus crack angle is shown in Fig. 4.28 for various values of the elastic stiffness parameter c. Note that even for a low value of c (i.e., large L_e), tubes with long cracks behave as if they were fully constrained. For $c \geq 0.5$, tubes with any crack behave as if they were fully constrained. Figure 4.28 also shows the maximum angular lengths of throughwall circumferential cracks corresponding to typical pressures during normal operation and design basis accident conditions. If we use the nominal values E = 207,000 MP)a (30,000 ksi) and $\bar{\sigma}$ = 483 MPa (70 ksi) for the mechanical properties in Eq. 4.6b, we then calculate

$$c = 300\frac{\delta_c}{L_e}. \tag{4.6b}$$

The value of the critical crack tip opening displacement δ_c must be obtained from failure tests on tubes with circumferential cracks. Plots of the calculated normalized failure (onset of crack extension) pressure as a function of the span are shown in Figs. 4.29a-b for a 180° crack at several locations, edge conditions, and for critical crack tip opening displacements of 0.25 and 0.75 mm (0.01 and 0.03 in.), respectively. Similar plots for a 240° crack and a 270° crack are shown in Figs 4.30a-b and 4.31a-b, respectively. Depending on the span, the model predicts that the failure pressure is increased significantly compared to that under a free-bending condition. As expected, a midspan crack is far more damaging than an edge crack. For a 180° throughwall crack in a clamped, simply supported tube, the failure pressure is undiminished from the burst pressure of an unflawed tube if the span is less than 0.5 and 1.4 m (20 and 55 in.) for critical crack opening displacements of 0.25 and 0.75 mm (0.01 and 0.03 in.), respectively. A similar tube with a 240° crack will behave as a fully constrained tube, i.e., it will experience a 33% reduction in failure pressure from the burst pressure of an unflawed tube if the span is less than 1.3 and 3.6 m (50 and 140 in.) for critical crack opening displacements of 0.25 and 0.75 mm (0.01 and 0.03 in.), respectively. A tube with a 270° crack will behave as a fully constrained tube, i.e., it will experience a 50% reduction in failure pressure from the burst pressure of an unflawed tube if the span is less than 2.3 and 7.0 m (90 in and 275 in.) for critical crack opening displacements of 0.25 and 0.75 mm (0.01 and 0.03 in.), respectively.
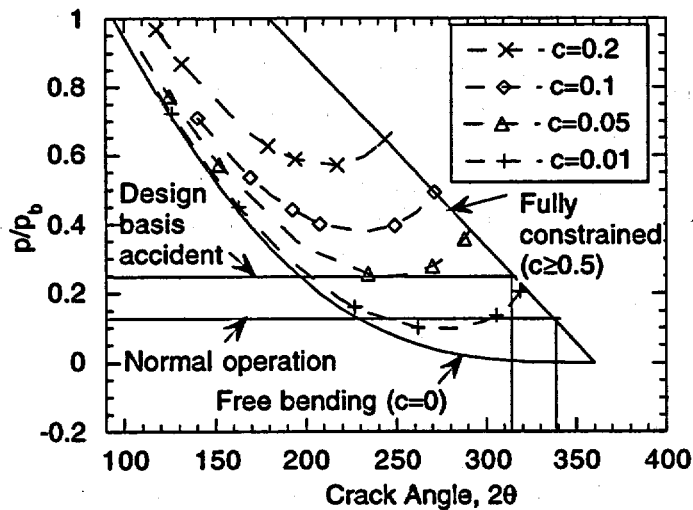
Fig. 4.28. Variation of failure pressure, normalized by unflawed burst pressure, of tube with crack angle of single throughwall circumferential crack.

(a)   (b)
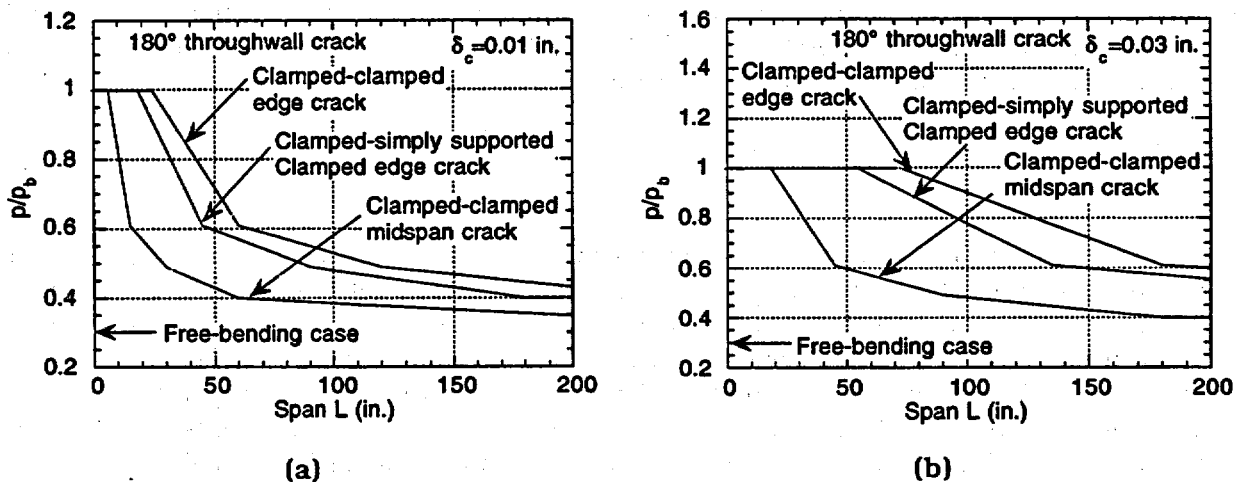
Fig. 4.29. Variation of failure pressure, normalized by unflawed burst pressure, of tube with 180° throughwall crack with span for several edge conditions, crack locations and δ_c values of (a) 0.25 mm (0.01 in.) and (b) 0.75 mm (0.03 in.).

The variation of the applied tearing modulus (using Eq. 4.13b) with pressure is shown in Figs. 4.32a-b for a 1.2-m (48-in.)-long tube with a 120° and 240° throughwall crack, respectively. Also, shown in the figures are the pressures at which a crack tip opening displacement of 1.3 mm (0.05 in.) is reached as indicative of the pressures for the onset of crack extension. In the case of the 120° crack, the J-term of Eq. 4.13a is small compared to the applied tearing modulus. The applied tearing modulus being less than $T_{MAT} = 200$, the crack should propagate stably after the onset of crack extension. For the 240° crack,
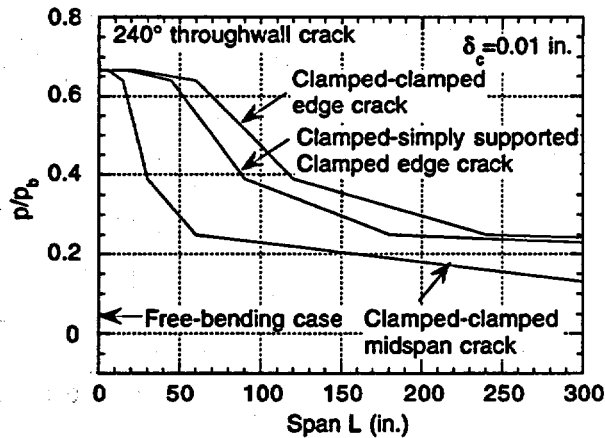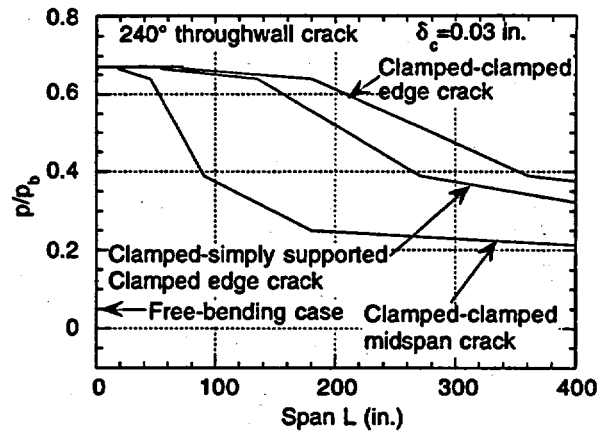
Fig. 4.30. Variation of failure pressure, normalized by unflawed burst pressure, of tube with 240° throughwall crack with span for several edge conditions, crack locations, and δ_c values of (a) 0.25 mm (0.01 in.) and (b) 0.75 mm (0.03 in.).
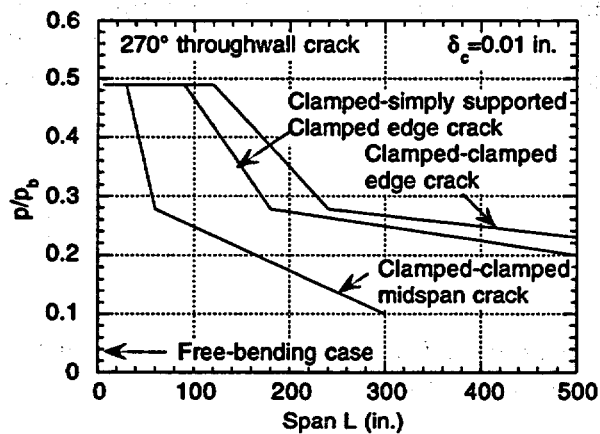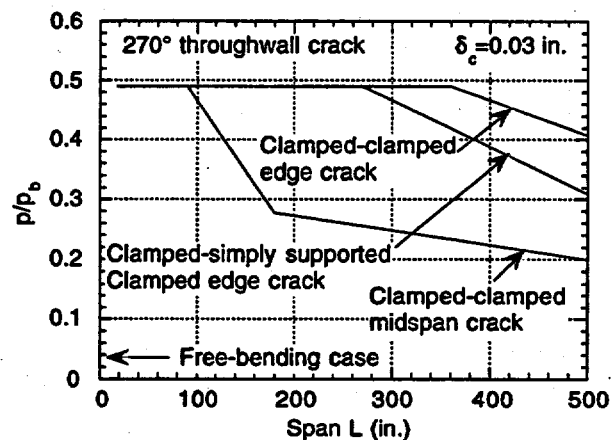
Fig. 4.31. Variation of failure pressure, normalized by unflawed burst pressure, of tube with 270° through-wall crack with span for several edge conditions, crack locations and δ_c values of (a) 0.25 mm (0.01 in.) and (b) 0.75 mm (0.03 in.).

the J-term is not negligible unless the pressure at the onset of crack extension is small ($p/p_b \ll 0.3$). However, since the J-term (positive) in Eq. 4.13a has a stabilizing influence, the initial crack growth will be stable in both cases.

Limitations of the model. The onset of yielding away from the crack plane can be calculated by using the current model and assuming a loading path consisting of first applying the membrane stresses due to pressure, keeping the bending stresses at zero,
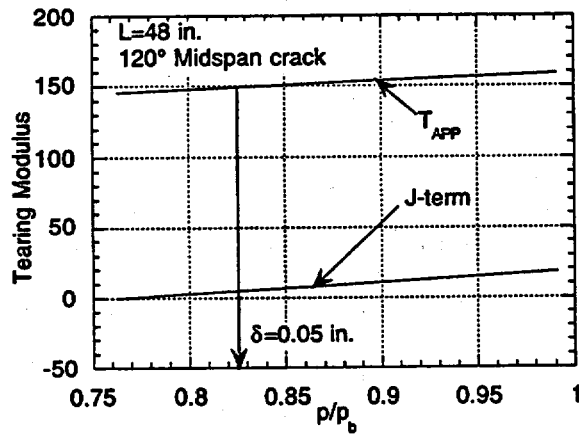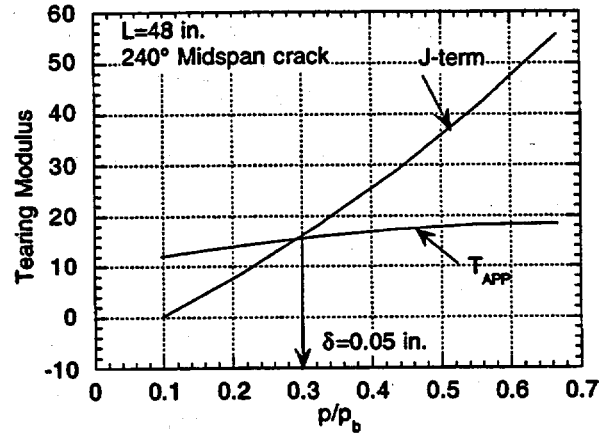
Fig. 4.32. *Variation of applied tearing modulus and J-term in Eq. 4.13 with pressure (normalized by the unflawed burst pressure) of clamped edge tube with midspan cracks of angular length (a) 120° and (b) 240°.*

and then applying the bending stresses holding the membrane stresses constant. Although the axial bending analysis in the current model is uniaxial, the axial yield stress S_y is adjusted to account for the biaxial stress effect by assuming it to vary with the hoop stress σ_h as follows (Fig. 4.33a):

$$S_y = \begin{cases} \sigma_y - \dfrac{\sigma_h}{2} & \text{for } \sigma_h \le \sigma_y \\[2mm] \dfrac{\sigma_y}{2} & \text{for } \sigma_h > \sigma_y \end{cases} \tag{4.14}$$

where σ_y is the virgin uniaxial yield stress. If we denote the bending moment to cause first yielding in an uncracked section just adjacent to the cracked section by M_y,

$$M_y = \frac{S_y I}{R}, \tag{4.15a}$$

and Eq. 4.2 can be written in a nondimensional form as follows:

$$\frac{M_L}{M_y} = \frac{4}{\pi} \frac{\bar{\sigma}}{S_y} \left(\frac{1}{2} \sin\theta - \sin\beta \right). \tag{4.15b}$$

Thus, the condition for first yielding in an undefected section just adjacent to the cracked section by bending is

$$\frac{M_L}{M_y} = \frac{4}{\pi} \frac{\bar{\sigma}}{S_y} \left(\frac{1}{2} \sin\theta - \sin\beta \right) = 1. \tag{4.16a}$$

Noting that yielding of the undefected tube section can occur either by axial bending or by yielding in the hoop direction by membrane hoop stress, we find that the pressure to cause first yielding (denoted by p_y) is the lesser of the following two values:

$$\frac{P_y}{P_b} = \begin{cases} \frac{2\sigma_y}{\bar{\sigma}} - \frac{2}{\pi}\left(\frac{1}{2}\sin\theta - \sin\beta\right) \\ \frac{\sigma_y}{\bar{\sigma}} \end{cases}. \qquad (4.16b)$$

Since β is a function of pressure (Eq. 4.3a), Eq. 4.16b must be solved numerically. A plot of the pressure to first yield versus crack length is shown in Fig. 4.33b for various values of yield to flow stress ratios.

4.5.2 Finite-Element Analysis

To provide a basis for comparison with the analytical models, an incremental elastic-plastic FEA using a multilinear kinematic hardening rule was conducted for a tube (L/R = 60, simply supported at one end and clamped at the other) with a 240° throughwall circumferential crack at the clamped end under internal pressure loading. The assumed stress-strain curve is shown in Fig. 4.34. The difference between kinematic and isotropic hardening rules should be small for the nearly radial loading path used for the problem at hand. Comparisons of the variation of the crack section rotation and support reaction with pressure are shown in Figs. 4.35a-b, respectively. The slight discrepancy between the FEA results and the model predictions at low pressures are due to neglecting the elastic deformation in the model. However, the FEA results diverge from the model calculations significantly as the pressure exceeds $\approx 50\%$ the unflawed tube burst pressure. This is because, at these higher pressures, tube sections away from the crack plane experience significant plastic deformation (Fig. 4.36), which is assumed to be negligible in the model. Note that with $\sigma_y/\bar{\sigma} = 0.5$, the analytical model predicts (Fig. 4.35b) onset of yielding in a tube containing a 240° crack at $p/p_b = 0.43$, which agrees very well with the FEA result. Thus, the limit of applicability of the current model depends on the crack angle as well as the strain hardening behavior ($\sigma_y/\bar{\sigma}$) of the material (Fig. 4.33b).

Plasticity allowed to occur away from crack section. When plasticity spreads to sections other than that containing the crack, Eq. 4.4 is no longer applicable, and a new nonlinear relationship between bending moment and rotation must be derived. We consider two types of plastic deformation laws for this analysis. First, we consider a material with a bilinear stress-strain curve (with tangent modulus E_T).

$$\frac{\varepsilon}{\varepsilon_y} = \begin{cases} \frac{\sigma}{\sigma_y} & \text{for } \sigma \leq \sigma_y \\ 1 + \left(\frac{\sigma}{\sigma_y} - 1\right)\frac{E}{E_T} & \text{for } \sigma > \sigma_y \end{cases}, \qquad (4.17a)$$

and second, a material with a power-law hardening stress-strain curve is considered,

$$\frac{\varepsilon}{\varepsilon_y} = \begin{cases} \frac{\sigma}{\sigma_y} & \text{for } \sigma \leq \sigma_y \\ \left(\frac{\sigma}{\sigma_y}\right)^{\frac{1}{m}} & \text{for } \sigma > \sigma_y \end{cases}. \qquad (4.17b)$$
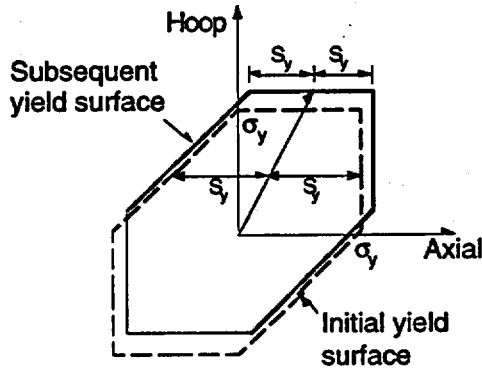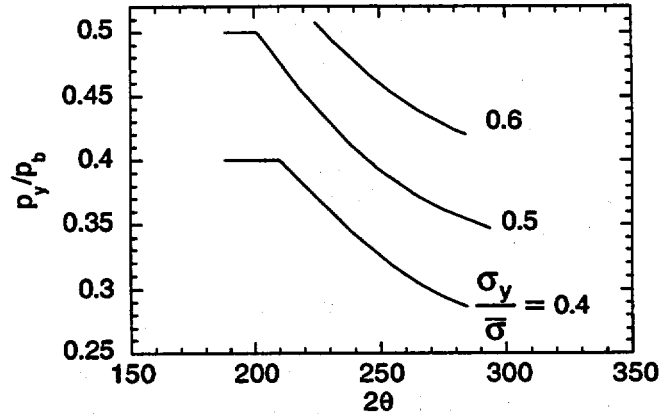
Fig. 4.33. *(a) Determination of axial yield strength Sy for bending analysis using Tresca criterion and (b) predicted variation of pressure to first yield the tube away from crack plane with crack angle as a function of ratio between yield and flow stress.*
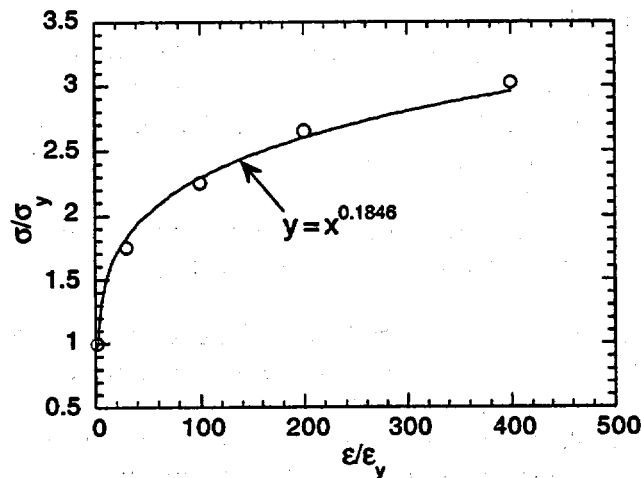
Fig. 4.34. *Normalized uniaxial stress-strain curve (symbols used in FEA) and power-law fit.*

In both cases, we continue to assume that the section containing the crack is at the plastic limit state with flow stress $\bar{\sigma}$, the assumption being that the crack section experiences extensive plastic deformation long before any plastic yielding occurs away from the crack section.

To keep the analysis tractable for the current analytical model, we make a simplifying assumption that the stresses and total deformation at any pressure can be obtained by considering a nonradial loading path, consisting of first loading radially to the final pressure (hoop to axial membrane stress ratio of 2:1) at zero axial bending stress and then applying the axial bending stresses, holding the pressure-induced membrane stresses
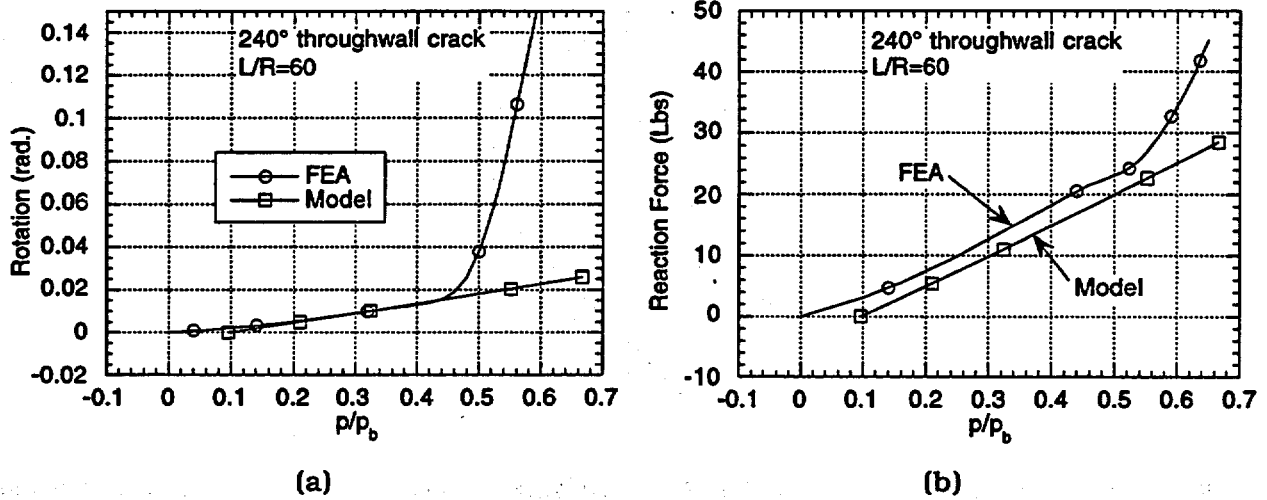
Fig. 4.35. Comparison of model prediction and elastic-plastic FEA results ($\sigma_y / \overline{\sigma} = 0.5$) for (a) crack section rotation and (b) support reaction force of tube simply supported at one end and clamped at the other (as in Fig. 4.29) at various normalized pressures.
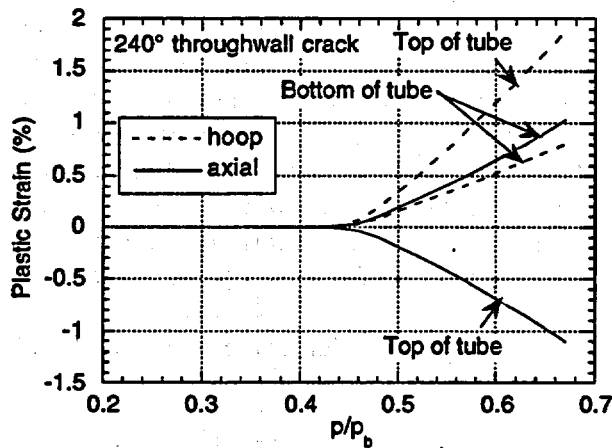
Fig. 4.36. Calculated (by FEA with yield stress/flow stress = 0.5) variation of plastic strains, with normalized pressure, at top and bottom of section located at axial distance 4R from crack in laterally supported tube (L/R = 60) with single 240° throughwall circumferential crack at clamped edge.
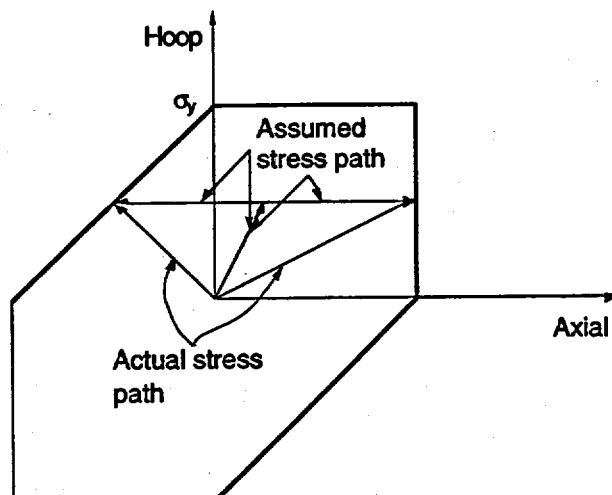
Fig. 4.37. *Radial loading path used in FEA is replaced in model by nonradial path consisting of loading to final pressure (at 2 to 1 stress ratio) followed by applying axial bending stress at constant hoop.*

constant (Fig. 4.37). This assumption allows us to use the same yield surface (Eq. 4.14 and Fig. 4.33a) for all axial locations and makes it possible to obtain an analytical solution for the bending problem. The relatively good agreement between the model prediction and the FEA results, to be discussed later, shows that this assumption is probably reasonable as long as no unloading or reversed yielding occurs.

With the above assumptions, we determine a relationship between the bending moment and rotation in the elastic-plastic regime by a detailed analysis of axial bending of the tube subjected to an end moment M_0 at a constant internal pressure p. For p > p_y, a length of the tube extending from z = 0 to z = z_y will deform plastically, while the rest of the beam L > z > z_y will remain elastic. The stress distributions in a plastically deforming section are shown in Figs. 4.38a and 4.38b for the bilinear and power law hardening stress-strain curve, respectively. At every section, there will be an elastic core extending from $\theta = -\beta_y$ to $\theta = \beta_y$., with β_y varying from $\beta_y = \beta_0$ at z = 0 to $\beta_y = \pi/2$ at z = z_y.

By stress integration and using the definition of z_y, the bending moment at any section is given by

$$\frac{M}{M_y} = \frac{2}{\pi \sin\beta_y}\left[\left(1 - \frac{E_T}{E}\right)\left(\beta_y + \frac{1}{2}\sin 2\beta_y\right) + \frac{\pi E_T}{2E}\right] = \frac{L-z}{L-z_y} \qquad (4.18a)$$

for the bilinear stress-strain curve and

$$\frac{M}{M_y} = \frac{2}{\pi \sin\beta_y}\left(\beta_y - \frac{1}{2}\sin 2\beta_y\right) + \frac{4}{\pi}\left(\frac{1}{\sin\beta_y}\right)^m \int_{\beta_y}^{\frac{\pi}{2}} \sin^{m+1}\theta\, d\theta = \frac{L-z}{L-z_y} \qquad (4.18b)$$

for the power-law hardening curve, where M_y corresponds to the bending moment at first yield away from the crack section.
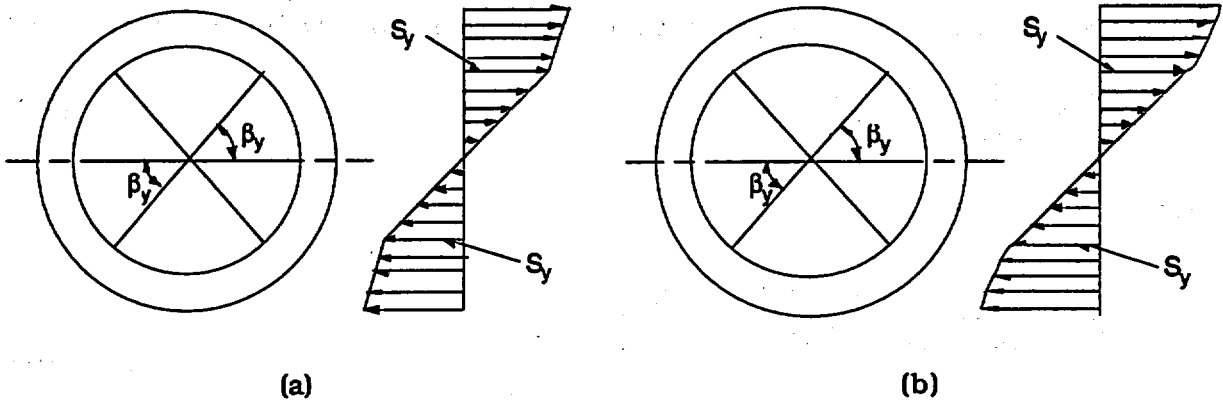
Fig. 4.38. *Stress distribution through section away from crack section after yield, (a) bilinear for bilinear stress-strain curve and (b) nonlinear for power-law hardening curve.*

Differentiating Eqs. 4.18a-b and solving,

$$\frac{d\beta_y}{dz} = \frac{1}{(L - z_y)} \frac{1}{f(\beta_y)}.$$ (4.19)

where

$$f(\beta_y) = \frac{2}{\pi} \frac{\left(1 - \frac{E_T}{E}\right)\left(\beta_y - \frac{1}{2}\sin 2\beta_y\right) + \frac{\pi E_T}{2E}}{\sin\beta_y \tan\beta_y}$$ (4.20a)

for the bilinear stress-strain curve and

$$f(\beta_y) = \frac{2}{\pi}\left[\frac{\beta_y - \frac{1}{2}\sin 2\beta_y}{\sin\beta_y \tan\beta_y} + \frac{2mI_m}{\sin^m\beta_y \tan\beta_y}\right]$$ (4.20b)

for the power-law hardening stress-strain curve with

$$I_m = \int_{\beta_y}^{\frac{\pi}{2}} \sin^{m+1}\theta\, d\theta.$$ (4.20c)

The equation for bending is given by

$$\frac{d^2 w}{dz^2} = -\frac{\kappa_y}{\sin\beta_y}.$$ (4.21a)

where w is the transverse deflection and

$$\kappa_y = \frac{M_y}{EI} = \frac{S_y}{ER}.$$ (4.21b)

Making a transformation of independent coordinate from z to β_y with the help of Eq. 4.19,

$$\frac{dw}{dz} = \frac{1}{(L - z_y)} \frac{1}{f(\beta_y)} \frac{dw}{d\beta_y} \tag{4.22a}$$

and

$$\frac{d^2w}{dz^2} = \left[\frac{1}{(L - z_y)}\right]^2 \frac{1}{f(\beta_y)} \frac{d}{d\beta_y}\left[\frac{1}{f(\beta_y)} \frac{dw}{d\beta_y}\right]$$

$$= -\frac{\kappa_y}{\sin\beta_y}. \tag{4.22b}$$

Integrating Eq. 4.22b from $\beta = \beta_0$ (i.e., $z = 0$) to $\beta = \pi/2$ (i.e., $z = z_y$), and denoting the slope at $z = 0$ by ϕ_0,

$$\left.\frac{dw}{dz}\right|_{z=z_y} = \phi_0 - \kappa_y(L - z_y)\int_{\beta_0}^{\frac{\pi}{2}} \frac{f(\beta_y)}{\sin\beta_y} d\beta_y . \tag{4.23a}$$

In a similar fashion,

$$w|_{z=z_y} = \phi_0\left((L - z_y)\int_{\beta_0}^{\frac{\pi}{2}} \frac{f(\beta_y)}{\sin\beta_y} d\beta_y - \kappa_y(L - z_y)^2 \int_{\beta_0}^{\frac{\pi}{2}} f(\beta_y)\int_{\beta_0}^{\beta_y} \frac{f(\beta_y)}{\sin\beta_y} d\beta_y d\beta_y . \tag{4.23b}$$

The slope and displacement at $z = z_y$ from the elastic part of the beam are

$$\left.\frac{dw}{dz}\right|_{z=z_y} = \frac{M_y(L - z_y)}{2EI} + C_1 \tag{4.24a}$$

and

$$w|_{z=z_y} = -\frac{M_y}{6EI}(L - z_y)^2 - C_1(L - z_y), \tag{4.24b}$$

where C_1 is an arbitrary constant. Combining Eqs. 4.24a and 4.24b,

$$(L - z_y)\left.\frac{dw}{dz}\right|_{z_y} + w|_{z_y} = \frac{\kappa_y}{3}(L - z_y)^2. \tag{4.24c}$$

Satisfying continuity of slope and displacement at $z = z_y$, using Eq. 4.24c, and solving gives

$$\frac{\phi_0 M_o}{\phi_y M_y} = \frac{3I_1 + 3I_2 + 1}{1 + I_3}, \tag{4.25}$$

where

$$\frac{M_o}{M_y} = \frac{2}{\pi \sin \beta_o} \left[\left(1 - \frac{E_T}{E} \right) \left(\beta_o + \tfrac{1}{2} \sin 2\beta_o \right) + \frac{\pi E_T}{2E} \right] \qquad (4.26a)$$

for the bilinear stress-strain curve and

$$\frac{M_o}{M_y} = \frac{2}{\pi \sin \beta_o} \left(\beta_o - \tfrac{1}{2} \sin 2\beta_o \right) + \frac{4}{\pi} \left(\frac{1}{\sin \beta_o} \right)^m \int_{\beta_o}^{\frac{\pi}{2}} \sin^{m+1} \theta \, d\theta \qquad (4.26b)$$

for the power-law hardening stress-strain curve,

$$\phi_y = \frac{1}{3} L \kappa_y = \frac{M_y L}{3EI}, \qquad (4.26c)$$

$$I_1 = \int_{\beta_o}^{\frac{\pi}{2}} \frac{f(\beta_y)}{\sin \beta_y} d\beta_y, \qquad (4.27a)$$

$$I_2 = \int_{\beta_o}^{\frac{\pi}{2}} f(\beta_y) \int_{\beta_o}^{\beta_y} \frac{f(\beta_y)}{\sin \beta_y} d\beta_y d\beta_y, \qquad (4.27b)$$

and

$$I_3 = \int_{\beta_o}^{\frac{\pi}{2}} f(\beta_y) d\beta_y. \qquad (4.27c)$$

We can represent the rotation in terms of a function G of the bending moment as follows, with the tangent modulus E_T as a parameter for the bilinear stress-strain curve:

$$\phi = \phi_y G \left(\frac{M}{M_y}; \frac{E_T}{E} \right). \qquad (4.28a)$$

In a similar fashion, for the power-law hardening case, we can represent the rotation in terms of a different function G of the bending moment with the exponent m as a parameter,

$$\phi = \phi_y G \left(\frac{M}{M_y}; m \right). \qquad (4.28b)$$

A plot of the end rotation versus the applied moment for various values of tangent modulus is shown in Figs. 4.39a-b for the case of bilinear stress-strain curve. Note that for perfect plasticity ($E_T = 0$), the limit moment is reached in about 1.7 times the rotation for initial yield. The bending moment capability of the section increases with increasing value of tangent modulus. However, the plastic rotation is considerably greater than the elastic rotation even for a tangent modulus of $E_T/E = 1/50$. In a similar fashion, a plot of the calculated end rotation versus the applied moment for the power-law hardening case is shown in Fig. 4.40. In both cases, the function G can be represented by a cubic polynomial of the bending moment (see Figs. 4.39b and 4.40):
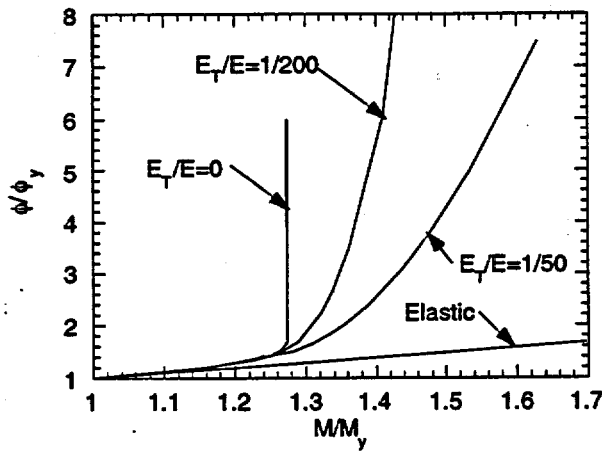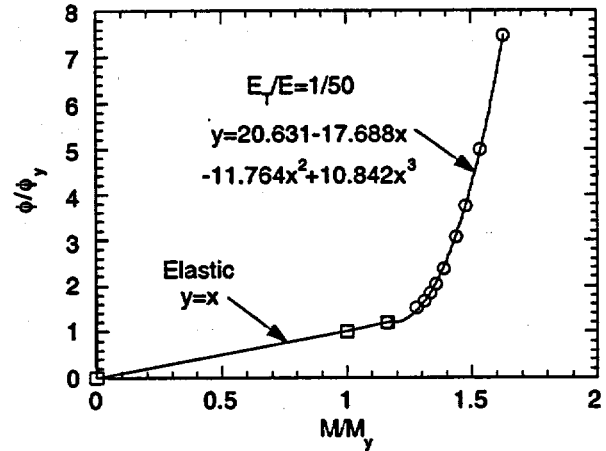
Fig. 4.39. *Rotation vs. applied bending moment for configuration of Fig. 4.24 (a) for various values of E_T and (b) polynomial fit to curve for $E_T/E = 1/50$.*
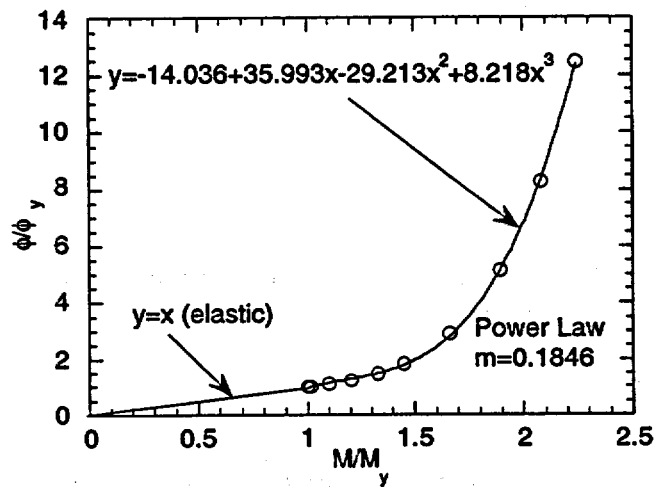
Fig. 4.40. *Model-calculated normalized rotation versus applied bending moment for configuration of Fig. 4.24 and polynomial fit to results for power-law hardening stress-strain curve with exponent $m = 0.1846$ (Fig. 4.34).*

$$G(x) = \begin{cases} x & \text{for } x \le 1 \\ A + Bx + Cx^2 + Dx^3 & \text{for } x > 1. \end{cases} \qquad (4.28c)$$

Eq. 4.4 can be generalized for the elastic-plastic case as follows:

$$-\frac{M_L}{M_y} + G^{-1}\left(\frac{\phi}{\phi_y}\right) = 0, \qquad (4.29a)$$

or, alternatively

$$\phi = \phi_y G\left(\frac{M_L}{M_y}\right).$$

(4.29b)

Onset of crack initiation. Combining Eqs. 4.29b and 4.5, at the point of crack initiation,

$$(\cos\beta_c + \cos\theta)G\left(\frac{M_L}{M_y}\right) = \frac{3E\delta_c}{LS_y} = \frac{3\pi E\delta_c}{4L\bar{\sigma}}\frac{4}{\pi}\frac{\bar{\sigma}}{S_y}$$

$$= \frac{4c}{\pi}\frac{\bar{\sigma}}{S_y},$$

(4.30a)

where M_L/M_y is given by Eq. 4.15b, c is defined in Eq. 4.6b, and Eq. 4.14 can be rewritten as follows:

$$\frac{S_y}{\bar{\sigma}} = \begin{cases} \dfrac{\sigma_y}{\bar{\sigma}} - \dfrac{p}{2p_b} & \text{for } \dfrac{p}{p_b} \le \dfrac{\sigma_y}{\bar{\sigma}} \\ \dfrac{p}{2p_b} & \text{for } \dfrac{p}{p_b} > \dfrac{\sigma_y}{\bar{\sigma}}. \end{cases}$$

(4.30b)

Equation 4.30a can be solved for the critical value $\beta = \beta_c$ which, when substituted in Eq. 4.3b, gives the crack initiation pressure p_c.

The onset of crack extension can also be expressed in terms of the critical value J_c of the plastic component of the deformation J integral J_P, and Eqs. 4.7, 4.8, and 4.9a-b still hold.

Instability. Proceeding as before, if the crack is to be unstable at onset of crack extension under constant loading, the following condition must be satisfied (using Eq. 4.29a):

$$\frac{dM}{d\phi} = -\frac{dM_L}{d\phi}\bigg|_I + \frac{3EI}{L}\frac{dG^{-1}\left(\frac{\phi}{\phi_y}\right)}{d\left(\frac{\phi}{\phi_y}\right)} = -\frac{dM_L}{d\phi}\bigg|_I + \frac{3EI}{L}\frac{1}{\dfrac{dG\left(\frac{M}{M_y}\right)}{d\left(\frac{M}{M_y}\right)}\bigg|_{M=M_L}} < 0,$$

(4.31)

where $\dfrac{dM_L}{d\phi}$ is measured at the onset of crack extension. Using Eqs 4.12a and 4.12b and following the procedure that was used to derive Eq. 4.13b, the condition for unstable failure is found to be

$$T_{APP} = \frac{2L}{3\pi R}(\cos\beta + \cos\theta)^2 \frac{dG\left(\frac{M}{M_y}\right)}{d\left(\frac{M}{M_y}\right)}\bigg|_{M=M_L} - \frac{EJ}{R\bar{\sigma}^2}\frac{\sin\theta - \frac{1}{2}\sin\beta}{\cos\beta + \cos\theta} > \frac{E}{\bar{\sigma}^2}\frac{dJ}{da} = T_{MAT}$$

(4.32)

Results. Figure 4.41a shows a comparison of the variation of crack section rotation with pressure as predicted by the model using a bilinear stress-strain curve with that calculated by FEA. A reasonable correlation between the clamped edge rotation by FEA and the model prediction can be obtained by assuming $E_T/E = 1/100$ and $\sigma_y/\bar{\sigma} = 0.5$. Figure 4.41b shows a similar comparison for the model using a power-law hardening stress-strain curve (Fig. 4.34). As expected, the model using power-law hardening stress-strain curve fits the FEA data better than that using the bilinear stress-strain curve. The stresses calculated by FEA are in good agreement with the elastic-plastic model (Fig. 4.42a-b) using either stress-strain curve.

Figs. 4.43 a-b show the calculated pressures for crack initiation vs. crack angle plots for various values of the toughness parameter c, calculated using the elastic-plastic model with a bilinear stress-strain curve and a power-law hardening curve, respectively. Note that for high values of c, crack initiation pressures (Figs. 4.43a-b) predicted by the models that allow for plastic deformation away from the crack section can be significantly lower than those (Fig. 4.28) predicted by the model in which plastic deformation is confined to the crack section. In particular, the minimums in the curves predicted by the latter model (Fig. 5) disappear in the former models (Figs. 4.43a-b). The plasticity effects are, of course, absent at lower values of c corresponding to lower crack initiation pressures.

Because the value of c for PWRs is expected to be in the range of 0.5-1, the occurrence of plasticity away from the crack plane is not a concern in PWRs. However, laboratory leak-rate and failure tests on circumferentially cracked tubes, such as those reported by the Belgians,[4] generally involve significant plastic deformation away from the crack plane. Failure curves that are based on tests that were performed on circumferentially cracked SG tubes by the Belgians are similar to those in Fig. 4.43b.

Crack opening areas for a 240° crack, calculated by the current model (Eq. 4.10c, with β_c calculated from Eq. 4.30a) and by the small-scale yielding Paris/Tada model,[12] are shown in Fig. 4.44. It is assumed that onset of crack extension does not occur before maximum pressure is reached. In Fig. 4.44, the curve labeled $L = \infty$ corresponds to the free-bending case, whereas the curve labeled $L = 0$ corresponds to the fully constrained case. Results from the Paris/Tada model, which is restricted to small-scale yielding in the crack plane and is independent of the span L, are plotted up to pressure levels significantly above the range of applicability. It is evident that lateral restraint to bending significantly reduces the COA when compared with the tube cross-sectional area, even under a design-basis accident condition $(p/p_b \approx 0.25)$.

The calculated tearing-modulus-vs.-pressure plots (Figs. 4.45a-b) show a marked increase in tearing modulus with plastic yielding using either stress-strain curve. The bilinear stress-strain curve (Fig. 4.45a) results in higher values of T_{APP} for the 240° crack than those (Fig. 4.45b) calculated with power-law hardening, because the stress increases linearly with pressure in the bilinear case, whereas it remains relatively bounded in the power-law hardening case (Fig. 4.34). Figure 4.45b shows that T_{APP} increases to high values for the power-law hardening case in a tube with shorter cracks ($\leq 180°$), indicating that the driving force for crack instability, which is negligible as long as plasticity is confined to the crack plane, increases rapidly with plastic yielding away from the crack plane. This is to be expected because the loss of bending stiffness of the tube with plastic
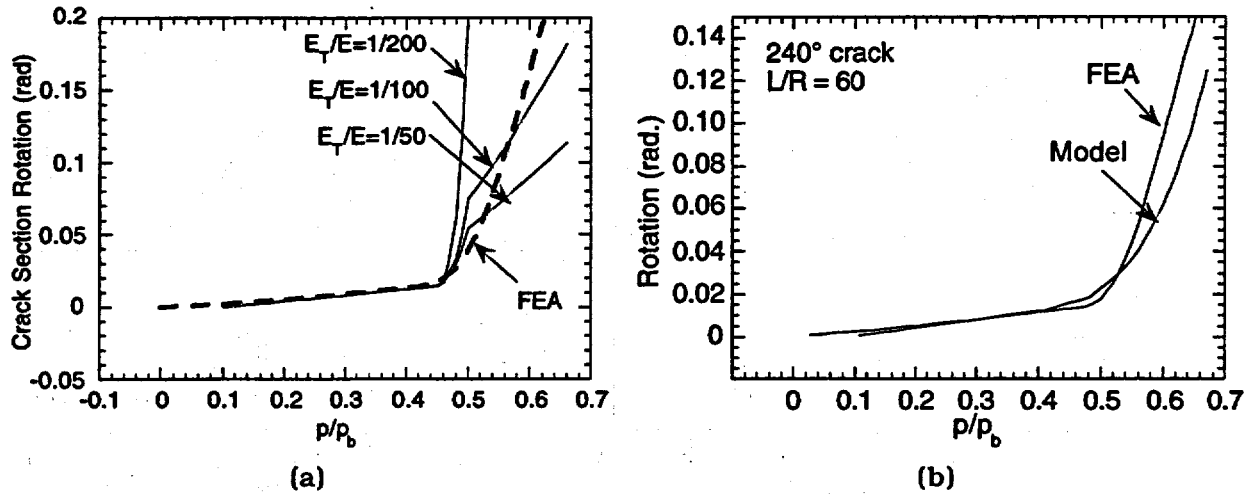
Fig. 4.41. Variation of crack section rotation with normalized pressure as calculated by FEA ($\sigma_y / \bar{\sigma} = 0.5$) and those calculated by a model that allows for plastic yielding away from crack plane using (a) bilinear stress-strain curve and (b) power-law hardening stress-strain curve.
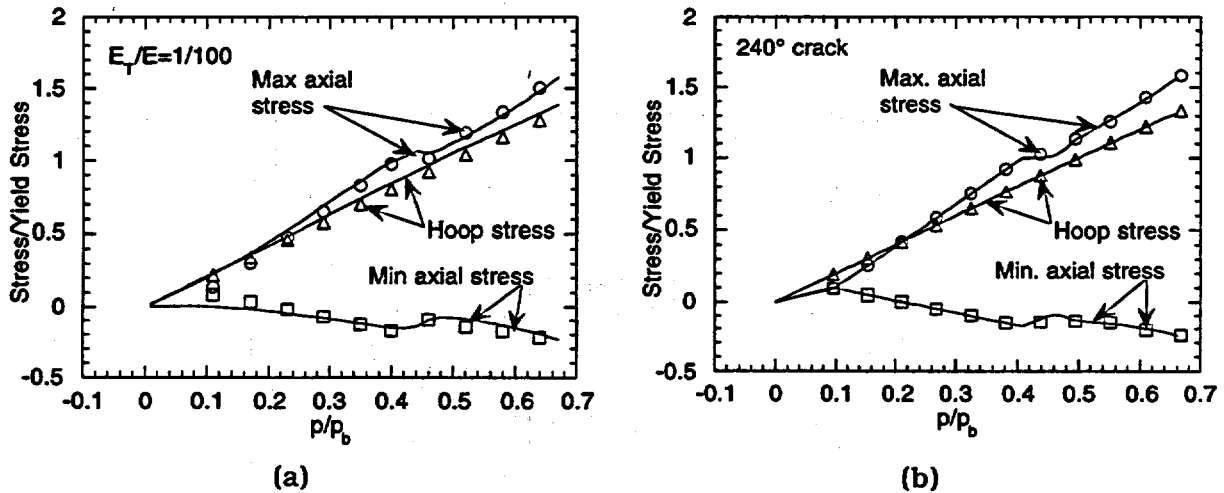
Fig. 4.42. Model predictions for stresses, allowing for plastic deformation ($\sigma_y / \bar{\sigma} = 0.5$) away from crack plane, using (a) bilinear stress-strain curve and (b) power-law hardening stress-strain curve and elastic-plastic FEA results for stresses at section located at distance 4R from crack plane in tube (L/R = 60) simply supported at one end and clamped at the other (as in Fig. 4.24) at various pressures. Symbols, and lines without symbols, represent model calculations and FEA results, respectively.
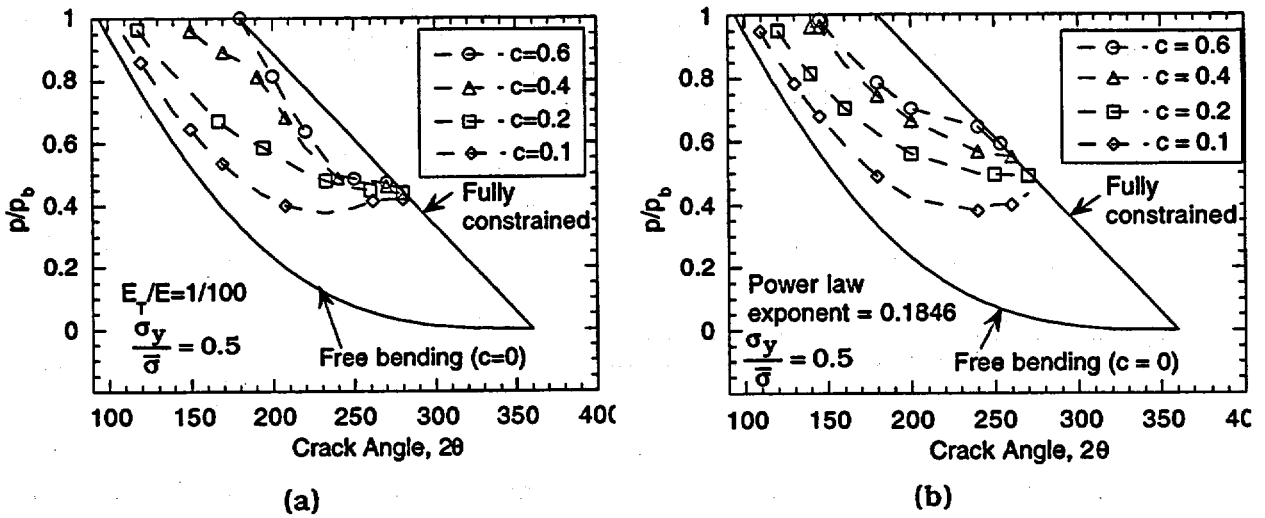
Fig. 4.43. Calculated variation of pressure, normalized by unflawed burst pressure, with crack angle for onset of crack growth in tube with single throughwall circumferential crack, using elastic-plastic model with (a) bilinear stress-strain curve and (b) power-law hardening stress-strain curve.
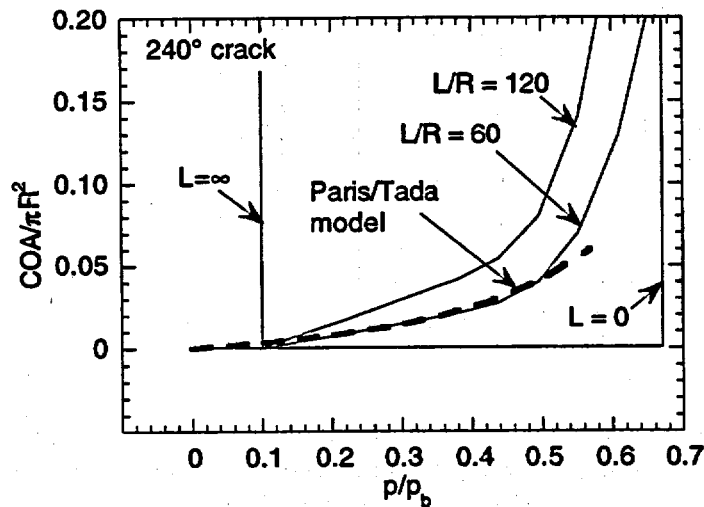
Fig. 4.44 Normalized crack opening area vs. pressure plots calculated by Paris/Tada model (dashed line) and by current model (solid lines) for L/R = 0 (fully constrained), 60, 120, and infinitely (free-bending) long simply-supported-clamped tube with 240° crack at clamped edge.
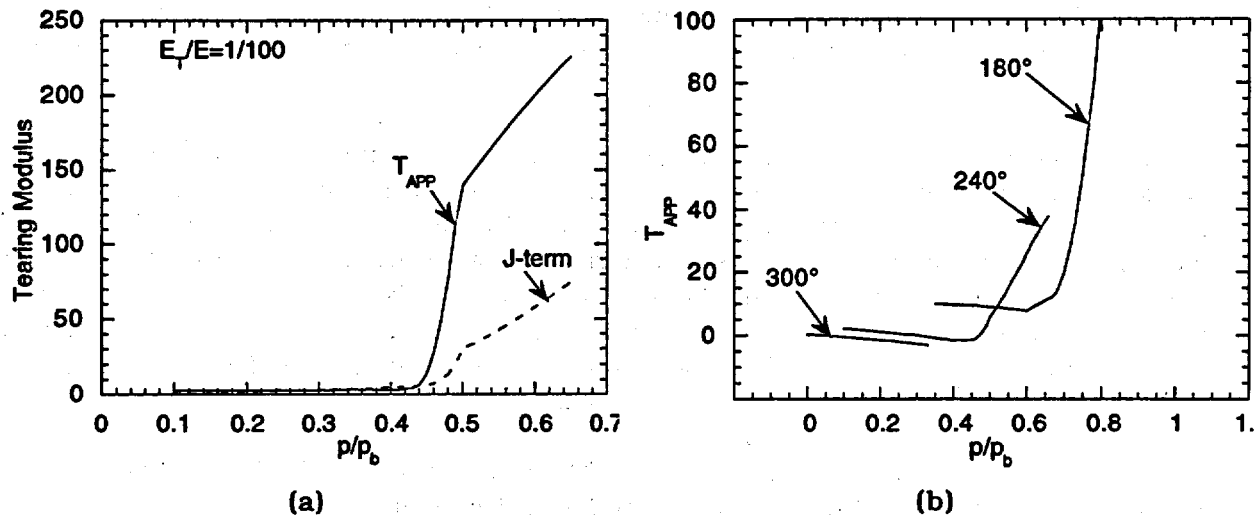
Fig. 4.45 Calculated variation of applied tearing modulus with pressure, normalized by unflawed burst pressure, for single throughwall circumferential crack in a tube, using elastic-plastic model with (a) bilinear stress-strain curve for 240° crack and (b) power-law hardening stress-strain curve for 180°, 240° and 300° cracks.

yielding produces a higher elastic follow-up, which causes the tube to behave like one with a much longer effective span. However, even with the enhanced values of T_{APP}, tubes with longer cracks ($\geq 240°$) may not fail by unstable tearing at the onset of crack extension (T_{MAT} for ductile alloys like Alloy 600 is typically ≈ 200) and will very likely fail by plastic collapse after some stable crack growth. Because, for values of c that are typical for SG tubes (0.5-1), the pressure for onset of crack extension (Fig. 4.43a-b) is already close to the pressure that corresponds to the fully constrained case, the extent of stable crack growth should be small.

Conclusions. An approximate model is presented for calculating crack opening area and failure pressure of laterally supported SG tubes with a throughwall circumferential crack at a clamped edge. The results show that the critical crack tip opening displacement, as well as the span and the boundary conditions, are important determining factors for the pressure at onset of crack extension. For typical mechanical properties and spans that are expected in PWR SGs, tubes with throughwall cracks behave as if fully constrained against rotation, and plastic deformation is confined to the section containing the crack. Crack opening areas during normal operation and design-basis accidents are small when compared with the tube cross-sectional area for a SG tube with $\leq 240°$ throughwall crack at the top of the tube sheet.

A model that allows for plastic deformation away from the crack plane is also proposed. The plasticity constitutive law is assumed to be either a bilinear stress-strain curve or a power-law hardening stress-strain curve. Comparison with finite element analysis shows that the FEA results are closer to those predicted by the power-law hardening model than those by the bilinear model, as would be expected. The predicted shapes of the crack initiation pressure versus crack angle plots by the power-law hardening model are smoother than those predicted by the bilinear model. The minima in the curves predicted by the earlier model, which assumes that plasticity is confined to the crack

section, disappear in both the elastic-plastic models that allow for plasticity away from crack section, and the curves are similar to the experimental curves obtained by the Belgians.

Although plasticity is confined to the crack section for normal operating and design-basis accident conditions of PWRs, significant plastic deformation usually occurs away from the crack section in leak-rate and failure tests of SG tubes in the laboratory. The simplified model, which can account for plastic deformation away from the crack plane, predicts failure pressure curves that are similar to curves derived from test data. The model also predicts a significant increase in the applied tearing modulus with the onset of plastic deformation away from the crack plane; however, failure by unstable tearing is more likely with short cracks (<180°) than with long cracks.

For typical SG tubes (span ≈0.6-1.2 m [24-48 in.]) with δ_c >0.75 mm (0.03 in.) (K_{JC} >220 MPa·m$^{1/2}$ [200 ksi·in.$^{1/2}$]) and containing a circumferential throughwall crack at the top of tube sheet, any crack of ≤180° does not reduce the failure pressure from the burst pressure of an unflawed tube. Also, tubes with throughwall cracks of ≥240° will behave as if they were fully constrained against bending and will have significantly greater failure pressures than the same tubes under free bending condition. Thus, for typical mechanical properties of SG tubes, the longest throughwall circumferential cracks at the top of tube sheet that are predicted to experience onset of crack initiation during normal operation and design basis accident conditions are 340° and 310°, respectively. A further conservative factor in the current model is the assumption that the tubes are free to expand or contract in the axial direction at the tube support plates. If the tubes are locked in at the tube support plates, the axial tensile force due to internal pressure must first overcome this lock-in force before the circumferential cracks see any driving force for crack initiation and growth.

4.6 Post-Test Analysis of Tests

All pressure and leak-rate tests conducted to date on specimens with laboratory-grown SCC cracks have been analyzed using available models for ligament rupture and leak rate. Failure pressures, leak rates, etc., depend on the mechanical properties (primarily flow stress) of the tubing. The minimum ASME code requirements for yield and ultimate tensile strengths of Alloy 600 SG tube are 240 and 550 MPa (35 and 80 ksi), respectively, which corresponds to a minimum flow stress of 400 MPa (58 ksi). The actual flow stress of SG tubes in most current plants can vary widely depending on the age and heat of material used. The yield strength can vary between 280 and 410 MPa (40 ksi and 60 ksi), while the ultimate tensile strength can vary between 620 and 760 MPa (90 and 110 ksi), which potentially cover a range of flow stress from 450-590 MPa (65-85 ksi). The yield and ultimate tensile strengths of our as-received tubing are 296 and 676 MPa (43 and 98 ksi), respectively, which fall right in the middle of the ranges reported above. However, because of the annealing and sensitizing heat treatments given to our tubes with laboratory-grown SCC cracks, their yield and ultimate tensile strengths are estimated to be reduced to 179 and 607 MPa (26 and 88 ksi), respectively. Thus, although the yield strength of our heat-treated tubing falls below the code minimum, the ultimate tensile strength is sufficiently above the code minimum to give a flow stress that is close to the code minimum. In order to compare results on one material with results on a different material, the effect of variations in the mechanical properties must be accounted for, i.e.,

the results must be normalized in terms of the flow stress. The analyses of the pressure and leak-rate tests have been used to develop procedures for accounting for flow stress effects. In addition, the analyses shed some light on the mechanisms of failure during the pressure tests.

In the case of the heat-treated tubing being used in our tests, the heat treatment reduces the room-temperature flow stress of the as-received tubing by ≈20%. Using the procedures that have been developed, data generated on annealed and sensitized material can be interpreted in terms of the behavior of the as-received material. The same procedures would be used to convert the present data to predict the behavior of tubing with a different yield strength.

4.6.1 Leak-Rate Tests on Notched Specimens

Leak-rate tests on 22.2-mm (7/8-in.)-diameter Alloy 600 tubes containing 12.7- and 25.4-mm (0.5- and 1.0-in.)-long throughwall axial EDM notches have been conducted on both as-received and heat-treated materials. The heat treatment, which is used to accelerate production of stress corrosion cracks in the laboratory, involves a solution treatment at 1100°C followed by a sensitizing treatment at 700°C, which reduces the yield strength of the tube from 296 to 179 MPa (43 to 26 ksi). Such a reduction in yield strength will have a significant influence on the crack opening area and, hence, on the leak rate. Therefore, we first investigate the predictive capability of the standard leak-rate equation for the leak-rate tests conducted on as-received and heat-treated specimens with EDM notches.

The formula used to calculate the volumetric leak-rate Q is as follows:

$$Q = 0.6A\sqrt{\frac{2\Delta p}{\rho}}, \qquad\qquad (4.33a)$$

or, using English units,

$$Q = 180.2A\sqrt{\frac{\Delta p}{\rho}}, \qquad\qquad (4.33b)$$

where A is the flaw opening area in in.[2], Δp is the pressure differential across the tube wall in psi, and ρ is the density (62.27 lbs/ft^3 at RT and 45.9 lbs/ft^3 at 288°C). In contrast to a circular hole, whose area remains relatively constant under increasing pressure, the area of a crack or a notch increases with pressure and must be taken into account for calculating the leak rate. Crack opening areas were calculated by the Zahoor model, which is described below.

Zahoor model for crack opening area. The crack opening area by the Zahoor model for an axial throughwall crack in a thin-walled tube is given by

$$A = 2\pi c_c^2 V_0 \sigma / E, \qquad\qquad (4.34)$$

where

σ = hoop stress = pR/h,

p is the differential pressure across the tube wall,

E is the Young's modulus, R and h are the mean radius and thickness of tube,

$$V_o = 1 + 0.64935\lambda_e^2 - 8.9683\text{x}10^{-3}\lambda_e^4 + 1.33873\text{x}10^{-4}\lambda_e^6,$$

$$\lambda_e^2 = c_e^2 / Rh,$$

$$c_e = c\left[1 + \frac{F}{2}\left(\frac{\sigma}{S_y}\right)^2\right].$$

$$F = 1 + 1.2987\lambda^2 - 2.6905\text{x}10^{-2}\lambda^4 + 5.3549\text{x}10^{-4}\lambda^6,$$

$$\lambda^2 = c^2 / Rh, \text{ and}$$

S_y is the yield strength and c is the crack half-length.

The flaw opening area for an EDM notch was obtained by adding the initial flaw area (equal to flaw length multiplied by flaw width) to the crack opening area given by Eq. 4.34. Crack opening areas calculated by Eq. 4.34 were found to agree well with FEA results (Figs. 4.46 a-b).

A comparison between calculated and observed leak rates at room temperature for a 12.7-mm (0.5-in.)-long EDM notch in as-received and heat-treated tubes is shown in Fig. 4.47a. Note that the curves for as-received and heat-treated tubes diverge as the pressure is increased beyond 6.9 MPa (1000 psi). At 17.2 MPa (2500 psi), the leak rate in a heat-treated material is greater by a factor of three than that in the as-received tube. The predicted leak rates are reasonably close to the observed leak rates for both tubes.

A similar plot for an as-received tube with a 25.4-mm (1-in.)-long EDM notch is shown in Fig. 4.47b. This test specimen was depressurized after a pressure of 13.8 MPa (2000 psi) was attained. Subsequently, it was repressurized and tested to failure. The measured crack opening areas were used to calculate the leak rates, which agree remarkably well with the observed leak rates (Fig. 4.47b). Thus, Eq. 4.33b appears to predict the leak rates through EDM notches at room temperature very well. Also, reasonable correlation between the Zahoor model predictions and the measured leak rates indicate that the crack opening areas are reasonably estimated by Eq. 4.34.

A leak-rate test at 288°C on an as-received tube with a 12.7-mm (0.5-in.)-long EDM notch has also been conducted. Because high-temperature tensile data are not available for the 22.2-mm (7/8-in.)-diameter tubing, the yield strength at 288°C needed for calculations was obtained from tensile data on 12.7-mm (0.5-in.)-diameter bar stock as reported by INEEL (Fig. 4.48a). The calculated leak rate is reasonably close to the measured value, as shown in Fig. 4.48b.
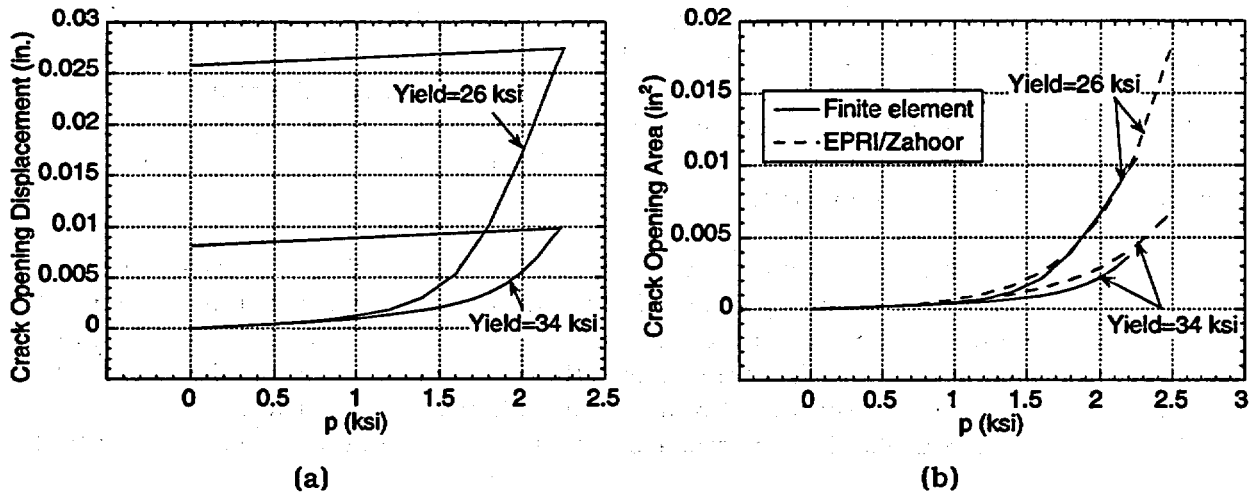
Fig. 4.46. Predicted (a) crack opening displacement (by FEA) and (b) crack opening area (by FEA and Zahoor model) of 12.7-mm (0.5-in.)-long throughwall crack (laboratory grown) in heat-treated tube as functions of pressure.
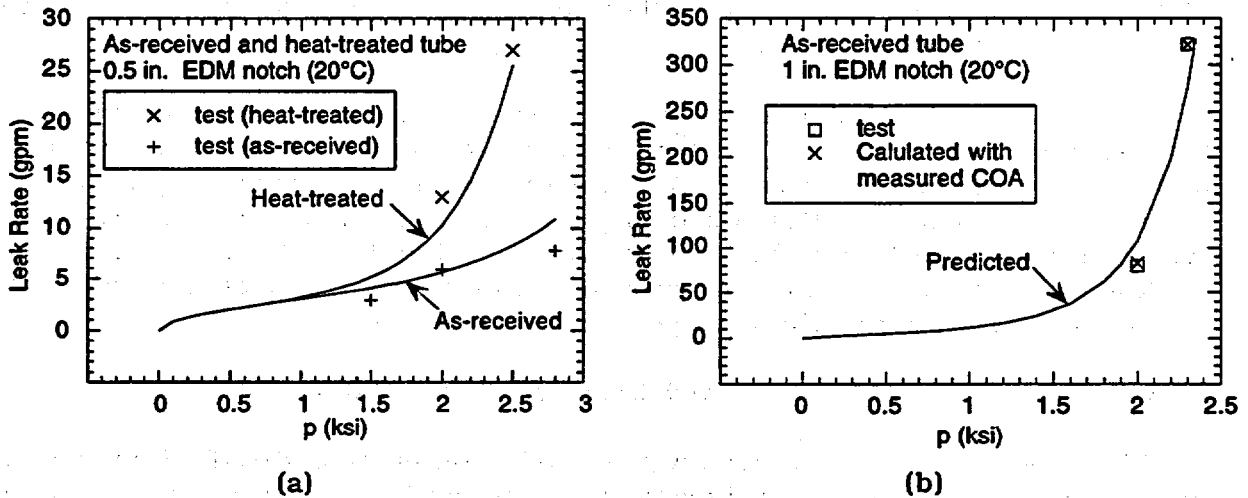
Fig. 4.47. Calculated (solid line) vs. experimentally measured (symbols) leak rates at 20°C for as-received and heat-treated 22.2-mm (7/8-in.)-diameter tubes with (a) 12.7-mm (0.5-in.) and (b) 25.4-mm (1-in.)-long throughwall axial EDM notches. Cross symbols in Fig. 4.47b denote calculated leak rates using post-test measured crack opening areas.

4.6.2 Calibration Curves to Correct for Flow Stress

All pressure and leak-rate tests on laboratory-grown stress corrosion cracks at ANL have been and will be conducted on Alloy 600 tubes subjected to prior annealing and sensitizing heat treatments. The yield and flow stresses of these heat-treated tubes are considerably lower than those of the as-received tubes. To convert the failure pressure and leak-rate data from the heat-treated tubes to the as-received tubes, we must multiply the measured failure pressure and divide the leak-rate data on heat-treated tubes by appropriate correction factors (>1).

Correction factor for ligament rupture and tube burst pressures. The room-temperature flow stress of our as-received Alloy 600 tube is estimated to be about 20% greater than that of the sensitized tube. Thus, a correction factor of 1.2 should be applied to either the ligament failure pressure or unstable burst pressure of the heat-treated tube to obtain that of the as-received 22.2-mm (7/8-in.)-diameter tube. Until flow stress data at high temperature are available, the same correction factor should also be applied at 282°C.

Correction factor for leak rate. The correction factor for accounting for the effect of changes in mechanical properties on leak rate is more complex, because it depends on pressure, temperature, and crack area or length. It also depends on whether the flaw is initially a tight SCC crack or a 0.19-mm (0.0075-in.)-wide EDM notch.

To derive the leak-rate correction factors, we used the Zahoor model (Eq. 4.34) to calculate the flaw opening area and Eq. 4.33b to calculate the volumetric leak rate through EDM flaws. The effect of the material flow properties on leak rate enters through their effect on the flaw opening area A.

Variation of the leak-rate correction factor with pressure, flaw length, and temperature are given in Fig. 4.49a for tight SCC cracks and in Fig. 4.49b for 0.19-mm (0.0075-in.)-wide EDM notches. These curves are based on room-temperature yield strengths of 296 and 179 MPa (43 and 26 ksi) for the as-received and heat-treated tubes, respectively. The yield strengths are assumed to be reduced by 10% at 282°C. Note that the leak-rate correction factors for notches are generally lower than those for cracks. Also, the longer the crack (or notch), the higher the correction factor.

4.6.3 Leak-Rate Tests on Specimens with Laboratory-Grown SCC Cracks

The leak-rate tests on laboratory-grown SCC cracks were described in the 1998 Annual Report. In this semiannual report, we present analyses conducted for these tests.

Estimation of throughwall crack length from leak-rate data. To apply the leak-rate correction factors (Fig. 4.49a) to a laboratory grown SCC crack, we must first establish an effective length for the throughwall segment of the crack after ligament rupture and verify that ligaments separating the axial segments are ruptured so that in effect we have a single throughwall crack. This creates an uncertainty for an initially part-throughwall laboratory grown SCC crack, because the geometry of the crack, such as the lengths of the throughwall segments of the crack after ligament rupture and whether the ligaments between the axial segments survive the test, cannot be reliably estimated from the pre-test
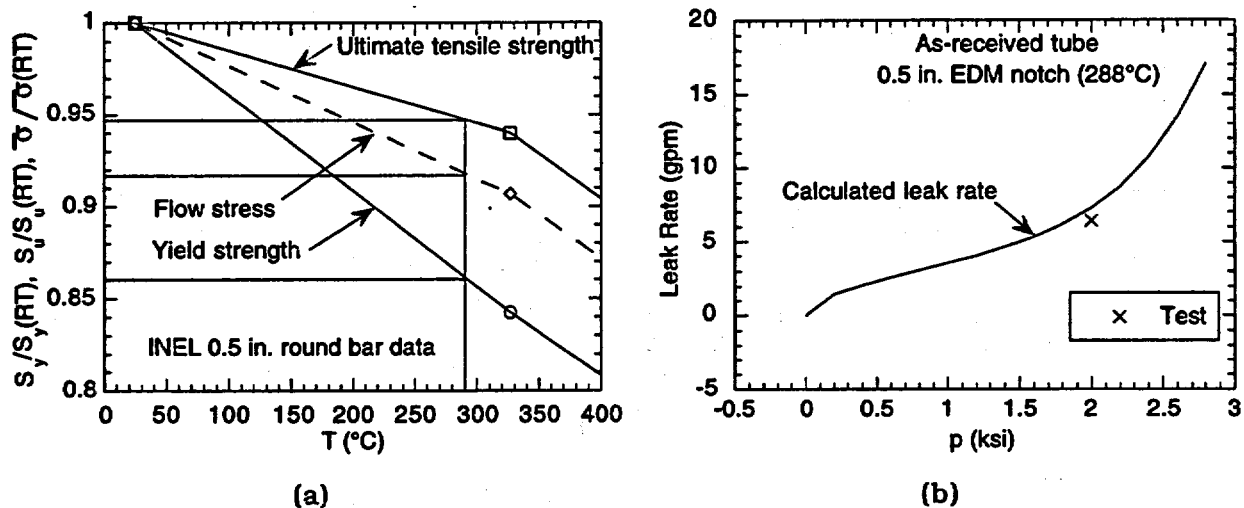
Fig. 4.48. (a) Variations of yield and ultimate tensile strengths and flow stress of Alloy 600 round bar stock with temperature and (b) comparison of calculated (solid line) versus experimentally measured (cross symbol) leak rates at 288°C for as-received 22.2-mm (7/8-in.)-diameter tube with 12.7-mm (0.5-in.)-long throughwall axial EDM notch.

EC +Point data. There are several ways for obtaining the effective throughwall crack length. Together with visual observation of the crack morphology at the OD surface, these lengths should be compared with each other to check for consistency.

1. The most rigorous but laborious and time-consuming way to obtain the length of the throughwall segment of the crack is by post-test sectioning of the specimen.

2. A far less laborious but nonetheless useful approach is to pressurize the ruptured tube by gas while the tube is submerged under water and measure the crack length from the length of the emerging bubble zone.

3. We can calculate analytically an effective throughwall crack length from the measured leak rate by using Eq. 4.33b and the Zahoor model for calculating the crack opening area (Eq. 4.34), assuming that even if the crack was initially segmented axially, all the ligaments between the segments are ruptured before the leak-rate data are taken.

4. Finally, we can use the pre-test crack morphology as measured by EC +Point method together with the ANL correlation for ligament rupture pressure to calculate the crack length, assuming that even if the crack was axially segmented initially, all the ligaments between the segments are ruptured before rupture of the through-thickness crack tip ligament.
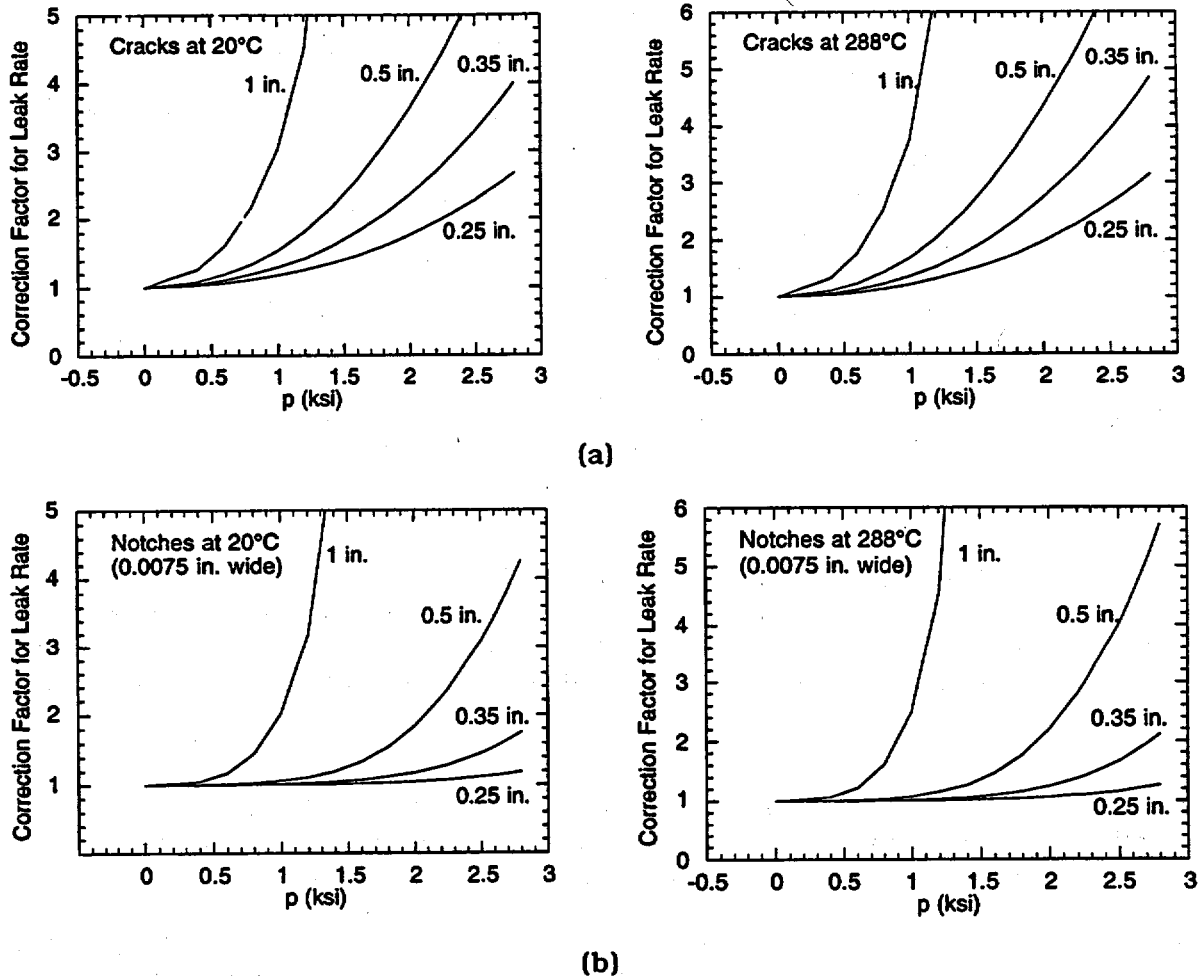
Fig. 4.49. *Correction factors for obtaining leak rates in as-received Alloy 600 tubes from sensitized tube data at 20°C and 288°C for tubes containing (a) single throughwall axial cracks without axial segments and (b) initially 0.19-mm (0.0075-in.)-wide rectangular throughwall axial notches.*

Estimation of throughwall crack length by ligament rupture model. Ideally, we can use the ANL correlation for ligament rupture pressure of part-throughwall rectangular cracks to estimate the length of the throughwall segments of the cracks after crack-tip ligament rupture. However, laboratory-grown SCC cracks are irregular in shape and have variable depth along their length. Instead of being a single planar crack, they are composed of a family of crack segments in different planes. Local variations in crack depth and geometry are smoothed out in the EC measurements because the finite resolution of the EC probes, and hence the EC data tend to show a relatively smooth variation of crack depth along the crack length. This is evidenced by the fact that although all the SCC specimens tested to date (including a "doped-steam" cracked specimen) have shown leakage under low gas pressure before testing, the EC +Point method cannot detect or identify the locations of these very small throughwall segments. However, no leakage of water was detected through these cracks until much higher pressures were applied.

Currently, no widely accepted models are available for predicting the ligament failure pressure of cracks with such complex geometries. From a limit analysis viewpoint, it can be argued that the collapse behavior of a crack tip ligament with an irregular point-by-point variation of crack depth should be similar to that of a crack with a smoothed-out "average" crack depth profile. For the present, we assume that the average profile measured by the EC +Point method is the one that is relevant for limit analysis. With this assumption, although the real crack may have short throughwall segments at a number of locations, from the viewpoint of plastic collapse of the ligament, the tube behaves as if it has a smoothly varying average ligament thickness (or crack depth) profile.

Because the measured crack depth profile by EC +Point is generally not rectangular (e.g., see Fig. 4.50a), the following procedure was used to establish the length and depth of an equivalent rectangular crack:[13]

1. Choose a crack depth d_o and assume that any crack segment with depth $d < d_o$ does not adversely affect the crack tip ligament rupture pressure of the tube. In other words, replace the original crack depth profile by a new crack depth profile in which any crack segment with depth $d < d_o$ is replaced by $d = 0$. The choice of d_o determines the length of an equivalent rectangular crack.

2. The depth of the equivalent rectangular crack is determined by equating its area to the area under the newly defined crack depth profile in step 1. For example, in Fig. 4.50a, the choice of $d_o = 70\%$ fixes the length and depth of the equivalent rectangular crack at 10 mm (0.4 in.) and 85%, respectively.

3. Generate a series of candidate equivalent rectangular cracks by parametrically varying d_o, use the ANL correlation for calculating the ligament rupture pressures for all the candidates, and select the one that gives the lowest ligament rupture pressure as the applicable equivalent rectangular crack. Generally, a couple of trials for d_o were sufficient for cracks with relatively uniform ligament thickness as in specimen SGL-104 (Fig. 4.50a). The length of the equivalent crack was used as an estimate for the length of the throughwall segment of the crack after ligament rupture.

Estimation of throughwall crack lengths for laboratory-grown SCC cracks. The procedure for estimating the throughwall crack length is illustrated here using the tests conducted at ANL to date. A summary of all throughwall crack lengths estimated by the different methods is included in Table 4.1. Figures 4.50a-c show the crack depth profile (by EC +Point) for specimen SGL-104, the calculated ligament rupture pressures corresponding to two equivalent rectangular cracks, and calculated leak rates for various crack lengths at pressures for which experimental leak rates (at 282°C) were measured, respectively. The ligament rupture model (Fig. 4.50b) predicts a failure pressure of 18.0 MPa (2610 psi), compared with experimentally measured 16.2 MPa (2350 psi), for an equivalent crack length of 10 mm (0.40 in.). The leak-rate model (Fig. 4.50c) predicts the effective throughwall crack length to be between 0.38 in. (9.6 mm) and 0.39 in. (9.9 mm) from the measured leak rates of 6.2 and 5.6 gpm at 2500 (17.2 MPa) and 2350 psi (16.2 MPa), respectively. The leak rate in this test did not increase during a 15 min constant pressure hold at 17.2 MPa (2500 psi). It should be noted that >24-h hold at constant pressure and room temperature did not increase the leak rate through a

Fig. 4.50. *(a) Estimated crack depth profile from EC +Point data, (b) calculated ligament failure pressures for two equivalent rectangular crack sizes, and (c) effective throughwall crack length estimated from leak-rate data for test SGL-104 conducted at 288°C.*

rectangular EDM slot. A post-test view of the crack at the OD surface is shown in Fig. 4.51, which also includes a marker identifying the estimated throughwall crack length. A comparison with Fig. 4.50a indicates that the estimated crack length corresponds to the crack length over which the depth equals or exceeds about 70% of the wall thickness. Note that the estimated throughwall crack length is significantly shorter than the OD surface crack length of 16 mm (0.63 in.).

Figures 4.52a-c show similar plots for test SGL-195, which was conducted at room temperature. The ligament rupture model predicts a failure pressure of 16.5 MPa
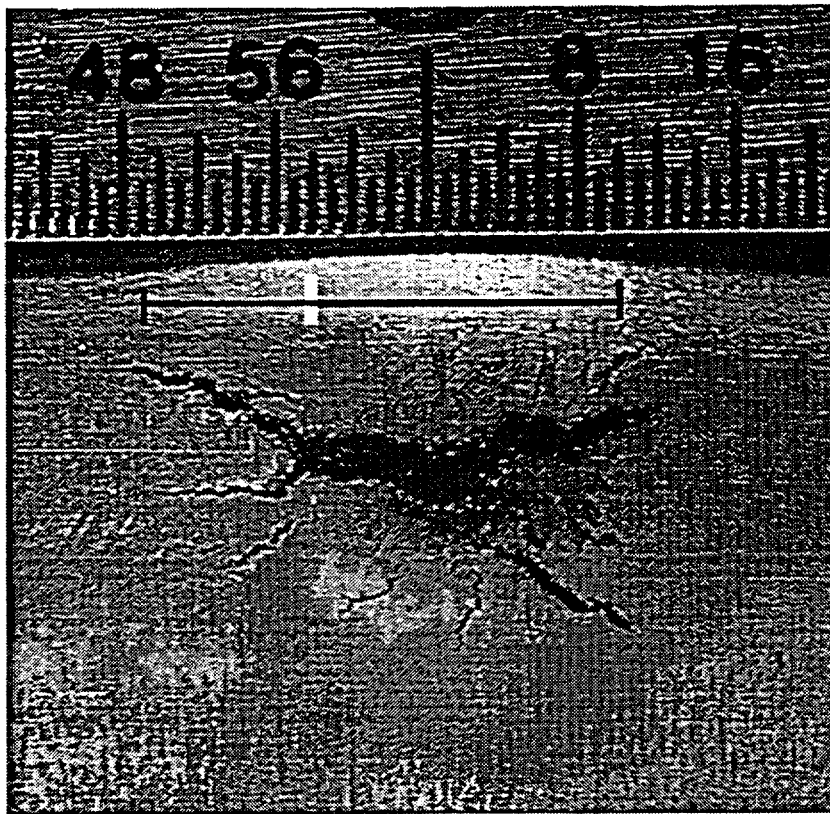
Fig. 4.51. Post-test view of OD crack of specimen SGL-104. Marker indicates effective throughwall crack length (10 mm or 0.39 in.) calculated from measured leak rate.

(2390 psi) for an equivalent crack length of 12.3 mm (0.48 in.). In this test, the leak rate was <0.04 L/min (<0.01 gpm) at 14.7 MPa (2129 psi), suggesting a throughwall crack length of <2 mm (<0.08 in.). The leak rate abruptly increased to 29.9 L/min (7.9 gpm) at 15.1 MPa (2188 psi) and then to 32.6 L/min (8.6 gpm) at 15.5 MPa (2250 psi). The estimated throughwall crack length corresponding to the largest leak rate is 12 mm (0.47 in.). The leak rate did not increase during a 15-min hold at 15.5 MPa (2250 psi). A post-test view of the crack at the OD surface is shown in Fig. 4.53, which also includes a marker identifying the estimated throughwall crack length. A comparison with Fig. 4.52a shows that the estimated crack length corresponds to the crack length over which the depth equals or exceeds about 70% of the wall thickness.

Figs. 4.54a-c show similar plots for test SGL-177, which was also conducted at room temperature. Note that in contrast to the previous cases, the ligament thickness in this specimen was highly nonuniform (Fig. 4.54a). The ligament rupture model (Fig. 4.54b) predicts a failure pressure of 30 MPa (4350 psi) for an equivalent crack length of 9 mm (0.35 in.). The predicted failure pressure is significantly greater than the experimentally observed 16.9 MPa (2450 psi). However, the leak rate in this test was essentially zero for the first 100-min hold at 16.9 MPa (2450 psi), after which a leak rate of 0.04 L/min
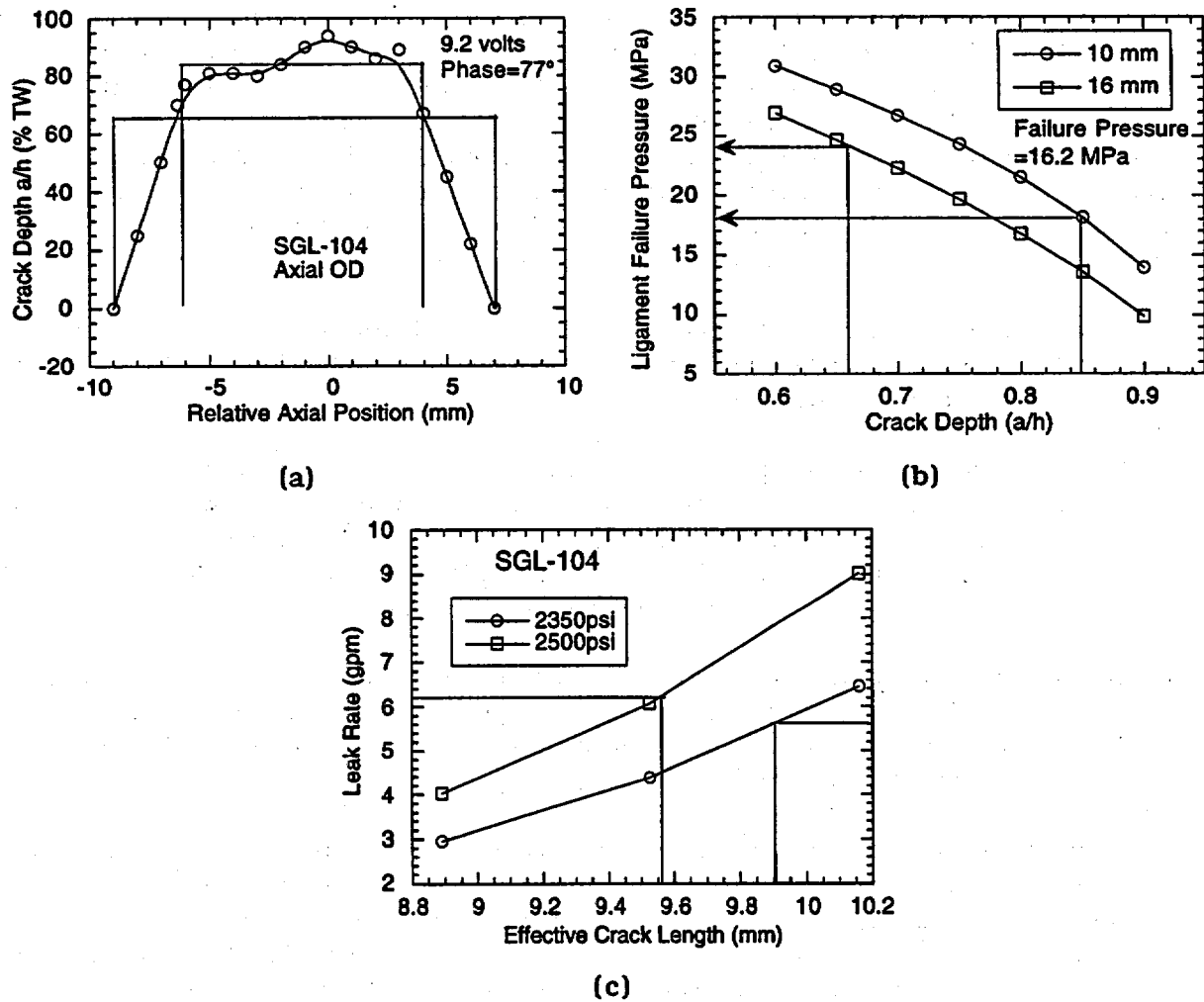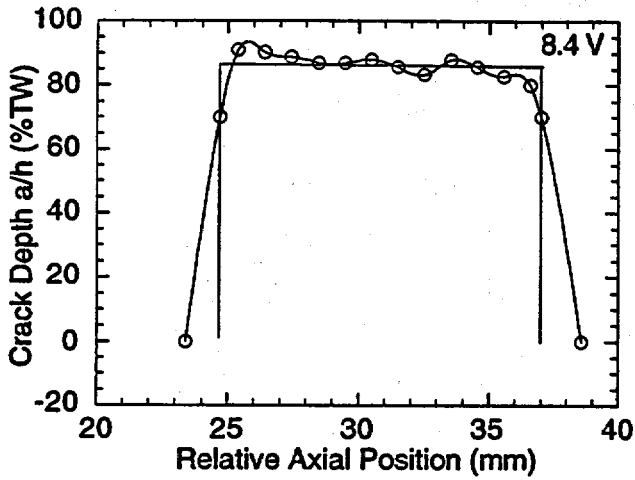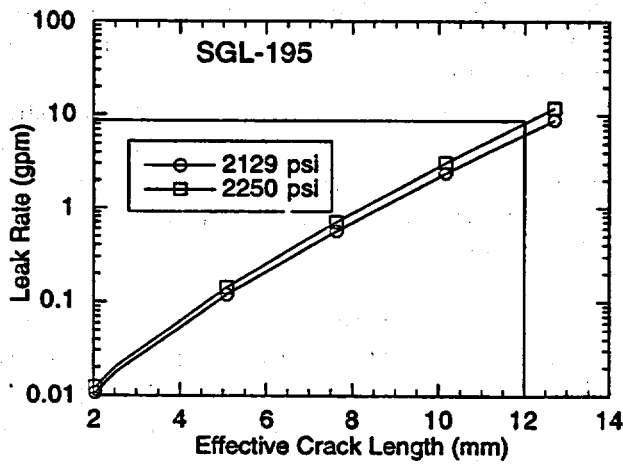
Fig. 4.52. *(a) Estimated crack depth profile from EC +Point data, (b) calculated ligament failure pressure for equivalent rectangular crack and (c) effective throughwall crack length estimated from leak-rate data for test SGL-195 conducted at 20°C.*
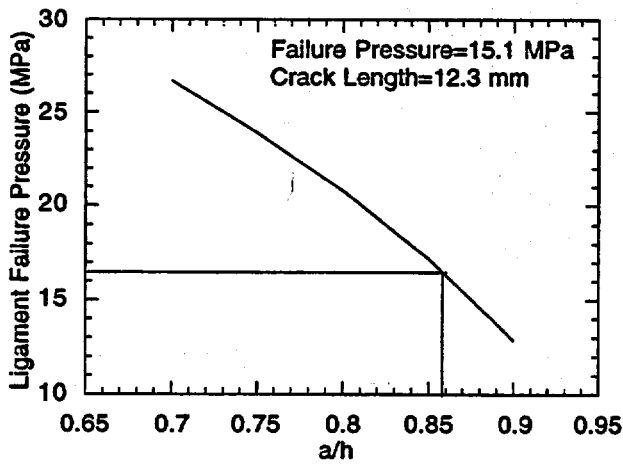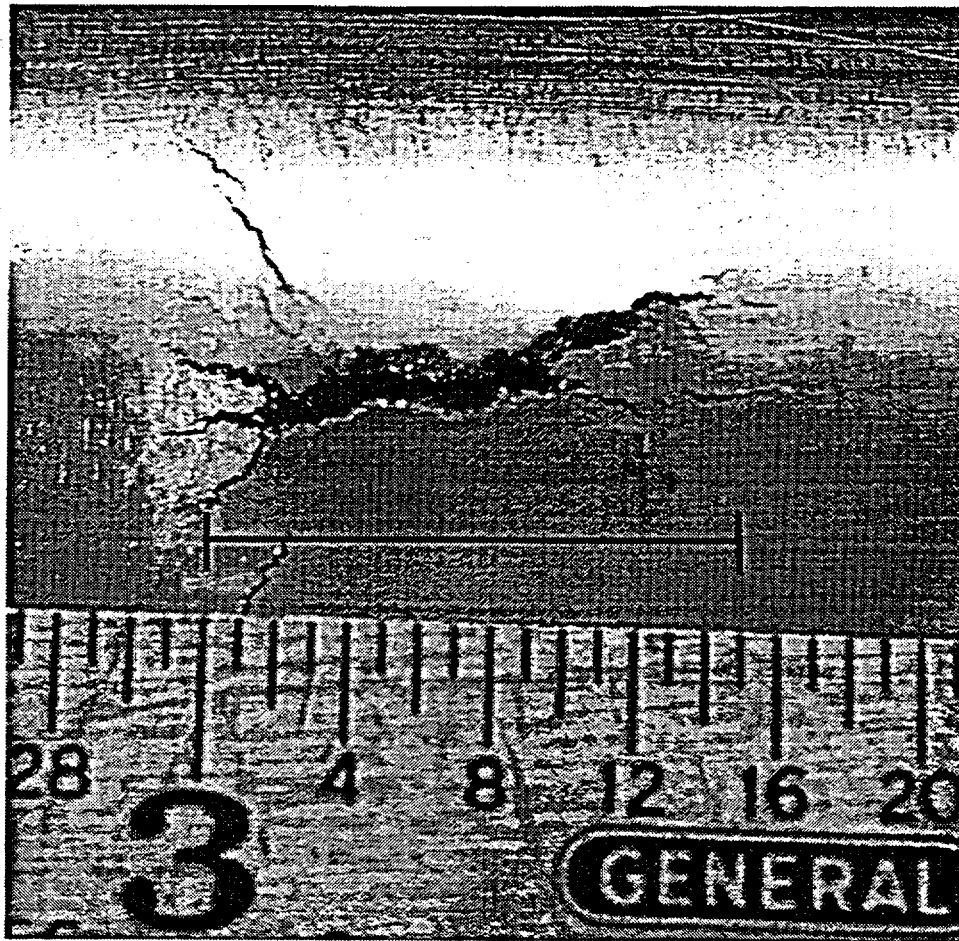
Fig. 4.53. Post-test view of OD crack of specimen SGL-195. Marker indicates effective throughwall crack length (12 mm or 0.47 in.) calculated from measured leak rate.

(0.01 gpm) was detected. The leak rate abruptly increased from 0.04 to 0.26 L/min (0.01 to 0.07 gpm) after a further 60-min hold at the same pressure. The leak-rate model (Fig. 4.54c) would imply that the throughwall crack length increased abruptly from 1.5 mm (0.06 in.) to 3.7 mm (0.15 in.). The leak rate increased to 1.7 L/min (0.44 gpm) when the pressure was increased to 19.3 MPa (2800 psi), suggesting that the throughwall crack length increased to 5.5 mm (0.22 in.), which again corresponds (Fig. 4.54a) approximately to the length over which the crack depth exceeds 70% wall thickness. A post-test picture of the crack (Fig. 4.55a) that also includes a marker of length 5.5 mm (0.22 in.). A comparison of the post-test crack (Fig. 4.55a) with its pretest dye-penetrant-enhanced view (Fig. 4.55b) shows that although some secondary cracks opened up, the surface length of the main crack did not increase during the test. This specimen was internally pressurized under water with 280 kPa (40 psi) air after the test. From the emerging air bubble, it was estimated that the length of the throughwall segment of the crack was ≈4 to 4.8 mm (0.16 to 0.19 in.). In view of the additional crack opening due to pressurization, the measured length of the throughwall segment of the crack is reasonably close to that
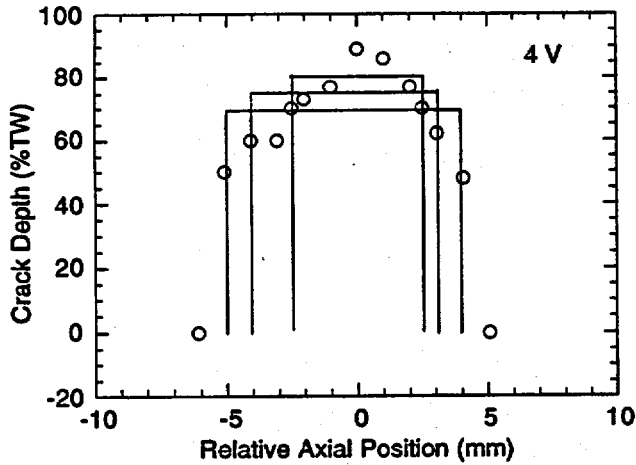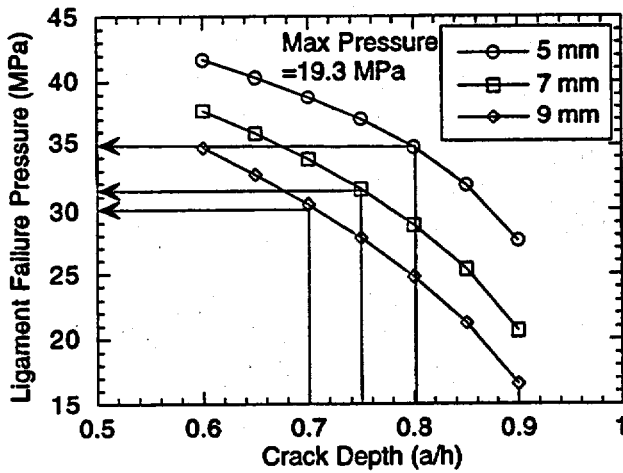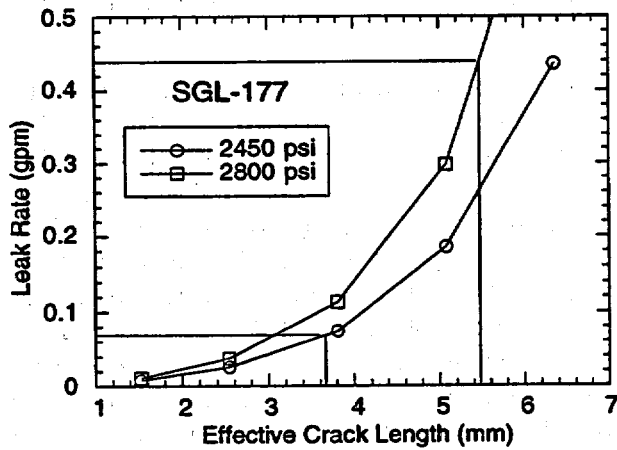
Fig. 4.54. (a) Estimated crack depth profile from EC +Point data, (b) calculated ligament failure pressure for two equivalent rectangular cracks and (c) effective throughwall crack length estimated from leak-rate data for test SGL-177 conducted at 20°C.

(a)   **(b)**
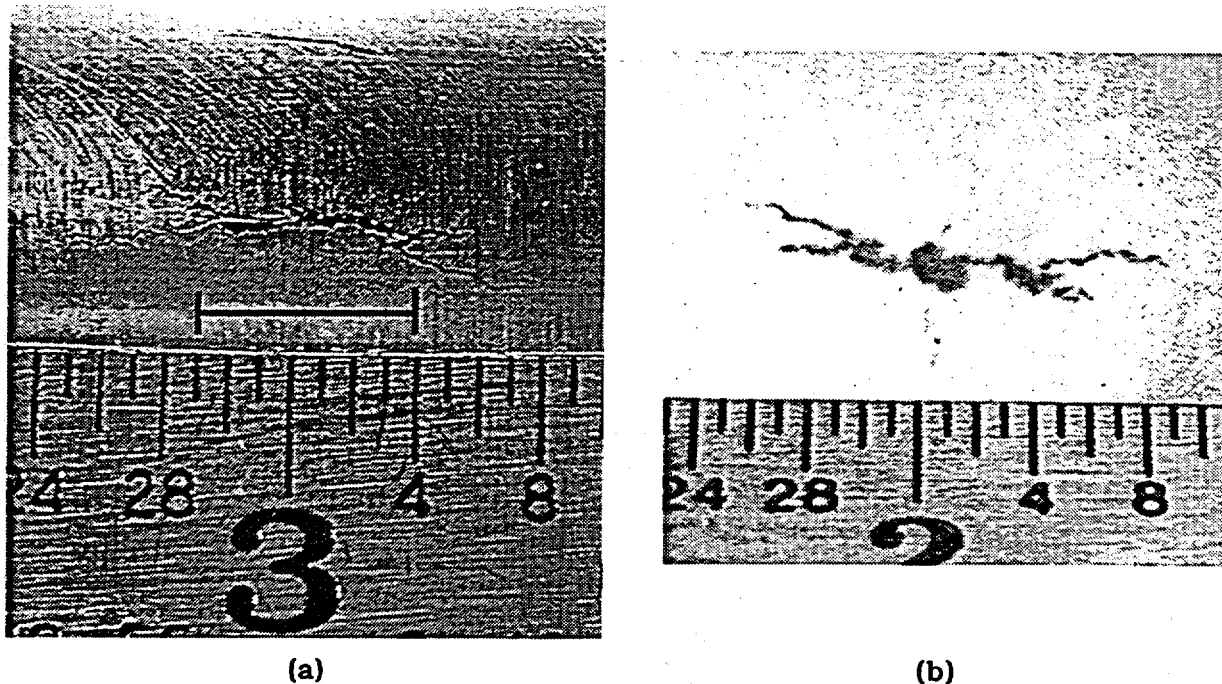
Fig. 4.55. (a) Post-test and (b) pre-test dye-penetrant-enhanced views of crack in test specimen SGL-177. Marker in (a) indicates effective throughwall crack length (5.5 mm or 0.22 in.) calculated from measured leak rate.

calculated from the measured leak rate. The two questions that remain unanswered from this test are (a) how long the leak rate would have continued to increase in a time-dependent fashion if the pressure were held constant at 19.3 MPa (2800 psi) indefinitely, and (b) whether the full ligament would have ruptured if the pressure, instead of being held constant, were rapidly increased to the calculated ligament rupture pressure.

Figures 4.56a-c show similar plots for test SGL-219, which was conducted at 282°C. Like test SGL-177, this specimen also had a highly nonuniform ligament thickness and may even have been segmented (Fig. 4.56a). The ligament rupture model (Fig. 4.56b) predicts a failure pressure of 20 MPa (2900 psi) for an equivalent crack length of 10.5 mm (0.41 in.). The predicted failure pressure is significantly greater than the experimentally measured 13.3 MPa (1925 psi). The leak rate for this specimen increased from 3.7 L/min (0.97 gpm) (the leak rate did not increase during a 90-min hold) at 13.3 MPa (1925 psi) to 14.0 L/min (3.7 gpm) at 16.2 MPa (2346 psi). Figure 4.56c suggests that the effective crack length is between 8.4 and 9.3 mm (0.33 and 0.37 in.). During an 11-min constant pressure hold at 16.2 MPa (2346 psi), the leak rate increased steadily from 14.0 to 39.0 L/min (3.7 to10.3 gpm,) which would suggest that the effective throughwall crack length increased to 11 mm (0.43 in.) during the hold period. The flow remained constant at 39.0 L/min (10.3 gpm) for the next 9 min at the same pressure. Note that although the final estimated throughwall crack length is reasonably close to that predicted by the ligament rupture model, the predicted rupture pressure is significantly less than the experimental maximum pressure. A post-test view of the crack at the OD surface is shown

Fig. 4.56. (a) Estimated crack depth profile from EC +Point data, (b) calculated ligament rupture pressure for two equivalent rectangular cracks, and (c) effective throughwall crack length estimated from leak-rate data for test SGL-219 conducted at 288°C.

Fig. 4.57. Post-test view of OD crack of specimen SGL219. Marker indicates effective throughwall crack length (11 mm or 0.43 in.) calculated from the measured leak rate.
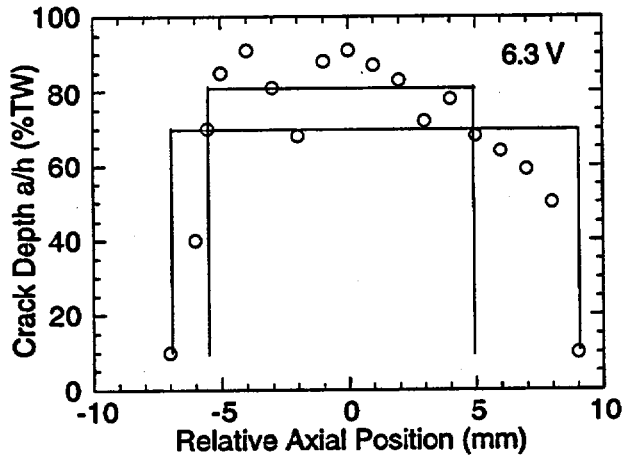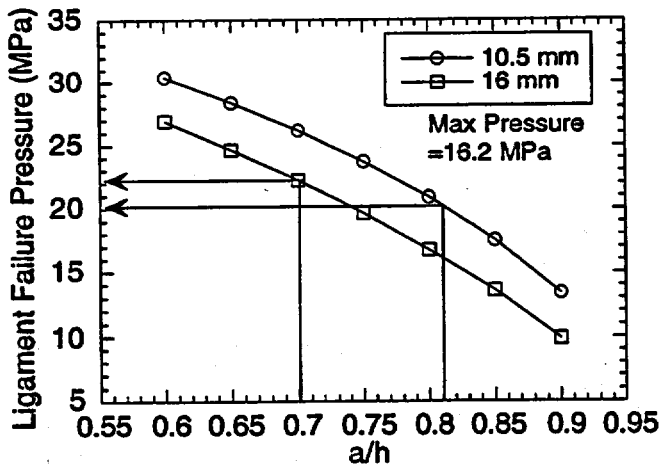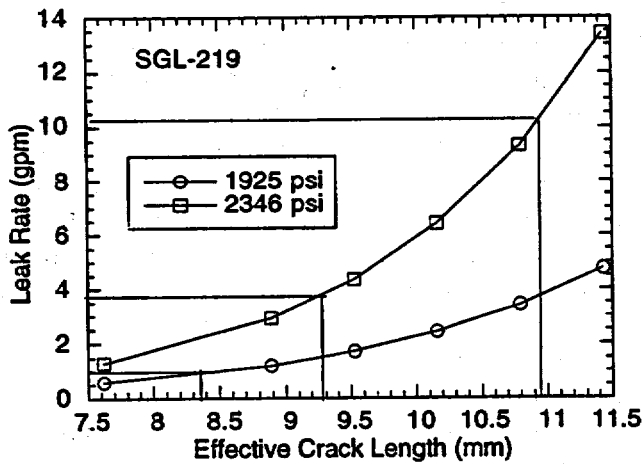
in Fig. 4.57, which also includes a marker identifying the estimated throughwall crack length. A comparison with Fig. 4.56a suggests that the estimated final crack length corresponds to the length over which the crack depth exceeds 70% of the wall thickness. Note that none of the ANL specimens showed the presence of OD axial segments separated by ligaments at the end of the tests, implying that all such ligaments most likely ruptured during the tests.

An additional pressure and leak-rate test was conducted on a tube with a SCC crack generated in doped steam. Figure 4.58 shows the pre-test crack depth profile by EC +Point. Note that the ligament thickness for this specimen was highly nonuniform, as in test specimen SGL-177. Two equivalent rectangular crack profiles (Figs 4.59a-b) were used for calculating the ligament rupture pressure. The yield strength and flow stress of the doped-steam tube were estimated from a few hardness tests at room temperature to be 240 and 485 MPa (35 and 70 ksi), respectively. The ligament rupture pressure was calculated to be 22.0 and 20.0 MPa (3190 and 2900 psi) at room temperature (Fig. 4.59a) and 282°C (Fig. 4.59b), respectively, for an equivalent crack length of 11 mm (0.43 in.). However, as in test SGL-177, this specimen developed a leak rate of 0.04 L/min (0.01 gpm) after a >3-h hold at 17.2 MPa (2500 psi) at room temperature, and the leak rate increased to 0.068 L/min (0.018 gpm) after an overnight hold at the same pressure. Figure 4.60 would imply that the effective throughwall crack length increased from 1.8 to 2.3 mm (0.07 to 0.09 in.) during this hold period. The leak rate then increased to 0.12 L/min (0.032 gpm) after a >5-h hold at 18.6 MPa (2700 psi), which would imply a
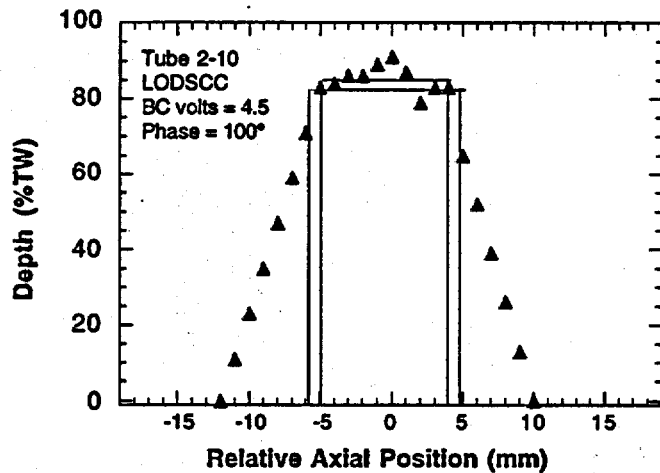
Fig. 4.58. Estimated crack depth profile from EC +Point data for tube 2-10.

(a)   (b)
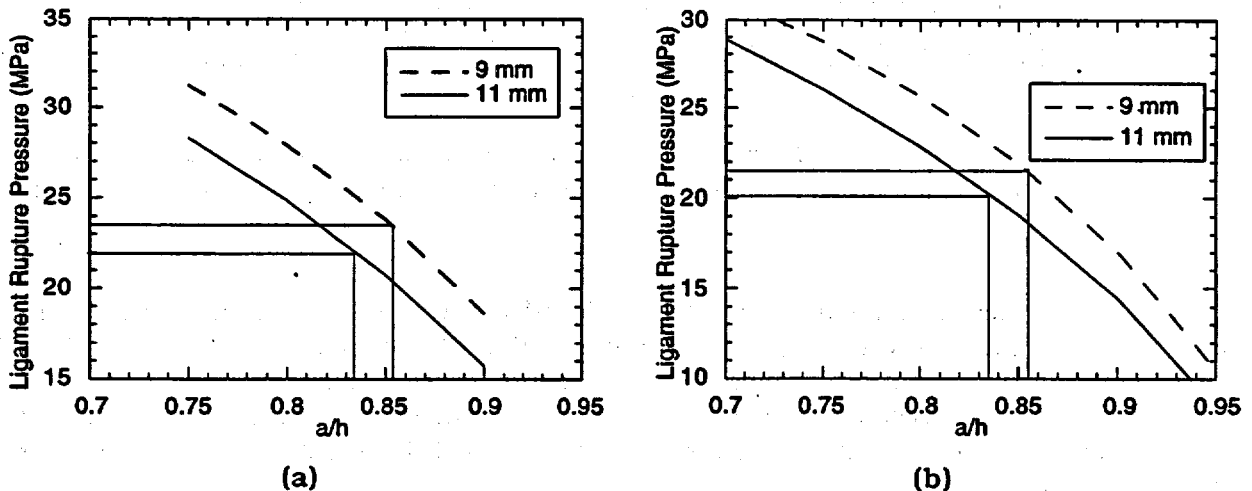
Fig. 4.59. Calculated ligament rupture pressure for two equivalent rectangular cracks in tube
2-10 at (a) room temperature and (b) 288°C.

final effective throughwall crack length of 2.8 mm (0.11 in.). The same specimen was
later pressurized to 18.6 MPa (2700 psi) at 282°C and held at constant pressure. The
leak rate was observed to increase from 0.30 to 0.72 L/min (0.08 to 0.19 gpm) during a
2–h hold. Figure 4.60 would imply that the effective throughwall crack length increased
from 3.6 to 4.8 mm (0.14 to 0.19 in.) during the hold period. Note that the ligament
rupture model overestimates the throughwall crack length, even though the final test
pressure is close to the predicted ligament rupture pressure (cf. SGL-219). A post-test
view of the crack at the OD surface is shown in Fig. 4.61, which also includes a marker
identifying the estimated throughwall crack length at 4.8 mm (0.19 in.).

In contrast to the ANL specimens, the estimated post-test throughwall crack length
for the doped-steam specimen is significantly shorter than that observed visually. A closer
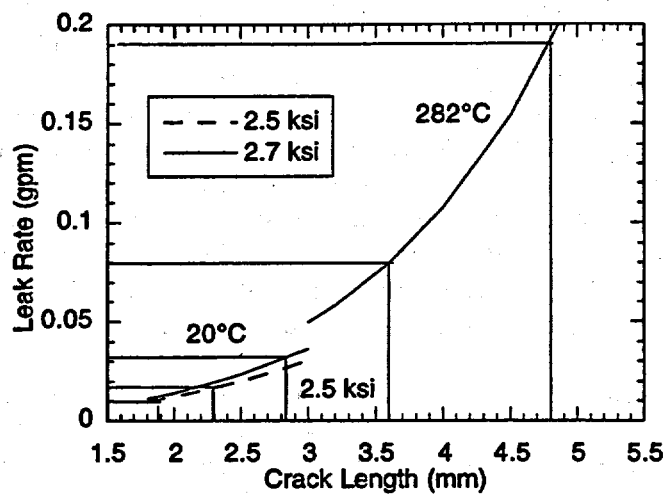
Fig. 4.60. *Calculated leak rate in tube 2-10 versus crack length for two pressures at room temperature and for 2.7 ksi at 282°C.*
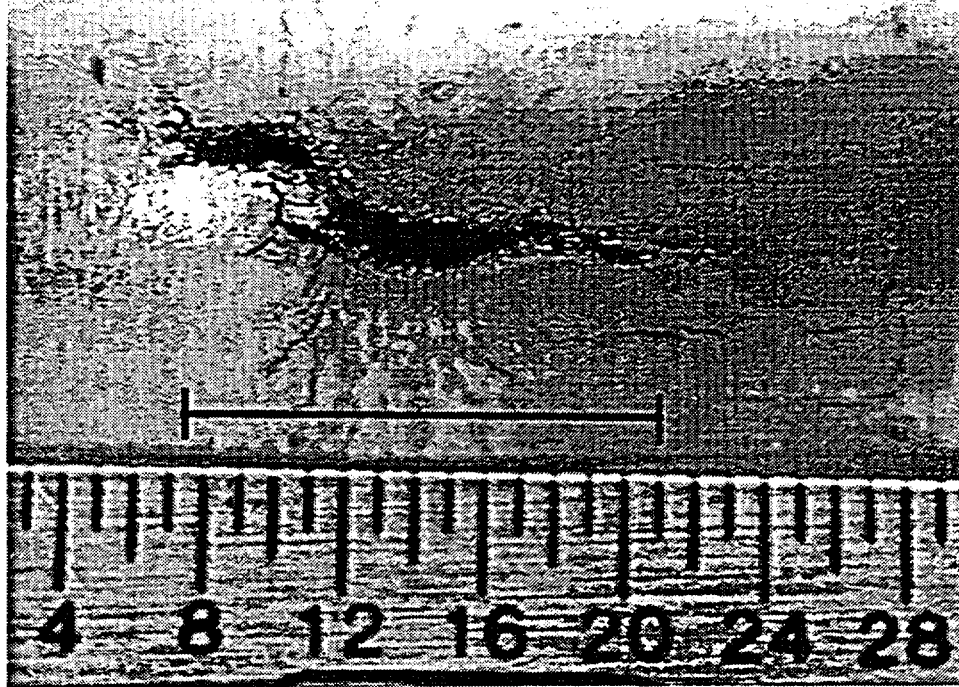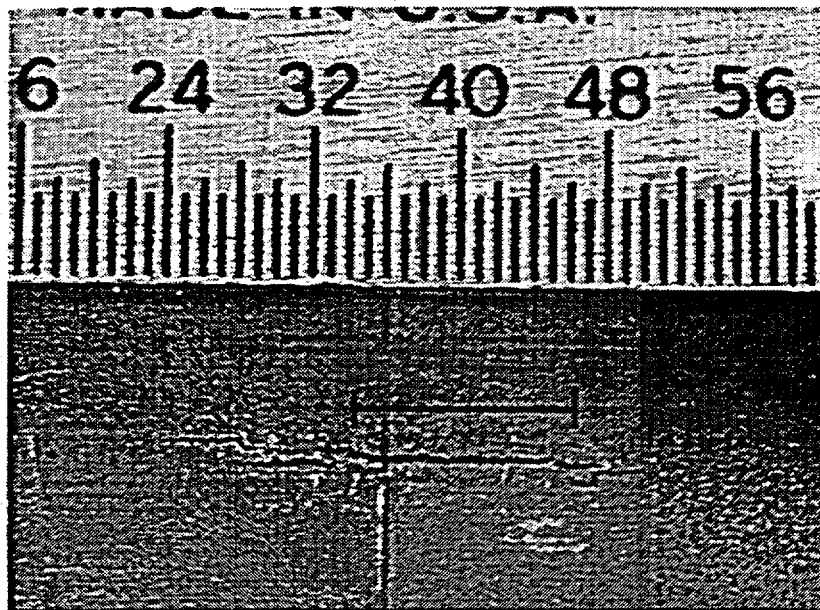

Fig. 4.61. *Post-test view of OD crack of specimen 2-10. Marker indicates effective throughwall crack length (4.8 mm or 0.19 in.) calculated from measured leak rate.*

examination of Fig. 4.61 shows that in contrast to the ANL specimens in which none of the ligaments between axial segments survived the test, the crack in the doped-steam specimen had at least three axial segments (undetected by EC +Point method) separated by 0.4-mm (0.015-in.)-thick surface ligaments that survived the pressure loading. It is not clear whether the ligaments between the segments persist through the full thickness of the tube wall. It is likely that the effective crack length calculated from the leak rate would be much closer to that observed visually if the stiffening effects of the ligaments on the crack opening area were taken into account. Also, the ligament rupture model using the equivalent rectangular crack approximation most likely underestimates the pressure to rupture the through-thickness crack tip ligament significantly (and overestimates the throughwall crack length) in this case for the same reason.

Discussions of results. If the pre-test crack depth profile is reasonably uniform and deep (80-90%) as measured by EC +Point, a significant portion of the through-thickness crack tip ligament can rupture abruptly at a pressure that can be calculated by the ANL correlation. Post-test pictures of the OD surface did not reveal the presence of any surface ligaments in these specimens. Effective throughwall crack lengths estimated by the ligament rupture model using the EC +Point data are reasonably close to those estimated from the leak-rate data and correspond closely to a segment of the crack that is >70% throughwall thickness. In these specimens, the leak rate generally increased abruptly from 0 or ≤0.04 L/min (≤0.01 gpm) to >19 L/min (>5 gpm) under increasing pressure loading, indicating sudden rupture of the ligament, and the leak rate did not increase under a constant-pressure hold subsequent to ligament rupture. It is not clear (although it appears likely) that leakage would have initiated eventually in similar specimens in a time-dependent fashion had they been subjected to a constant-pressure hold at a lower pressure before full ligament rupture.

For specimens with highly nonuniform crack tip ligament thickness (as measured by EC +Point) with predicted ligament failure pressures that are greater than our system capability (i.e., 19.3 MPa [2800 psi]), the ligaments can fail locally during a constant-pressure hold at a lower pressure than the predicted failure pressure. The effective throughwall crack lengths for these specimens can subsequently increase due to time-dependent ligament rupture at both room temperature and 282°C. In some cases, leakage began only after many minutes of constant-pressure hold, following which the leak rate often increased gradually or intermittently during constant-pressure holds (minutes), indicating that the ligament was undergoing time-dependent rupture. It is not clear how long the time-dependent ligament rupture process would have continued had the constant pressure been applied indefinitely. Based on very scant data, it appears that the time-dependent ligament rupture process occurs at a much slower rate (hours rather than minutes) in the higher-strength doped-steam tube than in the lower-strength heat-treated ANL tubes. Also, the time-dependent rupture process occurs more rapidly at 282°C than at room temperature. A procedure for converting the constant-pressure-hold data on time-dependent leak rate from heat-treated tube to as-received tube must be developed in the future.

In all ANL specimens tested to date, the lengths of the throughwall segments of the cracks calculated from leak-rate data are close to the lengths of the most open part of the cracks, as evident visually from post-test pictures of the specimens. None of these pictures showed the presence of axial segments separated by ligaments. For test SGL-177,

the post-test measured length of the throughwall segment of the crack (by the bubble technique) is reasonably close to that calculated from the measured leak rate. Also, the effective throughwall crack lengths calculated from the leak-rate data correspond to a length of the crack that is >70% throughwall thickness (as measured by EC +Point method). In contrast to the ANL specimens, the calculated throughwall crack length for the doped-steam specimen is much shorter than that observed visually. However, a post-test picture of the OD surface of this specimen revealed at least three axial segments separated by ligaments, showing that the effective throughwall crack length can be seriously underestimated from the measured leak rate if the effects of the ligaments on the crack opening area are not taken into account.

Procedure for calculating leak-rate correction factor. Based on the above discussion, we tentatively propose the following procedure for calculating the leak-rate correction factors for tests conducted between 10.3 and 19.3 MPa (1500 and 2800 psi) on laboratory-grown deep and approximately planar SCC cracks 9-16 mm (0.35-0.63 in.) long (with possibly a few initial nonleaking throughwall segments):

From the measured leak rate at a given temperature and pressure, estimate the effective throughwall crack length using Eq. 4.33a, the Zahoor model for flaw opening area (Eq. 4.34) and the flow properties of the annealed and sensitized material, assuming that even if the crack was initially segmented axially, all the ligaments between the segments are ruptured before the leak-rate data are taken. If the crack remains segmented at the time the leak rate is measured, a different set of correction factors must be developed to take into account the geometry of the remaining ligaments.

It is recommended that the calculated effective throughwall crack length should be confirmed by post-test immersion bubble test. If possible, throughwall crack lengths in a few of the SCC specimens should also be measured by post-test sectioning. In particular, it should be established whether any of the ligaments separating the axial segments survived the test.

The leak-rate correction factor can be obtained from Fig. 4.49a for a given temperature, pressure, and effective throughwall crack length. These curves are inapplicable if the crack remains axially segmented at the time the leak rate is measured. It should be noted that the correction factor gives the leak rate in the as-received tube having the same effective throughwall crack length as in the heat-treated tube subjected to the same temperature and pressure. This does not imply that the as-received tube with the same pre-test crack morphology as the heat-treated tube would experience the calculated leak rate if subjected to the same pressure history as the heat-treated tube.

Currently, we do not have a method for converting the time-dependent leak-rate data for the heat-treated tube to those for the as-received tube.

4.6.4 Conclusions about Failure Mechanisms

The conclusions here are drawn from limited number of tests on approximately planar (macroscopically) SCC cracks, 9-16 mm (0.35-0.63 in.) long, as measured by pre-test EC +Point, during pressure and leak-rate tests at 10.3-19.3 MPa (1500 to 2800 psi). They

require verification by further tests on specimens with different crack sizes and morphology, including post-test sectioning of some of the specimens.

In all specimens tested to date, including the one cracked using doped steam, very short throughwall segments already existed before testing, as evidenced by leakage of gas at 275 kPa (40 psi). However, the same specimens did not show measurable water leakage even up to 10.3 MPa (1500 psi), implying that these throughwall segments were so short and tortuous that they did not open up significantly under pressure to allow leakage of water. The time-dependent history and magnitude of leakage from a laboratory-grown SCC crack during pressure testing depends critically on the sequence of rupture events of the ligaments between axial segments and the through-thickness crack tip ligaments (some of which are initially breached). Two extreme scenarios are helpful in discussing these effects during pressurization of the tube, although in reality there will be a mixture. At one extreme (scenario 1), if all or even a significant fraction of the ligaments between the axial segments rupture before through-thickness rupture of a significant fraction of crack tip ligaments (including those that were already breached before the test), we would expect to see an abrupt initiation of large leakage when the crack tip ligaments finally fail by plastic collapse. It would be expected that in these cases, the ligament rupture model based on a long equivalent rectangular part-through crack would predict the rupture pressure reasonably well. ANL specimens SGL-104 and SGL-195 tended to follow this pattern.

At the other extreme (scenario 2), if the through-thickness crack tip ligament of one or more axial segments rupture before any of the ligaments separating the axial segments, the total leakage remains low because the crack-opening areas of the individual throughwall segments are small. In these cases, the initial pressure to cause measurable leakage can be much lower than the ligament rupture pressure calculated for a full rectangular part-through crack because the leakage will be due to gradual opening of short throughwall segments (including the pre-existing throughwall segments), as well as successive rupture of ligaments at the through-thickness tips of shallower segments with increasing pressure. The continuous or intermittent time-dependent increase of the leak rate during a constant-pressure hold may be due to anelastic effects and/or sequential rupture of the through-thickness ligaments of the crack segments. Although more data are needed to confirm this, the time-dependent rupture process appears to be faster at higher temperatures and lower flow stresses. Occasional failure of ligaments between axial segments can also contribute towards the intermittent increases of leak rate. However, as long as some of the ligaments separating the axial segments survive, the total leak rate under scenario 2 will be much lower than that under scenario 1. The doped-steam specimen appeared to follow this pattern. Ultimately, with increasing pressure, all the ligaments separating the axial segments will eventually rupture even under scenario 2, and the leak rates under both scenarios would converge. The actual failure path followed by any particular specimen is controlled by the relative thicknesses and widths of the various crack-tip ligaments and the ligaments between the various axial segments. Therefore, it is recommended that a series of specimens with multiple laser-cut notches (to keep the notch width small compared to ligament widths) with several ligament widths be tested to establish failure criteria for the various ligaments.

A shortcoming of the EC +Point method as it is practiced today is that although it can detect narrow through-thickness crack tip ligaments quite accurately, it fails to detect narrow ligaments between axial crack segments. Thus, if the +Point data are used ignoring

the presence of axial segments, the leak rate may be significantly overestimated. Conversely, the crack length can be seriously underestimated from the measured leak rate if the segmented nature of the axial crack is not taken into account. Although the ligaments between axial segments were ruptured in most of the ANL specimens, at least three survived in the doped-steam specimen up to 18.6 MPa (2700 psi) at 282°C. It would be extremely useful for future development of leak-rate and failure models for SG tubes if a procedure can be developed to estimate the number, size, and shape of the ligaments between axial crack segments from the EC +Point data.

5 Integration of Results, Methodology, and Technical Assessments for Current and Emerging Regulatory Issues (D. S. Kupperman and D. R. Diercks)

5.1 Electrosleeved Tubes

Several tube sections with cracks grown at ANL have been Electrosleeved by Framatome Technologies, Inc. (FTI). Results of EC and ultrasonic (UT) examinations of two test sections are presented in this report. Figure 5.1 shows the EC isometric plot of a CODSCC 90% TW of a 22.2-mm (7/8-in.)-diameter Alloy 600 test section before Electrosleeving. The scan was generated with a +Point probe at 300 kHz. The wall thickness is 1.25 mm (0.050 in.). Figure 5.2 shows the degraded EC isometric plot of the 90% TW CODSCC after Electrosleeving. This scan was also generated with a +Point probe at 300 kHz. The total wall thickness of the Electrosleeved test section is ≈2.1 mm (0.085 in.). Figure 5.3 shows the EC isometric plot of a 360° CIDSCC, ≈40% TW, of a 22.2-mm (7/8-in.)-diameter Alloy 600 test section before Electrosleeving. The scan was generated with a +Point probe at 300 kHz. The wall thickness is 1.25 mm (0.050 in.). Figure 5.4 shows the EC isometric plot of the CIDSCC after the test section was Electrosleeved. The scan was also generated with a +Point probe at 300 kHz. The total wall thickness is about 2.1 mm (0.085 in.). Although significant deterioration of the EC signal is evident after Electrosleeving, detection through the Electrosleeve of relatively deep cracks (>40% TW) is still possible, at least under laboratory conditions.

The two test sections examined with ECs were also examined with UT 65° shear waves launched in the Electrosleeve by means of a 3.5 MHz, 6-mm (0.25-in.)-diameter PZT crystal on a wedge curved to fit the ID surface of the Electrosleeved test section. This configuration results in the propagation of essentially guided waves in the test section wall. Figure 5.5 shows the ultrasonic echo (center of trace) from the 90% TW CODSCC parent tube of the Electrosleeved 22.2-mm (7/8-in.)-diameter Alloy 600 test section. The echo from the crack can be distinguished from spurious signals by its movement to shorter transit times as the probe approaches the crack. Crack echoes are recorded in a 12-15 μs window. Fig. 5.6 shows the ultrasonic echo expanded from the center of the trace in Fig. 5.5.

Figure 5.7 shows an UT echo from the 40% TW (0.5-mm-deep) CIDSCC in the parent tube of the second Electrosleeved test section. The total tube wall thickness with sleeve is again ≈2.1 mm (0.085 in.). The echo from the crack can be distinguished from spurious signals by its movement to shorter transit times as the probe approaches the crack. Again, the crack echo is recorded in a 12-15 μs window. This crack does not intersect either the ID or the OD of the Electrosleeved tube, and thus no corner reflector is present to provide a strong ultrasonic echo. The echo is the result of backscattered UT waves from the crack surface.

Figure 5.8 shows an UT reference echo from a 1.0-mm (0.040-in.)-deep COD-EDM notch in a 2.5-mm (0.010-in.)-thick wall of a 22.2-mm (7/8-in.)-diameter test section. The echoes are also recorded in a 12-15 μs window. This reference test section has been very useful for setting up the UT system and setting system parameters.
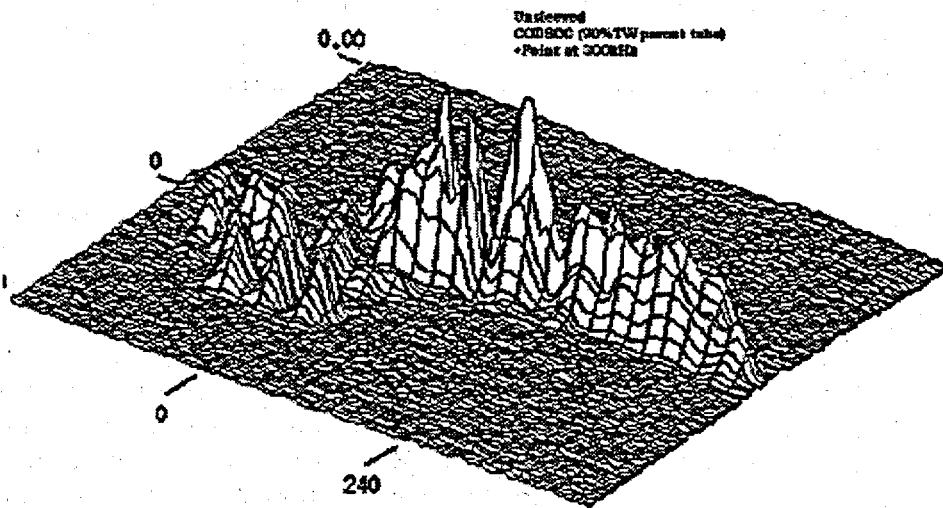
Fig. 5.1. *Eddy current isometric plot of CODSCC 90% TW of 22.2-mm (7/8-in.)-diameter Alloy 600 tube before Electrosleeving. Scan was generated with +Point probe at 300 kHz. Wall thickness is 1.25 mm (0.050 in.).*
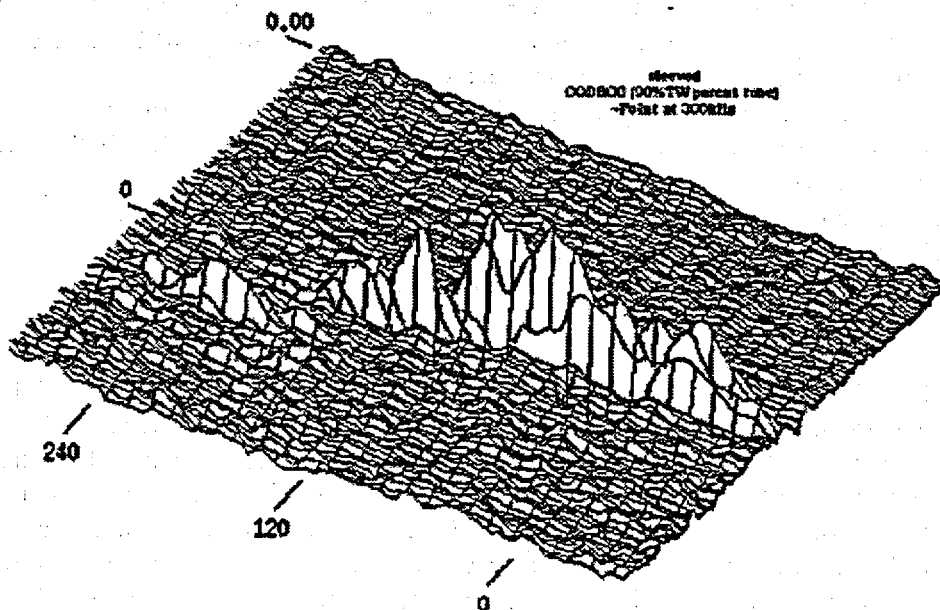

Fig. 5.2. *Eddy current isometric plot of CODSCC 90% TW of parent tube in 22.2-mm (7/8-in.)-diameter Alloy 600 Electrosleeved tube (courtesy of FTI). Scan was generated with +Point probe at 300 kHz. Total wall thickness is ≈2.1 mm (0.085 in.).*
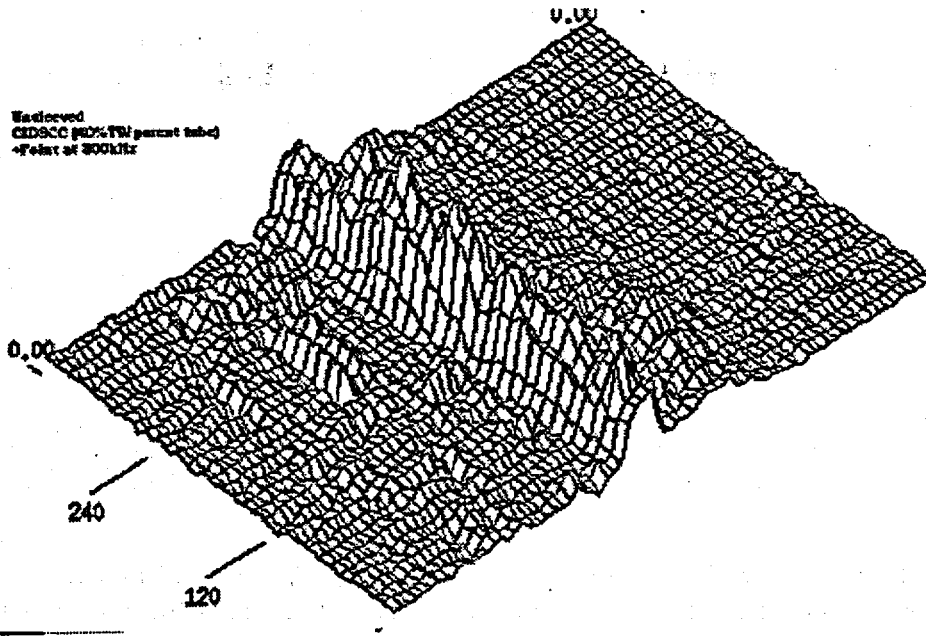
Fig. 5.3. *Eddy current isometric plot of CIDSCC ≈ 40% TW of 22.2-mm (7/8-in.)-diameter Alloy 600 tube before Electrosleeving. Scan was generated with +Point probe at 300 kHz. Wall thickness is 1.25 mm (0.050 in.).*
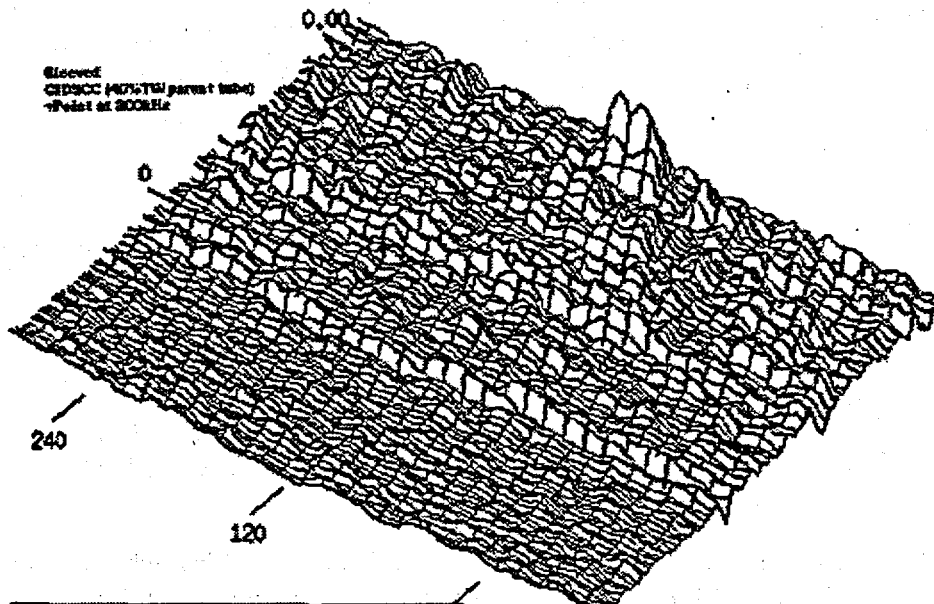

Fig. 5.4. *Eddy current isometric plot of CIDSCC ≈40% TW of parent tube in 22.2-mm (7/8-in.)-diameter Alloy 600 Electrosleeved tube (courtesy of FTI). Scan was generated with +Point probe at 300 kHz. Total wall thickness is about 2.1 mm (0.085 in.).*
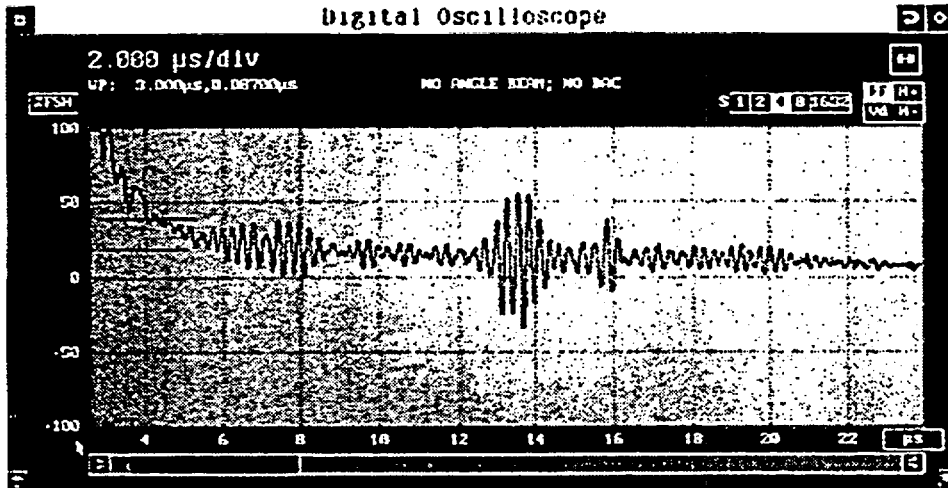
Fig. 5.5. *Ultrasonic echo (center of trace) from CODSCC, 90% TW in 1.25-mm (0.050-in.)-wall-thickness parent tube of Electrosleeved 22.2-mm (7/8-in.)-diameter Alloy 600 tube. Total tube wall thickness is ≈2.1 mm (0.085 in.). A 3.5 MHz, 6-mm (0.25-in.)-diameter PZT crystal on a wedge launches 65° shear waves from ID into Electrosleeve, effectively generating guided waves in tube wall. Echo from crack can be distinguished from spurious signals by its movement to shorter transit times as the probe approaches the crack. Crack echoes are recorded in a 12-15 μs window.*
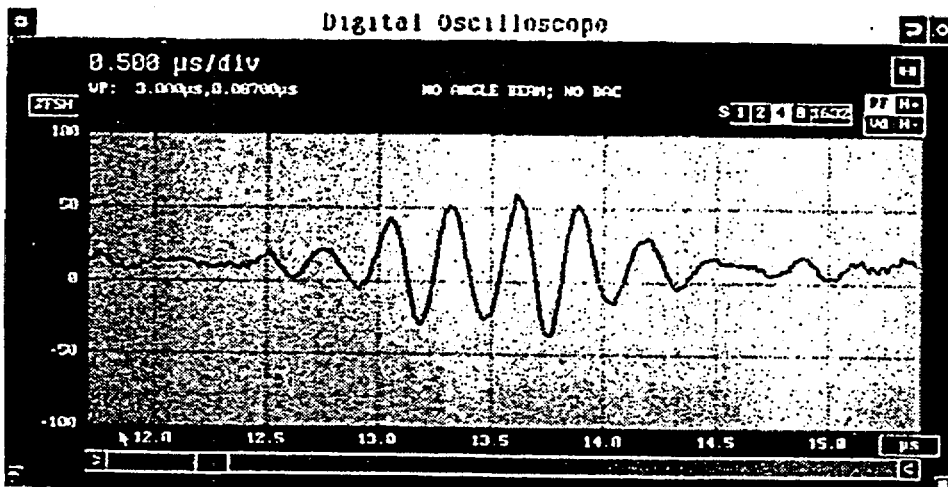

Fig. 5.6 *UT echo expanded from center of trace in Fig 5.5. This echo is from a CODSCC, 90% TW in 1.25-mm (0.050-in.)-wall-thickness parent tube of Electrosleeved 22.2–mm (7/8-in.)-diameter Alloy 600 tube. Total tube wall thickness Is ≈2.1 mm (0.085 in.).*
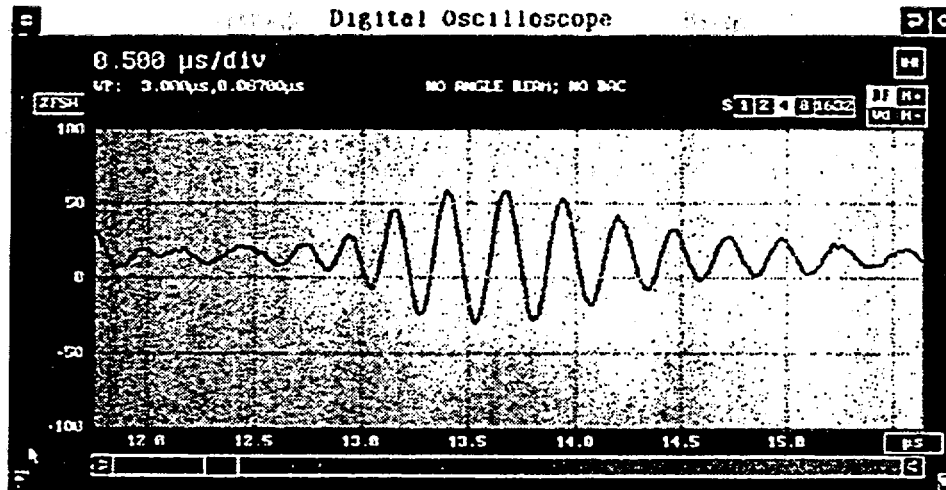
Fig. 5.7. *Ultrasonic echo from CIDSCC, 40% TW (0.5-mm-deep) in 1.25-mm (0.050-in.)-wall thickness parent tube of Electrosleeved 22.2-mm (7/8-in.)-diameter Alloy 600 tube. Total tube wall thickness with sleeve is ≈2.1 mm (0.085 in.). This crack does not intersect either ID or OD of Electrosleeved tube and thus no corner reflector is present to provide a strong ultrasonic echo. Echo is result of backscattered waves from crack surface.*
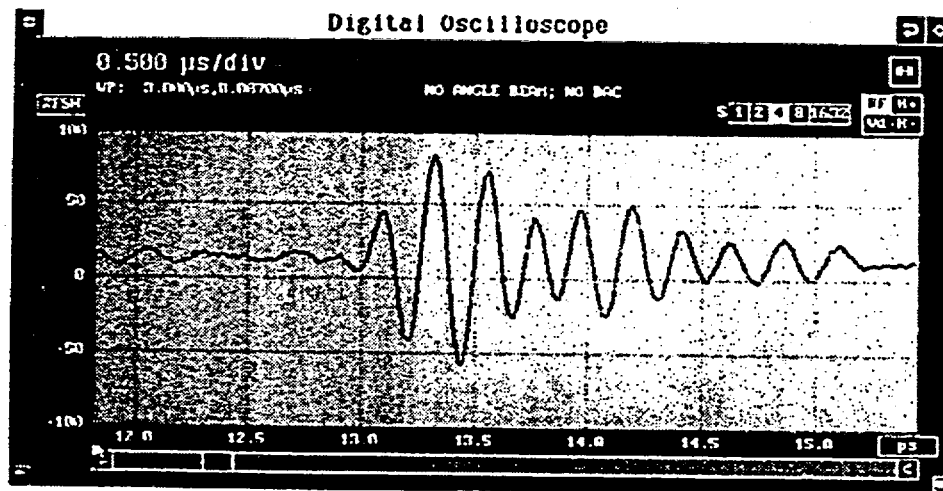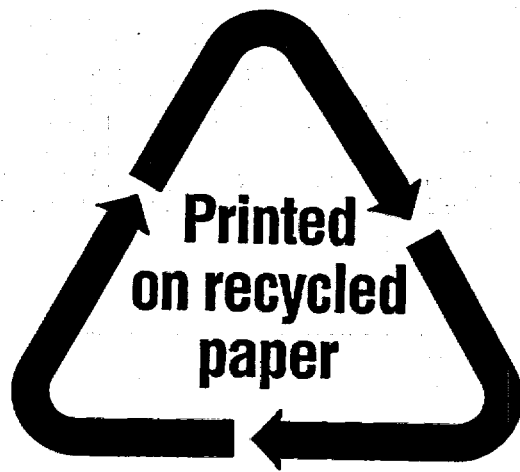

Fig. 5.8. *Ultrasonic reference echo from 1.0-mm (0.040-in.)-deep COD EDM notch in 2.5-mm (0.010-in.)-thick wall of 22.2-mm (7/8-in.)-diameter tube. Notch echoes are recorded in 12-14 μs window.*

For the CODSCC, CIDSCC and EDM notches, the UT echoes have a very good S/N ratio. By using a frequency of ≈3-4 MHz, the distortion of the UT signal from the rough ID surface of the Electrosleeve is minimized. Propagation of waves nearly parallel to the tube axis allows echoes to be generated from cracks that do not intersect either the ID or OD without the need for a corner reflector to provide a strong echo for crack detection.

References

1. D. R. Diercks, et al., Steam Generator Tube Integrity Program, Annual Report, October 1996-September 1997, NUREG/CR-6511, Vol. 4, ANL-98/15, U.S. Nuclear Regulatory Commission, Washington, DC (Jan. 1999).

2. D. R. Diercks, et al., Steam Generator Tube Integrity Program, Annual Report, October 1997-September 1998, NUREG/CR-6511, Vol. 6, ANL-99/8, U.S. Nuclear Regulatory Commission, Washington, DC (Oct. 1999).

3. Ranganath, S., and Mehta, H. S., "Engineering methods for the assessment of ductile fracture margin in nuclear power plant piping," Fracture Resistance Curves and Engineering Applications, ASTM STP 803, Philadelphia, 1983.

4. Hernalsteen, P., "Structural and Leakage Integrity of Tubes Affected by Circumferential Cracking," pp. 233-257 in Proceedings of the CNRA/CSNI Workshop on Steam Generator Integrity in Nuclear Power Plants, NUREG/CP-0154, ANL-96/14, NEA/CNRA/R(96)1 (Feb. 1997).

5. Wilkowski, G. M., et al., "Degraded-Piping Program - Phase II," Semiannual Report, NUREG/CR-4082, Vols. 1-8, USNRC, Washington, DC, 1984-1989.

6. Wilkowski, G. M., et al., "Short Cracks in Piping and Piping Welds," Semiannual Report, NUREG/CR-4599, Vols. 1-3, USNRC, Washington, DC, 1991-1994.

7. Tada, H., Paris, P. C., and Gamble, R. M., "A stability analysis of circumferential cracks for reactor piping systems," Fracture Mechanics, ASTM STP 700, Philadelphia, 1980.

8. Smith, E., "The effect of axial forces on the conservatism of the net-section stress criterion for the failure of cracked stainless steel piping," SMiRT-12, Vol. G, pp. 57-62, 1993.

9. Smith, E., "Leakage via a through-wall circumferential crack in a piping or tubing system under accidental loading conditions," Int. J. Pressure Vessels and Piping, Vol. 75, pp. 121-124, 1998.

10. Smith, E., "Factors influencing the crack-system compliance of a piping system," Int. J. Pressure Vessels and Piping, Vol. 75, pp. 125 -129, 1998.

11. Wilkowski, G. M., Nucl. Eng. and Des., Vol. 98, p. 195, 1987.

12. Paris, P. C., and Tada, H., "The application of fracture proof design methods using tearing instability theory to nuclear piping postulating circumferential throughwall cracks," NUREG/CR-3464, USNRC, Washington, DC, 1983.

13. K. E. Kasza and S. Majumdar, and J. Muscara, "Steam Generator Tube Integrity Testing/Analysis," presented at SMiRT-15 Conference. Seoul, Korea, Aug. 1999.

2. TITLE AND SUBTITLE

Steam Generator Tube Integrity Program

Semiannual Report
October 1998 - March 1999

3. DATE REPORT PUBLISHED

MONTH	YEAR
September	2000

4. FIN OR GRANT NUMBER
W6487

5. AUTHOR(S)

D.R. Diercks, S. Bakhtiari, K.E. Kasza, D.S. Kupperman,
S. Majumdar, J.Y. Park, W.J. Shack

6. TYPE OF REPORT

Technical; Semiannual

7. PERIOD COVERED *(Inclusive Dates)*

October 1998 - March 1999

8. PERFORMING ORGANIZATION - NAME AND ADDRESS *(If NRC, provide Division, Office or Region, U.S. Nuclear Regulatory Commission, and mailing address; if contractor, provide name and mailing address.)*

Argonne National Laboratory
9700 South Cass Avenue
Argonne, IL 60439

9. SPONSORING ORGANIZATION - NAME AND ADDRESS *(If NRC, type "Same as above"; if contractor, provide NRC Division, Office or Region, U.S. Nuclear Regulatory Commission, and mailing address.)*

Division of Engineering Technology
Office of Nuclear Regulatory Research
U.S. Nuclear Regulatory Commission
Washington, DC 20555-0001

10. SUPPLEMENTARY NOTES

J. Muscara, NRC Project Manager

11. ABSTRACT *(200 words or less)*

This report summarizes work performed by Argonne National Laboratory the Steam Generator Tube Integrity Program during the period October 1998 through March 1999. The program is divided into five tasks: (1) Assessment of Inspection Reliability, (2) Research on In-Service Inspection (ISI) Technology, (3) Research on Degraded Modes and Integrity, (4) Integration of Results, Methodology, and Technology Assessments for Current and Emerging Regulatory Issues, and (5) Program Management. Under Task 1, progress is reported on the status of the steam generator tube mockup, the effect of a thin oxide on the eddy current signal from stress corrosion cracks and the effectiveness of +Point eddy current techniques for profiling cracks. Under Task 2, efforts focused on the multiparameter analysis of eddy current NDE results, and estimated depth profiles are provided for a set of 24 laser-notched specimens. Under Task 3, pressure and leak-rate test results are reported for tubes with EDM flaws as well as a tube with part throughwall SCC produced by Westinghouse. The design and construction of a new high-pressure test facility has also been initiated. Laboratory-induced cracking has been produced in hundreds of steam generator tubes that we\ill subsequently be used for NDE studies and for pressure and leak-rate testing. In addition, models for predicting the onset of crack growth and for calculating crack opening area and leak rate from a throughwall circumferential crack in a steam generator tube have been developed. Leak-rate models haven been validated with tests on specimens with notched EDM slots, and simplified equations for calculating crack opening area have been verified with finite-element calculations. Finally, under Task 4, results of EC and ultrasonic examinations of two cracked test sections electrosleeved by FTI are presented.

12. KEY WORDS/DESCRIPTORS *(List words or phrases that will assist researchers in locating the report.)*

Steam Generator
Tubes
Stress Corrosion Cracking
Eddy Current Testing
Nondestructive Evaluation
In-service Inspection
Pressure Testing
Tube Burst
Leak Rate
Alloy 600, Inconel 600

13. AVAILABILITY STATEMENT
unlimited

14. SECURITY CLASSIFICATION

(This Page)
unclassified

(This Report)
unclassified

15. NUMBER OF PAGES

16. PRICE

UNITED STATES
NUCLEAR REGULATORY COMMISSION
WASHINGTON, D.C. 20555-0001

1975 **25** 2000
years